Title
Numerical and experimental investigation of the Argon Power Cycle for power generation efficiency improvement and emissions reduction

Author
Sierra Aznar, Miguel

Publication Date
2018

Peer reviewed|Thesis/dissertation

Numerical and experimental investigation of the Argon Power Cycle for power generation efficiency improvement and emissions reduction

by

Miguel Sierra Aznar

A dissertation submitted in partial satisfaction of the

requirements for the degree of

Doctor of Philosophy

in

Engineering - Mechanical Engineering

in the

Graduate Division

of the

University of California, Berkeley

Committee in charge:

Professor Robert Woodrow Dibble, Chair

Professor Jyh-Yuan Chen

Professor Enrique Iglesia

Summer 2018

Abstract

Numerical and experimental investigation of the Argon Power Cycle for power generation efficiency improvement and emissions reduction

by

Miguel Sierra Aznar

Doctor of Philosophy in Engineering - Mechanical Engineering

University of California, Berkeley

Professor Robert Woodrow Dibble, Chair

Carbon capture has been deemed crucial by the Intergovernmental Panel on Climate Change if the world is to achieve the ambitious goals stated in the Paris agreement. A deeper integration of renewable energy sources is also needed if we are to mitigate the large amount of green house gas emitted as a result of increasing world fossil fuel energy consumption. These new power technologies bring an increased need for distributed fast dispatch power and energy storage that counteract their intermittent nature. A novel technological approach to provide fast dispatch emission free power is the use of the Argon Power Cycle, a technology that makes carbon capture an integral part of its functioning principle. The core concept behind this technology is a closed loop internal combustion engine cycle working with a monoatomic gas in concert with a membrane gas separation unit. By replacing the working fluid of internal combustion engines with a synthetic mixture of monoatomic gases and oxygen, the theoretical thermal efficiency can be increased up to 80%, more than 20% over conventional air cycles. Furthermore, the absence of nitrogen in the system prevents formation of nitrogen oxides, eliminating the need for expensive exhaust gas after-treatment and allowing for efficient use of renewable generated hydrogen fuel. In the case of hydrocarbon fuels, the closed loop nature of the cycle affords to boost the pressure and concentration of gases in the exhaust stream at no penalty to the cycle, providing the driving force to cost effective gas membrane separation of carbon dioxide.

This dissertation investigates the potential benefits of the Argon Power Cycle to improve upon current stationary power generation systems regarding efficiency, air pollutants, and greenhouse gas emissions.

Dedicado a mi familia y amigos, en especial a Maryanne Peters.

Acknowledgments

My words here cannot express how grateful I am to all of you, whose support and effort helped me complete my PhD. I could not have gotten here without you.

First and foremost I would like to thank my dear friend and colleague Tim Sennott, one of the smartest engineers I have had the pleasure to work with. His huge effort during our time together at the laboratory lead to the beginning of this work and makes me hopeful Tim and I will manage to bring this new technology to live in the upcoming years.

I would like to thank David Vuilleumier, who was there to share sleepless night of work at the laboratory and prepare for our qualifying examinations. I would like to make special mention to my German friends, Simon Drost and Malte Schaefer, whose friendship and hands on support helped me go through many of the tough times at Berkeley. I will be always grateful to Johnathan Corvello and Bradley Cage, the most brilliant undergraduates I have had the pleasure to supervise, for their immense contributions to my research work. I do not forget visiting student Farouk Chorou whose passion and drive reminded me why I enrolled on my PhD in the first place. I would also like to acknowledge visiting student Xaver Müller for his contributions to my work.

I would like to thank professor J. Y. Chen, who worked beside me at the engine cells and ran model estimates when necessary. I would like to express my gratitude to professor F. Pello for his advice and words of support during my struggles. To my PI, professor R. W. Dibble, I would like to thank him for his friendship and for the science and engineering discussions we often had. I also keep words for professor P. Papadopoulos and professor E. Iglesia, whose courses were, without a doubt, the best classes I have taken at Berkeley.

I want to thank the Hesse Hall shop, specially Mike Neufer who was always there to help, providing his time and advice to successfully complete my projects.

Needless to say, I am grateful to the California Energy Commission who directly funded my research, and to Bosch and Parker Hannifin for their in-kind contributions to my research endeavors.

Finally, I would like to thank all my relatives and friends who were there when I most needed them, specially the Peters family for their friendship and support and my girlfriend Hannah for her unconditional support and understanding during what felt like an everlasting journey.

Nomenclature

a	Crankshaft radius	mm
A/F	Air to fuel ratio	-
A_p	Piston area	m^2
A_W	Cylinder wall area	m^2
B	Piston Bore	mm
$BS\chi_i$	Brake specific emission for specie i	g/kWh
c	Speed of sound	m/s
C	Generic constant	-
$c_{p,mix}$	Mass weighed mean heat capacity at constant pressure	J/kg K
c_p	Heat capacity at constant pressure	J/kg K
c_v	Heat capacity at constant volume	J/kg K
$CA10$	Crank angle at which 10 % heat has been released	CAD
$CA50$	Crank angle at which 50 % heat has been released	CAD
$CA90$	Crank angle at which 90 % heat has been released	CAD
$CAEOC$	Crank angle at the end of combustion	CAD
$CASOC$	Crank angle at the start of combustion	CAD
$\chi_{i,dry}$	Dry concentration of species i	-
$\chi_{i,wet}$	Wet concentration of species i	-
Δp	Pressure difference	bar
ΔT	Temperature difference	K
$\dot{m}_{\chi,i}$	Mass flow of specie i	g/h
$\dot{m}_f$	Fuel mass flow	g/h
$\dot{Q}_W$	Heat power losses through the cylinder wall	W
η_B	Brake efficiency	-
η_C	Combustion efficiency	-
$\eta_{G.E}$	Gas exchange efficiency	-
η_M	Mechanical efficiency	-
η_T	Thermodynamic efficiency	-
f	Friction coefficient	-
F_B	Brake force	N
F_{rf}	Friction force	N
γ	Adiabatic index	-
γ_i	Membrane selectivity for species i	-
h	Specific enthaply	kJ/kg K
h	Planck's constant	m^2 kg/s

J_i	Mass flux of species i	kg/m^2 s
k	Polytropic index	-
κ_B	Boltzman's constant	m^{2}kg/s^{2}K
l	Piston rod length	mm
λ	Lambda	-
m_{bb}	Blowby mass per cycle	kg
$m_{cyl,0}$	Initial mass in the cylinder at time of inlet valve closure	kg
$m_{e,cyl}$	Effective mass in the cylinder	kg
M_{exh}	Mean molar mass of exhaust gases	g/mol
M_i	Molar mass of species i	g/mol
μ	Absolute viscosity	Pa s
N	Engine Frequency	Hz
N	Normal to surface force	N
n_θ	Subset of n samples at different θ.	-
n_c	Number of crank revolution per engine cycle	rev/cycle
N_p	Number of different combustion product species	-
ω	Engine rotational speed	rad/s
$\overline{s}_p$	Piton mean velocity	m/s
p	Thermodynamic state variable Pressure	Pa
P_B	Brake power	W
P_i	Membrane permeability of species i	mol/m^{2}sPa
ϕ	Equivalence ratio	-
ϕ	Membrane stage cut	-
Q	Heat release during combustion	J
q_e	Electrical Partition Function	-
Q_f	Chemical energy contained in the fuel	MJ/kg
Q_G	Combustion heat released	J
$Q_{LHV,i}$	Lower heating value of species i	MJ/kg
Q_{LHV}	Lower heating value	MJ/kg
Q_{loss}	Combustion heat loss	J
q_n	Nuclear Partition Function	-
q_{rot}	Rotational Partition Function	-
q_{tr}	Translational Partition Function	-
q_{vib}	Vibrational Partition Function	-
Q_W	Heat losses through the cylinder wall	J
R	piston rod to radius ratio	-
r	radius	m
R_{bs}	Bore to stroke ratio	-
r_c	Compression ratio	-
R_{fluid}	Specific gas constant of the fluid	J/kg K
r_p	Pressure ratio	-
R_u	Universal gas constant	J/mol K
ρ	Mass density	kg/m^3
S	Piston stroke	mm
S	Sommerfeld number	-

s_L	Laminar flame speed	m/s
t	Time	d
T	Thermodynamic state variable Temperature	K
T_B	Brake torque	Nm
θ	Crank angle	rad
U	Internal energy	J
U	Overall heat transfer coefficient	W/m^2 K
V	Thermodynamic state variable Volume	m^3
V_d^*	Actual volume displacement	m^3
V_c	Combustion chamber volume	m^3
V_d	Cylinder displacement volume	m^3
v_p	velocity of the moving piston	m/s
V_T	Total cylinder volume	m^3
W_{aux}	Auxiliar systems consumed work	J
W_B	Brake work	J
W_{pump}	Pumping work	J
W_{rf}	Rubbing friction work	J
W_T	Work in the thermodynamic cycle	J
Z	Compresibility factor	-

Abbreviations

AC	Alternative current
AFR	Air to fuel ratio
APC	Argon Power Cycle
AQ	Air Quality
ASU	Air Separation Unit
ATDC	After Top Dead Center
BDC	Bottom Dead Center
BECCS	Bioenergy Production with Carbon Capture and Sequestration
BMEP	Brake energy mean effective pressure
BSCO	Brake specific carbon monoxide emissions
BSCO2	Brake specific carbon dioxide emissions
BSFC	Brake specific fuel consumption
BSNOx	Brake specific nitrogen oxides emissions
BSO2	Brake specific oxygen content
BSTHC	Brake specific total hydrocarbons emissions
BTDC	Before Top Dead Center
CAD	Crank Angle Degree
CAES	Compress Air Energy Storage
CAM	Cam shaft phasing
CCS	Carbon Capture and Sequestration
CEC	California Energy Comission
CFR	Cooperative Fuel Research engine
CGA	Compress Gas Assosiation standards
CHP	Combined Heat and Power
CLMEP	Conbustion losses mean effective pressure equivalent
CNG	Comprassed Natural Gas
CVC	Constant Volume Chamber
DC	Direct Current
DISI	Direct Fuel Injection Spark Ignited
EGR	Exhaust Gas Recirculation
EIA	U.S. Energy Information Administration
EOR	Enhanced Oil Recovery
EROI	Energy Return of Investment
EVC	Exhaust Valve Closing
EVO	Exhaust Valve Opens

FDM	Finite Difference Method
FMEP	Friction losses mean effective pressure equivalent
FuelMEP	Fuel energy mean effective pressure equivalent
FVM	Finite Volume Method
GCHR	Gross cumulative heat release
GDP	Gross Domestic Product
GHG	Greenhouse Gases
GT	Gas Turbine
HES	Hydrogen Energy Storage
IEA	International Energy Agency
IGN	Ignition Timing
$IMEP_G$	Gross indicated mean effective pressure
$IMEP_N$	Net indicated mean effective pressure
IPCC	Intergovernmental Panel on Climate Change
IVC	Inlet Valve Closing
IVO	Inlet Valve Opening
LHV	Fuel Low Heating Value
LNG	Liquefied Natural Gas
MAP	Manifold Air Pressure
MBT	Maximum Brake Torque
MEP	Mean Effective Pressure
NDC	National Determined Contributions
NG	Natural Gas
NI	National Instruments
NMHC	Non Methane Hydrocarbons
NOx	Nitrogen Oxides
NTC	Negative Temperature Coefficient
OECD	Organization for Economic Cooperation and Development
OEM	Original Equipment Manufacturer
PFI	Port Fuel Injection
PFR	Primary Fuel Reference
PID	Proportional-Integral-Derivative controller
PM	Particulate Matter
PMEP	Pumping losses mean effective pressure equivalent
$PMEP_{pump}$	Pumping work mean effective pressure equivalent
$PMEP_{valves}$	Valve flow losses mean effective pressure equivalent
QLMEP	Heat losses mean effective pressure equivalent
QMEP	Heat after combustion mean effective pressure equivalent
RES	Renewable Energy Sources
RICE	Reciprocating Internal Combustion Engine
RON	Research Octane Number
SI	Spark Ignited
ST	Steam Turbine
SYNGAS	Synthetic Gas consisiting mainly of H_2 and CO
TDC	Top Dead Center

THC	Total Hydrocarbons
UCB	University of California at Berkeley
UHC	Unburnt Hydrocarbons
US	United States of America
VOC	Volatile Organic Compound
WOT	Wide Open Throttle
xMEP	Pressure representation of energy flow x

List of Tables

2.1 Lower heating value of CO, H_2 and CH_4 [99]. 29
2.2 Gaseous composition of dry air [102–104]. 42
2.3 Properties of gaseous Ar, N_2 and CO_2 at standard conditions. 42

3.1 ASU outcome characteristics as determined by ASPEN Plus. 58
3.2 Membrane selectivities for common species. 66

4.1 Cooperative Fuel Research (CFR) engine specification. 72
4.2 Engine operation and control equipment. 72
4.3 Cooperative Fuel Research (CFR) engine specification. 75
4.4 Solenoid direct injector specifications. 95
4.5 Direct injector discharge coefficient calculated with Ar, He, N_2 at 100 bar and 23°C and discharging to atmospheric conditions. Estimated real flow rates for H_2 and CH_4 are also indicated. 96
4.6 Mean spread angle for CH_4 and H_2 in argon and nitrogen atmospheres. Values indicate mean and 90% confidence intervals. 100
4.7 General results from direct injection of H_2 at a compression ratio of 8 and 15% O_2 107

B.1 Air separation unit process state properties. 163
B.2 Air separation unit process state properties continued. 164

List of Figures

1.1 Evolution of CH_4, CO_2, N_2O concentrations [8–22]. 2
1.2 Major world socioeconomic and emission trends for OECD and non-OECD regions [36]. 3
1.3 World energy consumption by energy source [41]. 5
1.4 California's May mean net load and solar energy supply evolution since 2014 [44]. 6
1.5 California's May mean net load ramp rate evolution since 2014 [44]. . 7
1.6 CAISO average real time hourly pricing of electricity for the month of March since 2014 [44]. 8
1.7 U.S. dry shale gas production estimates since 2000 [71]. 10
1.8 Commodity price comparison of oil, natural gas and coal in the US market since 1990 [75]. 11
1.9 U.S. Electricity Net Generation by energy source [76]. 12

2.1 Prospective process diagram for a hydrogen fired Argon Power Cycle plant.(1) RICE (2) Heat exchanger (3) Coalescing filter (4) Condenser (5) Electrolyzer. 18
2.2 Prospective process diagram for a gas fired Argon Power Cycle plant.(1) RICE (2) Heat exchanger (3) Coalescing filter (4) Condenser (5) Membrane system (6) Air separation unit (ASU). 19
2.3 System dimensions as it scales with power output for RICE. The scale is not linear as efficiency and number of engine cylinders increases. A 250 MW gas turbine is depicted for reference. 20
2.4 4 Stroke engine cycle process. 21
2.5 Example of a four stroke SI engine cylinder-piston geometry. V_c: Combustion chamber volume; V_d: Volume displacement; V_T: Total cylinder volume; TDC: Top Dead Center; BDC: Bottom Dead Center; S: Stroke; B: Bore; l: Rod length. 23
2.6 Contribution of different molecular modes of motion to the specific heat of monatomic gases, N_2 and CO_2. 32
2.7 Effect of specific heat and compression ratio on the thermodynamic efficiency of the Otto cycle. With the superscript p represents thermodynamic efficiency estimated with the cool air assumption. The Carnot efficiency is plotted for reference. 33

2.8 P-v diagram comparison of a perfect gas, ideal gas, and a real air Otto cycle fired with natural gas. For reference: r_c=10.4:1; A/F=17.1; and Q_{LHV,CH_4}=50 MJ/kg. 34
2.9 Real engine operating at 40 kPa intake manifold pressure; +40 CAD cam phasing advance. The shaded area represents the energy losses due to the breathing process in the engine. 35
2.10 Concept of PMEP values in internal combustion engines. 37
2.11 Striebeck diagram. Coefficient of friction is plotted against the Sommerfeld number. The overall coefficient of friction results from the sum of hydrodynamic friction and solid friction, projecting different regimes of influence at different engine speeds. Boundary regime: mainly solid friction. Mixed regime: progressive reduction and increment of solid and hydrodynamic friction respectively. Hydrodynamic regime: mainly hydrodynamic friction. Figure is adapted from [95]. 38
2.12 Summary of the different energy flows, losses and efficiency terms. Figure adapted from [97]. 40
2.13 Power efficiency comparison between conventional power generation technologies under ISO standard 3046 [101]. 41
2.14 Theoretical gas turbine cycle efficiency (Brayton) with (bold lines) and without heat recuperation (thin lines). Computed assuming perfect gas with $c_p = c_p(298K)$. 44

3.1 Left: 0D single zone engine cylinder model. Right: 0D 2 zone engine cylinder model. The subscripts in and out represent inlet and outlet respectively. The subscript bb and w stands for blowby and wall respectively. 48
3.2 Simulated thermodynamic efficiency of the engine with different working fluids and fueled with methane and hydrogen at different compression ratios. 54
3.3 Simulated thermodynamic efficiency of the engine with different working fluids and fueled with methane and hydrogen at a compression ratio of 12 and different ignition timing. 55
3.4 Oxygen production by distillation of liquid air [116]. 56
3.5 Expanded diagram of the air separation unit shown in figure 2.2. . . . 57
3.6 Relative efficiency penalty on gas fired power system resulting from the implementation of ASU assumed three different specific energy consumption per ton of O_2. Natural gas is assumed to hold the properties of CH_4 with a lower heating value of 50 MJ/kg. 59
3.7 Hollow fiber membrane module schematic. 60
3.8 Cross section view of the fiber bundle in a shell feed hollow fiber membrane setup. 62
3.9 Illustration of molecule permeating from the retentate to the permeate through the membrane interface. 64
3.10 Expanded diagram of the membrane system in figure 2.2. 66

3.11 Top: Membrane system energy consumption as a percentage of RICE power output. Bottom: Output CO_2 mole fraction as a function of cycle pressure and recirculated CO_2. 67

4.1 Finalized CFR experimental setup at UC Berkeley. 73
4.2 Engine experimental setup schematic for the CFR engine at UC Berkeley. 74
4.3 Energy conversion network. 76
4.4 Example of engine pressure trace and derived motoring pressure trace and average mean cylinder temperature. 78
4.5 Example of cumulative net and gross heat released profile and piston work. Some characteristics angles are shown for reference. 79
4.6 Thermodynamic efficiency for the air breathing engine fueled with methane and hydrogen at different compression ratios. 82
4.7 Ignition timing and combustion phasing for the air breathing engine fueled with methane and hydrogen at different compression rations. H_2: Solid •; CH_4:Open ∘. 83
4.8 Indicated mean effective pressure and peak pressure for the air breathing engine fueled with CH_4 and H_2 at different compression ratios.IMEP: Solid •; Peak pressure:Open ∘. 84
4.9 Methane and hydrogen comparison for air at a constant compression ratio of 8. Top: average in cylinder pressure and apparent heat release rate trace. Bottom: average cumulative apparent heat released and piston work profile. 85
4.10 Engine efficiency breakdown for the air breathing engine fueled with methane and hydrogen at different compression ratios. H_2: Solid •; CH_4:Open ∘. 86
4.11 Main exhaust emission for the air breathing engine fueled with methane at different compression ratios. 87
4.12 Thermodynamic efficiency comparison between the air breathing engine and argon fed engine fueled with methane at different compression ratios and oxygen dilutions. 88
4.13 Indicated mean effective pressure and peak pressure comparison between the air breathing engine and argon fed engine fueled with CH_4 at different compression ratios and oxygen dilutions. IMEP: Open ∘; Peak pressure: Solid •. 89
4.14 Combustion phasing comparison between the air and argon breathing engine fueled with methane at different compression ratios. White: Ar-21%O_2; Black: Ar-15%O_2; Grey: Air. 90
4.15 Exhaust temperature comparison between the air and argon breathing engine fueled with methane at different compression ratios. 91
4.16 Influence of dilution (top) and lambda (bottom) on the thermodynamic efficiency and combustion phasing. 92
4.17 Several performance parameters comparison between the air and argon breathing engine fueled with hydrogen at different compression ratios. 93

4.18 Isothermal and isentropic energy cost of compression as a percentage of fuel's LHV for methane and hydrogen, assuming ideal gas behavior. 94
4.19 Injector flow rate measuring setup. 95
4.20 Top view of the schlieren setup (top) and instrument diagram of the constant volume chamber (bottom). 97
4.21 High-speed schlieren imaging results for CH_4 (left) and H_2 (right) injection at different pressures into a constant volume chamber filled with N_2 and Ar at 10 bar and 23°C. 98
4.22 High-speed schliren imaging of CH_4 (col 1-2) and H_2 (col 3-4) jets at 100 bar into N_2(col 1-3) and Ar (col 2-4) atmospheres at 10 bar. . . . 99
4.23 3-Dimensional depiction of the engine cylinder with the spark plug, intake valve and direct injector in their corresponding locations. . . . 100
4.24 Thermodynamic efficiency comparison between the air breathing engine and argon breathing engine port and direct fuel injected with CH_4 at different compression ratios and oxygen dilutions. 101
4.25 PFI and DI comparison for argon at a constant compression ratio of 10. Top: average in cylinder pressure and apparent heat release rate traces. Bottom: average cumulative apparent heat released and piston work profiles. 102
4.26 Average in cylinder pressure and apparent heat release rate traces for the argon breathing engine fed with 15% O_2 and direct injected methane at several compression ratios. 103
4.27 Thermodynamic efficiency and combustion phasing for the argon breathing engine fed with 15% O_2 and direct injected methane at several compression ratios. 104
4.28 Thermodynamic efficiency and combustion phasing for the argon breathing engine fed with 15% O_2 and direct injected methane at a compression ratio of 14 and incresing fuel dilution. 105
4.29 Unburnt hydrocarbon emissions for the argon breathing engine port fuel injected and direct fuel injected. 106
4.30 Average in cylinder pressure and apparent heat release rate traces for the argon breathing engine fed with 15% O_2 and H_2 at several compression ratios. 107
4.31 Average pressure and heat release rate traces for SYN-GAS in air and CO_2 working fluids. 108
4.32 Estimated average in-cylinder temperature for SYN-GAS in air and CO_2 working fluids. 109
4.33 In-cylinder cumulative energy as a function of crank angle. The different forms of energy shown are fuel energy, gas internal energy and piston work. 110
4.34 Influence of lambda on the combustion phasing (top) and thermodynamic efficiency (bottom) of the air and CO_2 breathing engines fueled with SYNGAS. 111

Table of Contents

Abstract i

Acknowledgments iii

Nomenclature vii

Abbreviations xi

List of tables xiii

List of figures xvii

Table of Contents xviii

1 Introduction 1
- 1.1 Background . . . 1
- 1.2 The clean energy transition . . . 4
- 1.3 The emergence of Natural Gas . . . 9
- 1.4 Dissertation Outline . . . 14
- 1.5 Dissertation contribution . . . 14

2 The Argon Power Cycle 17
- 2.1 Literature review . . . 17
- 2.2 Introduction to the APC and its applications . . . 18
- 2.3 RICE fundamentals . . . 21
  - 2.3.1 Engine kinematics . . . 21
  - 2.3.2 Engine Brake parameters . . . 24
  - 2.3.3 Internal combustion engine efficiency . . . 25
- 2.4 Argon as the working fluid. . . . 40
- 2.5 Closed loop recirculation . . . 42
- 2.6 Why RICE? . . . 43
- 2.7 Summary . . . 45

3 Numerical Investigation 47
- 3.1 Internal Combustion Engine modeling . . . 47
  - 3.1.1 Mass conservation . . . 49
  - 3.1.2 Energy conservation . . . 50

3.2 Cryogenic Air separation modeling 56
3.3 Hollow fiber membrane modeling 59
3.3.1 Numerical Model 62
3.3.2 Hollow fiber membrane for the APC 65
3.4 Summary 68

4 Experimental Investigation **71**
4.1 Experimental Setup 71
4.1.1 Internal combustion engine testing facility 71
4.1.2 The combustion analysis system 76
4.1.3 Heat release and combustion timing characterization 78
4.2 Experimental results 81
4.2.1 Air breathing engine operation 81
4.2.2 Argon breathing engine operation 87
4.2.3 Carbon dioxide breathing engine operation 108
4.3 Summary 112

5 Conclusions and recommendations **113**
5.1 Conclusions 113
5.2 Recommendation 115

Bibliography **127**

A US Patent: Recirculating Noble Gas Internal Combustion Power Cycle **129**

B Air separation process results **163**

C Engine data postprocessing code **165**

Chapter 1

Introduction

This thesis aims to provide a better understanding of the potential for cost effective emission reduction of the Argon Power Cycle (APC), an innovative technology, implemented on reciprocating internal combustion engines (RICE).

1.1 Background

Earth's global warming and the greenhouse effect are not a new phenomena known to human kind. First reported by French scientist Joseph Fourier in 1824 [1,2], global warming has been extensively studied and discussed since. In 1861, Irish physicist, John Tyndall, explored the effect of different gases on the greenhouse effect [3]. Thirty five years later, in 1896, Swedish chemist Svante August Arrhenius concluded that human activity could increase earth's temperature by increasing the amount of carbon dioxide in the atmosphere [4]. It took nearly a century and a substantial number of studies for the first United Nations conference on the environment to take place in 1972, where concerns regarding non sustainable practices were raised. In 1988, the Intergovernmental Panel on Climate Change (IPCC) was formed with the goal to provide clear scientific view on the potential environmental and socio-economic impact of climate change [5].

Today, greenhouse gas (GHG) atmospheric concentrations are at levels that are unprecedented in at least 800 thousand years. Concentrations of carbon dioxide (CO_2), methane (CH_4) and nitrous oxide (N_2O) have all shown large increases since 1750 as can be seen in figure 1.1. In November 2016, as a result of the observed trends, the world reached global consensus over the occurrence of global warming and the need to combat it. This consensus was ratified with the signature, by hundred ninety five countries, of the Paris Agreement [6]. In this agreement, each country committed, through national determined contributions (NDCs)[1], to take the necessary measures that reduce their GHG emissions and prevent global warming above two degree Celsius with respect to 1850-1900 period [7]. This agreement, although drafted around environmental and societal discussion, is ultimately an agreement on

[1] The NDCs obey to the realities the different regions in the world are facing in regards to economic activity, population prospects, and level of technological development.

how each country will conduct its energy and economic policy in the upcoming years.

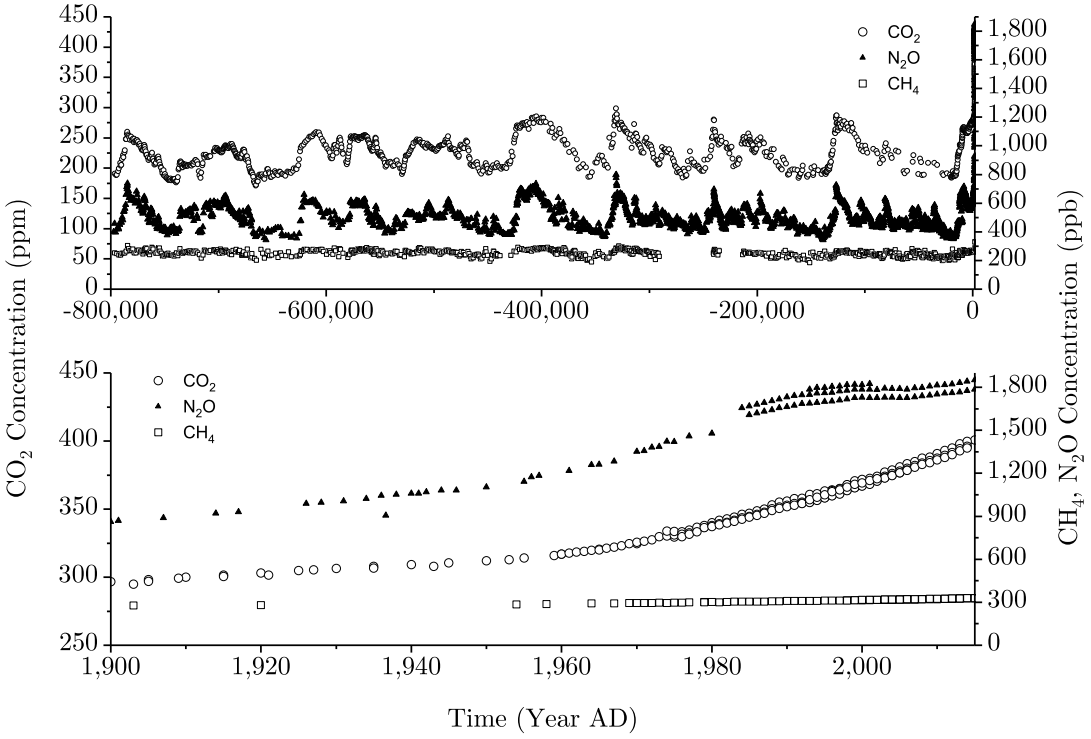

Figure 1.1: Evolution of CH_4, CO_2, N_2O concentrations [8–22].

Today, more than 68% of the GHG emitted worldwide originates from the energy sector[2], mainly in the form of CO_2 [23, 24]. This number varies by country and economic regions but it still dominates the total share of GHG emissions for all cases nonetheless. The reason for that is 78-82% of the primary energy demand worldwide is fulfilled with fossil fuels [23,25,26]. Although it is foreseen that the energy mix change with increasing use of non fossil based energy sources, trends indicate that 50-75% of the primary energy demand will still be supplied by fossil fuels in 2040 [25–28].

Developed regions such as North America and Europe have managed to decouple their contributions to global warming from their economies, mainly as a result of more efficient power generation and an increasing percentage of renewable energy sources (RES) in their portfolios. However, regions such as Africa and Asia still depict a strong correlation between their economies, energy consumption and emissions as can be seen in figure 1.2. This fact is exacerbated by a faster population growth, mainly in African countries, and the contributions of China and India, the most populous countries in 2017.

Worldwide, the population is growing at a rate of nearly 1% per year and is ex-

[2]Energy sector includes any form of power generation, including fuel combustion for transportation.

pected to reach 9.7 billion by 2050 [29,30]. Moreover, the global economy is expected to grow at a rate of 3% per year, the result of shrinking poverty levels and a growing middle class in countries which to do not belong to the Organization for Economic Co-operation and Development (OECD) [30,31]. This combination of population growth and economic activity is driving an increase in demand for energy in these regions. It has been estimated that the global energy consumption will grow on the range of 25-45% during the period from 2015 to 2040, driven mainly by non-OECD countries [25–28]. Altogether, the current state of the energy supply and the foreseeable scenario will translate into a 34% increase in global greenhouse gas emissions by 2040.

This constant increase in GHG emissions will also accelerate changes in weather patterns, yielding a substantial reduction in air quality (AQ). The reason being that ozone generation is catalyzed via increasing temperatures and residence time of its precursors in the atmosphere [32]. Ozone precursors, such as nitrogen oxides (NO_x) and volatile organic compounds (VOCs), together with particulate matter (PM) are expected to rise in accordance with increasing fossil fuel consumption and subsequent combustion [33, 34]. Unless prompt action is taken to decarbonize the energy sector, the reduction in AQ is expected to become the largest cause of environmentally related premature deaths worldwide by 2050 [35].

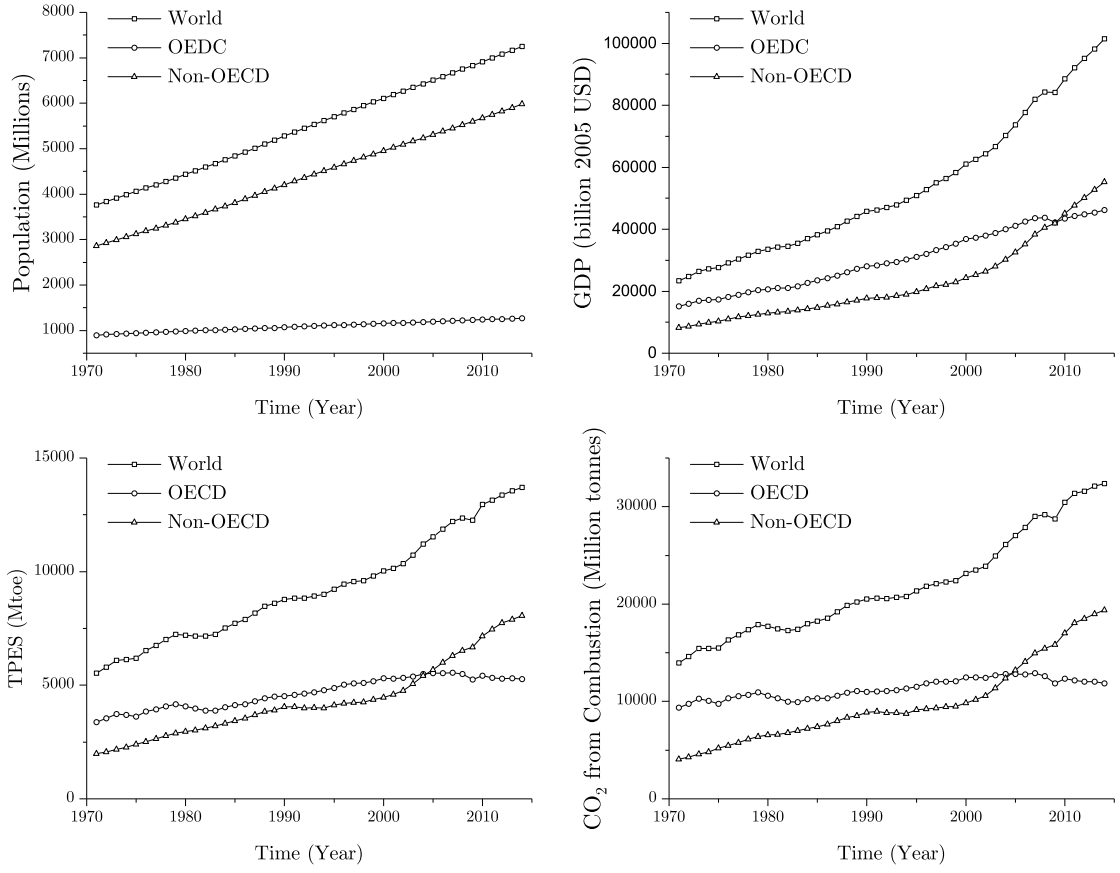

Figure 1.2: Major world socioeconomic and emission trends for OECD and non-OECD regions [36].

1.2 The clean energy transition

Tremendous efforts are being applied to transitioning to new cleaner and more sustainable energy sources. Governments are continuously developing laws and regulations to guide economies toward growth patterns that respect and maintain natural resources. A major target for potential emission reduction is the electric power sector, the biggest consumer of primary energy and largest contributor to GHG and criteria pollutant[3] emissions worldwide [23, 37]. As the world acknowledges the urgent need to reduce GHG emissions and preserve AQ, power generation portfolios evolve to integrate a larger share of RES. An accelerated deployment of non polluting energy sources such as RES and nuclear power could greatly reduce the overall global emission by, in accordance with the decarbonization efforts, supporting an ever increasing electrification of the economy, particularly the industrial and transportation sectors [38, 39].

Nuclear energy

Introduction of new large nuclear power capacity is not foreseen in OECD countries, which have shown no rising trends on the nuclear capacity. This is due in part to the influence of public opinion, with Germany serving as an example by phasing out nuclear energy by 2022 [40], but mainly due to the small increase in energy demand in these regions. This combination of factors disincentivize investment in large power plants with no guaranties of profitable capacity factors[4].

On the other hand, non-OECD regions have seen great addition of nuclear capacity, establishing nuclear energy as the second fastest growing source of energy worldwide. With a radical increase in energy demand, China leads the addition of nuclear capacity to fulfill their baseload needs while making an effort to curb their carbon footprint and mitigate their AQ challenges. Nonetheless, nuclear is not foreseen to represent a large share of the world energy supply in the long term (figure 1.3) [26].

Renewable energy

In 2016, renewable generation became the fastest growing energy source worldwide (figure 1.3) and this trend is expected to continue with solar photovoltaic leading the addition of new capacity [27, 42].

Although renewable energy promises to solve the energy security and climate change alltogether, integral changes are required to accommodate for a larger share of intermittent RES. With an increasing amount of RES, the electric grid is faced with the need to overcome reliability challenges. The susceptibility of RES to weather conditions and climate limits when and where they can operate, causing the power grid

[3]Criteria pollutants are defined as the group of particulate matter, photochemical oxidants (including ozone), carbon monoxide, sulfur oxides, nitrogen oxides and lead.

[4]Capacity factor is a measure of the amount of hours of actual operations over the potential operational time of the plant per year.

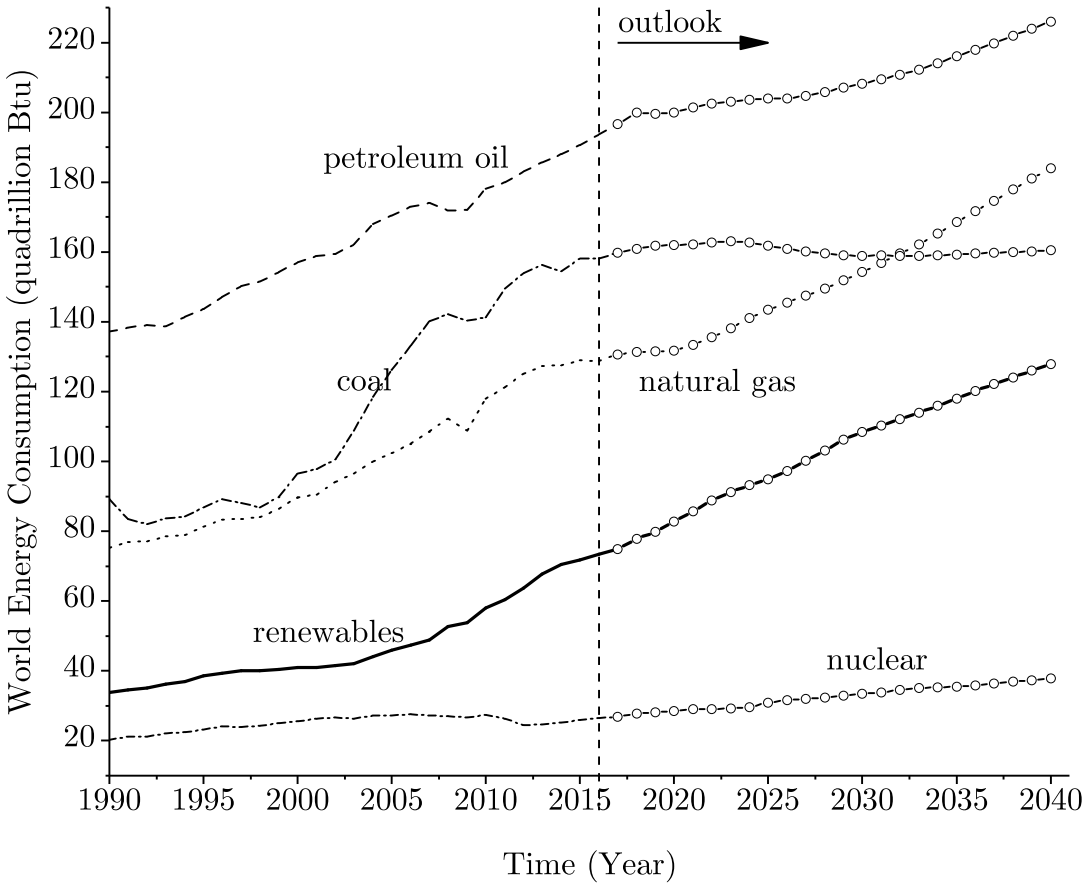

Figure 1.3: World energy consumption by energy source [41].

to face conditions of short and steep supply ramps, risk of oversupply and a decrease in frequency response resources. As a result, an increasing demand for flexible small and medium scale power generation and energy storage systems emerges [43].

The California power grid serves as a clear example of the above challenges due to California's ambitious goals to serve 30% of its energy demand with RES by 2020 and 50% by 2030 respectively. Already in 2016, the California Energy Commission (CEC) reported that 29% of the the energy consummed in the state was generated by RES [45]. Since 2011, solar capacity in California has grown steadily, from hundreds of MW to GW today. With an ever increasing capacity and consequent supply of intermittent RES, the net load to be supplied by conventional power takes on a more acute shape, with increasing frequency and magnitude of load ramps. The resulting net load curve resembles that of a duck silhouette (figure 1.4) with a "duck tail"starting in the early morning, when people start into their day. As the sun comes up, solar capacity begins its contribution to the supply, shaping the "duck belly". It is later in the day, when the sun sets, that the biggest ramp (the "duck's neck") is faced by the grid operator and much of the flexible capacity is called in. Finally, soon after 9:00 pm, much of the generation is shut down as people begins to go to sleep.

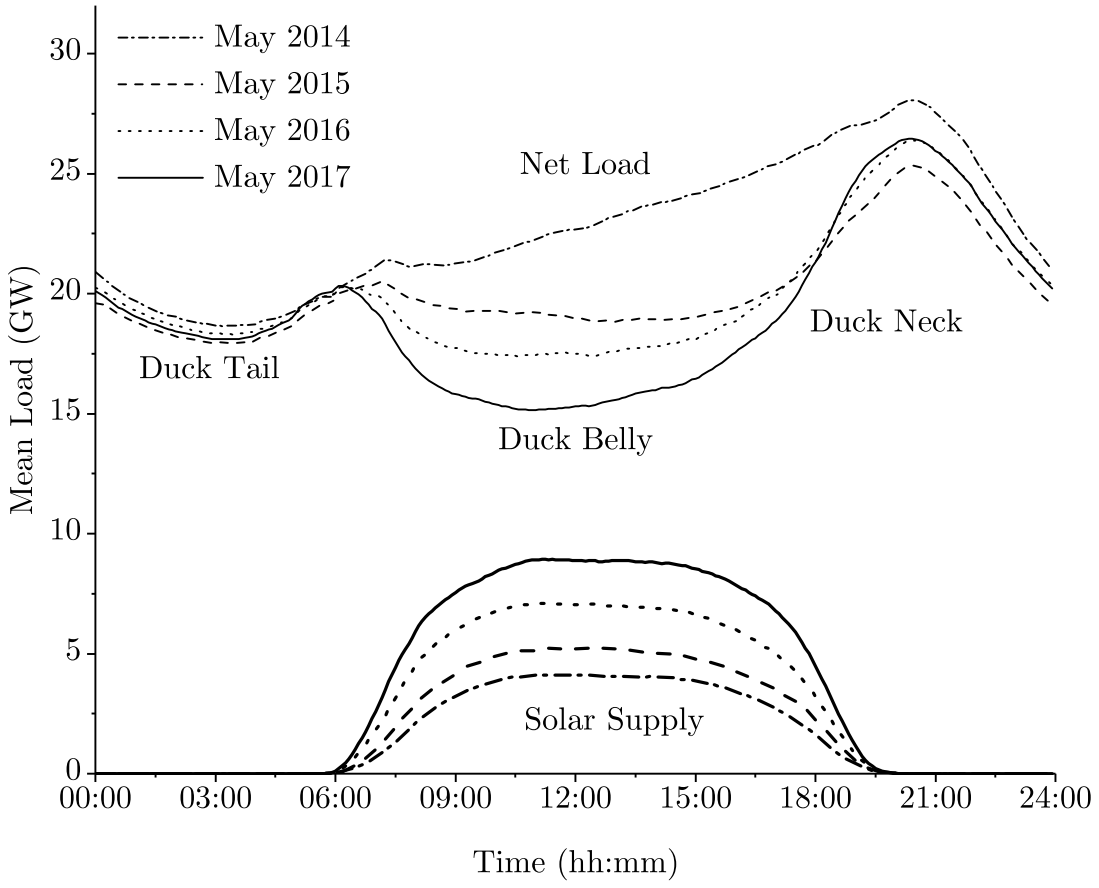

Figure 1.4: California's May mean net load and solar energy supply evolution since 2014 [44].

The evolution of the net load profile is also depicted in figure 1.4. As more solar has come online, the slope of the ramps have become steeper, reaching maximums of up to 200 MW per minute. Although the available data is limited to five minute intervals, it is easy to see in figure 1.5 how ramp rates of up to 70 MW per minute are common with fluctuation of up to 20 MW per minute. However, the biggest challenge from renewable generation is confronted by the power markets. With the introduction of more wind and solar, the price of electricity is being driven down, a result of a shift in the supply-demand curve of the electricity[5]. With lower electricity prices, utilities struggle to break even, more so if they have invested on capital intentive systems such as solar or wind farms. Consequently, the power markets are doomed to have a harsh, yet required, transformation [46]. This phenomena is already being witnessed in California. Figure 1.6 showcases the average real time price of electricity

[5]Unlike conventional generation, where the fuel represents more than 80% of its marginal cost of operation, renewable based generation has little to no operational cost, driving the market equilibrium price down.

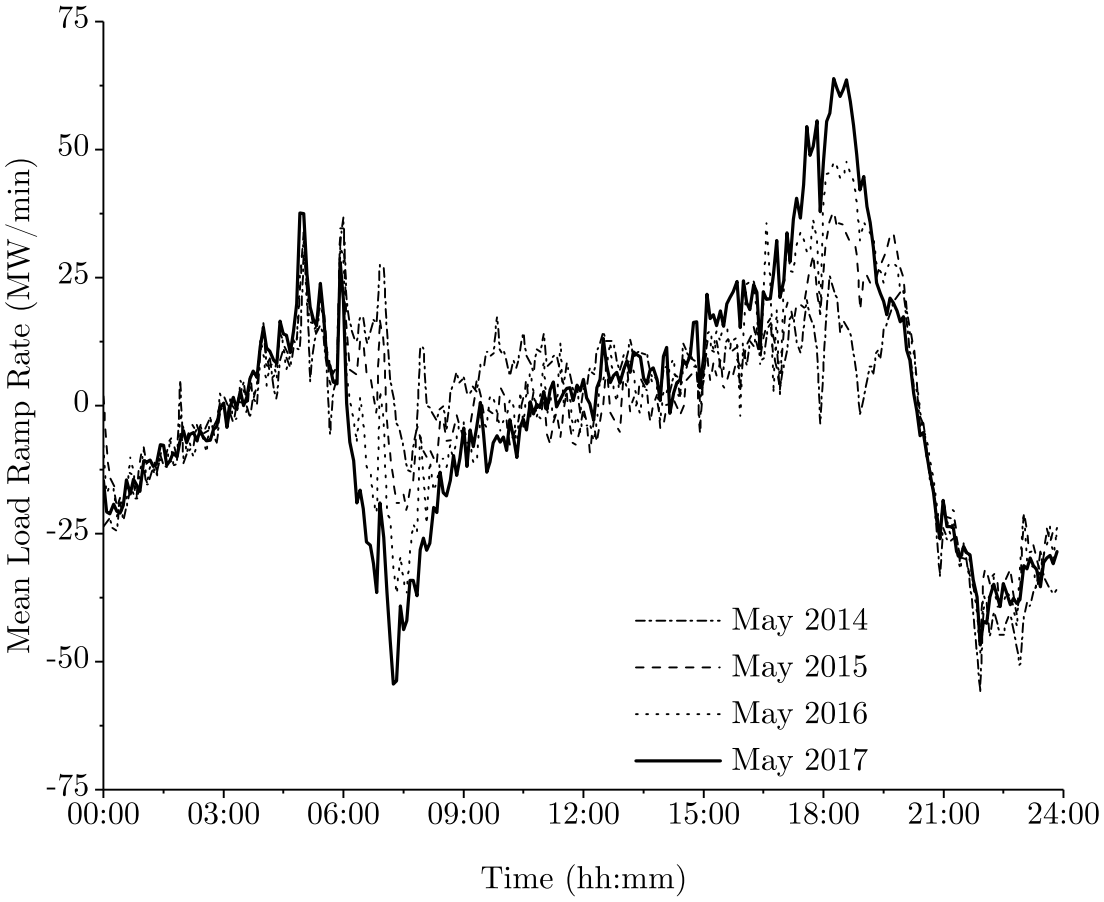

Figure 1.5: California's May mean net load ramp rate evolution since 2014 [44].

for the month of March since 2014. Spot prices have fallen continuously during hours when solar power is active, while on the contrary, peak prices have increased when conventional generation takes over. Because of the ever increasing magnitude and frequency of the load ramps(figure 1.5), conventional generation is struggling to cope with the resulting load, causing substantial frequency imbalance and grid instability [47]. Ancillary generating units come online quickly to provide frequency stabilization, but they do it at a premium, increasing the spot electricity prices during peak hours. Furthermore, and more importantly, the inability of the conventional generation capacity to ramp down rapidly enough is increasing the risk of oversupply, which in turn does not only reduce the price of the electricity, but forces negative prices. These trends are likely to be seen all around the world as power grids operators see an increase on their solar and wind capacity.

Electrical energy storage

In dealing with the current challenges faced by the electric grid, California has mandated the integration of 1.325 GW of energy storage by 2020. By spreading renewable

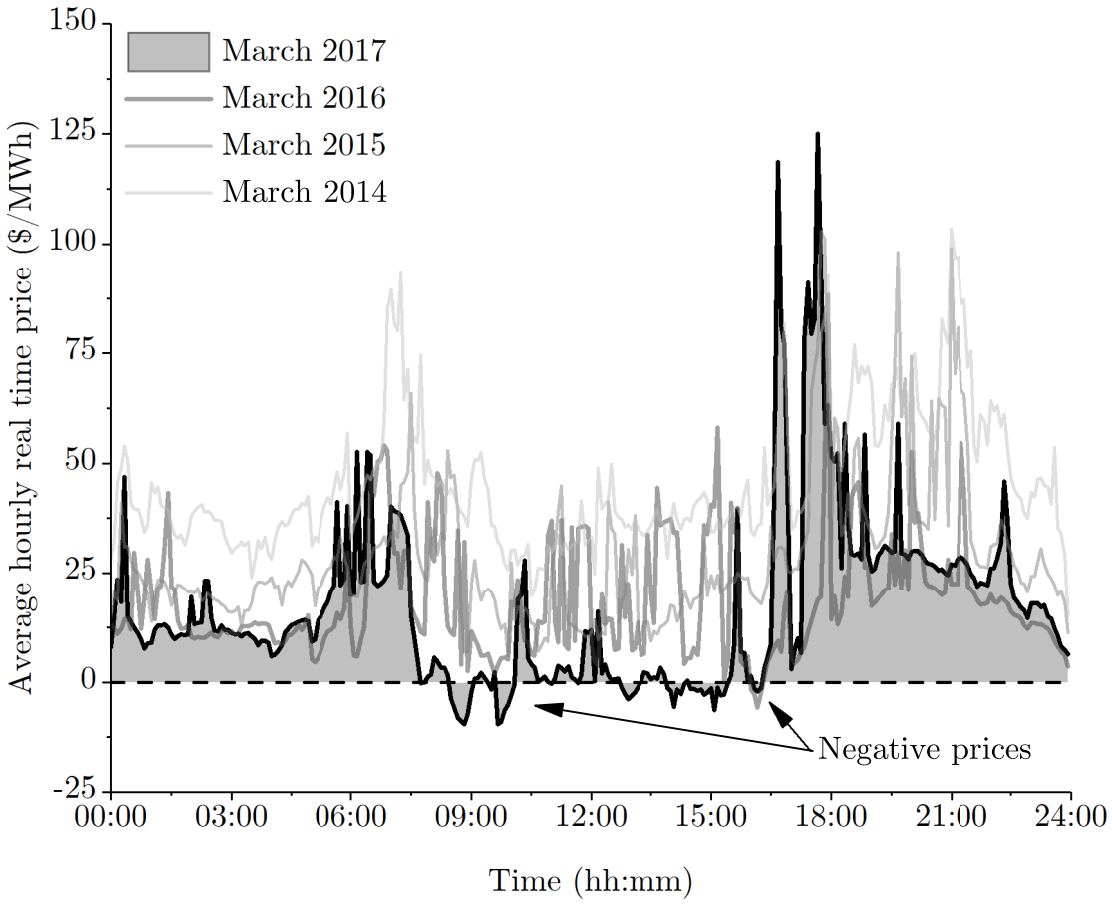

Figure 1.6: CAISO average real time hourly pricing of electricity for the month of March since 2014 [44].

power generation across longer periods of time, the steep ramps seen in figure 1.4 can be softened. Taken to the limit, this measure could turn intermittent solar and wind into dispatchable generation, in line with California's goals to fill 50% of its energy needs with renewable energy by 2030 [48, 49].

Nowadays, there is a strong momentum behind the development and integration of batteries, with 60% of the energy storage projects in the U.S. dedicated to the integration of this technology and a growth rate of 105% since 2013 [50–52]. Specifically, lithium-ion batteries seem to be the popular choice due to their high energy densities, discharge power capacities and ultra high efficiencies [53]. Batteries are well suited to overcome high frequency load fluctuations in the grid due to their great power discharging capabilities [54]. However, the long term storage required to shift renewable energy by several hours or even days is far out of reach for a technology whose benchmark cost of storage falls above 270 USD per kWh [55].

Cost effective alternatives to batteries, in the long to seasonal energy storage space, are pumped hydro and compressed air energy storage (CAES) although they are limited by their environmental impact and availability of natural resources (e.i. caves,

reservoirs, etc) [56]. Solar fuels generation, derived from electrochemical conversion of energy, are emerging as a technology promising tremendous energy densities, up to 20 times higher than current storage technology alternatives.

As a promising energy carrier, hydrogen (H_2) can store a relatively large amount of energy ($170\frac{kWh}{m^3}$) at relatively low cost (19 USD per kWh) [57, 58]. Moreover, H_2 energy storage (HES), with negligeble self discharge and no natural resource requirements, provides the flexibility to use the energy stored in a variety of applications (i.e. feed power back to the electric grid, injecting the H_2 directly into the natural gas grid or to fuel cell vehicles refuelling infraestructure) [57,59–63]. Through the use of an electrolyzer, H_2 and oxygen (O_2) can be produced at an efficiency as high as 75% (LHV) [57,64–66]. The overall energy return on investment (EROI) is dependent upon the system used for the reverse conversion process. Today, the average EROI for HES lays around 40% which is substantially lower thant that of pumped hydro (75-85%), CAES (42-55%) or batteries (60-95%) [56, 67, 68].

Other solutions pass through drawing market strategies that make the pool of generating resources greater (by geographically expanding the electricity markets), incentivizing consumers to react to real time pricing, or smart use of electric equipment (i.e. electric vehicles, home utilities, etc) to reduce peak demand and power gradients. These measures are complex and still require a substantial amount of research and development.

Current practice today relies on the use of flexible capacity. Ideally, flexible power systems feature the capability to switch their load up and down quickly, react quickly to grid operator commands and are resilient to withstand start-stop cycling multiple times a day. The auxiliary nature of these systems motivates load serving entities to prioritize low upfront investment and seek profitability during period of high demand, when electricity spot prices peak. The capacity factor of these systems is often lower than 10% given they are only call at periods of high demand or steep ramps. Besides, the amount of hours they are allowed to operate is often limited by environmental regulation. Consequently, it is not economically appealing to invest in capital intensive high efficiency systems but rather in medium scale gas turbines (GT) and reciprocating internal combustion engines (RICE) which together feature enough power density and ramp up capabilities to fulfill the flexibility requirements. Fueled by fossil fuels, they struggle to address GHG and AQ concerns by emitting high volumes of CO_2 and criteria pollutants. This can be attributed to the relative low efficiency, exacerbated by the need to perform cold starts with no scheduled warm up periods[6].

1.3 The emergence of Natural Gas

The low efficiency of flexible resources makes its profitability even more susceptible to fuel price fluctuations. This strong dependence on the stability of the energy markets is driving power suppliers to progressively transition to cheaper and predictible fuel

[6]During cold start, heat engines efficiency is extremely low due to incomplete combustion and large system tolerances due to unbalanced thermal expansions.

resources. Natural gas (NG) is an abundant fuel around the globe whose price, unlike oil, is indifferent to the acostumed political instabilities of the middle east. Particularly in the US, with the boost in shale gas production since 2009 (figure 1.7), the abundance of NG has created a glut helping maintain low prices and motivating a substantial increase on the gas fired power generation (figure 1.8) [69]. This is accentuated by the planned retirement of nuclear and coal capacity which, despite the radical growth in renewables, is vastly being replaced by gas fired capacity (figure 1.9) [26]. In California alone, the amount of peaker power plants has grown from 29 in 2001 to 74 in 2014, not counting for small RICE plants which provide ancilliary services and load balancing [70].

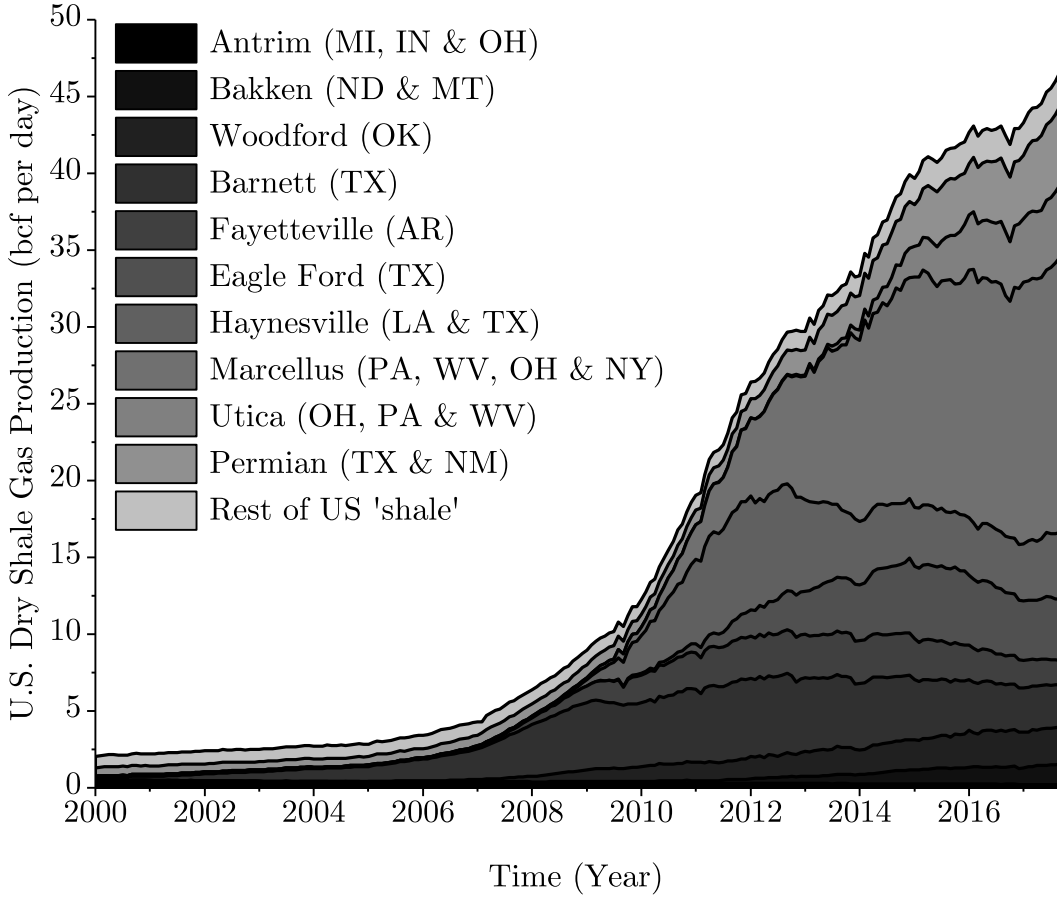

Figure 1.7: U.S. dry shale gas production estimates since 2000 [71].

Although still a fossil fuel, NG is a considered a cleaner alternative to oil and coal results of its lower carbon to hydrogen ratio. Moreover, its high heating value and octane rating allows for further optimization of the combustion process, often rendering more efficient power systems. It is estimated that by 2040, the share of oil and coal has decreased in favor of increasing NG, the fastest growing fossil fuel based energy source [26].

Globally, an increase in NG consumption may strengthen the growth of a worlwide liquefied natural gas (LNG) market, exemplified with increased drilling operations in the north west coast of Australia which, together with the US, is expected to become one of the largest exported of LNG globally in years to come [25, 28, 72, 73]. With the US serving as reference, the establishment of a robust global NG market may generate expectations of fairly constant prices, maintaining the incentive for private investment on NG fired power capacity and infrastructure [74].

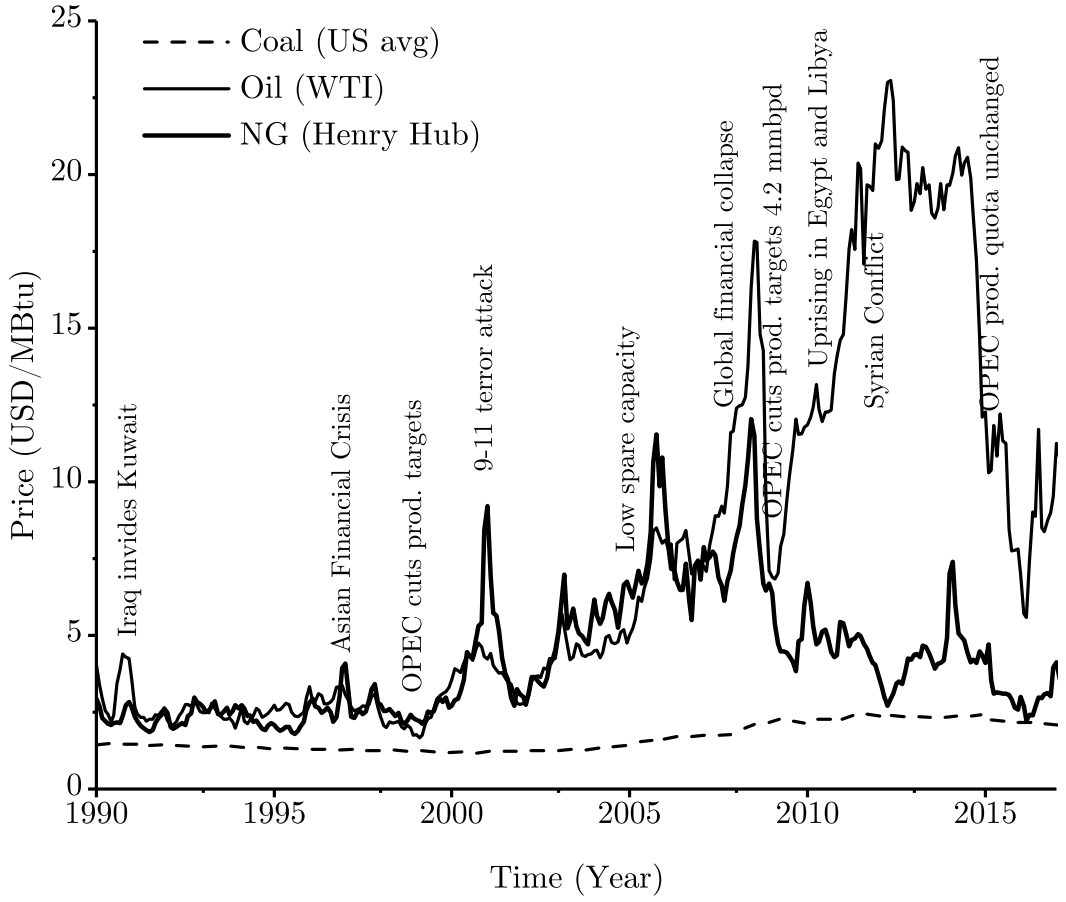

Figure 1.8: Commodity price comparison of oil, natural gas and coal in the US market since 1990 [75].

This change in the power generating portfolio is already having an effect on the US power sector which has seen a steady decrease in CO_2 emissions since 2005. Decarbonization of the power sector will continue, but unless more radical measures are taken, conditions are not projected to lead to sufficient emissions reduction to halt global temperature rise to less than 2 degrees Celsius [69].

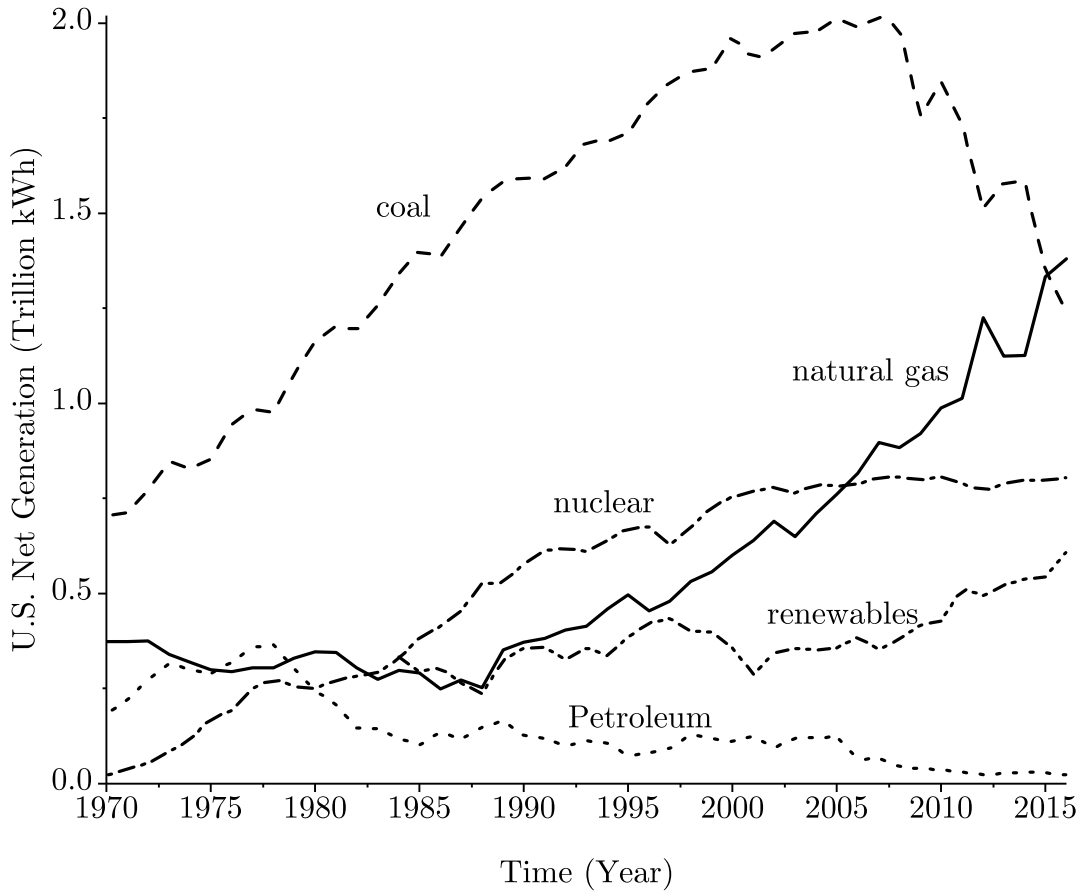

Figure 1.9: U.S. Electricity Net Generation by energy source [76].

Carbon Capture and Sequestration is crucial

The expectation of NG to become the fuel of choice for decades to come, together with the increased use of coal in non-OECD countries justifies the development of carbon capture and sequestration (CCS) technologies that help prevent the lock-in of more GHG emissions during the transitioning period towards RES. Both the IPCC and the International Energy Agency (IEA) have come to the conclusion that no climate model scenario can achieve the goal stated in the Paris agreement without the integration of CCS. Specifically, the IEA estimates that at least four thousand million tonnes per year of CO_2 need to be captured from now until 2040 if we are to limit temperature rise to less than two degrees Celsius over the 1850-1900 period [7, 77].

In spite of the attention that CCS has received since it was first acknowledged as a promising technology in 1995, not much progress has been accomplished and the number of projects currently operating or being deployed worldwide can be counted by no more than a few tens [7]. Because the mitigating nature of CCS, there is little to no business case attained to its integration. Unlike improvement in efficiency and

[7] GCCSI reports 39 large CCS projects worldwide in development [78].

integration of renewables, CCS cannot promise returns based on lower marginal cost or enhanced energy security. As a result, financial support for its development is and has been always strongly tied to the regulatory and political climate. The IEA reports that in the last decade a financial support disparity of nearly 2.5 trillion USD has built between renewable energy and carbon capture development and integration efforts [79].

There are a few naturally made market incentives to operate carbon capture plants, but they fall short to the scale necessary for climate change mitigation purposes [80]. Enhanced oil recovery[8] (EOR) is the major driver for CCS development and represents the totality of large scale privately funded carbon capture projects today. However, EOR applications are limited to plants in the vicinity of an oil producing well, and therefore is not optimal to assume EOR would be the long term drive for CCS integration. Other alternatives to EOR exist, such as bioenergy production with CCS (BECCS), a process by which CO_2 generated during the biofuel synthesis is stored underground, is a promissing technology. If succesfully integrated, BECCS would become the most effective carbon negative technology, helping balance off emissions in the long term [78]. Other relevant usage of the captured CO_2 is farming. By maintaining constant and elevated concentrations of CO_2 in greenhouses, the yield of the crop is increased for as much as 30% [81–83]. This is particularly interesting for small power systems which could help fulfill the increasing flexibility needs of the power grid while simultaneously improving the productivity of agricultural industry, effectively rendering a profitable business case for CCS beyond EOR.

However, with little research and development work resulting from a lack of financial support, cost of CCS technology remains extremely high, which, in the absence of a business case, makes CCS very unattractive. Current technologies, such as solvent gas separation, are mature enough as a result of its extensively use by the gas industry, however, its cost is unjustified for a process that, unless proper policy is set in place, will yield no profit, even more so, it will penalize the profitability of the plant [79, 80, 84].

In the specific case of NG, the prospects for succesfull CCS are limited. Unlike gas purification or coal power plant exhaust treatment processes, where CO_2 concentrations are relatively high, the concentration of CO_2 at the stack of a NG plant is lower than 10%. This circumstance, due to the fundamental of gas separation, causes a potential increase in the energy required to carry out the the process and thus the profitability of the plant is downgraded further from that equivalent to a coal fired plant. The efficiency penalties lay in the order of 10-20% absolute points of the original plant efficiency [85]. New methods for carbon capture needs to be made available to allow natural gas to thrive without further harming the delicate climate.

In general, it is clear that the world, and our energy sector more so, has embarked on a challenging and long transition towards a more sustainable socioeconomic development. The energy markets are in need of a transformation which helps deal with the apparent dichotomy between renewable and profitable energy. Furthermore,

[8]EOR is the process of pressurizing a tertiary oil well with carbon dioxide reducing the viscosity of the crude oil, and ultimately, the energetic cost of extraction.

financial tools need to be put in place to support investment in CCS, now more critical than ever before with the proliferation of natural gas in the western world and coal elsewhere. However, as much as the market mechanisms can be asked to adapt, a more profound change needs to be made in the actual way in which we generate power. We have relied on conventional technology for decades and it is not fuel what we are running out of but clean air. Renewable energy have to be implemented more quickly and this endeavor needs to be supported by technologies that strongly obey to the description of truly flexible and clean, ready to participate today and join in a sustainable energy future in which fossil fuel are no longer the standard form of fuel.

With the purpose to support this effort, this thesis presents a new technology, the APC, with the capabilities to provide the flexibility required, while cost effectively enabling the integration of CCS with natural gas, and HES at a fraction of the cost of fuel cells. In the reminder of this chapter, the outline of this work and the contribution to the field are presented.

1.4 Dissertation Outline

In this chapter, the background and motivation for the development of new zero emission flexible power generation technologies have been introduced. In order to better understand the potential benefits of the APC, details on the technology and its unique characteristics are presented in Chapter 2.

In chapter 3, a brief introduction to the the fundamentals behind thermodynamic power cycles is presented with special emphasis on internal combustion engine plants and membrane separation processes. Furthermore, details on the numerical model developed are explained in sufficient detail. The chapter concludes with a discussion of the numerical results.

Chapter 4 introduces the experimental apparatuses used and presents the experimental results carried out in a constant volume chamber and a single cylinder engine.

Finally, in Chapter 5, the conclusions drawn from this work are summarized and recommendations for future research on this topic are given.

1.5 Dissertation contribution

The aim of this work has been to bring light to the use of alternative working fluid on internal combustion engines as a strategy to improve power generation with carbon capture at no detrimental cost to neither the power generating system nor the carbon capture system. Key contributions to the scientific community are highlighted below.

- The APC concept, a new type of power generation system for clean power generation.
- The use of different working fluid in RICE, purposely aimed at improving efficiency and reducing emissions.

- The use of different fuels of industrial interest, including methane (CH_4), hydrogen (H_2) and synthetic syngas (50% H_2 50% CO).
- The application of different injection strategies to enable the use of H_2 fuel at current RICE operating conditions.
- Numerical modeling of the APC with emphasis on the combustion and membrane gas separation processes.

Chapter 2

The Argon Power Cycle

The Argon Power Cycle is an innovative solution intended to help overcome the challenges being faced by the energy sector today. This new thermodynamic cycle improves the performance of RICE, a fast dispatch technology, while making it a ready platform for the integration of post combustion carbon capture. Altogether, the APC promises to be a cost effective strategy that allows wider integration of renewable energy. It does so by accounting for the physical mechanisms needed to improve upon current thermal conversion efficiency, and the main drivers for effective mass transfer processes. In the following sections, the details of the APC will be discovered, briefly diving into the reasons and arguments for its performance characteristics.

2.1 Literature review

The idea of the APC for HES was first suggested by Laumann in 1978 [86] who called it the Hydrogen-Fueled Engine. In 1980, De Boer and Hulet developed the test stand upon Laumann's idea with the intention to power submarines, space systems and ultimately zero polluting vehicles [87]. They acknowledged the challenges of working with stoichiometric mixtures of H_2 and O_2 due to the high tendency to self ignition and knock[1]. This phenomena limited the useful power output that it could be extracted from the engine. They performed a preliminary study and observed the potential for efficiency improvement influenced mainly by the use of a monoatomic gas. In 1982 Ikegami et al. operated an engine under similar conditions and concluded that compression ignition operation of the hydrogen engine with a monoatomic gas was stable and manageable, also witnessing the increase in thermal efficiency. They also noted an increase in the cycle temperature and pressures, and a consequent increase in the heat and friction losses of the system [88]. Toyota in 2010 followed up on the idea of applying this engine strategy at vehicle scale as hinted by De Boer. They observed a substantial thermal efficiency increase and for first time, operated the engine in closed loop configuration. They corroborated the feasibility of the system but concluded that a bigger challenge to the succesfull inplementation of this thermodynamic cycle is the

[1]Knock is the term used in the RICE community to refer to the undesired preignition of the fuel air mixture within the engine cylinder.

acumulation of CO_2, primarily from lubricant oil combustion [89]. In 2011, our group at UC Berkeley replicated the previous results and determined that under premixed condition, the optimum engine geometry was determined by a compression ratio of 5 to 1 at which point the highest efficiency was achieved [90].

The work presented on this dissertation builds upon previous results, and aims to evaluate the feasibility of this cycle fueled by carbon based combustibles, specifically natural gas, both numerically and experimentally.

2.2 Introduction to the APC and its applications

The APC is meant to operate under two major conditions. The first one, aimed at improving the EROI of HES through the efficient and clean conversion of H_2. The second one focuses on the clean conversion of carbon based fuels, mainly natural gas and biogas, by incorporating CCS as an integral part of the power system solution.

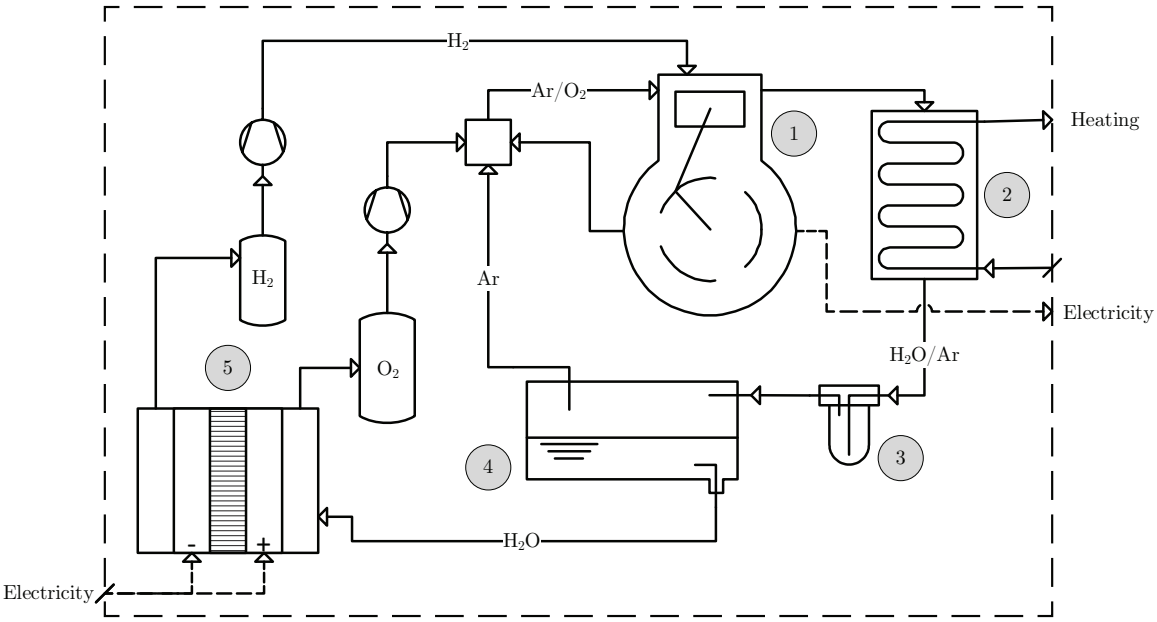

Figure 2.1: Prospective process diagram for a hydrogen fired Argon Power Cycle plant.(1) RICE (2) Heat exchanger (3) Coalescing filter (4) Condenser (5) Electrolyzer.

The APC plant depicted in figure 2.1 represents a simplified process diagram for a hydrogen fired power plant. Excess electricity, otherwise curtailed from wind farms or other sources, is consumed by an electrolyzer (5) that dissociates water, generating high purity H_2 and O_2 at pressures as high as 35 bar [91–93]. The H_2 and O_2 are stored in separate metal tanks and they are fed to the cycle when commanded by the grid operator [58]. H_2 and O_2 are then introduced into the Ar gas stream or directly injected into the engine cylinder (1) where they combust. The resulting gas, a mixture of water vapor and Ar, is exhausted toward the heat exchanger (2) where it is cooled down to near saturation, at which point the gas flows through a coalescing

filter (3) where particles resulting from oil combustion are captured. Finally, the water vapor is condensed in the condenser unit (4) and fed back to the electrolyzer. The heat rejected by the engine is released to the surroundings or used in a combined heating and power (CHP) framework increasing the overall efficiency of the system. In this configuration, this power cycle can reach an efficiency as high as 80%, which in combination with the electrolysis system would yield a EROI in the order of 50-60%.

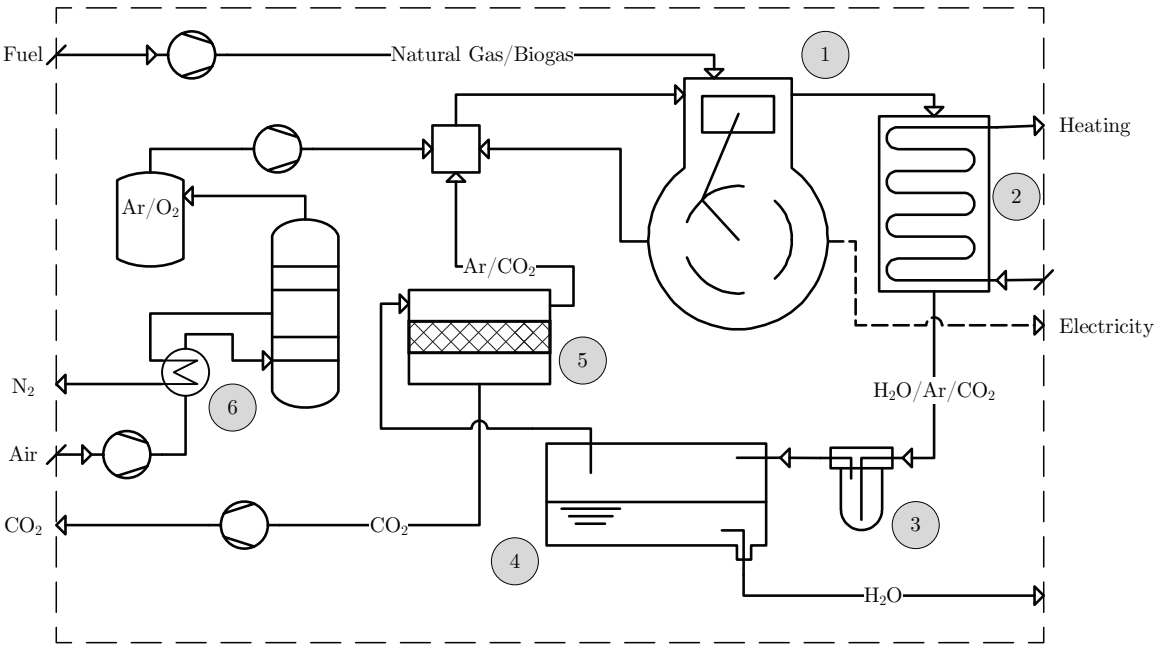

Figure 2.2: Prospective process diagram for a gas fired Argon Power Cycle plant.(1) RICE (2) Heat exchanger (3) Coalescing filter (4) Condenser (5) Membrane system (6) Air separation unit (ASU).

Although a promising technology for HES, the H_2 economy is yet to grow and fully develop. In the meantime, as introduced in chapter 1, the use of fossil fuel continues to increase, filling the electric grid demand for flexibility and reliability. For this purpose, strategies that allow for cost effective CCS are of extreme necessity. Figure 2.2 presents a prospective and simplified process diagram for an APC plant meant to operate in natural gas while capturing 100% of the generated CO_2. This plant could theoretically operate at an efficiency as high as combined cycle gas turbine power plants (CCGT) while not only capturing its emissions but also not generating any criteria pollutants or consuming any valuable water.

This plant feeds from the natural gas line or on-site biogas. The O_2 used originates from an in site cryogenic air separation unit (ASU) (6) optimized to separate O_2 from N_2 only. The generated oxygen is fed to the plant gas stream, primarily consisting of Ar and CO_2. The fuel is fed either prior to the RICE (1) or directly injected into the engine cylinder where the mixture of fuel and oxidizer combust. The exhaust gas resulting from combustion is then cooled down in the heat exchanger (2) to near water saturation temperatures at which point it flows through a coalescing filter (3) where particles resulting from oil and other foreign components combustion are captured.

The water vapor is condensed in the condenser unit (4) and subtracted from the system as a source of cooling water or for any other purpose. The dried gas is then fed to a membrane gas separation system (5) that extracts part of the CO_2 and delivers an enriched Ar gas stream back to the engine intake. The CO_2 captured is either compressed for storage or delivered to any facility for further use. As in the case of HES, the heat rejected by the engine is released to the surroundings or used in a CHP framework increasing the overall efficiency of the system.

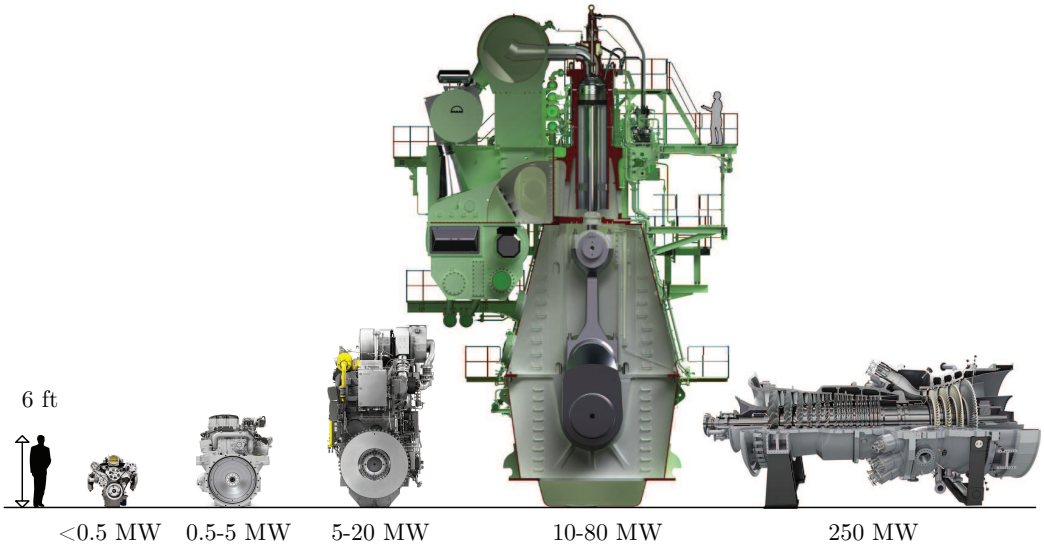

Figure 2.3: System dimensions as it scales with power output for RICE. The scale is not linear as efficiency and number of engine cylinders increases. A 250 MW gas turbine is depicted for reference.

It is important to understand that the use of the term RICE hints at the use of internal combustion engines for transportation purposes as we are most accustomed to. However, an APC plant is meant to operate at a scale from tens to hundreds of megawatts, justifying the investment and impact of this technology in the energy sector. For reference, figure 2.3 presents an scale comparison of several RICE system and a common GT for power generation purposes.

The key to the great theoretical performance of the plants presented above resides in a combination of several factors, most importantly, the synergistic relationship among the systems involved,which allows reducing the efficiency penalty they impose onto the system on their own. Of those factors, three major ones are to be highlighted:

1. The use of a monatomic gas as a working fluid,
2. the implementation of a 100% close loop configuration,
3. and the use of a RICE as the conversion system of choice.

In order to better understand the impact of the three above factors, in the remaining of this chapter, an introduction to the fundamental principles affecting the

performance of the internal combustion engine is given and set in context with the APC. Furthermore, the arguments for the use of Ar and a close loop recirculated configuration are given.

2.3 RICE fundamentals

In this section, a brief introduction to the basic performance indicators of a RICE are presented, with special emphasis on the thermodynamic efficiency. This is done with the intention to provide the reader the fundamentals for understanding the results presented in the forthcoming chapters. It is also expected the reader to understand by the end of this section how at power plant scale, RICE engines can truly approach ideal behavior, and how the thermodynamics are the true boundary to enhancing the performance of these magnificent machines.

2.3.1 Engine kinematics

RICE convert thermal energy into mechanical energy through the linear displacement of a piston (figure 2.4. Although the piston, in a four stroke engine, consumes four strokes to complete a power cycle, the thermodynamic cycle is completed within only two of them: the compression (2) and expansion (3) strokes. In the specific case of the SI engine, the different stages are as follows:

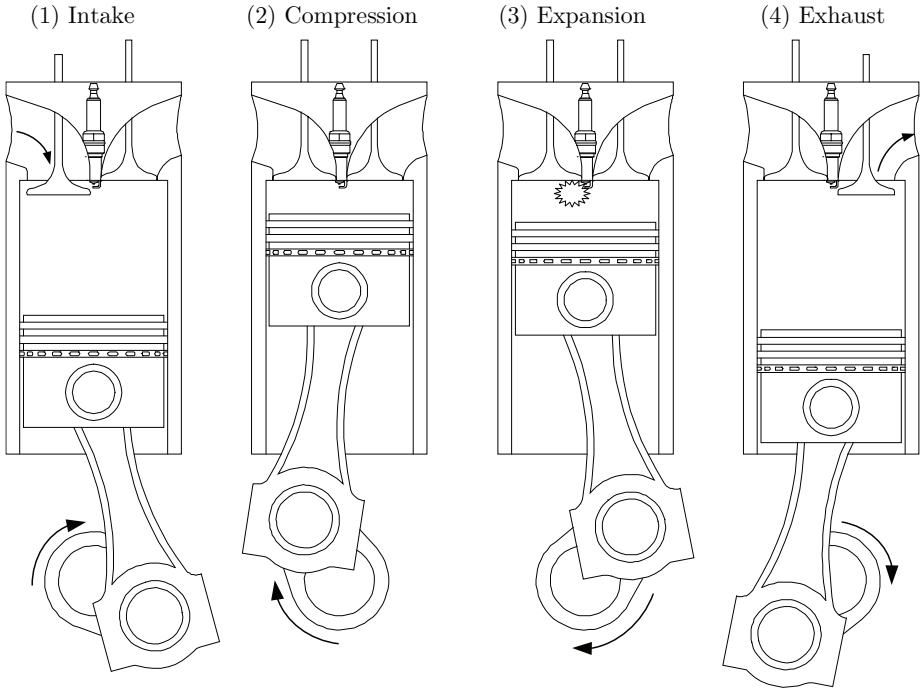

Figure 2.4: 4 Stroke engine cycle process.

1. Intake stroke. The process starts with the piston at the very top of its travel or top dead center (TDC). The inlet valve opens, and the piston travels down inducing the air-fuel mixture to come inside the cylinder.

2. Compression stroke. When the piston has reached the bottom end of the stroke or bottom dead center (BDC), inlet valve closes and air inside is compressed by the piston traveling upward. When the piston reaches TDC, the combustion event is triggered either by reaching ignition temperatures or commanded by a spark event.

3. Expansion stroke. The combustion event had occurred and the sudden pressure rise in the cylinder resulting from the fuel energy being released, pushes the piston downwards delivering mechanical work to the crankshaft.

4. Exhaust stroke. When the piston approaches BDC, the exhaust valve opens and the piston, on its way up, pushes the burnt gases out of the cylinder, at which point the intake stroke begins.

A typical geometry of a single piston SI engine is shown in figure 2.5. The piston transforms linear velocity into rotational speed via a piston rod and crank mechanism. The piston moves in a reciprocal manner, up and down, drawing a sinusoidal trajectory described by

$$s(\theta) = a \cdot cos(\theta) + \sqrt{l^2 - a^2 sin^2(\theta)} \ , \tag{2.1}$$

with an amplitude equivalent to half the stroke (S) determined by the crankshaft radius (a) and piston rod length (l). The frequency (N) is determined by the crankshaft rotational speed (ω)

$$S = 2 \cdot a \tag{2.2}$$

$$N = \frac{\omega}{2\pi} \tag{2.3}$$

The volume trapped between the cylinder head and the piston ($V(t)$) varies in time from a minimum, when the piston is at the very top, to a maximum, when the piston is at the very bottom. The minimum volume, at TDC, is called the combustion chamber volume V_c. The volume generated by the piston in motion is called the displaced volume V_d and varies in time, with the angular position (θ) of the piston rod

$$\theta = \omega \cdot t \ , \tag{2.4}$$

$$V_d(\theta) = (a + l - s(\theta)) \cdot A_p \ , \tag{2.5}$$

The total capacity of the cylinder V_T is the sum of the combustion chamber volume V_c and the maximum volume displaced by the piston.

$$V_T = V_c + V_d(180^\circ) \ , \tag{2.6}$$

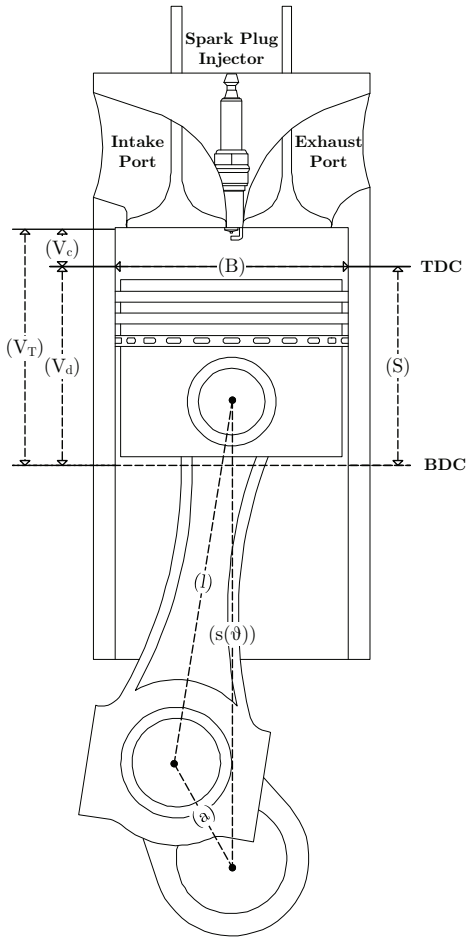

Figure 2.5: Example of a four stroke SI engine cylinder-piston geometry. V_c: Combustion chamber volume; V_d: Volume displacement; V_T: Total cylinder volume; TDC: Top Dead Center; BDC: Bottom Dead Center; S: Stroke; B: Bore; l: Rod length.

where the surface area A_p is derived from the piston's diameter or bore B as follows

$$A_p = \frac{\pi B^2}{4} \ , \tag{2.7}$$

The mean linear velocity of the piston is used to compare different characteristic stroke engines and is given by

$$\overline{s}_p = 2 \cdot S \cdot \omega \ , \tag{2.8}$$

These set of parameters define the kinetic characteristics of the engine and serve to carry out the subsequent combustion analysis from the physical properties measured during experiments. Three important ratios are derived from the above equations: the compression ratio (r_c),the bore to stroke ratio (R_{bs}) and the piston rod to radius ratio (R) as defined in [94]. The first ratio

$$r_c = \frac{V_d + V_c}{V_c}, \tag{2.9}$$

is a direct indicator on how efficient the engine is, as it will be explained in section 2.3.3. Less influential is

$$R_{bs} = \frac{B}{S}, \tag{2.10}$$

which characterizes the rotational speed range at which a given engine operates. Large bores to stroke ratios are characteristics of fast spinning engines and vice versa. This allows to optimize an engine on a power versus torque bases as inferred from the power-torque relationship in equation 2.12. The third ratio

$$R = \frac{l}{a}, \tag{2.11}$$

is an indicator of engine's size.

2.3.2 Engine Brake parameters

Regarding engine performance, it is common to use terms such as brake power, brake thermal efficiency among many other brake terms. Brake values are related to the net output of the engine. Outside research environments, an engine is normally defined by what it has to offer to the operator and the integral aspect of the machine are overlooked. The different and most relevant terms are introduced below. In this document, brake terms will be identified by a subscript "B" or the prefix "b".

Brake power and torque

Brake torque and brake power are the most important values regarding the engine performance. They indicate the potential of the engine to generate work and the rate at which the work is generated, respectively. They are related through

$$P_B = \omega T_B \ , \tag{2.12}$$

where ω is the rotational velocity of the engine in radians per second. The torque is computed through

$$T_B = F_B \cdot r \ , \tag{2.13}$$

where F_B is the brake force generated by the engine's pistons and r the radius of the rotational motion. In general this parameter is read by a dynamometer, with F_B being the force measured at the dyanmometer arm and r the dynamometer arm length. Torque relates to engine brake work W_B through

$$W_B = \int_{\theta_0}^{\theta_i} T_B d\theta \ , \tag{2.14}$$

where $d\theta$ represents a differential of crank angle degree and θ_0 and θ_i are an initial and final crank angle position of the piston rod.

Brake specific fuel consumption

The fuel consumption of an engine is of great relevance. The amount of fuel being consumed is indicated by the fuel mass flow ($\dot{m}_f$). More relevant than the fuel flow is the fuel flow per unit of brake power. In other words, the amount of fuel needed to produce a kWh of brake work. This measurement is defined as the brake specific fuel consumption (BSFC) and it is given by

$$\text{BSFC} = \frac{\dot{m}_f}{P_B} \ . \tag{2.15}$$

This terms is often used as a measure of engine's efficiency when the comparison is being made between same fuel operated engines.

Brake specific emissions

As in the case of fuel consumption, it is useful to normalize emissions values in order to compare different size engines. Brake specific emission $\text{BS}\chi_i$ expressed in g/kWh and is computed for species i as follows

$$\text{BS}\chi_i = \frac{\dot{m}_{\chi,i}}{P_B} \ , \tag{2.16}$$

where $\dot{m}_{\chi,i}$ is the total mass flow of species i which is obtained by

$$\dot{m}_{\chi,i} = \dot{m}_f \left(1 + \frac{A}{F}\right) \frac{M_i}{M_{exh}} \cdot \chi_{i,wet} \ , \tag{2.17}$$

$$\frac{A}{F} = \frac{\dot{m}_{air}}{\dot{m}_f} \ , \tag{2.18}$$

where $\frac{A}{F}$ is the ratio of air to fuel ratio at which the engine is being operated. M_i and M_{exh} are the molar mass of species i and exhaust respectively, and $\chi_{i,wet}$ is the wet volumetric concentration of species i [2] given by

$$\chi_{i,wet} = (1 - \chi_{H_2O}) \cdot \chi_{i,dry} \ , \tag{2.19}$$

with $\chi_{i,dry}$ the dry volumetric concentration of specie i normally measured with a gas analyzer device.

The terms introduced above will be widely use in this work. More terms are defined in literature, but for simplicity they will be introduced as they are needed.

2.3.3 Internal combustion engine efficiency

In this section, the fundamental concepts behind the performance of RICE are introduced. For the sake of simplicity and clarity of this dissertation, only the four stroke

[2] Wet concentration regards the volumetric concentration of species on a mixture with water content. On the contrary, dry concentration relates to water free or dry mixtures.

spark ignited (SI) engine will be described. Broader and more detailed information on RICE can be found in [94–96].

The basic purpose of a RICE is to transform chemical energy, stored in the fuel, into mechanical work. This conversion is achieved through a thermodynamic cycle. In general, the engine performance is assessed based on how much work it is able to deliver (W_B) from a given amount of chemical energy (Q_f). The ratio of these two quantities is denominated Brake Efficiency and is given by

$$\eta_B = \frac{W_B}{Q_f} \,, \tag{2.20}$$

where Q_f represents the energy contained in the consumed fuel (m_f). The brake efficiency term in equation 2.20 describes how well an engine performs, although it does not tell the reason why. To be able to improve and develop better and more sophisticated engines, it is important to know the sources of inefficiencies and the aspects of the engine that are already fully developed. To do so, more variables than just the overall efficiency have to be evaluated [97]. A common way to disect the influece of different parameter on the overall efficiency is given by

$$\eta_B = \eta_C \cdot \eta_T \cdot \eta_{G.E} \cdot \eta_M \tag{2.21}$$

In this equation, the engine brake efficiency is broken down into four different terms. Each of them representing a different source of irreversibilities in the energy conversion process.

1. Combustion efficiency η_C.
2. Thermodynamic efficiency η_T.
3. Gas exchange efficiency $\eta_{G.E}$.
4. Mechanical efficiency η_M.

These terms follow in order from the very beginning, the energy contained in the fuel, to the very end, the work delivered by the engine.

Mean Effective Pressure

Though efficiency is an effective approach to compare the performance between different engines and operation conditions, the evaluation of different type of energy losses such as heat losses or mechanical losses cannot be directly achieved by assessing their direct values because they are strongly influenced by the size of the engine. For this purpose, it is useful to normalize with size the different parameters resulting from the engine operation.

The mean effective pressure is the result of normalizing energy parameters with the displacement volume of the engine. Because the displaced volume V_d is a predefined

and constant parameter of any engine, it serves greatly to this purpose. Thus, any energy quantity x can be expressed in terms of pressure by

$$\text{xMEP} = \frac{x}{V_d} \,, \tag{2.22}$$

where xMEP is the representation of the energy flow x in terms of pressure. Normalized values allow for comparison of different energy streams from different engines. Thus, equation 2.20 can be also expressed in the form

$$\eta_B = \frac{\text{BMEP}}{\text{FuelMEP}} \,, \tag{2.23}$$

where BMEP and FuelMEP are the pressure equivalents for the brake work and the energy contained in the fuel, respectively. They are computed as follows

$$\text{BMEP} = \frac{P_b n_c}{V_d \omega} \,, \tag{2.24}$$

$$\text{FuelMEP} = \frac{Q_f}{V_d} \,, \tag{2.25}$$

where n_c is the number of revolution per engine cycle, and Q_f is the energy brought in by the fuel at each cycle.

In this work, mean effective pressure equivalents will be used to refer to energy flows, and conclusion are drawn based on these values. An easy conversion to the original values is possible by multiplying by the displacement volume V_d of the engine in question.

Combustion efficiency

The first term, η_C in equation 2.21 indicates the effectiveness with which the energy from the fuel is extracted to produce heat. It is strongly dependent on the type of fuel used, combustion chamber geometry, and combustion temperatures among other parameters [94, 95]. It is expressed as the ratio between the energy released by the combustion event and the total energy contained in the fuel.

$$\eta_C = \frac{Q}{Q_f} = \frac{\text{QMEP}}{\text{FuelMEP}} \tag{2.26}$$

where Q is the energy released during combustion. The energy contained in the fuel Q_f reads

$$Q_f = m_f \cdot Q_{\text{LHV}} \tag{2.27}$$

where m_f is the fuel mass and Q_{LHV} is the lower heating value of the fuel. The energy released during the combustion event can be computed through an energy balance. This technique requires numerous assumptions which diminish the accuracy of the results. Nonetheless, if the emissions before the catalyst are known, the energy lost due to incomplete combustion can be measured. The useful energy could be

inferred from the difference between energy contained in the fuel and the energy lost. If the total amounts of remaining reactants and reaction intermediates (THC), such as remaining fuel or other hydrocarbons are known, the chemical energy leaving the system through the exhaust gases can be written as

$$Q_{loss} = m_f \cdot (1 + \frac{A}{F}) \sum_{i=1}^{N} \frac{M_i}{M_{exh}} \cdot \chi_{i,wet} \cdot Q_{\mathrm{LHV},i}; \quad i = 1, ..., N_p. \tag{2.28}$$

where $Q_{\mathrm{LHV},i}$ is the lower heating value of the different N_p hydrocarbons present in the exhaust stream. Therefore, a good approximation of the energy losses due to incomplete combustion can be obtained from the amount of the most energy dense compounds such as total remaining unburnt hydrocarbons (THC), carbon monoxide (CO) and Hydrogen (H_2). The first two terms are obtained through a five gas analyzer device. The last is obtained by approximation with the aid of the water gas shift reaction

$$\mathrm{CO} + \mathrm{H_2O} \leftrightarrow \mathrm{CO_2} + \mathrm{H_2} \tag{2.29}$$

with equilibrium constant given by

$$K = \frac{\chi_{\mathrm{CO}} \chi_{\mathrm{H_2}O}}{\chi_{\mathrm{CO_2}} \chi_{\mathrm{H_2}}} \ , \tag{2.30}$$

which, for temperatures within 600 to 2000 K, can be approximated [98] by

$$log(K) = -2.4198 + 0.0003855T + \frac{2180.6}{T} \ , \tag{2.31}$$

where T is the temperature of the exhaust, normally around 700 to 1000 K. At this temperature range the chemistry is frozen and one can assume the equilibrium constant to be around 3.5. Normal lower heating values for the aforementioned compounds are shown in table 2.1. Notice that the concentration of H_2O is not given by the gas analyzer which measures only exhaust gas that has been dried. In order to approximate this value, we balance the chemical equation for the combustion reaction. For methane it reads

$$a\,\mathrm{CH_4} + b\,(\mathrm{O_2} + 3.727\mathrm{N_2}) \rightarrow c\,\mathrm{CO_2} + d\,\mathrm{H_2O} + 3.76b\,\mathrm{N_2} \tag{2.32}$$

To obtain the molar concentration of water

$$\chi_{\mathrm{H_2O}} = \frac{d}{c + d + 3.727b} \tag{2.33}$$

Finally, with all the values available we can normalizing the combustion losses by

$$\mathrm{CLMEP} = \frac{Q_{loss}}{V_d} \ . \tag{2.34}$$

The energy available in the combustion chamber can be written then in the form

$$\mathrm{QMEP} = \mathrm{FuelMEP} - \mathrm{CLMEP} \ , \tag{2.35}$$

Table 2.1: Lower heating value of CO, H_2 and CH_4 [99].

Compound	Formula	Lower heating value (MJ/kg)
Methane	CH_4	50.01
Carbon monoxide	CO	10.112
Hydrogen	H_2	119.96

and thus the combustion efficiency can be expressed as

$$\eta_C = 1 - \frac{\text{CLMEP}}{\text{FuelMEP}} \, . \tag{2.36}$$

Thermodynamic efficiency

The thermodynamic efficiency represents the effectiveness with which the engine achieves the thermodynamic cycle. It is a a measure of how well it uses the heat from combustion Q to produce work W_T. The thermodynamic efficiency can be written as

$$\eta_T = \frac{W_T}{Q} \tag{2.37}$$

The most common thermodynamic cycle used in natural gas fueled engines is an Otto cycle (illustrated in figure 2.8). This cycle consists of four different thermodynamic processes:

- Adiabatic compression (point 1 to 2).
- Isochoric compression (point 2 to 3).
- Adiabatic expansion (point 3 to 4).
- Isochoric expansion (point 4 to 1).

The total work delivered by the engine over the thermodynamic cycle can be calculated by integrating the pressure function from the start to the end of the cycle.

$$W_T = \int_1^4 p \cdot dV \tag{2.38}$$

Making use of the thermodynamic relationships for adiabatic and isochoric processes, and assuming perfect gas, the theoretical efficiency for in ideal Otto cycle can be written in the form:

$$\eta_T = 1 - \frac{1}{r_c^{\gamma-1}} \, , \tag{2.39}$$

where γ is the adiabatic index or heat capacity ratio of the working fluid

$$\gamma = \frac{c_p}{c_v} \, . \tag{2.40}$$

and r_c is the compression ratio as shown in equation 2.9. From equation 2.39 it can be concluded that the thermodynamic efficiency of the engine is only dependent on the compression ratio (r_c) determined by the engine's geometry and the working fluid being used ($\gamma_{w.fluid}$). The term working fluid refers to a substance or a mixture thereof, serving the purpose of carrying the energy that is transferred or transformed within a thermodynamic cycle. The main task of the working fluid is to store and release the energy within the process in the best way possible, maximizing, in the case of conventional power systems, the conversion of thermal energy into mechanical energy.

In general, molecules store energy by incresing their degrees of motion or by realizing an electronic or nuclear transition to a new electron or atomic structure [100]. More specifically, in the case of energy storage by motion, a molecule can exercise translation, rotation and vibrational motion. If we narrow our scope to the special case of ideal gases, at sufficiently low pressure and high temperature, it can be assumed these energy storage modes to be independent from one another, at which point, the energy stored on each mode can be discreetly evaluated. From statistical thermodynamics we learn to represent the energy contained in a molecule through the use of the molecular partition function

$$q(V,T) = q_{tr}q_{rot}q_{vib}q_e q_n \tag{2.41}$$

where $q_{tr}, q_{rot}, q_{vib}, q_e$, and q_n are the statistical representation of the energy stored in translation, rotation, vibration, electronic and nuclear storage modes available to the molecule respectively. Noble gases particularly, due to its single atom nature, cannot exercise either rotation nor vibrational motion. As a results, their molecular partition function can be simplified to

$$q(V,T) = q_{tr}q_e q_n \tag{2.42}$$

Furthermore, assuming either electrical nor nuclear transition occurs in the range of temperatures of interest, the molecular partition function can be further simplified to

$$q(V,T) = q_{tr} \tag{2.43}$$

$$q_{tr} = \left(\frac{2\pi M \kappa_B T}{h^2}\right)^{3/2} V \tag{2.44}$$

where κ_B and h are the Boltzman's and Planck's constant respectively. Further mathematical procedure would yield the expressions describing the thermodynamic state properties[3] of the molecules at different temperatures. For simplicity, we focus here in a specific property of interest: the specific heat at constant volume c_v.

$$c_v = \left(\frac{\partial U}{\partial T}\right)_V \tag{2.45}$$

[3]This is the case assumed the molecules behave as an ideal gas.

with U the internal energy. For the case of a monatomic gas this expression yields

$$c_{v,Ar} = \frac{3}{2}R_u \tag{2.46}$$

where R_u represent the universal gas constant. Similarly, for diatomic and linear polyatomic molecules such as N_2 and CO_2 the resulting expression for c_v

$$c_{v,N_2} = \underbrace{\frac{3}{2}R_u}_{\text{translation}} + \underbrace{R_u}_{\text{rotation}} + \underbrace{R_u \sum_{j=1}^{3n-5} \left[\left(\frac{\theta_{vib,j}}{T} \right)^2 \frac{e^{\frac{\theta_{vib,j}}{T}}}{\left(e^{\frac{\theta_{vib,j}}{T}} - 1 \right)^2} \right]}_{\text{vibration}} \tag{2.47}$$

where $\theta_{vib,j}$ is the j vibration temperature for the molecule in question. Figure 2.6 depicts the resulting trend from each of the three molecules as they increase their temperature at constant volume conditions. One can observe how CO_2, with the most modes of motion available (6), stores substantial amounts of energy in its vibrational modes. Nitrogen does so as well, however to a lesser degree. Finally, we can observe how noble gases store all its energy in translational motion. Note that the area under the curves in figure 2.6 is a direct representation of the internal energy of the molecule (U). Thus, with relatively low amount of energy, monoatomic gases quickly rise in temperature.

This difference in the way each molecule stores energy has a great and direct effect on the efficiency of thermal to mechanical energy conversion processes. These processes exploit the thermodynamic relationship between temperature and pressure to generate high pressures, ultimately producing what is often refereed to in thermodynamics as boundary work. Consequently, the working fluid affording the highest pressure increase per unit of energy supplied will carry out a greater conversion from thermal energy to mechanical energy. Exploiting the ideal gas relation between c_p and c_v, and rewriting equation 2.39

$$\eta_T = 1 - \left(\frac{1}{r_c} \right)^{\frac{R_u}{c_v}} \tag{2.48}$$

it is easier to observe that working fluids with the lowest molar c_v offer the greatest potential for efficient thermal to mechanical energy conversion. Thus, monatomic gases, with the lowest c_v, are the ideal working fluids for thermal energy conversion processes. Figure 2.7 depicts the resulting theoretical efficiency of the Otto cycle for Ar, N_2 and CO_2. In this plot, the effect of different c_v and r_c for cycles operating over the same temperature range can be seen.

Theoretically, a RICE with compression ratio of 10 and air ($\gamma_{N_2} = 1.4$) could achieve an efficiency of 60%. In reality, such number is not achieved and the engine efficiency falls within the range 40-50%. The reason for the discrepancy lies in the temperature dependence of c_v which increases with temperature. No such effect is seen in the case of monatomic gases, in which case, as seen in figure 2.6, c_v remains constant.

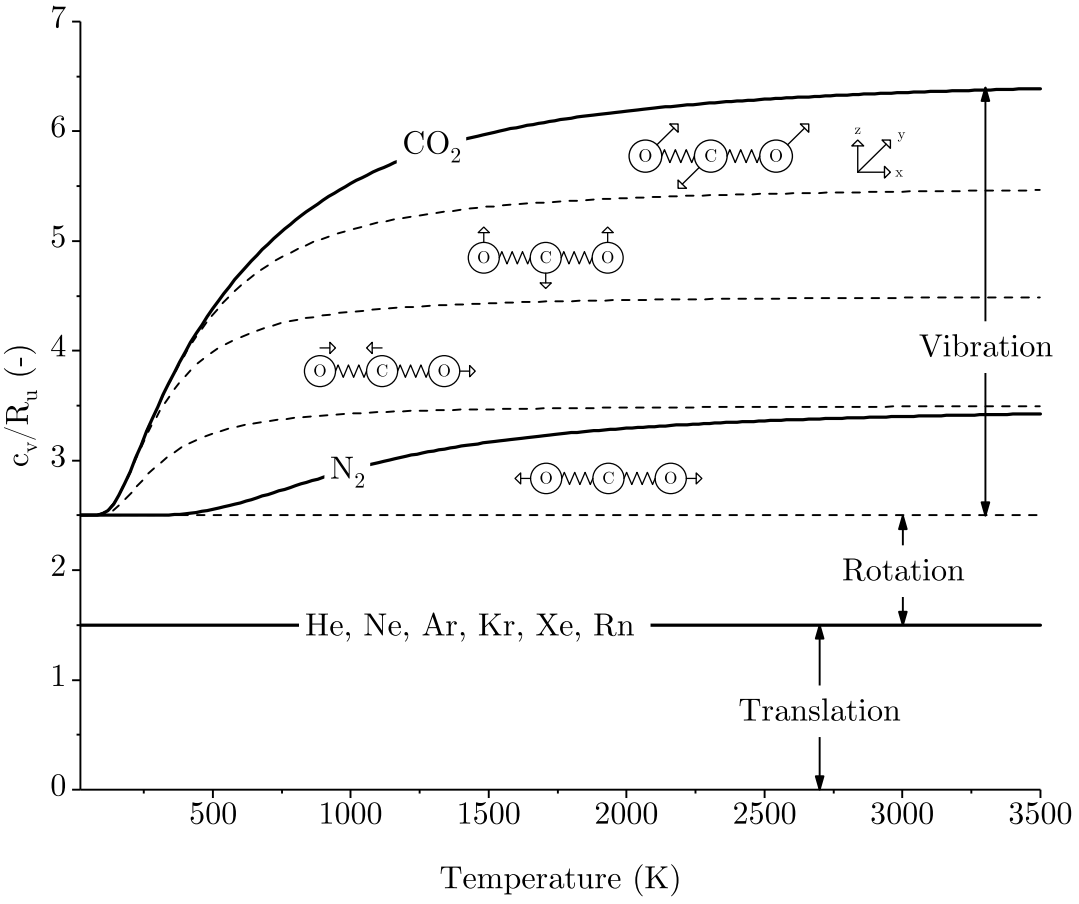

Figure 2.6: Contribution of different molecular modes of motion to the specific heat of monatomic gases, N_2 and CO_2.

Figure 2.8 shows a real example of an SI engine operating on the Otto cycle. Although the potential efficiency of the cycle is 45% for the conditions replicated in the example, the cycle does not achieve more than a 35% efficient conversion. The reason being that neither the adiabatic nor isochoric processes are truly accomplished.

(a) Because of the high temperatures reached by the gases during combustion, the temperature gradient between the gas and the cylinder wall increases, thus enhancing heat flow through the cylinder wall. These type of losses are more noticeable in small engines where the area to volume ratio of the cylinder is higher.

(b) Another major source of efficiency loss results from the destruction of exergy when the exhaust gas is released to the atmosphere. Because the gases have to be withdrawn from the cylinder,the exhaust valve opens (EVO) before reaching BDC, maintaining the pressure in the cylinder always above atmospheric pressure. Though this measure sacrifices boundary work, it reduces the need of pumping the exhaust gases. Consequently, under expanded hot exhaust escapes the cylinder. A way to

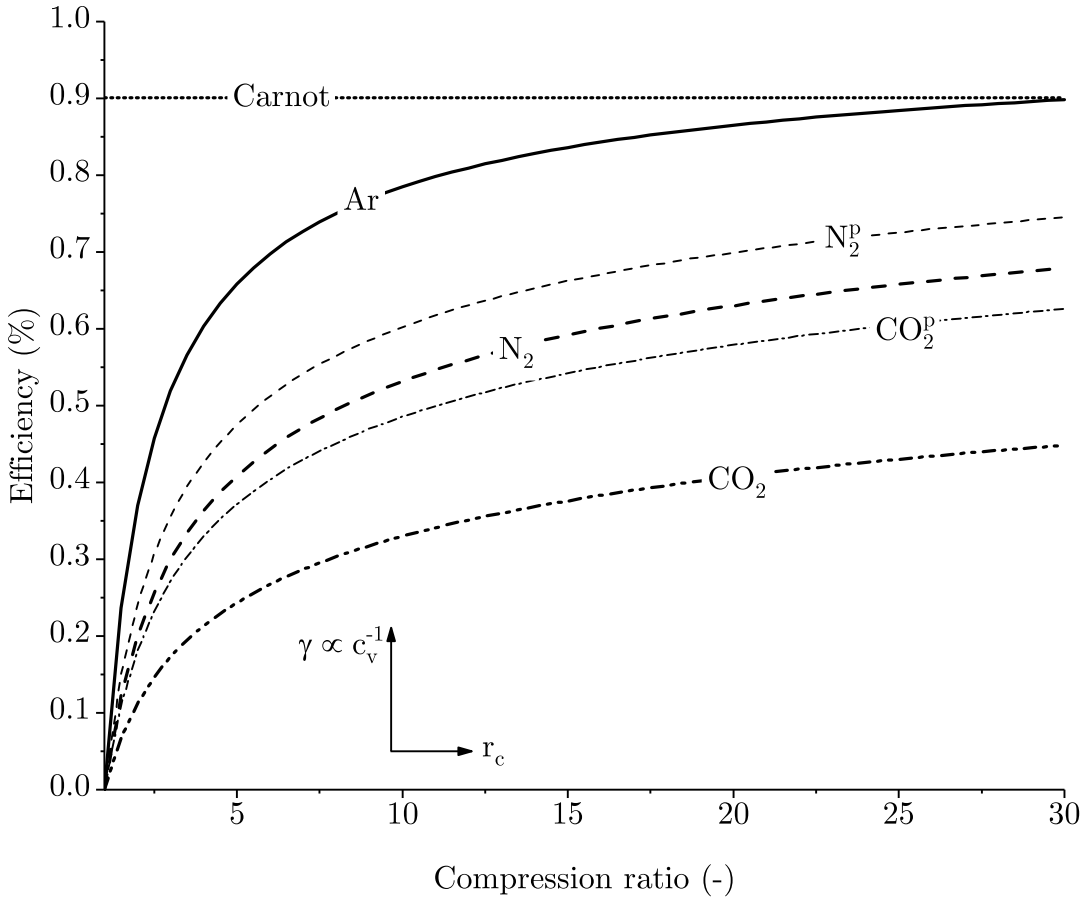

Figure 2.7: Effect of specific heat and compression ratio on the thermodynamic efficiency of the Otto cycle. With the superscript p represents thermodynamic efficiency estimated with the cool air assumption. The Carnot efficiency is plotted for reference.

reduce this parasitic loss in large engines is to use a bottoming cycle (e.i. Rankine cycle) or use the exhaust as a source of heating for an adjacent industrial process.

(c) A third limitation exists for the real engine cycle. Because the flame speed of common fuels is not infinitely high, the combustion event takes longer than desired and combustion is still ongoing when the piston is on its way downwards, passing TDC. The heat addition does not occur at constant volume, preventing pressure from reaching its theoretical maximum.

Similarly to the combustion process, the different energy flows occurring during the thermodynamic cycle can be written in terms of MEP. The gross indicated (per cylinder) work generated over the course of the compression and power strokes is written as

$$\mathrm{IMEP}_G = \frac{W_T}{V_d} \tag{2.49}$$

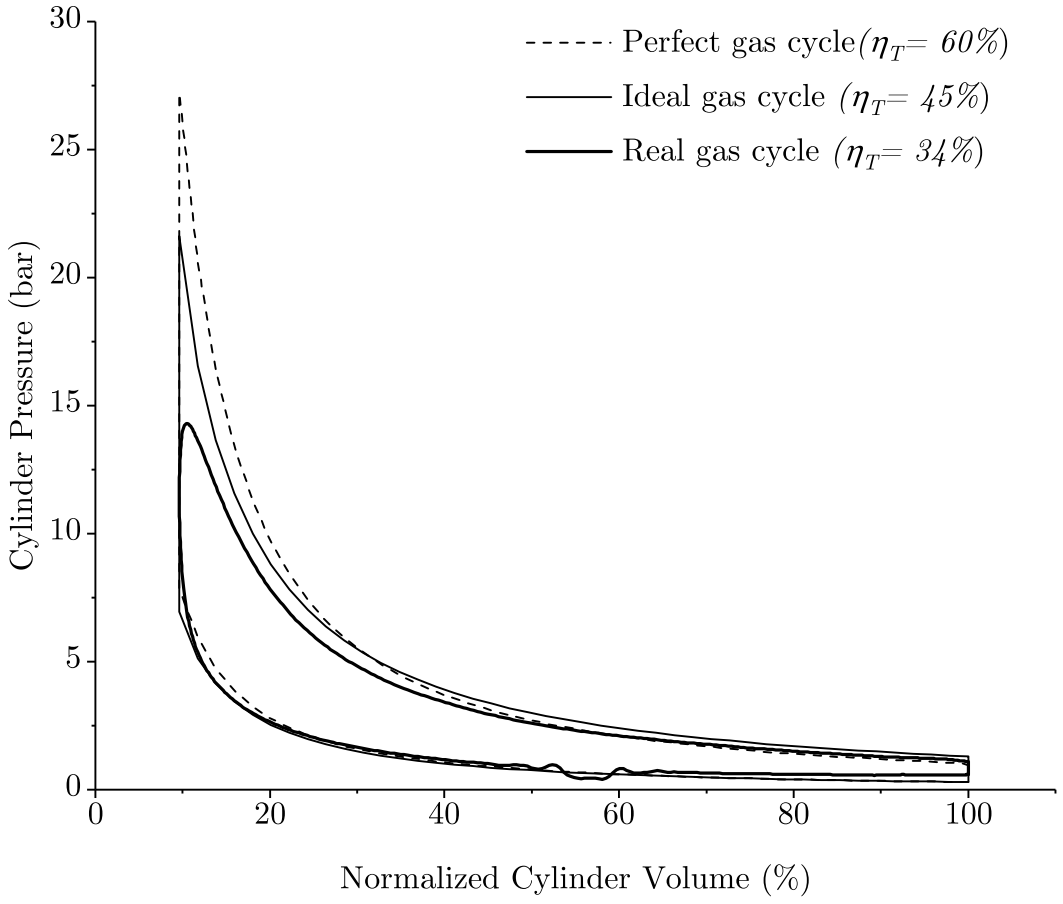

Figure 2.8: P-v diagram comparison of a perfect gas, ideal gas, and a real air Otto cycle fired with natural gas. For reference: r_c=10.4:1; A/F=17.1; and Q_{LHV,CH_4}=50 MJ/kg.

the thermodynamic losses

$$\text{QLMEP} = \frac{Q - W_T}{V_d} \tag{2.50}$$

With all these considered, the thermodynamic efficiency can be written in the form

$$\eta_T = \frac{\text{QMEP} - \text{QLMEP}}{\text{QMEP}} = \frac{\text{IMEP}_G}{\text{QMEP}} \tag{2.51}$$

where QMEP is the energy available after combustion.

Gas exchange efficiency

While the ideal thermodynamic cycle consist of four processes, a real four stroke (4S) engine cycle follows six. The intake and exhaust strokes carry out the breathing of the engine, while the compression and power stroke realize the Otto cycle. The two

extra strokes consume piston work which otherwise could have reached the crankshaft as occurs in a two stroke engine. Therefore, a difference is made between the total work exerted by the piston (IMEP_G), and the work available to spin the crankshaft, the net indicated work IMEP_N.

$$\text{IMEP}_N = \text{IMEP}_G - \text{PMEP} \tag{2.52}$$

where PMEP represents the work consumed by the piston to pump fluid in and out of the cylinder.

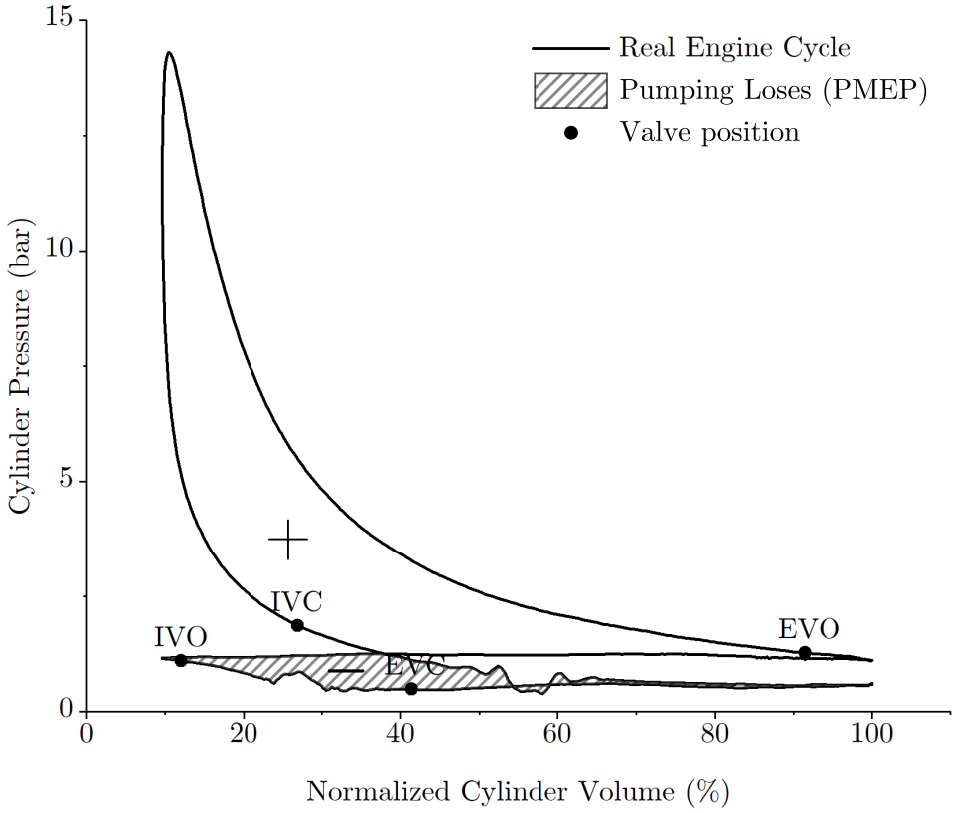

Figure 2.9: Real engine operating at 40 kPa intake manifold pressure; +40 CAD cam phasing advance. The shaded area represents the energy losses due to the breathing process in the engine.

The meaning of PMEP can be better understood with the aid of figure 2.9. The shadowed area represents the pumping work consumed by the piston and the white area is the real work delivered by the piston. Following equation 2.52 the subtraction of the shaded area from the non-shaded area results in the net work delivered by the cylinder. This difference between gross and net work is accounted in the gas exchange efficiency which indicates how efficiently the breathing is carried out.

$$\eta_{GE} = \frac{\text{IMEP}_N}{\text{IMEP}_G} \tag{2.53}$$

The overall pumping loss on the cylinder (PMEP) is the combination of the intrinsic pumping work needed ($\text{PMEP}_{\text{pump}}$) and the pressure drop created across the valves ($PMEP_{valves}$)

$$\text{PMEP} = \text{PMEP}_{pump} + \text{PMEP}_{valves} \tag{2.54}$$

The first term represents the energy consumed by the piston to bring a certain amount of fluid, from an initial state at p_{inlet} to a final state at p_{outlet}. Figure 2.10 illustrates the concept. The intake pressure (p_{inlet}) is the pressure at the start of the compression stroke (-180^oCAD); the exhaust pressure is the pressure at which the fluid fronts the exhaust stroke (180^oCAD). The pumping work is the rectangular area enclosed by both these asymptotes, from exhaust to intake BDC stroke (V_d)

$$W_{pump} = \int_{180}^{-180} p\, dV = (p_{exhaust} - p_{intake})V_d \tag{2.55}$$

which in MEP form

$$\text{PMEP}_{pump} = p_{out} - p_{in} \tag{2.56}$$

The second term in equation 2.54 identifies the extra energy needed to overcome the pressure drop that inlet and outlet valves cause across them. This pressure drop is substantially higher at high loads when the mass flow is high, and barely noticeable at low loads. Because the cross sectional area of the valves is constant, velocity increases linearly with load thus causing the pressure drop across the valves to increase. Valve pressure losses are minimal in figure 2.10 because of the combination of optimum cam timing and low load (40 kPa manifold pressure). The overall pumping loss in the cylinder *PMEP* is easy to obtain by integrating the cylinder pressure trace over the intake and exhaust stroke (shadowed area in figure 2.9). The valves losses are then obtained by

$$\text{PMEP}_{valves} = \text{PMEP} - \text{PMEP}_{pump} \tag{2.57}$$

The gas exchange or breathing efficiency can then be written

$$\eta_{GE} = \frac{\text{IMEP}_G - \text{PMEP}}{\text{IMEP}_G} \tag{2.58}$$

It is worth noting how as the intake port and valves size is increased and the engine speed decreased, the pressure drop across the valve and port bodies is reduced. This brings a great advantage to large scale RICE which are less susceptible to this parasitic loss.

Mechanical efficiency

In the analysis performed so far, the power generated by the piston is not yet reaching the crankshaft. While the piston is being actuated, shear forces appear between the piston and the cylinder. This shear stress consumes part of the power the piston is producing and therefore the overall efficiency is further reduced. Besides the friction

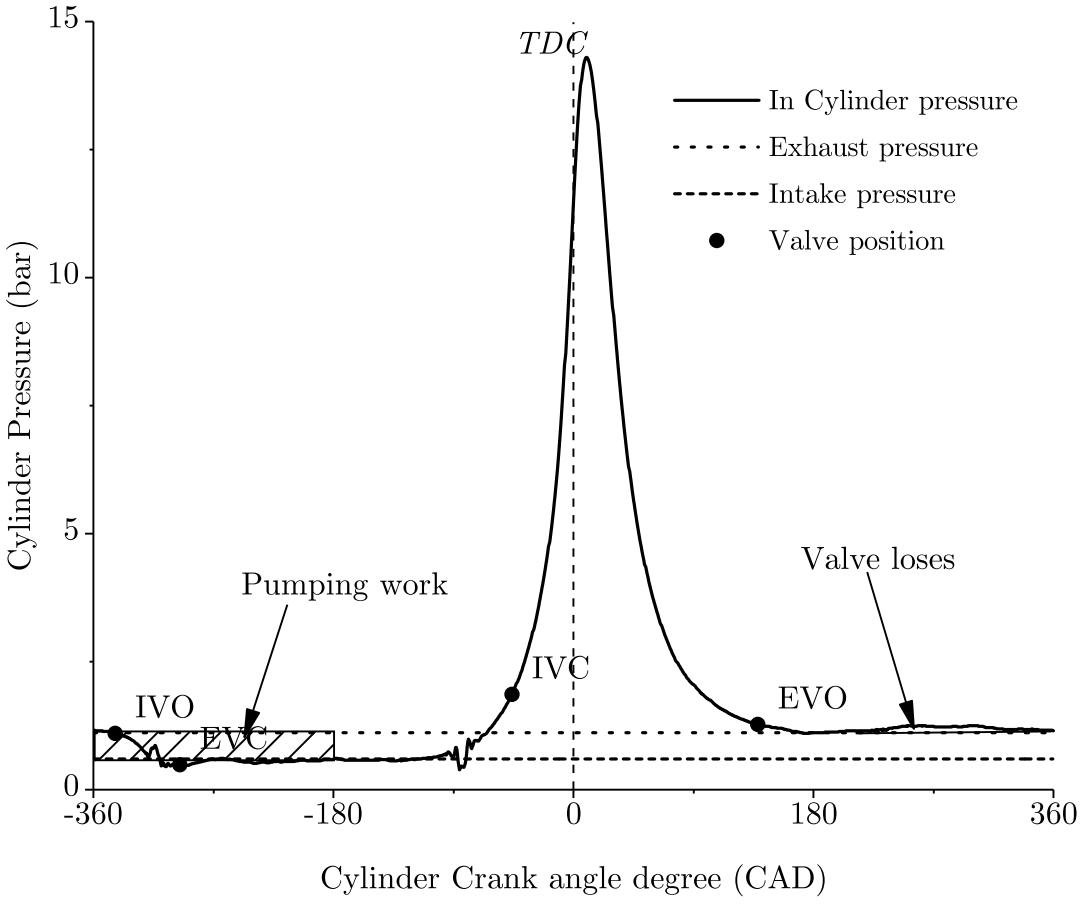

Figure 2.10: Concept of PMEP values in internal combustion engines.

caused by the piston-cylinder group, other components also sum to the mechanical work being consumed, i.e. the valve train, consisting of sliding connection rods, camshaft and rockers consume power from the engine to actuate, generating friction forces as well. All this power consumed by the aforementioned activities is included in the term

$$\text{FMEP} = \frac{W_{rf} + W_{aux}}{V_d} \tag{2.59}$$

where W_{rf} refers to rubbing friction work and W_{aux}, to the work consumed by the auxiliary systems. Although FMEP takes into consideration auxiliary components, friction losses refers to the energy lost owing to shear stresses over the bearing components. Figure 2.11 illustrates the main influencing factor on the generation of friction. The coefficient of friction is plotted against the Sommerfeld number

$$S = \frac{\mu v_p}{p} \tag{2.60}$$

which relates μ the absolute viscosity of the lubricant fluid, the velocity of the moving

piston v_p, and p the pressure over the bearing area.

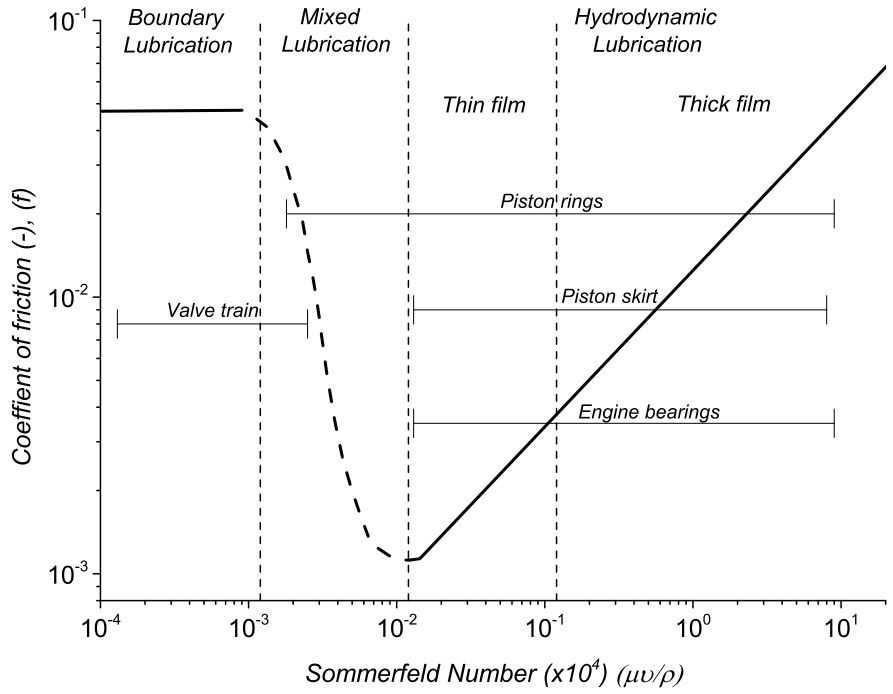

Figure 2.11: Striebeck diagram. Coefficient of friction is plotted against the Sommerfeld number. The overall coefficient of friction results from the sum of hydrodynamic friction and solid friction, projecting different regimes of influence at different engine speeds. Boundary regime: mainly solid friction. Mixed regime: progressive reduction and increment of solid and hydrodynamic friction respectively. Hydrodynamic regime: mainly hydrodynamic friction. Figure is adapted from [95].

Friction work should be computed as

$$W_{rf} = \int F_{rf} dx; \quad F_{rf} = f(\mu, v, p) \cdot N \tag{2.61}$$

where f is the coefficient of friction and N the normal forces to the bearing surface. Because W_{rf} is not easy to measure with experimental devices, the following strategy is followed

$$\text{FMEP} = \text{IMEP}_N - \text{BMEP} \tag{2.62}$$

where BMEP, as mentioned in section 2.3.3, refers to the work delivered to the client end of the crankshaft (measured with a dynamometer) and IMEP_N refers to the net indicated work. The mechanical efficiency indicates how well manufactured an engine

is, in terms of surface machining. It is defined

$$\eta_M = \frac{\text{BMEP}}{\text{IMEP}_N} = \frac{\text{IMEP}_N - \text{FMEP}}{\text{IMEP}_N} \tag{2.63}$$

Friction losses are normally accentuated with engine load as shown in figure 2.11; i.e an engine at high load will lose more power within the piston-cylinder system than at low load. Similarly, a boosted engine (an engine fed with compressed air) will lose more power through friction than an atmospheric aspirated one because the pressure over the bearing surfaces increases. Along the the same lines, higher engine speed (ω) causes an increase in friction losses because of higher linear velocity (v_p). In general, large engines with a a lower perimeter to bore area ratio and operating at lower speed are less susceptible to such parasitic losses.

Engine Brake Efficiency

As a result of all the phenomena introduced in the previous sections, the end work produced by the engine (*BMEP*) is considerably less than the theoretical potential. Introduced in section 2.3.3, the overall engine efficiency

$$\eta_B = \frac{\text{BMEP}}{\text{FuelMEP}} \tag{2.64}$$

can be computed by combining each of the term shown in figure 2.12.

Common RICE brake efficiency are shown in figure 2.13. It can be seen how large bore low speed engines [4] achieve their theoretical efficiency. As the engine scale is reduced and the speed is increased to maintain power density, efficiency quickly decays.

It is straight forward to conclude that for the brake efficiency to improve, each of the inefficiencies of the engine must be reduced. This is achieved through different technological solutions such as:

(a) Improving the combustion process through reducing reaction quenching, combustion incompleteness, dissociation of products, and increasing combustion speed.

(b) Reduction of heat transfer through the walls, and increasing the effective compression ratio.

(c) Reduction of pumping work through a better breathing process. Avoid engine's part load regimes. Reduce flow losses across breathing valves.

(d) Better machining of the engine block, reduce bearing surface, improve lubricants properties.

however, as seen in figure 2.13, at large scales the parasitic losses become negligible and thus none of the measures above has the potential to make an impact. The only remaining alternative is to extend the achievable thermodynamic efficiency (η_{th}) the system can pursue.

[4] Common r_c for these engines falls withing the range of 10-14 and engine speeds below 600 rpm.

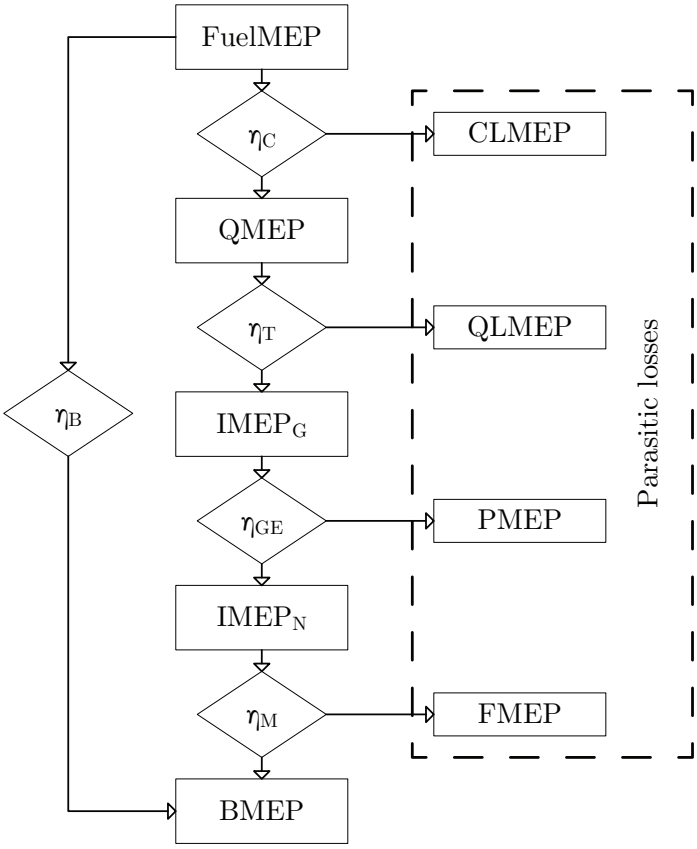

Figure 2.12: Summary of the different energy flows, losses and efficiency terms. Figure adapted from [97].

2.4 Argon as the working fluid.

The use of monatomic gases, primarily argon, as the system's working fluid affords a quantum jump in the theoretical maximum efficiency achievable by RICE as indicated in section 2.3.3. However, the benefits of using a monatomic gas is not limited to the aforementioned. This strategy also allows for cleaner combustion, most importantly, clean combustion of H_2 primarily. Due to their singular electron configuration, with a closed shell of electrons, monatomic gases are incredibly nonreactive. Only krypton (Kr), xenon (Xe) and radon (Rn), the heavier of all the monatomic gases, has been succesfully reacted, although with extremely reactive element such as fluorine (F), Chlorine (Cl) and oxygen (O). Attempts to react helium (He), neon (Ne) and argon (Ar) has not been successful [102]. Therefore, this set of gases are considered, under common industrial processes conditions, inert gases or noble gases in allusion to its passive nonreactive nature.

A common concern that arises when burning H_2 is the greater generation of nitrogen oxides (NO_x[5]) compared to other fuels. In conventional power conversion systems, the most common working fluid used is air, given it already contains the oxidizer and,

[5] NO_x mainly representing NO and NO_2.

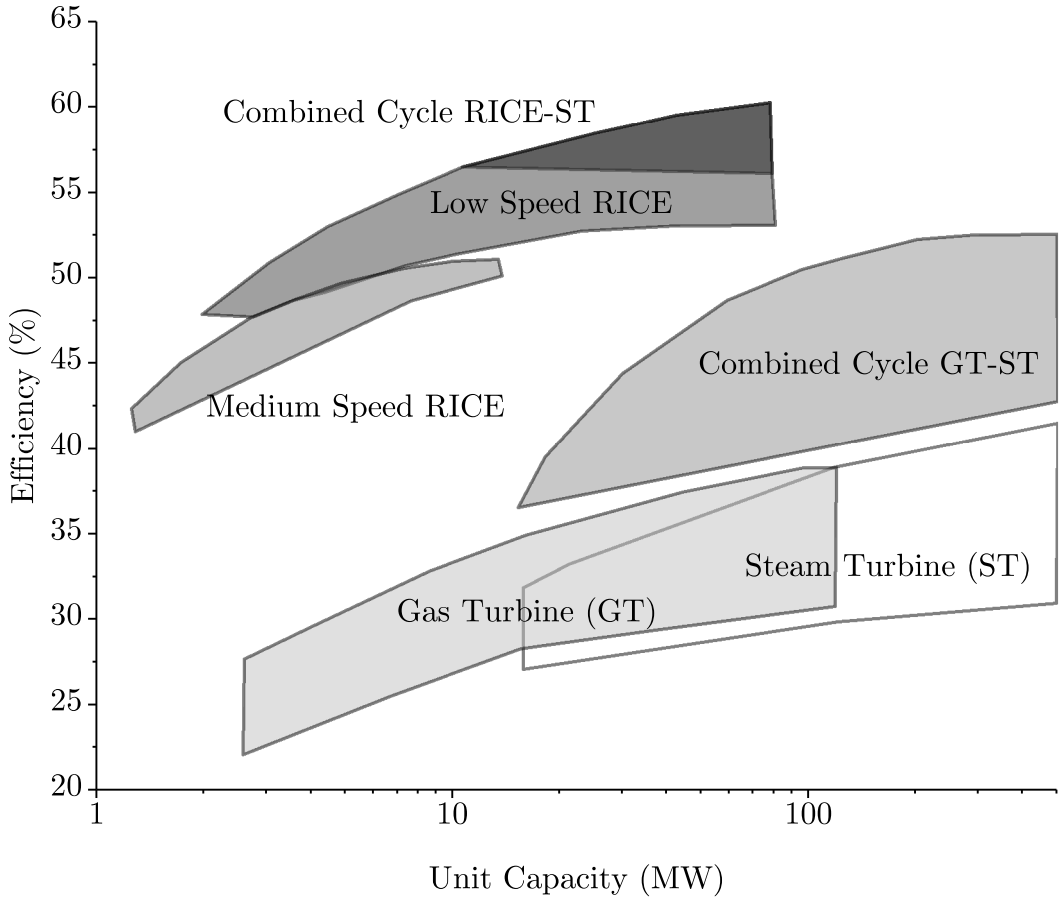

Figure 2.13: Power efficiency comparison between conventional power generation technologies under ISO standard 3046 [101].

most importantly, it is abundant and free. However, air is not an optimum working fluid. Since air consists primarily of N_2 and O_2 (table 2.2) combustion of fuel-air mixtures results in a large generation of harmful NO_x. This is the result of combining nitrogen (N_2) and O_2 at relatively high temperatures ($> 1700K$) resulting from the fast oxidation of H_2. In using a truly inert gas, the concern regarding criteria pollutant introduced in chapter 1 vanishes.

The reasoning behind the choice of Ar among the group of noble gases is its wider availability, and consequently, its affordability. Worldwide, Ar is produced in bulk as a byproduct from air separation plants and a minor fraction originating from ammonia plant tail gas separation units [102]. From an engineering perspective, heavier gases such as Kr, Xe or Rn would serve a better purpose as working fluids due to their lower thermal conductivity (κ). The reason being, as the temperature in the cycle increase with the use of monatomic gases, heat transfer away from the system increases. The use of the heavier gases helps counteract the increase heat losses (QLMEP) resulting from higher temperatures. Argon, although not the heaviest of the noble gases, has yet better heat insulation characteristics than that of N_2.

Table 2.2: Gaseous composition of dry air [102–104].

Constituent	Symbol	Mole fraction (%)
Nitrogen	N_2	78.084
Oxygen	O_2	20.947
Argon	Ar	0.934
Carbon dioxide	CO_2	0.037
Neon	Ne	0.001818
Helium	He	0.000524
Methane	CH_4	0.00017
Krypton	Kr	0.000114
Hydrogen	H_2	0.000053
Nitrous oxide	N_2O	0.000031
Xenon	Xe	0.0000087
Ozone	O_3	< 0.0008
Carbon monoxide	CO	< 0.000025
Sulfur dioxide	SO_2	< 0.00001
Nitrogen dioxide	NO_2	< 0.000002
Ammonia	NH_3	< 0.00000003
Radon	Rn	$(0.06 - 18) \times 10^{-23}$

Table 2.3: Properties of gaseous Ar, N_2 and CO_2 at standard conditions.

	Symbol	Units	Ar	N_2	CO_2
Density	ρ	kg/m^3	1.6617	1.17	1.808
Dynamic viscosity	μ	kg/m s	2.23×10^{-5}	1.76×10^{-5}	1.46×10^{-5}
Specific heat	c_p	J/kg K	522	1.041	845
Thermal conductivity	κ	W/m K	0.0174	0.02547	0.01622
Prandtl number	P_r	-	0.669	0.7174	0.7615
Thermal diffusivity	α	m^2/s	2.01×10^{-5}	2.1×10^{-5}	1.06×10^{-5}

The use of a monatomic gas is strongly motivated by the thermodynamic theory, which indicates the potential for a quantum jump on energy conversion efficiency. The choice of Ar, although mandated by the availability of the gas, is also reasonable optimized in relation to the current working fluid of choice, N_2.

2.5 Closed loop recirculation

The need to source and concentrate the Ar from the atmosphere demands this new cycle to conserve its now valuable working fluid. Unlike conventional power system which operates in an open cycle framework, the exhaust of the APC has to be fully recuperated with the exception of the combustion products, further demanding the use of effective condensation and separation measures.

On the other hand, the close loop configuration permits raising the cycle lowest pressure to any desired state up to the mechanical limitation of the equipment involved [6]. By increasing the cycle pressure, the power density of the plant is increased at no substantial energetic penalty.

The cycle high operating pressure may also aid in the extraction of CO_2 via the condenser and membrane separation system. In the case of the condenser, at sufficiently low temperatures and high pressure, substantial CO_2 can dissolve in the condensed water. This phenomena can be enhanced by increasing the CO_2 concentration in the exhaust stream by recirculation. The positive partial pressure dependence of the Henry's law indicates that as CO_2 accumulates in the working fluid stream, the rate at which it dissolves in the water increases. Posterior depressurization of the water to atmospheric conditions ensures the dissolved CO_2 is released. It is worth noting that Ar, like CO_2 will also dissolve in water but at a lower rate given its lower Henry's constant. This is a concern to account for in order to prevent Ar from escaping the gas stream.

In the case of the membrane system, the main driver for the permeation of the gas in question is directly proportional to the partial pressure difference between both sides of the membrane. The high pressure and artificially increased CO_2 concentration of the exhaust stream increases the driving force for effective permeation, reducing the energetic penalty imposed on the power system.

Finally, the use of a condenser to fulfill the close loop configuration helps reduce the water consumption of the plant, an increasing concern with the integration of distributed scale power systems. Water resulting from combustion, either from H_2 or alternative hydrocarbon based fuels (C_xH_y), is collected and recirculated back to the electrolizer, or in the case of C_xH_y, reused for cooling or any other purpose. This feature makes power systems with this configuration extremely valuable for applications in remote regions where access to cooling water is not guaranteed.

2.6 Why RICE?

An attentive reader may wonder by now, given figure 2.3 and the conclusions drawn above, why would not be more beneficial to integrate the APC in a gas turbine (GT).

Most large size gas fired plants today consist primarily of a GTs in combination with a steam turbines (ST). The benefits obtained in the conversion process resulting from the use of monatomic gases is, in the case of a gas turbine, not justified. Current gas turbine efficiency benchmark is dictated by the material capabilities rather than by the thermodynamic process itself. Current axial compressor are close to isentropic, with thermal efficiency close to 92% [105]. The substitution of its working fluid by a monatomic gas will no longer increase the system efficiency but decrease its power density. This can be seen by paying attention to the thermal efficiency equation,

[6] Common RICE engine allowable boost pressure falls between 4-5 bar.

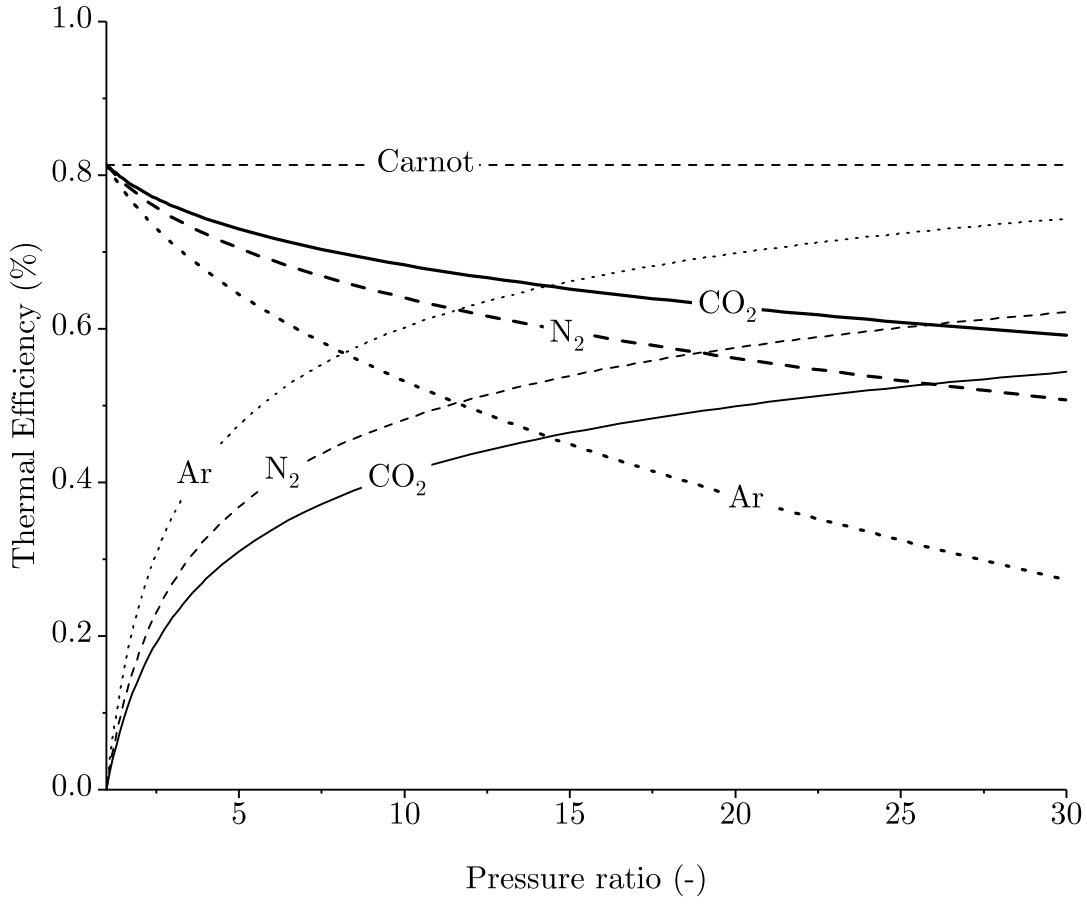

Figure 2.14: Theoretical gas turbine cycle efficiency (Brayton) with (bold lines) and without heat recuperation (thin lines). Computed assuming perfect gas with $c_p = c_p(298K)$.

assumed ideal gas

$$\eta_{th} = 1 - \frac{1}{r_p^{\frac{-R_u}{c_p}}} \tag{2.65}$$

Similarly to RICE, with increasing c_p, the efficiency increases. The energy introduced into the system must be proportionally reduced to ensure the maximum temperature is not surpassed. Alternatively, a reduction of the pressure ratio of the turbine would achieve a similar result. In general, given the material limitations, the maximum efficiency can be achieved either by means of using a monatomic gas or by increasing the pressure ratio as can be seen in figure 2.14. As mentioned in section 2.4, with air being free and available it makes no economic sense to consider a working fluid replacement in this case.

It is worth noting however, if the Brayton cycle is fitted with a heat recuperation stage, the thermodynamic theory indicates that the optimum working fluid, as op-

posed to what it was indicated previously, is a gas with the highest molar specific heat capacity at constant pressure (c_p). Effective recuperation of the energy remaining in the exhaust stream allows the system to maintain relatively high system temperatures and remain closer to the Carnot efficiency limit while extending the amount of fuel energy that can be introduced into the system. The addition of the heat recuperation stage to the original Brayton cycle efficiency equation yields the following expression for the gas turbine cycle efficiency

$$\eta_{th} = 1 - \left(\frac{T_1}{T_3}\right) r_p^{\frac{-R_u}{c_p}} \tag{2.66}$$

where T_1 and T_3 are the minimum and maximum temperatures occurring prior to the compressor and after the combustor respectively. This expression indicates that gases such as CO_2 are a better choice than either N_2 or any monatomic gas. Confirmation of this concept is the ongoing research and development efforts by renowned engineering companies such as General Electric (GE) and Exelon who are investigating the closed loop Bryton cycle operating with supercritical CO_2. This technology main allure is the ease to capture carbon given the high purity and concentration of it in its gas stream.

The use of RICE is justified beyond the limitation of GTs. The circumstances the energy market is today the RICE offers the greatest ramping capabilities to the grid at the lowest cost, with the ability to provide black start[7] and a nearly flat efficiency-load curve.

2.7 Summary

From all concepts introduced in this chapter, four major ones should be kept in mind:

1. Current large stationary RICEs approach their theoretical performance. The only means of substantial improvement is to push the thermodynamic boundaries.

2. Replacing the working fluid by a monatomic gas translates into a quantum jump in thermodynamic efficiency for RICE. Moreover, the choice of heavy gases with low thermal conductivity reduces the heat losses thermal power plants are accustomed to. The use of a true non-reacting inert gases prevents the formation of thermal nitrogen oxides resulting from extremely high combustion flame temperatures. By avoiding the use of nitrogen, the system is inherently emissions free.

3. The close loop nature of the cycle serves primarily as a means to conserve the valuable argon gas. However, the closed loop configuration further allows the rise of the cycle lowest thermodynamic state (ambient conditions) to any

[7]Black start refers start up procedures where the power system is fully independent from the grid and able to start without auxiliary power.

desired state up to the mechanical limitation of the equipment involved. By increasing the cycle pressure, the power density of the cycle can be increased at no substantial energetic penalty. The cycle high operating pressure also aids in the extraction of CO_2, both in the condenser as well as in the membrane system, by enhancing the driving force for the gas separation processes.

4. Closed loop cycles in general are preferable to open loop cycles given their minimal water consumption. The ability to collect and use the water resulting from combustion for cooling or any other purpose makes these systems extremely valuable for applications in remote regions where access to cooling water is not guaranteed.

Chapter 3

Numerical Investigation

In this chapter a brief introduction to the numerical models used in this work is given. Although this work is focused on the understanding of the RICE performance under the APC conditions, estimating the added energetic cost of air and exhaust gas separation is briefly investigated to measure the usefulness of this cycle. Furthermore, a numerical model of the RICE was built in order to coarsely predict the experimental results I would later obtain. Three different numerical models were used: (1) A zero dimensional (0D) RICE combustion model (2) 0D cryogenic air separation process and a (3) one dimensional (1D) membrane gas separation model.

3.1 Internal Combustion Engine modeling

The physical processes occurring in an internal combustion engine are complex and numerous. Complete RICE engine models incorporate all physical phenomena spanning from the friction forces on the piston-cylinder interface, all the way to the turbulence mixing of gaseous jets or sprays. The level of detail demanded guides the choice of a modeling strategy, whether using a 0D model for thermodynamic and combustion analysis or a highly detailed three dimensional (3D) models able to resolve the turbulence mixing. For the purpose and scope of this work, primarily focused on the evaluation of the effect of argon on the engine thermodynamic process, a 0D model was deemed sufficient.

In this model, the gas contained within the control volume, delimited by the piston and cylinder walls, is assumed to be homogeneously mixed at any point in time (single zone model). The thermodynamic properties such as temperature, chemical composition, and pressure are assumed constant across space. A modification of this model is made for specific engine operation conditions such as spark ignition (SI). In this case, the control volume is split into two zones, both obeying to the aforementioned assumptions (two zone model). Figure 3.1 shows the two variants of the model, with the single zone and two zone models depicted in the left and right of the figure respectively. Notice that all the phenomena considered in the single zone model are also analyzed in the two zone model despite not being shown in the figure.

In the specific case of the two zone model, the volume of each zone is determined

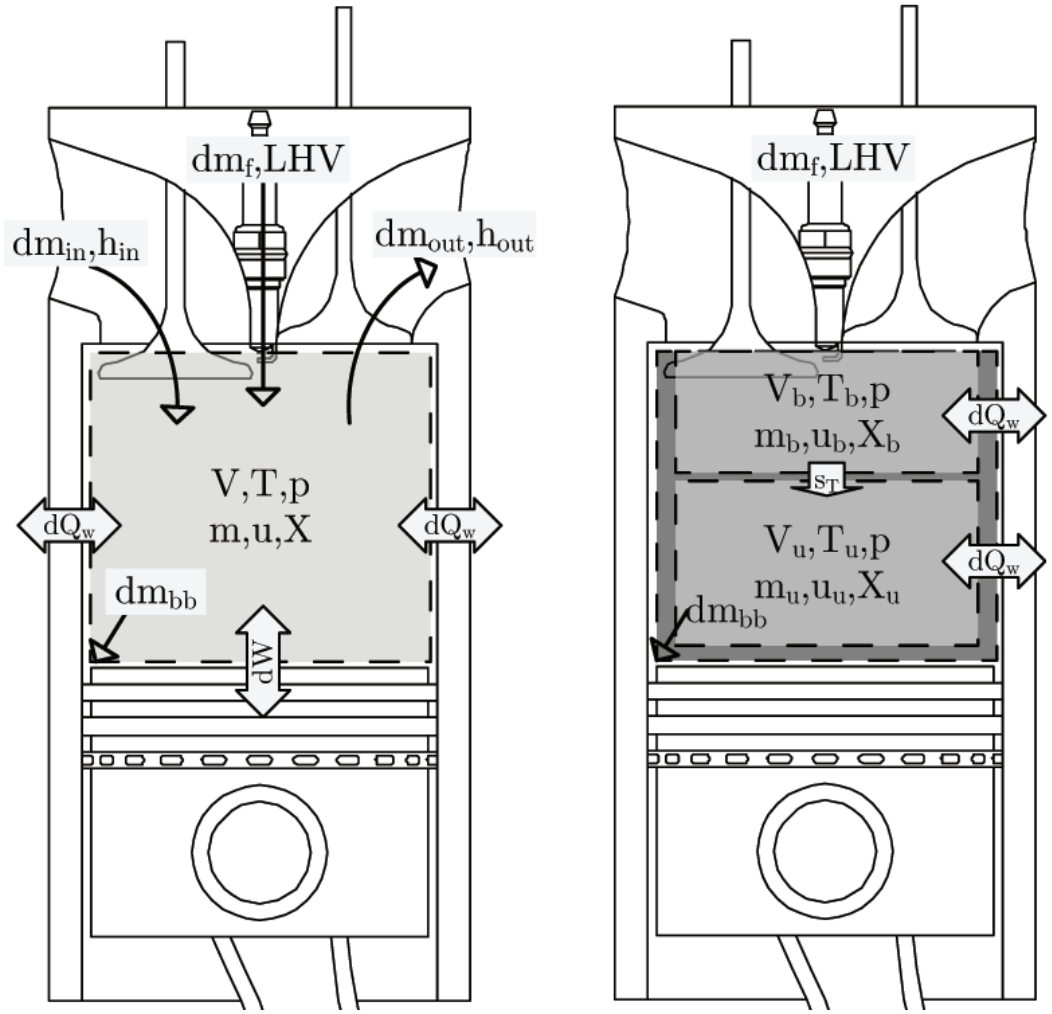

Figure 3.1: Left: 0D single zone engine cylinder model. Right: 0D 2 zone engine cylinder model. The subscripts in and out represent inlet and outlet respectively. The subscript bb and w stands for blowby and wall respectively.

by its thermodynamic state, with the sum of both volumes totaling the entire volume of the chamber. One of the zones is meant to represent a mixture of fresh components, primarily fuel and oxidizer (subscript "u") and the second zone represents the burnt zone (subscript "b"), where the products of combustion accumulate. The use of two zones allows to characterize the heat release from combustion with a higher level of accuracy by incorporating a pseudo flame front that travels from the burnt zone to the unburnt zone at a speed determined by the kinetics of the fuel oxidation reaction.

In general, the governing equations for the 0D model reduce to the conservation of mass and energy within the control volume.

3.1.1 Mass conservation

The mass conservation equation for the engine cylinder system depicted in figure 3.1 can be written as

$$\frac{dm_{cyl}}{d\theta} = \frac{dm_{in}}{d\theta} + \frac{dm_{out}}{d\theta} + \frac{dm_{bb}}{d\theta} + \frac{dm_f}{d\theta} \tag{3.1}$$

with m_{cyl} the total mass in the cylinder, m_{in} and m_{out} the mass coming in and out through the inlet and exhaust valves, m_f the mass of fuel injected into the cylinder, and m_{bb} the mass that flows through the piston-cylinder wall interface due to the imperfection of the surface to surface seal [94–96]. This specific phenomena is called blowby and will be refereed as such in the remaining of this work. Equation 3.1 can be further simplified if the model is restricted to the period of time during which both inlet and exhaust valve are closed (IVC:EVO). In this case the conservation of mass reduces to

$$\frac{dm_{cyl}}{d\theta} = \frac{dm_{bb}}{d\theta} + \frac{dm_f}{d\theta} \tag{3.2}$$

The initial mass in the cylinder is determined by the thermodynamic state of the gas given by a prescribed inlet temperature and pressure and the volume determined by the position of the piston at the θ of inlet valve closure (IVC) as indicated in section 2.3.1.

$$m_{cyl,0} = \frac{V_{IVC} p_{IVC}}{R T_{IVC}} \tag{3.3}$$

with R the gas constant for the gas mixture in question. The mass fuel flow rate and duration of the injection into the cylinder is prescribed by the user. Therefore, by modeling the rate of leakage of gas through the piston-cylinder interface and with the initial cylinder mass, the evolution of the mass in the system as a function of θ can be inferred. Several models can be used to model the rate of leakage [106–108]. All models exploit the relation of the mass flow through an orifice with $p^{1/2}$. According to Ebner and Jaschek [109] the total amount of mass leaving the system totals between 0.5% to 1.5% of the initial cylinder mass. In this simulation the model by Grzegorz Koszaka and Mirosaw Guzik is used [106]. This model demands the knowledge of the orifice size between the piston rings (seals) and assumes sonic flow of the gas mixture across it.

$$\frac{dm_{cyl}}{dt} = \psi A_c \sqrt{\gamma P_0 \rho_0} \left(\frac{2}{\gamma + 1} \right)^{\frac{\gamma+1}{2(\gamma-1)}} \tag{3.4}$$

where the thermodynamic properties (γ, P_0, ρ_0) are taken from the gas in the cylinder, A_c, the crossectional area of the orifice, and ψ a discharge coefficient obtained from experiments.

In the case of the two zone model, an extra constraint is added and reads

$$\frac{dm_{cyl}}{d\theta} = \frac{dm_{bb}}{d\theta} + \frac{dm_f}{d\theta} + \frac{dm_b}{d\theta} + \frac{dm_u}{d\theta} \tag{3.5}$$

where the m_b, the mass within the burnt zone increases as the fuel oxidizer mixture in the unburnt zone burns at a rate determined by the kinetics of the reaction. In the case of direct injection simulations, the mass flow from the unburnt zone to the burn zone is assumed to be equal to the sum of injected fuel and stoichiometric unburnt mixture. In other words, perfect and stoichiometric mixing is assumed as the fuel enters the combustion chamber. This is a highly idealized representation of the actual process occurring within the cylinder but it allows a better approximation than a single zone model nonetheless.

In the case of a premixed fuel oxidizer mixture with no fuel injection, but with the assistance of a spark event, the rate at which mass enters the burnt zone is defined by the turbulent flame speed (S_T) and an assumed flame front area (e.g. the piston area). This is dependent upon the mixture composition and the thermodynamic state of the unburnt zone. A flame speed lookup table is built for the model to use. This lookup table contains laminar flame speeds for a wide range of mixtures and thermodynamic conditions foreseen to occur during the simulation. The model accesses this lookup table to pull and interpolate a laminar flame speed value which is translated to a turbulent flame speed (s_T) by means of an estimated turbulent factor as described by Heywood [94].

3.1.2 Energy conservation

In order to evaluate the efficiency and work generated by the thermodynamic cycle, the conservation of energy equation for closed system is used

$$\Delta U = Q - W \tag{3.6}$$

where U is the total internal energy of the gas contained in the cylinder and Q and W are the heat and work crossing the boundaries of the system as shown in figure 3.1. This expression can be rewritten for our specific case as

$$\frac{dU_{cyl}}{d\theta} = \frac{dQ_{heat}}{d\theta} + \frac{dQ_w}{d\theta} - p\frac{dV}{d\theta} + h_{in}\frac{dm_{in}}{d\theta} + h_{out}\frac{dm_{out}}{d\theta} + h_{bb}\frac{dm_{bb}}{d\theta} + h_f\frac{dm_f}{d\theta} \tag{3.7}$$

where Q_{heat} stands for the heat released by the oxidation reaction, Q_w represent the heat crossing the cylinder walls, and pdV is the boundary work exerted over the piston. The terms h_{in} and h_{out} refer to the specific enthalpy of the mass flow entering and leaving the system through the intake and exhaust valves. Finally, the terms h_{bb} and h_f represent the specific enthalpy leaving and entering the system with the blowby mass flow and fuel mass flow respectively.

Similarly, as in the case of the mass conservation equation (3.1), this equation can be simplified if the model is restricted to the period of time during which inlet and exhaust valve are closed (IVC:EVO). In this case equation 3.7 reduces to

$$\frac{dU_{cyl}}{d\theta} = \frac{dQ_{heat}}{d\theta} + \frac{dQ_w}{d\theta} - p\frac{dV}{d\theta} + h_{bb}\frac{dm_{bb}}{d\theta} + h_f\frac{dm_f}{d\theta} \tag{3.8}$$

where $\frac{dQ_{heat}}{d\theta}$ and $\frac{dQ_w}{d\theta}$ require the implementation of a chemical reaction model and a heat transfer model, commonly refereed to as heat release and heat loss model respectively.

Heat release model

The heat from combustion is modeled by means of a chemical reaction mechanism, specifically for methane, GRI 30 was used [110]. In this mechanism, the global oxidation reaction for methane

$$CH_4 + 2\ (O_2 + 3.76N_2) \rightarrow CO_2 + 2H_2O + 7.52N_2 \tag{3.9}$$

is represented as a series of 325 elementary reactions whose rate of reaction k in kmol/m^{3}s is described by

$$k_f(T) = AT^b \exp(-E/\hat{R}T) \tag{3.10}$$

where A is the pre-exponential term in 1/cm^3 mol s, b is the non dimensional temperature dependent exponent and E_a is the activation energy in kJ/mol. The net production rate of each species at a given thermodynamic state is given by the sum of the contributions by each of the elementary reactions. Cantera software [111] is used to evaluate the reaction rate of each elementary reaction and compute the net production rate of every species in the mechanism. The heat released at each step is then computed as

$$\frac{dQ_{heat}}{dt} = \sum_{i=1}^{N_c} \dot{w}_i MW_i u_i \tag{3.11}$$

where u_i, MW_i, and $\dot{w}_i$ are the standard-state internal energy, molecular weigh, and net production rate of species i at a given thermodynamic state. In order to compute the thermodynamic properties (i.e. u_i) of each species present in the gas, the model makes use of the tabulated NASA polynomials, a curve fit polynomial of the heat capacity, enthalpy and entropy of each of the species defined in the chemical mechanism [112, 113]. The range of validity of these polynomial fits is limited to temperatures between 300 to 3000 K. Equation 3.11 can be referenced to crank angle degrees (θ) by considering the following relation

$$d\theta = \omega dt \tag{3.12}$$

In the case of the two zone model, the spark event that triggers the oxidation reaction is model by means of a differential volume with a prescribed high temperature sufficient to trigger autoignition. At this point, the differential volume becomes the initial volume of the burnt zone.

As indicated in the mass conservation section, the mass traveling from the unburnt zone to the burnt zone is determined by means of an estimated turbulent flame speed and a flame front chosen equal to the piston area.

Heat loss model

The evaluation of the heat transfer across the wall of the cylinder can be expressed as

$$\frac{dQ_w}{dt} = A_{cyl}h(T_w - T) \tag{3.13}$$

where A_{cyl} is the cylinder area in direct contact with the gas at a given time t, h is the convective heat transfer coefficient and T_w and T are the avergae temperatures of the wall and the gas respectively. Computing the convective heat transfer coefficient within the cylinder has been commonly done by means of Woschni developed heat loss model [94, 96]. In this model, the gas within the cylinder volume is assumed to emulate an stationary, fully turbulent pipe flow which follow the semi-empirical correlation

$$Nu = CRe^{0.8}Pr^{0.4} \tag{3.14}$$

with Re the Reynolds number, Pr the Prandtl number and Nu the Nusselt number given by

$$Re = \frac{\rho w D}{\mu} \tag{3.15}$$

$$Pr = \frac{\rho \mu}{\kappa} \tag{3.16}$$

$$Nu = \frac{hD}{\kappa} \tag{3.17}$$

where κ is the thermal conductivity, and μ the dynamic viscosity. Assuming ideal gas, the mean pipe diameter D to be the piston bore B, and the characteristic flow speed w to be the mean piston speed (s_p), the resulting expression for the convective heat transfer coefficient on the inner side of the cylinder wall can be described by

$$h = CB^{-0.2}p^{0.8}s_p^{0.8}\frac{Pr^4\kappa}{(\mu RT)^{0.8}} \tag{3.18}$$

Furthermore, if one considers the potential relation of both viscosity and thermal conductivity with temperature, the expression can be further simplified to a temperature and pressure dependent function

$$h = CB^{-0.2}p^{0.8}s_p^{0.8}T^r \tag{3.19}$$

where C and r the temperature exponent are experimentally derived constants that takes the value of 127.93 and -0.53 respectively [114]. In order to account for the effect of combustion on the heat transfer coefficient a modification to the characteristic speed is made based on experimental data

$$w = C_1 s_p + C_2 \frac{V_d T_{IVC}}{p_{IVC}V_{IVC}}(p - p_{mot}) \tag{3.20}$$

with p_{mot} the pressure trace resulting from the non-firing engine cycle. Constant C_1 and C_2 are obtained from adjusting to experimental data

$$C_1 = 2.28 + 0.308sw \tag{3.21}$$

$$C_2 = 0.00324 \tag{3.22}$$

with sw the swirl ratio, a ratio of the radial to axial velocity of the gases in the cylinder. This number normally lies between $0 < sw < 3$. A swirl ratio of 0 was assumed given the geometry of the engine head and the low speed of operation. As a result, the convective heat transfer coefficient takes the form

$$h = CB^{-0.2}p^{0.8}w^{0.8}T^{-0.53} \tag{3.23}$$

Finally, with all the term in equations 3.2 and 3.8 the system of differential equations can be solved. In this work, the MATLAB ode45 solver was used for this purpose.

Figure 3.2 shows a the results of a parametric study carried out with the in house developed 0D model. This study was focused on evaluating the influence of compression ratio, fuel type, and argon content. It is easy to see how, as the Ar content in the working fluid is increased, the engine yields higher thermodynamic efficiency. It is interesting to see however that the efficiency peaks around a compression ratio of 8 for the case of 90% Ar while it monotonically increases for all other cases. This is attributable to the fact that, for all cases, the ignition timing (IGN) was kept constant at 5 crank angles of degree before TDC. As the compression ratio is increased, the temperature in the system increases which combined with early ignition generates relatively higher combustion temperatures. Ultimately, this increase in temperature results in increasing heat losses which counterbalance the benefits obtained from higher cycle temperatures. In the cases where the working fluid contains higher percentage of O_2 and thus more fuel is burnt, the balance of power generated to increasing heat losses is expected to be reached at much higher compression ratios. In any case, it is clear that this efficiency trend is caused by a lack of point by point optimization. If the ignition timing is optimized, higher temperatures can be prevented by delaying combustion further into the expansion stroke, given that higher temperature would help maintain stable flame propagation.

Another interesting result is the higher efficiency achieved with the use of CH_4 in comparison to H_2. This supports the above hypothesis, as the engine operated with hydrogen, with a higher energy density, reaches higher peak pressures and temperatures, enhancing the heat losses to the wall. Once again, the optimization of ignition timing could help reduce heat losses by delaying ignition and reducing peak temperatures.

This can be better seen in figure 3.3 where pressure traces of optimized ignition timing conditions has been plotted. In this case, the results show how for high Ar the best ignition timing is further beyond TDC, while for air is ignition is best triggered before TDC. Nevertheless, efficiency improvement after ignition timing optimization

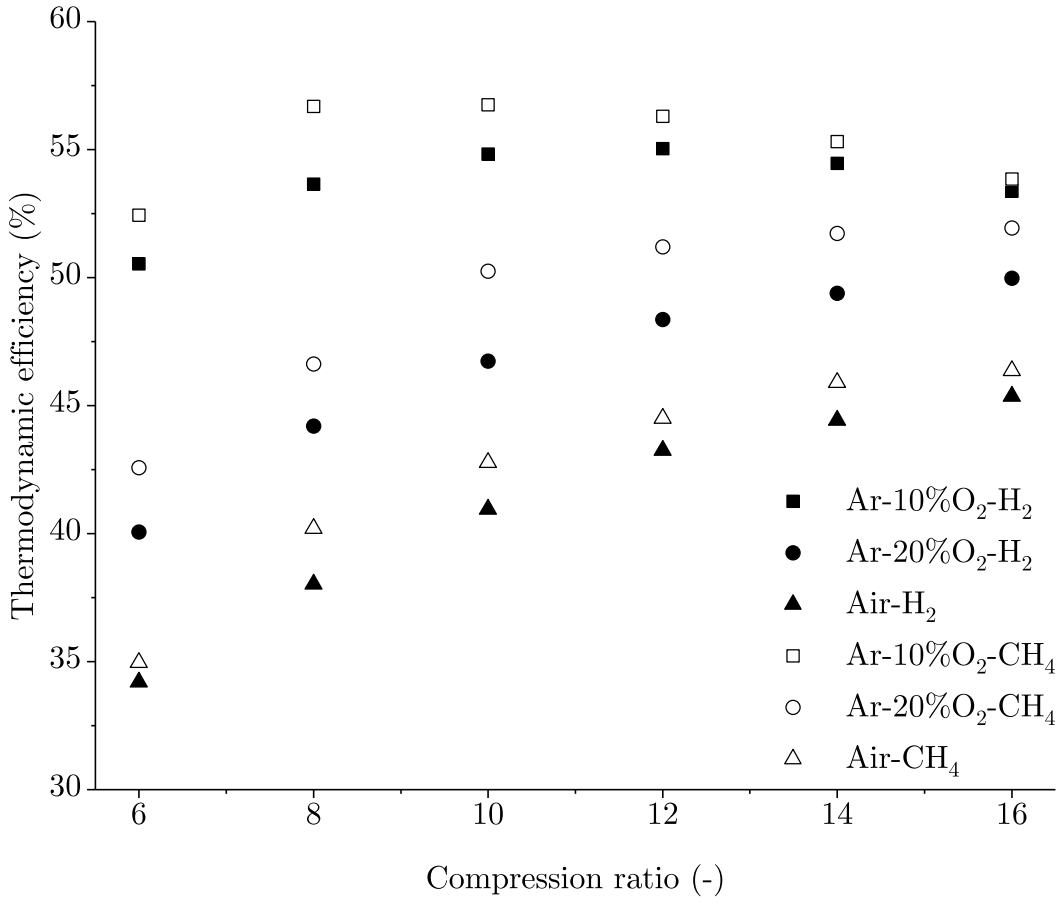

Figure 3.2: Simulated thermodynamic efficiency of the engine with different working fluids and fueled with methane and hydrogen at different compression ratios.

were not substantial and fall within 1-2%. The reason for this apparent lack of sensitivity to the ignition timing is the result of extremely high burning rates. At the point of ignition, a very small volume of gas is heated up to trigger ignition, as which point the flame propagates at the turbulent flame speed. The flame front area for these simulation was pick to be as large as the piston area. This resulted in a tremendously fast burning rates. Moreover, at very high compression ratios, the piston is very close to the top of the cylinder head, lending little travel distance for the flame to propagate, and resulting in a really fast, nearly instant, combustion of the entire fuel-oxygen mixture. As a result, the model renders near isochoric heat release where the pressure rise is instant, within few crank angle degrees.

The small set of results presented above indicate there is need to better model the flame propagation phenomena. A geometrical function which factors in the location of the piston and accounts for the initiation, growth and diminishing flame front could greatly help reduce the inherent oversimplification of the system when using a 0D model. This model is currently being extended to account for the above but it is not further presented here given the limited scope of this work.

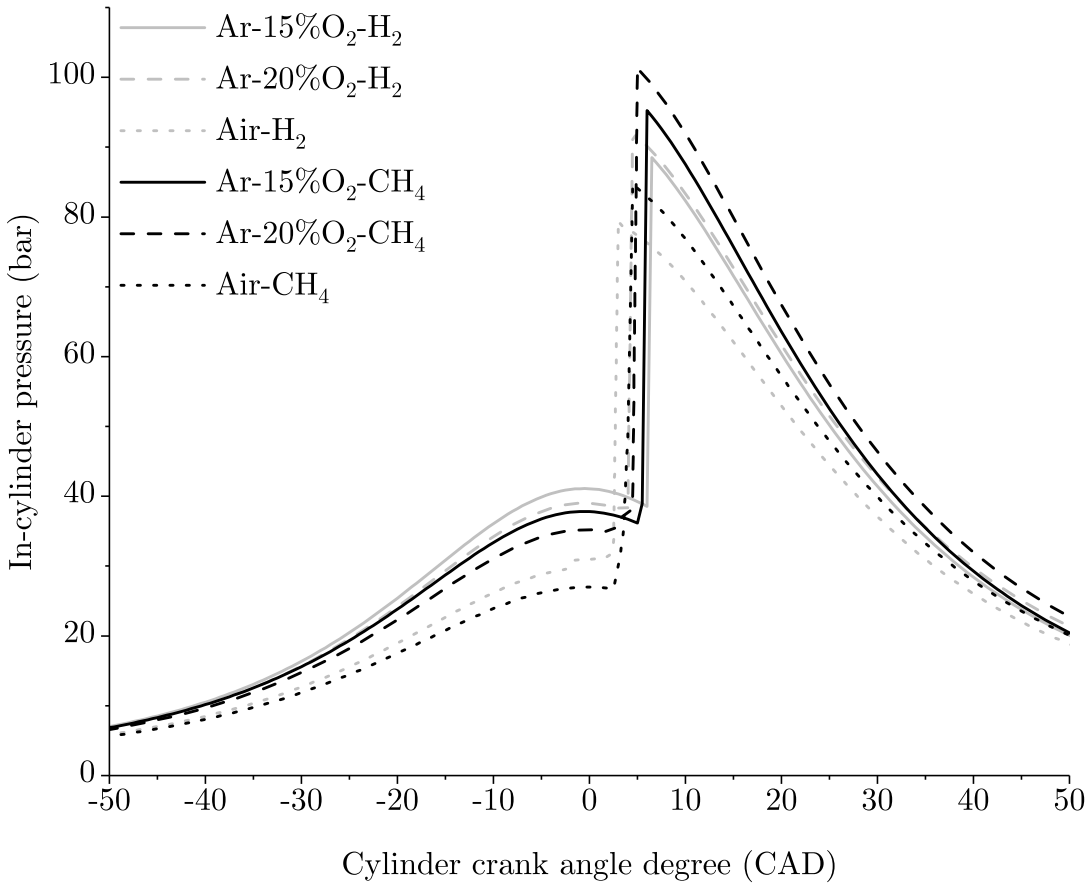

Figure 3.3: Simulated thermodynamic efficiency of the engine with different working fluids and fueled with methane and hydrogen at a compression ratio of 12 and different ignition timing.

3.2 Cryogenic Air separation modeling

As explained in chapter 2, the application of the APC for CCS requires the separation of O_2 from N_2. Although alternative separation processes are used by the industry, cryogenic separation remains the only technology with the potential to provide the purity and flow rates required for power plant scale [115–117]. Nowadays, the most common air separation unit (ASU) is shown in figure 3.4 [102]. It shows a double column design with a high and low pressure columns. This arrangement is preffered due to the higher O_2 yields [102].

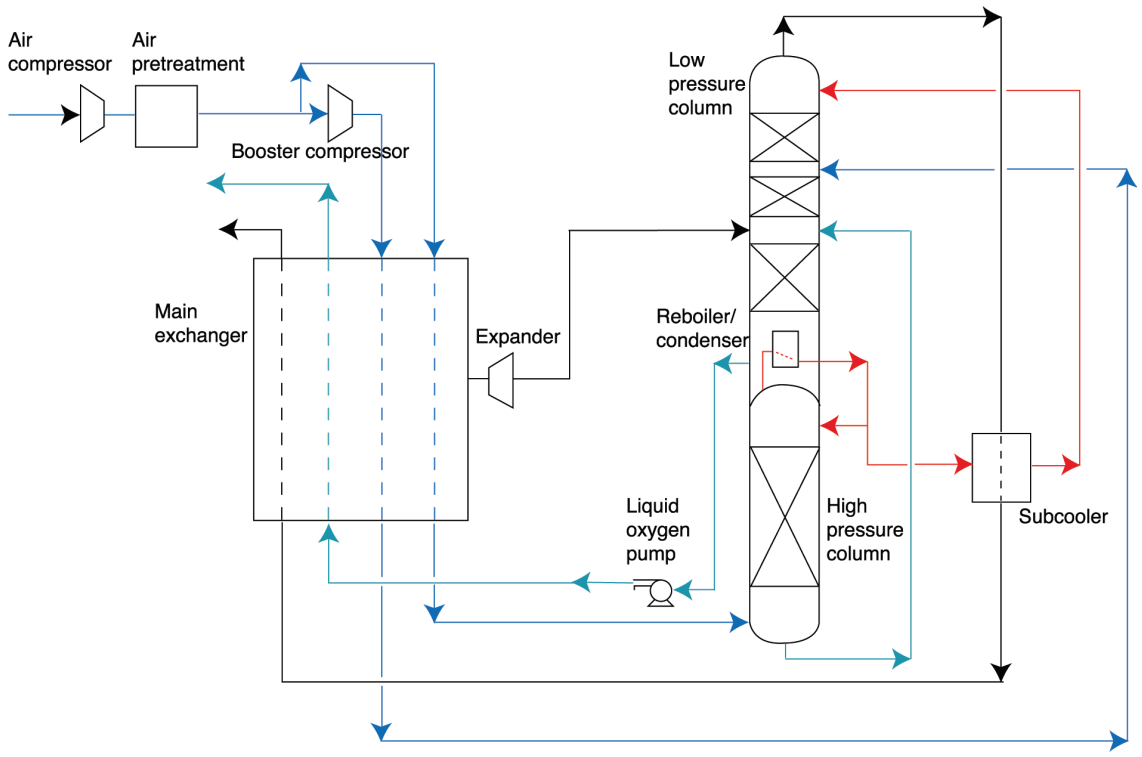

Figure 3.4: Oxygen production by distillation of liquid air [116].

In this process, air is filtered and compressed from atmospheric pressure up to 5-6 bar. At pressure, the air is treated to remove water, CO_2, and N_2O, all components with higher boiling temperatures than O_2. Traces of carbon based compounds are also removed to prevent the self ignition of high purity oxygen streams further in the plant. The filtered air is driven to the main heat exchanger where air is cooled against the cold products from the plant and fed to the double pressure column.

Prior to the main heat exchanger, a fraction of the air stream is diverted and compressed further up to 30-50 bar. This high pressure stream has a shorter residence time at the main heat exchanger. After being cooled, it is later depressurized down to 1-2 bar by a turbine or valve and it is ready to enter the low pressure section of the distillation column (top of the column).

The main air stream leaving the main heat exchanger is at approximately -170°C close to its boiling point. It is then fed to the bottom of the high pressure column

(bottom) where the N_2 boils off and rises in the column while O_2 enriched air rests at the bottom. The gaseous N_2 raises through the columns stages up to the condenser where it condenses and is removed from the column in its liquid form. This stream is further cooled and expanded via a heat exchanger (subcooler) and a valve respectively, and finally fed to the top stage of the low pressure column. Similarly, the enriched O_2 air accumulated at the bottom of the high pressure column is cooled down and directed to the middle stages of the low pressure column where remaining N_2 evaporates and leaves from the top of the column in its gaseous form. High purity O_2 deposits at the bottom of the low pressure column where it serves as the the heat sink for the gaseous N_2 condensing at the top of the high pressure column. From the top of the low pressure column, a stream of gaseous and liquid oxygen is extracted. As a result three major streams are obtained from the low pressure columns: (1) Gaseous N_2 (top), (2) Gaseous O_2(bottom) and (3) liquid O_2(bottom). Both oxygen streams contain traces of N_2 but mostly Ar whose boiling point is in between that ones of N_2 and O_2.

A crucial factor in the feasibility of the APC is to be provided with sufficient make-up Ar from the ASU. This is the case due to the nature of the membrane separation process. Unless liquefied, the permeated stream leaving the membrane unit (figure 2.2) will contain a percentage of Ar leaving the system together with the CO_2. A balance between the incoming and outgoing Ar flows needs to be carefully arranged to ensure the feasibility of the process. The goal of this simple numerical evaluation was to estimate the percentage of Ar contained in the O_2 stream that feds the APC.

Aspen Plus software was used to simulate the ASU. Peng-Robinson equation of state were recommended and chosen to evaluate the process thermodynamics. The double column was set as a combination of two independent columns in which energy flows and temperatures from condenser and reboiler were interrelated. The process diagram simulated is shown in figure 3.5.

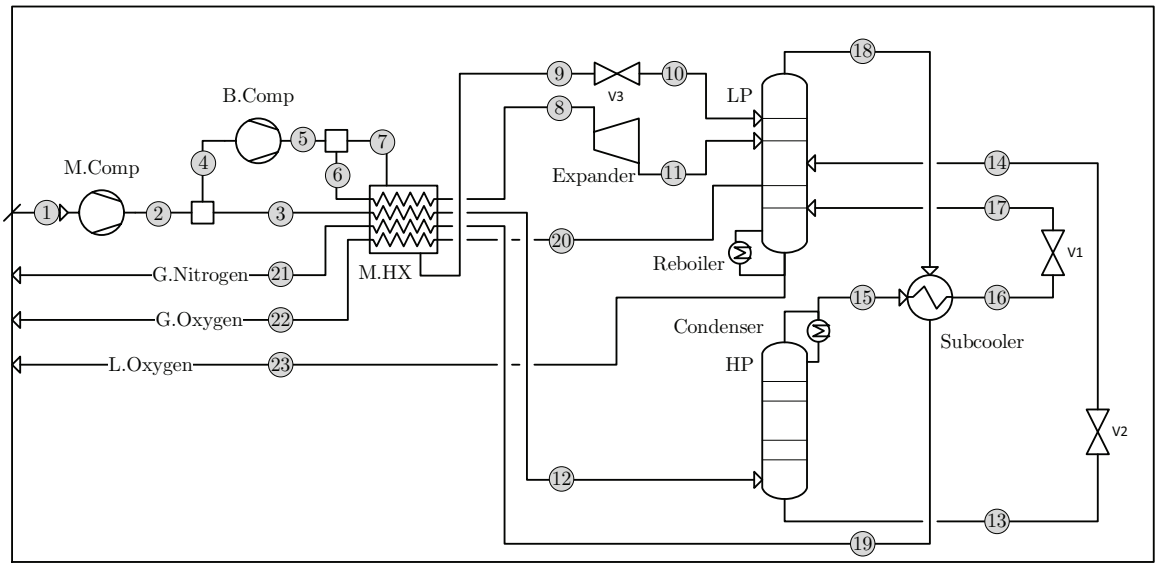

Figure 3.5: Expanded diagram of the air separation unit shown in figure 2.2.

An isentropic efficiency of 75% was assumed for both, with inter-cooling across each of the 4 stages (cooling down to 20 °C). The high and low pressure columns resulted in 30 and 55 stages respectively and operated at 4 and 1.3 bar respectively. A total pressure drop of 0.1 bar was assumed across the columns and heat exchangers. The process diagram results are shown in appendix B. A sensitive analysis was carried out to optimize the process variables. This analysis included varying the ratio of mass flows between the two different flow splits after the main compressor (M.Comp) and boost compressor (B.Comp) and their respective outlet pressures. The ratio of recycled condensate in the high pressure column condenser was also varied. All together, a sufficiently optimized process yielded the following results:

Table 3.1: ASU outcome characteristics as determined by ASPEN Plus.

Node property	Unit	Liquid Oxygen	Gaseous Oxygen	Gaseous Nitrogen
Temperature	C	-180.8	9.3	9.3
Pressure	Pa	1.30E+05	1.20E+05	1.10E+05
x_{O_2}	-	0.973	0.96	3.27E-04
x_{Ar}	-	0.027	0.04	1.84E-03
x_{N_2}	-	3.20E-12	1.20E-11	0.9978
Mole Flow ratio	%	0.67%	21.16%	78.17%
Mass Flow ratio	%	0.75%	23.60%	75.65%

In agreement with the literature, the energy consumption from this plant falls around 200 kWh/tO_2 [118, 119]. Industrial gas delivery enterprises have indicated specific energy consumption ratings closer to 160 kWh/tO_2 when optimum when optimum heat management is implemented. Therefore, it is justified to assume 200 kWh/tO_2 is a reasonable assumption as a mean to compute the energy penalty in the overall power plant. Most importantly, it was observed that up to 4% Ar can be obtained and carried out into the system with the oxygen stream.

Overall, the energy consumption can be translated into an efficiency penalty to the overall plant depending on the assumed efficiency of the RICE alone. Figure 3.6 presents the relative efficiency penalty derived from the ASU to the overall system efficiency.

This demonstrates that a reasonable range for the efficiency penalty falls within 8 to 12 % penalty assumed an energy consumption of 200 kWh/tO_2. No effort was made to evaluate either the demand for cooling water nor the air pre-treatment stage on this simulation. It is then conservative to assume that energy consumption above the prescribed 200 kWh/tO_2 is expected. Thus, with a cost of O_2 of 250 kWh/tO_2, a more conservative estimate indicates a efficiency penalty ranging from 10 to 14% based upon the RICE achieved efficiency.

It is worth noting that, as indicated in the previous chapter, access to cooling water is provided by the power system itself through the condensation of the combustion products. This may in turn reduce the operational cost of the ASU.

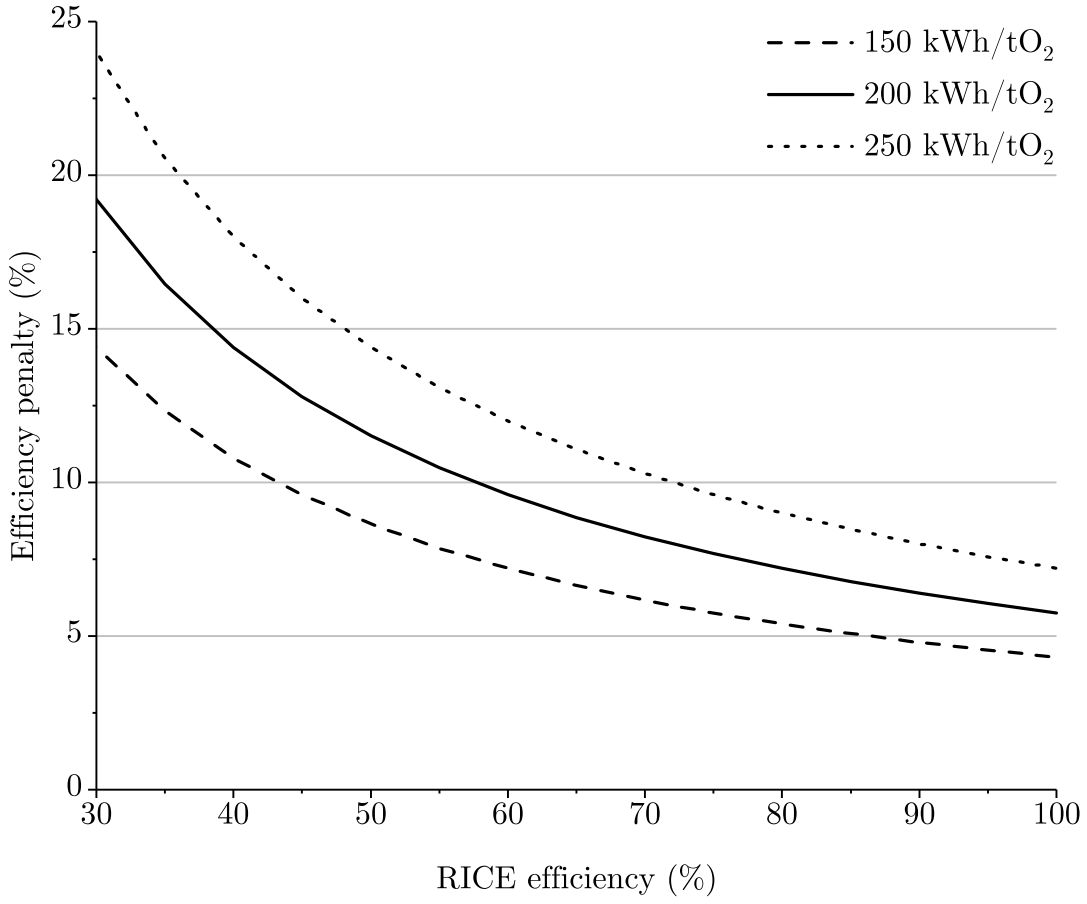

Figure 3.6: Relative efficiency penalty on gas fired power system resulting from the implementation of ASU assumed three different specific energy consumption per ton of O_2. Natural gas is assumed to hold the properties of CH_4 with a lower heating value of 50 MJ/kg.

3.3 Hollow fiber membrane modeling

Besides the need for pure O_2, the APC also requires the extraction of acumulated CO_2 from the main gas stream. Although, amine-based carbon separation is a well developed carbon capture technology with large scale pilot projects already operational, this technology is capital intensive and adds substantially to the operational cost of the power generation plants [120]. Polymeric membrane separation, on the other hand, is a promising technology for cost-effective integration of carbon capture but it is yet to prove its effectiveness to gain the favors of the power generation sector [121]. The separation efficacy of membrane systems are strongly dependent on the gas stream pressure and the CO_2 concentration. As a result, membranes are not optimal for natural gas power systems whose exhaust streams are often at little above atmospheric pressure and with CO_2 concentrations well bellow 10%. Yet, polymeric gas membrane separation is widely used in the power and industrial sec-

tors, from refinery hydrogen recovery (H_2-HC), syn-gas upgrading (H_2-CO), sour gas treating (H_2S-HC), natural gas dehydration (H_2O-HC) to EOR and landfill gas upgrading (CO_2-CH_4), proving their efficacy if the conditions are right. Polymeric gas membrane separation presents the advantage, compared to adsorption, absorption or cryogenics, of low capital investment, ease of operation and low energy consumption [122, 123]. The APC makes use of membrane separation carbon capture as an intrinsic component of the system in an effort to render a system in which carbon capture and power generation processes work synergistically to deliver a cost effective emissions free power system.

In an effort to prove the feasibility of the gas separation processes numerical simulation of a polymeric membrane unit was carried out under APC operating conditions. This model, developed in the house primarily by student Farouk Chorou and the author, was constructed purposely for this project and specifically customized for hollow fiber type membranes. Many alternative membrane materials and configuration exist, but this type of membrane has proven very effective at industrial scale gas separation applications and therefore they are deemed appropiate for the purpose of this work [124].

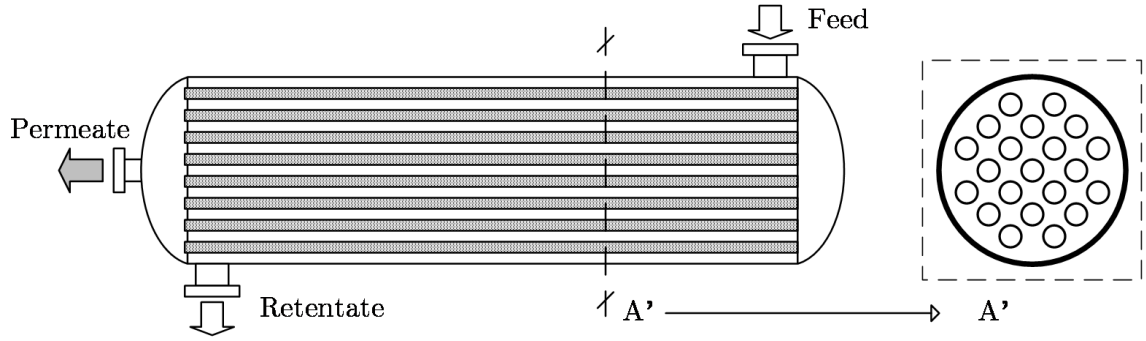

Figure 3.7: Hollow fiber membrane module schematic.

As seen in figure 3.7, a hollow fiber membrane module resembles a tube and shell heat exchanger, where the fibers are the equivalent to the copper tubes. The gas stream entering the membrane unit, the feed, flows through the tube or shell side and permeates through the fiber walls (as the heat would do in a heat exchanger). After permeation, the remaining gas on the fiber, the retentate, leaves the unit through the opposite end. The fluid that has permeated, the permeate, exits the unit through an outlet passage at either end of the membrane depending on whether it has been designed for counter current or co-current operation.

The mass transfer mechanism by permeation is simple. The total flux of gas permeating the membrane interface is directly proportional to the pressure difference between feed and retentate and to the permeability of the membrane material. Due to the heterogeneous nature of the gases being separated, choosing the right membrane material results on different degrees of permeability for each species present in the feed stream. Thus, given a specific membrane, the total flux of gas across the membrane J (kg/m^{2}s), results from the sum of each individual species flux J_i across it. Equation

3.24 shows how the species permeation phenomena is driven by the partial pressure difference of each species across the membrane.

$$J = \sum_{i=1}^{N_c} J_i, \qquad J_i = P_i \left(X_i^r p^r - X_i^p p^p \right), \qquad i = 1, 2, ...N_c \tag{3.24}$$

where P_i is the species i permeability (in mol/m^{2}Pa s), X_i^r and X_i^p are the mole fraction of species i at the retentate and permeate side respectively, and p^r and p^p are the pressures at the permeate and retentate side respectively. It can be easily observed that for efficient permeation, a combination of high pressure and concentration gradient operating conditions are desired.

Regarding the membrane itself, two major performance indicators need to be taken into account to judge the expected effectiveness of the gas separation. The first one, the permeability (P_i), indicates the magnitude of a species flow permeating the membrane per unit of area. Therefore, its magnitude will determine the permeating area requirements for the membrane module. The second one, the selectivity (γ), shown in equation 3.25, is a non dimensional term indicative of how well the membrane permeates a specific species versus the rest of species present on the feed stream.

$$\gamma_i = \frac{P_i}{P_{i,min}}, \qquad i = 1, 2, ...N_c \tag{3.25}$$

Here N_c is the total number of species present in the stream and $P_{i,min}$ is the smallest of all species permeability. In general, cost-effective permeation demands a combination of a highly permeable and selective membrane with a sufficient pressure and concentration gradient across it.

A convenient parameter to define for evaluating membrane performance is the stage cut

$$\phi = \frac{Q^p}{Q^f} \tag{3.26}$$

where Q^P and Q^f are the permeate and feed volumetric flow rates respectively. The stage cut serves as a point of reference along the membrane module, with it being zero at the inlet of the membrane, where no flow has yet permeated, and one at the virtual infinite end of the membrane where both the feed and permeate stream are in equilibrium with each other and permeation no longer takes place. For the special case of hollow fiber membranes, the stage cut can be expressed as a function of fiber radius and gas velocities as follows

$$\phi = \frac{u_z^p \pi R^{p2}}{u_{z,in}^r \pi \left[R^{o2} - R^{r2} \right]} \tag{3.27}$$

where u_z^p and u_r^p are the axial velocity of the gas streams at the permeate and retentate side, with R^0, R^r and R^p being the characteristic radiuses of the hollow fiber geometry as shown in figure 3.8.

A more in depth description of the working principles of membrane gas separation and membranes in general can be found in the literature [84, 122, 124–126]. These

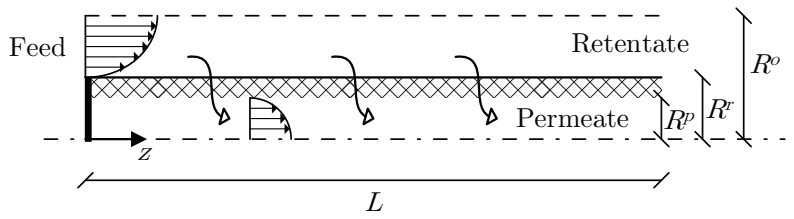

Figure 3.8: Cross section view of the fiber bundle in a shell feed hollow fiber membrane setup.

sources provide in depth fundamentals on membranes and discuss the advantages and disadvantages of alternative membrane material and system arrangements.

3.3.1 Numerical Model

The model reduces the membrane module to a single hollow fiber equivalent, comprised of a hollow fiber with wall thickness $R^r - R^p$ and a cylindrical control volume of radius R^0. The model solves the system of conservation equations (3.28 - 3.32) at both sides of the membrane.

$$\frac{\partial(\rho)}{\partial t} + \frac{\partial(\rho u_z)}{\partial z} = \sum_{i=1}^{N_c} \dot{\omega}_i \tag{3.28}$$

$$\frac{\partial(\rho u_z)}{\partial t} + \frac{\partial(\rho u_z u_z)}{\partial z} = -f - \frac{\partial p}{\partial z} \tag{3.29}$$

$$\frac{\partial(\rho c_{p,mix} T)}{\partial t} + \frac{\partial(\rho c_{p,mix} T u_z)}{\partial z} = \frac{\partial}{\partial z}\left[\kappa_{mix}\frac{\partial T}{\partial z}\right] + \sum_{i=1}^{N_c} \dot{\omega}_i h_i \tag{3.30}$$

$$\frac{\partial(\rho Y_i)}{\partial t} + \frac{\partial(\rho Y_i u_z)}{\partial z} = \frac{\partial}{\partial z}\left[D_i \rho \frac{\partial Y_i}{\partial z}\right] + \dot{\omega}_i, \qquad i = 1, 2, ...N_c - 1. \tag{3.31}$$

$$\sum_{i=1}^{N_c} Y_i = 1 \tag{3.32}$$

with ρ the density, f the momentum dissipation through friction, $c_{p,mix}$ and $c_{p,i}$ the heat capacities at constant pressure of the mixture and single species respectively, κ_{mix} the average thermal conductivity of the mixture, h_i the specific enthalpy of species i, and D_i the diffusion coefficient of specie i. Furthermore, the model exploits the symmetries of the problem and reduces the system to a one dimensional problem along the z coordinate, in which the cylindrical geometry is accounted for by a geometric factor β in m^{-1}. This factor is contained within the source term $\dot{\omega}_i$, and accounts

for the difference in surface area at the interface between the retentate and permeate streams.

$$\dot{\omega}_i = \beta J_i \qquad \text{with} \qquad \beta = \begin{cases} \beta^r = -\frac{2R^r}{R^{o2} - R^{r2}} \\ \beta^p = \frac{2R^r}{R^{p2}} \end{cases} \tag{3.33}$$

The source term in this system of equations accomplishes the numerical coupling of energy and species conservation between the permeate and retentate. Notice, β takes a negative sign for the retentate, as flow is leaving, and positive for the permeate, as the flow is entering. Thermodynamic and transport property libraries are used to update the fluid properties as they changes along the membrane. Equally, a equation of state could be used, such as the ideal gas equation of state, to evaluate the density as function of pressure and temperatures of the gaseous stream.

$$p = \rho \left(\frac{R_u}{M_{mix}} \right) T \qquad \text{with} \qquad M_{mix} = \left(\sum_{i=1}^{n} \frac{Y_i}{M_i} \right)^{-1} \tag{3.34}$$

where R_u is the universal gas constant and M_{mix} is the average molecular weight of the gas stream. Figure 3.8 illustrates the cross section of the hollow fiber across the length of the membrane, L in m. The superscripts r is indicative of retentate properties whereas the superscripts p indicates permeate properties. The control volume is indicated by dashed lines and arrows are used to indicate the direction of the flow.

Momentum dissipation

The momentum dissipation along the membrane walls is assumed to follow the correlation given for pipe flow [127].This correlation is a function of the gas viscosity, flow velocity and hydraulic diameter D_h of the flow passage.

$$f = \frac{32 u_z \nu_{mix} \rho}{D_h^2} = \begin{cases} D_h^r = 4[R^o - R^r] & \text{for retentate} \\ D_h^p = 2R^p & \text{for permeate} \end{cases}, \qquad Re = \frac{D_h u_z}{\nu_{mix}} \tag{3.35}$$

Notice that this correlation hold only for low Reynolds numbers, typically encountered in gas separation (with very small hydraulic diameters), i.e. $Re_{D_h} < 2100$ for pipe flow and $Re_{D_h} < 2000$ for annulus flow. The friction factor f, on the retentate side is multiplied by a factor (0.5), as only half of the parabolic velocity field of the feed flow is within our control volume. A slight discrepancy arises from the pipe flow correlation as it assumes that the density is constant and that the flow is well developed. This assumption does not hold at the inlet regions, estimated to be $0.035 D_h Re$, due to the permeating phenomena along the membrane walls [127].

Joule-Thomson expansion

As the gas permeates through the membrane it undergoes an isenthalpic expansion from the feed pressure to that one of the permeate. This effect may induces a temperature change in the gas, driving temperature across the membrane down enough

to the point of water condensation. This has a negative effect on the membrane performance, as water droplets quickly clog the membrane pores.

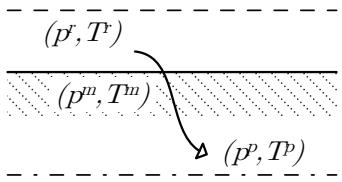

Figure 3.9: Illustration of molecule permeating from the retentate to the permeate through the membrane interface.

Although the pore clogging phenomena is not accounted for in this model, knowledge on whether condensation may occur is of critical relevance. Therefore, the Joule-Thomson effect is evaluated via the following assumptions: (1) The pressure and temperature of a molecule right at the retentate side of the membrane interface are those of the retentate bulk stream (i.e p^r, T^r), (2) the isenthalpic expansion occurs within the membrane itself, (3) the molecule is assumed to reach the permeate side at a pressure p^m equal to that of the permeate stream p^p, and at a temperature T^m that results from the integration of equation 3.36.

$$dh_i = c_{p,i} \left[dT - \mu_i dp \right] \tag{3.36}$$

where μ_i is the Joule-Thomson coefficient for species i. When equation 3.36 is integrated between the retentate and permeate of the membrane, as shown in figure 3.9, it yields:

$$h_{p,i} = c^m_{p,i} T^m = c^r_{p,i} \left[T^r - \mu_i p^r \right] + c^m_{p,i} \mu_i p^m \tag{3.37}$$

Finally, the overall temperature at a point z within the permeate $T^p(z)$ results from the solution of the energy equation considering the source term entering the permeate at T^m.

Simplified model

Several assumptions are made to effectively simplify the model: (1) The flow is steady; (2) Joule-Thomson effect is negligible on the axial direction, (3) The membrane geometry is fixed and axisymmetric; it does not deform as demonstrated by Pan, [128], (4) Permeabilities P_i are constant, and assumed to be that from pure species permeation data. It may be expanded to be a function of pressure, temperature and gas composition if higher accuracy is required [129, 130];

With the aforementioned assumptions, and the different models for mass transfer (equation 3.24), momentum dissipation (equation 3.35) and isenthalpic expansion (equation 3.36), the system of equations 3.28 - 3.31 reduces to:

$$\frac{\partial \left(\rho u_z \right)}{\partial z} = \sum_{i=1}^{n} \beta J_i \tag{3.38}$$

$$\frac{\partial\left(\rho Y_i u_z\right)}{\partial z} = \frac{\partial}{\partial z}\left[D_i \rho \frac{\partial Y_i}{\partial z}\right] + \beta J_i \qquad \text{with} \qquad i = 1 \cdots N_c - 1 \tag{3.39}$$

$$\frac{\partial\left(\rho u_z u_z\right)}{\partial z} = -\frac{\partial p}{\partial z} - f \tag{3.40}$$

$$\frac{\partial\left(\rho C_{p,mix} T u_z\right)}{\partial z} = \frac{\partial}{\partial z}\left[k_{mix} \frac{\partial T}{\partial z}\right] + \sum_{i=1}^{n} (\beta J_i) h_i \tag{3.41}$$

with the following boundary conditions for the retentate side:

$$\left(u_z T\right)^r (z=0) = \left(u_z T\right)^r_{in} \qquad ; \qquad \frac{\partial\left(u_z T\right)^r}{\partial z}\Big|_{z=L} = 0 \tag{3.42}$$

$$\left(u_z Y_i\right)^r (z=0) = \left(u_z Y_i\right)^r_{in} \qquad ; \qquad \frac{\partial\left(u_z Y_i\right)^r}{\partial z}\Big|_{z=L} = 0 \tag{3.43}$$

$$p^r (z=0) = p^r_{in} \tag{3.44}$$

and the following boundary conditions for the permeate side:

$$\left(u_z T\right)^p (z=0) = 0 \qquad ; \qquad \frac{\partial\left(u_z T\right)^p}{\partial z}\Big|_{z=L} = 0 \tag{3.45}$$

$$\left(u_z Y_i\right)^p (z=0) = 0 \qquad ; \qquad \frac{\partial\left(u_z Y_i\right)^p}{\partial z}\Big|_{z=L} = 0 \tag{3.46}$$

$$p^p (z=L) = p^p_{out} \tag{3.47}$$

The resulting system of equations is equivalent to a non-linear boundary value problem. The numerical method chosen to solve the problem was the finite difference method (FDM) in combination with the Piccard iteration method in order to resolve the non-linearity. Extensive literature on FDM and analogous numerical methods such us finite element methods and finite volume methods can be found in the literature and will not be discussed here.

3.3.2 Hollow fiber membrane for the APC

The mass transfer problem presented above is now used to evaluate the performace of several membrane modules in a system arrangement suitable for the APC. The system chosen for implementation is a three module "serial enricher" with recycle. This system has proven the most cost effective by the industry [84]. The diagram of the system is depicted in figure 3.10.

In this system arrangement, the retentate stream of each module is recirculated back to the feed stream of the previous membrane module and the permeate stream is fed to a subsequent module. The permeate flow is recompressed up to the nominal feed pressure prior to entering the next membrane module. The main design condition

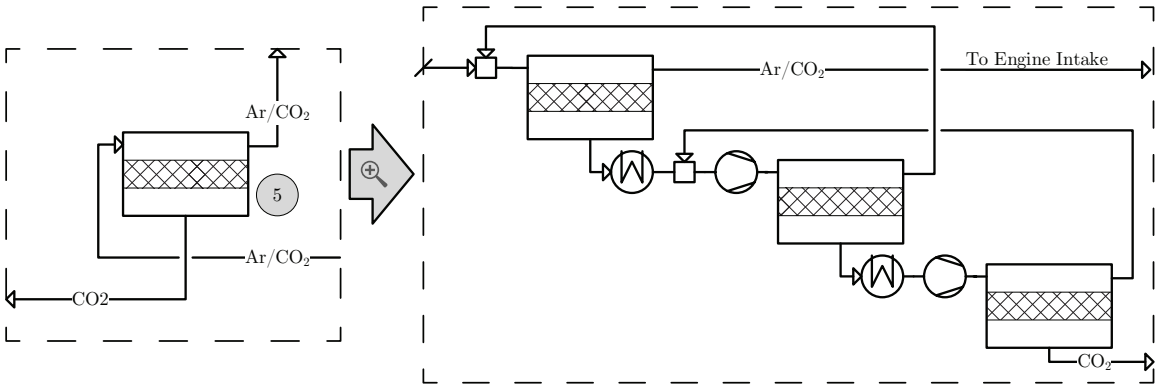

Figure 3.10: Expanded diagram of the membrane system in figure 2.2.

is to maintain the recirculated streams composition and pressure equal to that of the permeate stream of the previous membrane, keeping the entropy generation to a minimum. This condition ultimately defines the stage cut for each membrane, given a fixed feed and permeate pressures.

A parametric evaluation was carried out to evaluate the effect of cycle pressure and recirculated CO_2 on the energy consumption of the entire membrane gas separation system. For simplicity, the gas stream entering the membrane was assumed to be fully dried, at the engine boost pressure, and with an amount of CO_2 resulting from the sum of the recirculated stream and the products of stoichiometric combustion. The feed pressure was varied between 4 and 6 bar to evaluate actual RICE boost pressures. The working fluid mixture composition is fixed and assumed to consist of 15% O_2 with the remaining 85% consisting of a mixture of Ar and CO_2. The concentration of recirculated CO_2 facing the engine intake was varied from 5% all the way to 20%, always maintaining 15% O_2 concentration. The compressors are assumed isentropic and operate between atmospheric (permeate) and cycle pressures (feed). The membrane characteristics are listed in table 3.2 and were suggested by Membrane Technology Research Inc. as a good representation of the state of the art.

γ_{H_2O}	9000
γ_{CO_2}	1000
γ_{O_2}	80
γ_{Ar}	60
γ_{CH_4}	1

Table 3.2: Membrane selectivities for common species.

Figure 3.11 shows the membrane system energy consumption per mole of CH_4 burnt by the RICE at different boost pressures and recirculated CO_2 mole fractions.

The data shown in figure 3.11 represents the energy penalty over the RICE power output operating at a brake efficiency of 70%. It is straight forward to evaluate the effect of RICE efficiency. With decreasing brake efficiency, the amount of CO_2 per watt output linearly increases and so does the energy consumption of the membrane

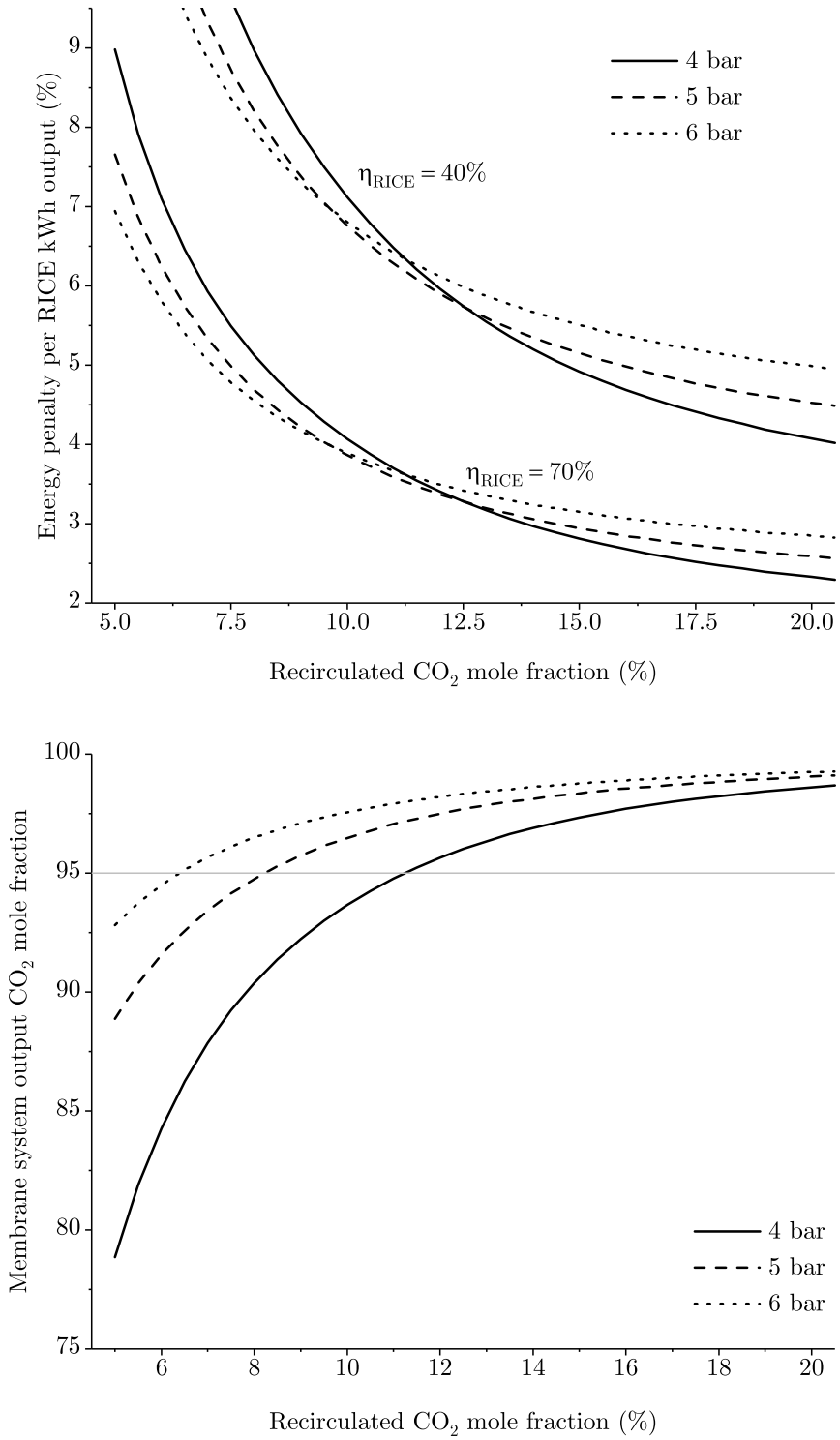

Figure 3.11: Top: Membrane system energy consumption as a percentage of RICE power output. Bottom: Output CO_2 mole fraction as a function of cycle pressure and recirculated CO_2.

system. Another noticeable trend is the crossover in the consumption from high to low pressure and high to low recirculated amount of CO_2. As the amount CO_2 recirculated decreases, the amount of Ar permeating the membranes increases causing an increase in the isentropic work consumed by the compressors. On the other hands, as the recirculated CO_2 is increased, the ratio of specific heats of the permeating gas stream approaches that of CO_2. Therefore the higher consumption at high cycle pressure is simply due to a higher pressure ratio across the compressors. It is then an obvious choise to aim for a high fraction of CO_2 recirculation and maintain a reasonable cycle pressure. This conclusion however is erroneous. Although not within the scope of this work, it can be expected that an increase of CO_2 in the recirculated stream limits the potential efficiency reachable by the RICE. Therefore, a trade off between RICE efficiency and membrane system efficiency needs to be carefully evaluated. In this case, flexible cycle pressure may compensate for a limited amount of recirculated CO_2. A look at the membrane system output CO_2 mole fraction, depicted in figure 3.11, helps understand why. At low recirculated CO_2 and low cycle pressure, the purity of the output gas stream decreases well below 95%, the minimum acceptable mole fraction for pipeline standards [116]. Higher cycle pressure (i.e. 6 bar) expands the operational range down to 6% while maintaining a reasonable membrane system efficiency and overall system power density.

It is worth noting that, as estimated from the ASU model, the O_2 gas stream contains up to 4% Ar. It is straight forward to see that under stoichiometric conditions, the oxidation of one mole of CH_4 generates an equal molar amount of CO_2 and requires two moles of O_2. This is, per every one mole of CO_2 generated, the system is fed 0.042 moles of Ar. Therefore, the membrane system is allowed to spare up to 7.7% Ar or generate a CO_2 stream with a purity as low as 92.3%.

Finally, correcting for the assumptions made, one may evaluate the more realistic energy penalty by assuming a realistic compressor efficiency ($\leq$ 90%) and assuming the RICE operating at a lower brake efficiency (50%). In such case, the highest energy penalty, at low pressure (4 bar) and level of recirculation ($\leq$ 5% CO_2) is as high as 14%. In the optimistic case the theoretical APC efficiency is achieved (70%), and the APC closed loop features are exploited, the energy penalty may reduce to below 4%.

3.4 Summary

In this chapter three models have been discussed: (1) A zero dimensional (0D) RICE combustion model (2) 0D cryogenic air separation process and a (3) one dimensional (1D) membrane gas separation model. A few major conclusions have been drawn from the numerical work presented:

1. The 0D RICE model overpredicts the burn rate, regarless of the fuel or working fluid. This demand the introduction of a more detailed flame propagation model which accounts for the location of the spark plug and the growth behaviour of the flame as it develops from a little kernel into a larger flame traveling across the combustion chamber.

2. Despite the oversimplification of the flame propagation phenomena, the model indicates how the use of hiher percentage of Ar in the working fluid yields higher efficiency. Extreme dilution may result in disproportional heat losses relative to the amount of energy being released in the cylinder although this conclusion is condition to whether or not the engine is being operated at the right ignition timing.

3. As expected, combination of Ar coupled with higher O_2 concentration yields higher peak pressures and thus temperatures. A balance between heat losses and power density is expected to be of importance when tuning the engine for optimum operation.

4. A model of a standard double column ASU was built using ASPEN PLUS. Results show tha, assumed standard air compositions, up to 4% Ar is delivered with the O_2 stream at a cost of 200 kWh/tO_2. This energy cost, normalized by the the LHV of methane, represents an approximate 6 percentage points penalty over the overall efficiency of the plant.

5. Assumed the system is provided with 4% Ar, a plant operating on methane (natural gas surrogate) is allow to purge as much as 7.7% argon with its CO_2 stream.

6. A 1D membrane model predicts that the cost of extracting CO_2 from the Ar stream may cost as little as 2% of the LHV of the fuel. This is condition to the plant being operated at sufficiently high CO_2 recirculation levels and at nominal cycle pressures above 4 bar.

Chapter 4

Experimental Investigation

In this chapter, the results of the experimental work are presented. The chapter begins by introducing the experimental setup used and its main specifications. It is followed by a brief description of the experimental approach and the experimental results obtained.

4.1 Experimental Setup

For the purpose of testing the APC operating engine conditions, a new test cell had to be designed and built. The test cell previously in place was decommissioned, and the engine and dynamometer re-purposed for this work. The design and construction of this new cell, though not scientific work, was a major part of the experimental work realized by the author along this research project. Besides the engine test cell, a constant volume chamber (CVC) and a flow measurement rig was used as means to obtain preliminary experimental data on the performance of the direct injection system.

4.1.1 Internal combustion engine testing facility

The engine used on this work is a Waukesha Cooperative Fuel Research (CFR) FI/F2 combination rating unit, whose main specifications are listed in table 4.1. Except for the engine block, the rest of the engine cell was designed purposely to operate under the new prescribed conditions. Figures 4.1 and 4.2 show a picture of the completed test cell and a simplified P&D diagram of the setup respectively.

The engine is coupled to an induction type dynamometer that can actuate both as a motor as well as a generator. The dynamometer assists during the start up of the engine and later maintains a constant operating engine speed by acting as a load. Engine speed and torque are measured at the dynamometer by means of the dynamometer power controller and a strain gauge load cell.

The gaseous fuel is fed to the engine from compressed gas tank. A stainless steel double stage pressure regulator is set in place to control the high pressure fuel line. A safety shut down valve, emergency shut down switch and relief valve are set to shut

Table 4.1: Cooperative Fuel Research (CFR) engine specification.

Property	Value	Units
Type	F1/F2	-
Displacement	611	cc
Compression ratio	4:1-17:1	-
Speed range	300-1200	rpm
Bore	82.5	mm
Stroke	114.3	mm
Connecting rod length	254	mm
Valve configuration	Overhead	-
Combustion Chamber	Flathead	-
Valves	2	-
IVO	-343	CAD ATDC
IVC	-153	CAD ATDC
EVO	148	CAD ATDC
EVC	-353	CAD ATDC

off the fuel line in case of pressure regulator failure or if commanded by the engine operator. A Coriolis mass flow meter accurately measures the fuel flow before the fuel line reaches a split. At this point a second pressure regulator further reduces the line pressure to feed the gaseous port solenoid injector. The high pressure line is then directed to the direct injector. A pressure transducer is installed on each line to keep record of injection pressures.

Table 4.2: Engine operation and control equipment.

System type	Mfr.	Part.No
Gaseous port fuel Injector	*Bosch*	NGI2
Modified gaseous direct fuel Injector	*Bosch*	HDEV
Liquid port fuel Injector	*AC Delco*	217-3410
Ignition Coil	*AC Delco*	D577
Spark plug adapter	*AVL*	ZF43H7LPRT

The liquid fuel line feeds from a gasoline tanks and is pressurized by means of an inline gasoline pump. The line pressure is controlled by an automotive pressure regulator. The flow is recirculated back to the tank in order to maintain a constant injection pressure. No direct fuel metering was integrated although fuel flow is measured indirectly by means of an exhaust wide band lambda sensor.

The working fluid supply system, often called the air supply system, is designed to accommodate the supply of either room air, compressed air or custom binary mixtures of oxygen and other gases. During engine start and engine warm up, it is sometimes convenient to operate on room air. This is facilitated by a quick disconnect ISO flange, near the intake manifold, which can be opened or closed at the engine's operator

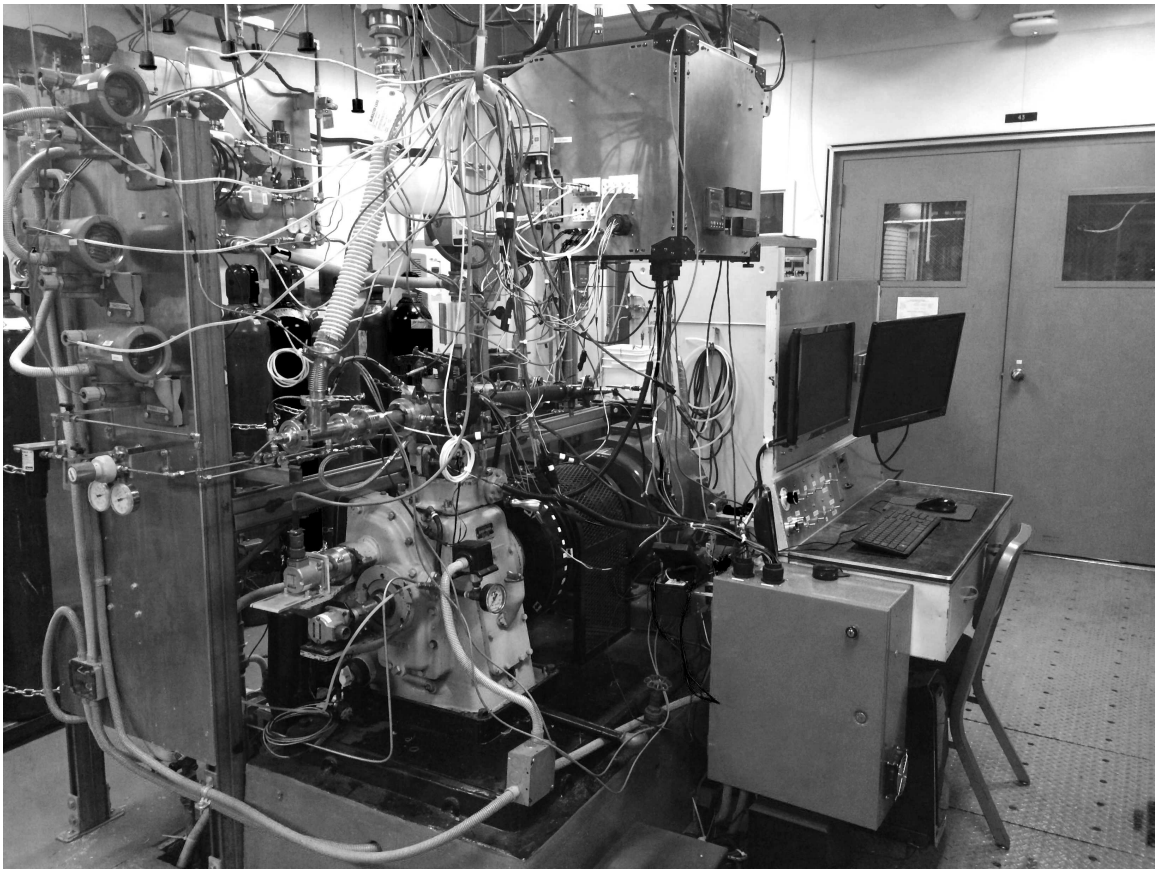

Figure 4.1: Finalized CFR experimental setup at UC Berkeley.

convenience. In the case of compressed air, the gas flow rate is controlled through a pressure regulator and measured by an in line Coriolis mass flow meter. In the case of the binary mixture, the total mass flow rate and composition is controlled by means of two remotely controlled modulated valves in combination with two corresponding Coriolis mass flow meters. The pressure prior to the modulated valves is set by two gas pressure regulators, one of which is heated. This measure ensures that the line does not freeze due to the Joule-Thompson effect. This is particularly the case when operating with CO_2. Moreover, the oxygen line is made out of copper, cleaned as per ASTM G93 and G127 standards, and sized for recommended flow velocities in order to ensure the removal of any foreign surface matter which could self ignite when colliding with the tube walls. Valve seats and seals are purposely made out of Kalrez® to reduce the risk of self ignition due to sonic flows across the valve opening orifice.

The compressed air line and the binary mixture line converge at a flow split, prior to which a check valve is set on each line. This measure reduces the time constant of the transitioning process from air to custom mixture and vice verse. The switch between working fluids is achieved by means of two remotely actuated solenoid valves which simultaneously open and close the corresponding lines. After the flow split, an electric heater is used to preheat the flow to a desired temperature, ensuring constant engine operating conditions. At the engine intake, both temperature and absolute

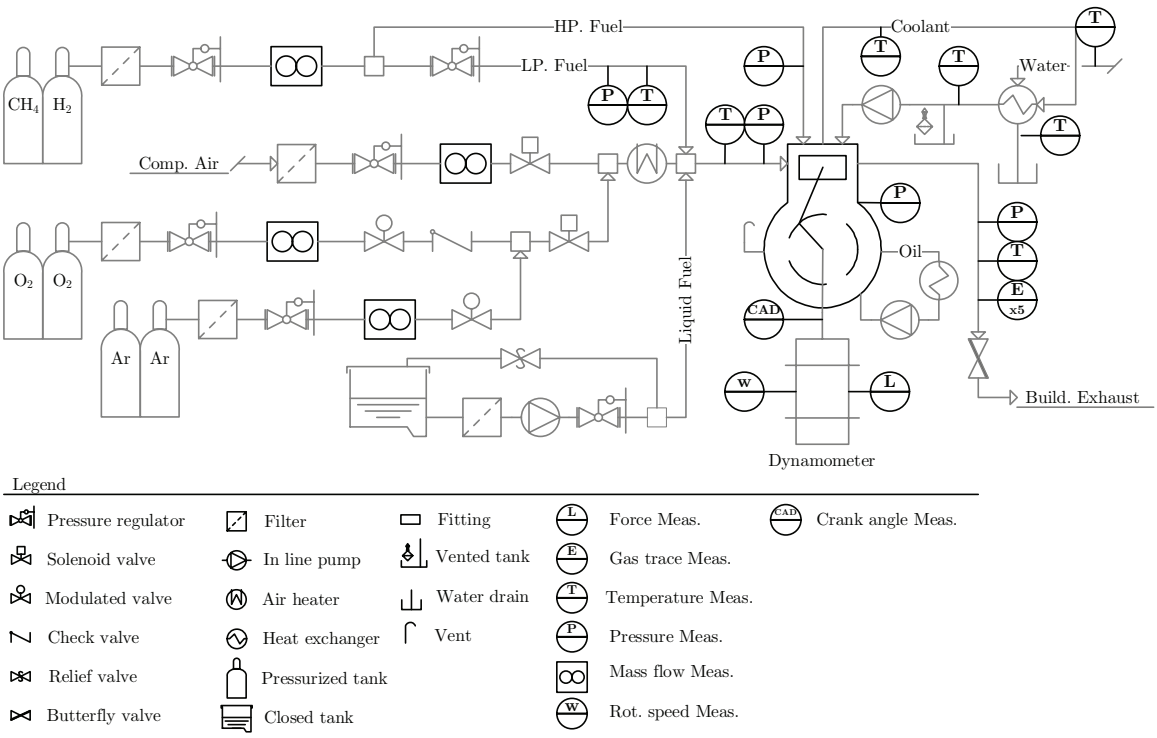

Figure 4.2: Engine experimental setup schematic for the CFR engine at UC Berkeley.

pressure are measured.

At the engine, the pressure within the cylinder is measured through a modified spark plug which incorporates a differential piezoelectric pressure transducer. Piston angular position is measured with a differential optical encoder purposely located in the camshaft and referenced to TDC. Temperature is measured immediately after the engine exhaust valve to record accurate gas temperatures before substantial heat transfer occurs at the exhaust manifold. Further downstream, and using a ceramic temperature insulator, an absolute pressure transducer is used to measure exhaust gas pressure. A small percentage of the exhaust gas stream is deviated to a condenser and fed to a five gas analyzer for continuous evaluation of unburnt hydrocarbons (UHC), O_2, CO, CO_2, and NO_2.

The engine coolant system consists of a closed loop coolant fluid circuit which exchanges heat with an open loop city water system via a shell and tube heat exchanger. Coolant temperature is controlled via a remotely actuated valve that regulates the city water flow rate. Temperatures before and after the heat exchanger are measured in both the coolant and city water side. An auxiliary oil cooling system is not necessary for this engine, given that the engine crankcase is large enough to dissipate the heat and maintain the oil temperature within operational range while is being recirculated by the oil pump.

The different sensors used across the test cell are listed in table 4.3 for reference.

Table 4.3: Cooperative Fuel Research (CFR) engine specification.

Sensor type	Property	Mfr.	Part.No
Thermocouple(k)	Water in temperature	*Omega*	KMQSS
Thermocouple(k)	Water out temperature	*Omega*	KMQSS
Thermocouple(k)	Exhaust temperature	*Omega*	KMQSS
RTD	Intake temperature	*Omega*	RTDM12
RTD	Coolant in temperature	*Omega*	RTDM12
RTD	Coolant out temperature	*Omega*	RTDM12
NTC thermistor	Fuel temperature	*Sensata*	51CP26-01
Abs. pressure sensor	PFI pressure	*Sensata*	51CP26-01
Abs. pressure sensor	DI pressure	*Bosch*	DS-HD-KV4
Piezoresistive P. Transd.	Intake pressure	*Kistler*	4045A2
Piezoelectric P. Transd.	In-Cylinder pressure	*AVL*	GH13Z-24
Abs. pressure sensor	Exhaust pressure	*Omega*	PX209
Coriolis Mass flow meter	Fuel mas flow rate	*Emerson*	CMFS007M
Coriolis Mass flow meter	O_2 mas flow rate	*Emerson*	CMFS010M
Coriolis Mass flow meter	Inert mas flow rate	*Emerson*	CMFS010M
Coriolis Mass flow meter	Air mas flow rate	*Emerson*	R025S1319U
Optical encoder	Piston angular position	*BEI*	XH25D-SS-1440-ABZC
Strain gauge load cell	Dynamometer arm force	*Interface*	SM-100
Flame ionization detector	UHC emissions	*Horiba*	FMA-220
Magneto-pneumatic Analyzer	O_2 concentration	*Horiba*	MPA-220
Non-dispersive infrared Analyzer	CO concentration	*Horiba*	AIA-220
Non-dispersive infrared Analyzer	CO_2 concentration	*Horiba*	AIA-220
Chemiluminescent Analyzer	NOx concentration	*Horiba*	CLA-220

The data acquisition and engine control systems, depicted in figure 4.3, are merged together as one within a *National Instruments* cRIO chassis 9074 and operated by LabVIEW® software. This system allows the acquisition of data from the different sensors while accurately and deterministically [1] outputting the signals that control injection timing, ignition timing and modulated valves set point commands.

Corresponding signal charge amplifiers are used for piezoresistive and piezoelectric pressure transducer in order to filter and amplify the signal from 0-10mV range up to 0-10V, thus allowing for accurate reading of the measurement. Because of the periodic nature of the cylinder motion, the acquisition timing and frequency is synchronized

[1]The cRIO operates at 40 MHz clock, which for the purpose of this experiments is beyond sufficient for deterministic control of the engine.

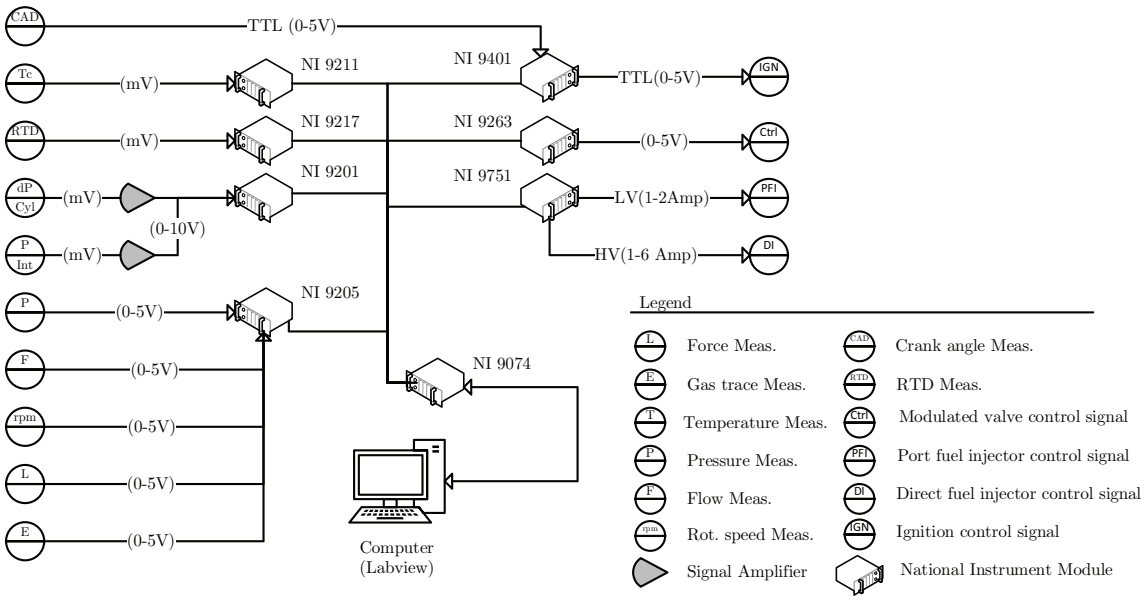

Figure 4.3: Energy conversion network.

to the output from the optical encoder. As a result, the signal acquisition frequency varies with engine speed. Specifically for this work, the engine speed was kept at 600 rpm and thus, the data acquisition frequency was set to 5 Hz for time averaged signals such as temperatures, mass flow rates and pipe systems pressure. In the case of intake and in cylinder pressure, the acquisition frequency was set at 28.8 kHz, equivalent to 8 samples per engine crank angle of degree. Finally, the data is logged into the computer and saved into an output file.

4.1.2 The combustion analysis system

With the purpose of analyzing the engine performance introduced in section 2.3.3, integral engine measurements are required to monitor the thermodynamic state of the gas during the engine cycle. The thermodynamic state of the gas trapped in the cylinder can be deduced by the generalized gas equation of state.

$$PV = nZR_uT \tag{4.1}$$

where R_u is the universal gas constant and Z is the compressibility factor which reduces to 1 at low ρ_{gas}, when the gas can be consider ideal [131]. Therefore, by means of two state variables (i.e. p, T) and the molar composition of the gas, the state of the gas is known. As we have seen in section 2.3.1, the volume (V) can be deduced from the angular position of the crankshaft(θ) through equation 2.5. Either temperature or pressure and mass within the cylinder would then be sufficient to derive the thermodynamic state of the gas and thus the thermodynamics characteristics of the process such as W_T, Q and ΔU. The temperature (T) within the cylinder is not homogeneous and strong gradients exist across the flame front and towards the cylinder walls. Unlike temperature, pressure(p) propagates at the speed of sound

$c = \sqrt{\gamma R_s T}$ [132], which for the time scale at which the samples are taken it is fast enough to make the overall pressure approximately uniform and inform on the overall pressure within the cylinder at any time. Therefore, with the combination of pressure and volume, the thermodynamic state within the cylinder can be estimated through the ideal gas equation of state.

In-cylinder pressure

As previously mentioned, the in-cylinder pressure is measured with a differential piezoelectric pressure transducer. The output signal represents a random Δp_s unreferenced signal. A reference absolute pressure p_0 is needed to translate differential pressure values (Δp_s) into absolute pressure p at a given crank angle θ. The process of coupling the sensor pressure measurement p_s to an absolute reference pressure p_0 is often referred as pegging of the pressure signal [133–135]. This reference pressure is normally measured by an atmospheric pressure transducer installed at the intake port of the cylinder. This method is known as inlet pressure referencing [133]. With this method, it is assumed that the absolute pressure within the cylinder is equal to that of the intake port at the time the inlet valve is about to close (IVC).

Knowledge of the pressure trace in combination with the cylinder volume allows to compute the net work generated by the piston (as indicated in equation 2.38), and in combination with all other sensor data such as gas emission traces, mass flow rates and pressures, the characteristics values (figure 2.12) that indicate engine performance can be estimated as explained in section 2.3.

In-cylinder mass

Besides the pressure, the specific volume of the gas is also required to define the thermodynamic state of the gas. In the case of this experimental setup we have knowledge on the mass flow into the engine cylinder. The mass encapsulated in the cylinder is however the sum of this mass flow and the mass of gas trapped from the previous cycle. The mass trapped in the cylinder can be calculated with the knowledge of the cylinder volume and pressure at the point of EVC and with the assumption that the temperature of the gas is that one measured at the exhaust port. The trapped mass can be then calculated and added to the integral of the mass flow along an engine cycle to yield the initial in-cylinder mass.

Similarly, as in the numerical simulation, a blowby model is used to estimate a rate of gas leakage through the cylinder-piston interface, and derive an in-cylinder mass profile over time. The specific volume can now be computed as the ratio of cylinder volume over in-cylinder mass at any given time during the cycle.

With the in-cylinder pressure and mass profiles, the average in-cylinder temperature can be calculated by means of the ideal gas equation of state

$$T(\theta) = \frac{p(\theta)V(\theta)}{m_{cyl}(\theta)R_s} \tag{4.2}$$

An example of the temperature profile is shown in figure 4.4.

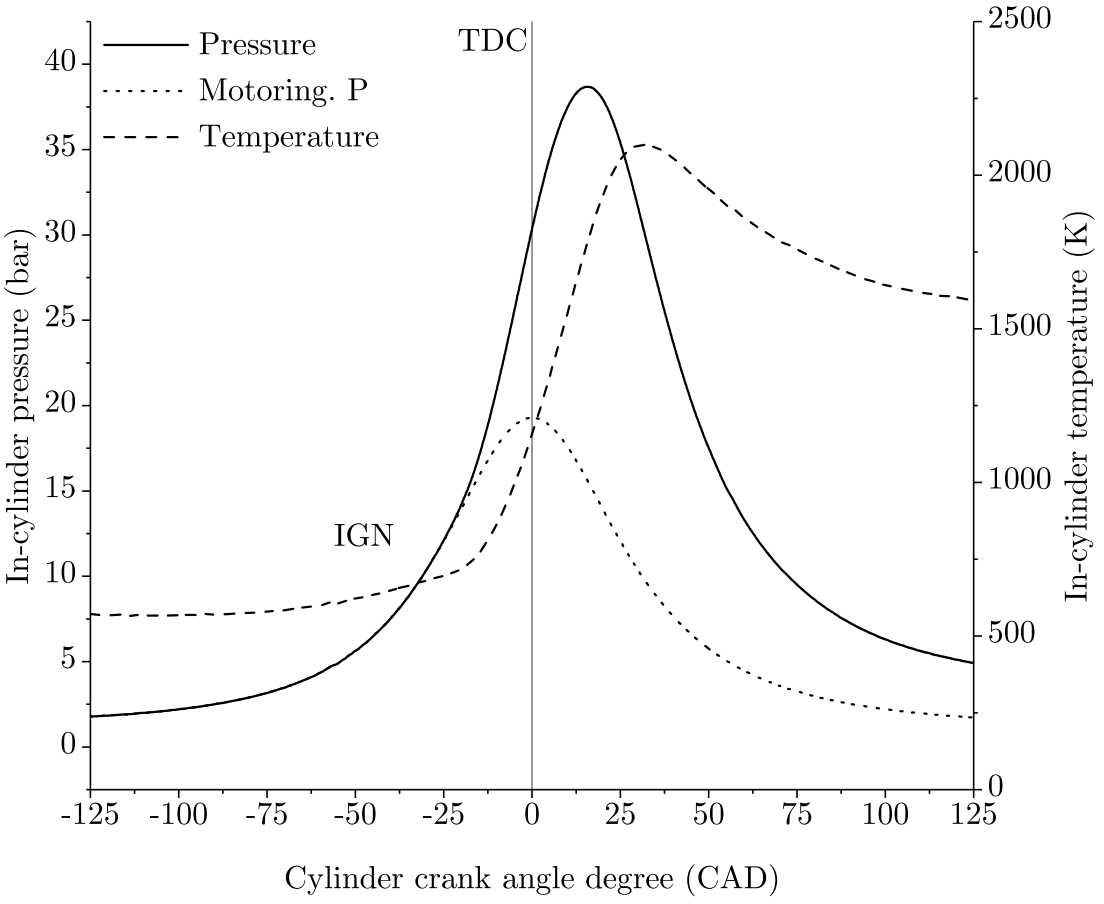

Figure 4.4: Example of engine pressure trace and derived motoring pressure trace and average mean cylinder temperature.

4.1.3 Heat release and combustion timing characterization

With the values for pressure, temperature and mass in the cylinder, the heat release rate due to combustion can be estimated following equation 3.8. This expression can be further simplified if we consider that the heat loss through the walls and the energy lost or gained through blow by and fuel injection is already accounted for on the resulting pressure trace being measured. In such case, the energy balance can be simplified and rewritten as

$$\frac{dQ_{heat,n}}{d\theta} = \frac{dU_{cyl}}{d\theta} + p\frac{dV}{d\theta} \tag{4.3}$$

where the term $\frac{dQ_{heat,n}}{d\theta}$ stands for the net heat release rate or apparent heat release rate. The value for the specific internal energy can be computed through

$$u = h - RT \tag{4.4}$$

where h and R are the specific enthalpy and specific gas constant of the fuel-air

mixture. Considering the gas mixture as an ideal gas, the specific enthalpy is only dependent on $T(\theta)$ and can be easily obtained through the NASA polynomial[2] [113].

With knowledge of the heat release rate and its integral, the cumulative heat released ($Q_{heat,n}$), the combustion timing can be characterized by means of characteristics crank angles CASOC, CA10, CA50, CA90, and CAEOC. These parameters represent the crank angles at which 3%, 10%, 50%, 90% and 97% of the total heat on the fuel have been apparently released, respectively. They are derived from a normalized trace of the cumulative net heat released as can be seen in figure 4.5.

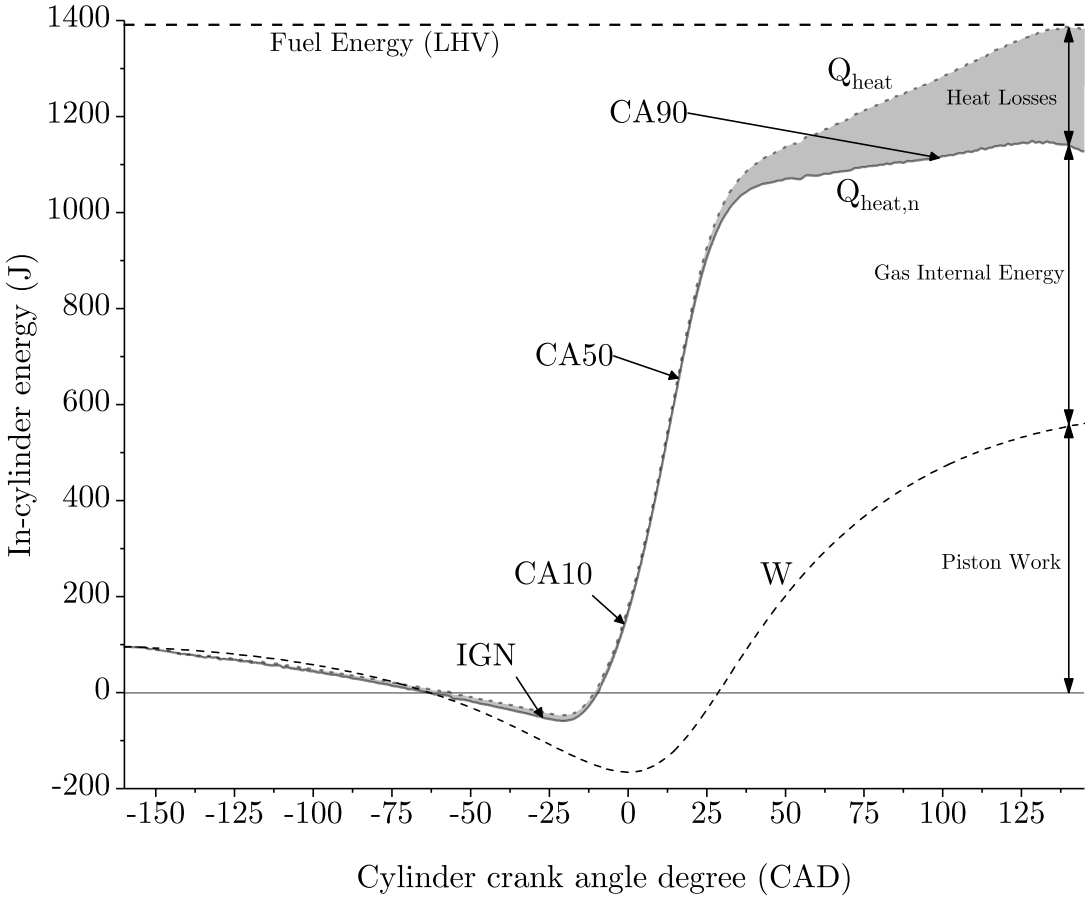

Figure 4.5: Example of cumulative net and gross heat released profile and piston work. Some characteristics angles are shown for reference.

A more detailed characterization of the combustion event can be realized if a heat loss model is implemented. This model infers the actual amount of heat released or gross cumulative heat released (Q_{heat}). The same model presented in section 3.1.2 for the numerical analysis is used here to estimate the heat transfer coefficient and ultimately compute the heat losses. It is worth noticing that, in order to implement this heat loss model, knowledge of a non firing pressure trace is required. This trace

[2] `http://combustion.berkeley.edu/gri-mech/data/nasa_plnm.html`

can be either collected from a non firing cycle or estimated based upon the fact that the piston cylinder system performs a near isentropic compression and expansion process when combustion is not triggered. The compression and expansion strokes are not adiabatic, as explained in section 2.3.3 and thus, the behavior of the gas in the cylinder is better approximated by a polytropic process which obeys

$$PV^n = P(\theta)V(\theta)^n = C \tag{4.5}$$

with n the polytropic index, which equals γ for an adiabatic process, and C a constant value. Taking two pressure and volume samples at two values of crank angle (θ_1, θ_2) where the polytropic approximation holds, (between IVC and before ignition) an estimated n can be obtained. . Applying logarithms on both side of the equation 4.5 it reads

$$log(P) + n\, log(V) = log(C) = C' \tag{4.6}$$

Developing it further

$$log(P) = C' - n\, log(V) \tag{4.7}$$

where n is the negative slope of a linear equation. Therefore, by means of a linear fit of the form

$$y = ax + b \tag{4.8}$$

over a subset of pressure ($p(\theta_i)$) and volume ($V(\theta_i)$) samples, C' is obtained as b and consequently $n = a$.

Now, an apparent motoring pressure trace can be drawn and used to feed the heat loss model. An apparent motoring trace is shown in figure 4.4. If carried out rigorously, this approach of implementing a heat loss model provides a more accurate values for CA_{50}, CA_{90}, and CA_{EOC}. In this work, although the gross heat released is estimated, the characteristic crank angles are estimated based on the apparent heat release to reduce the uncertainty of the results. This was considered given the strong dependence of the heat loss model to experimental correlations. For the case of argon no such correlation exist and the standard heat models are somewhat not appropriate.

In the upcoming section I make use of the analysis models introduced to evaluate and present the results obtained during this project.

4.2 Experimental results

The ultimate goal of this work is to demonstrate and better understand the potential benefits that the APC could bring in terms of engine efficiency, performance and emissions. A way to uncover these benefits in a scientific manner is by means of a comparison between the maximum achievable performance under conventional operating conditions (air) and maximum achievable performance under the new operating conditions (argon-oxygen). In this work I limited to the use of methane as a surrogate of natural gas, and hydrogen as a mean of energy storage. I first operated the engine platform under air breathing conditions in order to set the efficiency benchmark for both fuels. I later operated the engine under argon breathing conditions and compared the results with the ones previously obtained with air.

Irregardless of the working fluid or fuel in use, the engine was always operated at stoichiometric conditions, at equal intake pressure and temperature (1 atm, 40 Celsius), and under constant and similar engine coolant temperatures (70 Celsius). Most importantly, the operation points collected were limited to the delivery of maximum brake torque (MBT), condition at which the engine delivers the highest brake efficiency. This was done by sweeping the spark timing at each new condition in search of the most efficient point. Once MBT is found and the system conditions have reached steady state, 300 cycles are collected building up sufficient data points for the computation of statistics values. The different engine performance parameters are compared across a sweep of compression ratios from 5 to 16 in incremental steps of 1.

4.2.1 Air breathing engine operation

In this section, the air breathing engine results are presented. The engine was operated with both methane and hydrogen. MBT was found for the full range of compression ratios for which knock did not occur. As shown in figure 2.7, and for the purpose of comparison, an efficiency versus compression ratio chart seemed optimum and self explanatory. Figure 4.6 shows the expected trend presented in chapter 2.

As the compression ratio is increased, the indicated thermodynamic efficiency increases, ultimately leveling off at compression ratios beyond 12. This efficiency plateau occurs at noticeable low compression ratios unlike the theoretical equivalent which occurs farther along, around a compression ratio of 20. This discrepancy is the result of finite burning speeds forcing the ignition timing to remain substantially advanced relative to top dead center. Figure 4.7 shows the combustion phasing parameters including IGN for both hydrogen and methane. Whereas hydrogen burns very rapidly (from CA10 to CA50 in less than 4 CAD), methane is rather slow, moving away from an isochoric heat addition process as theoretically desired for an Otto cycle. It can be observed how the timing between CA10 and CA50 remains fairly constant for both fuels although the duration is substantially different. Moreover, in the case of methane, there is a substantial decrease in the timing between IGN and CA10 as compression ratio increases, indicative of lower ignition delay as the in-cylinder temperature increases.

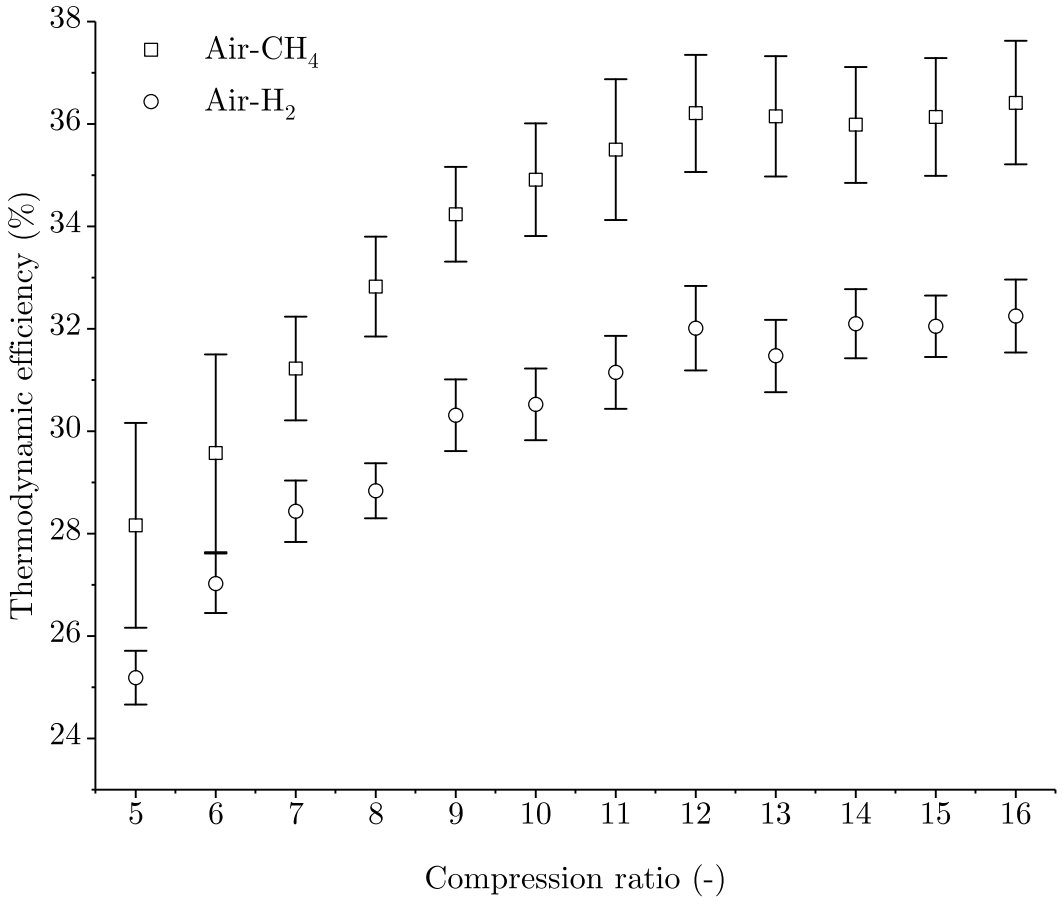

Figure 4.6: Thermodynamic efficiency for the air breathing engine fueled with methane and hydrogen at different compression ratios.

In general, indicated thermodynamic efficiency increased as both peak pressure and temperatures in the cycle increased. At sufficiently high compression ratios however, the sum of compression work, heat losses, and blow-by overwhelm the thermodynamic efficiency gains. Altogether, the benchmark thermal efficiency for methane in air was found to be approximately 36% passed a compression ratio of 12 at which point the highest IMEP was achieved (8.6 bar). Increasing the compression ratio beyond this point brought no benefits in terms of efficiency or load gain. At a compression ratio of 16 cycle to cycle variation was great and the engine operating condition fairly unstable. This is the result of in-cylinder temperatures approaching that of methane autoignition and thus control over combustion phasing was rather limited.

In the case of hydrogen however, the maximum efficiency (32%) was reached at the highest compression ratio, monotonically increasing with the compression ratio. The efficiency however was lower than that of the methane fueled engine, while the IMEP was substantially higher (11.5 bar) as can be seen in figure 4.8.

These results seems counterintuitive given the better combustion phasing provided by hydrogen. The reason for this odd thermal efficiency difference is attributable to

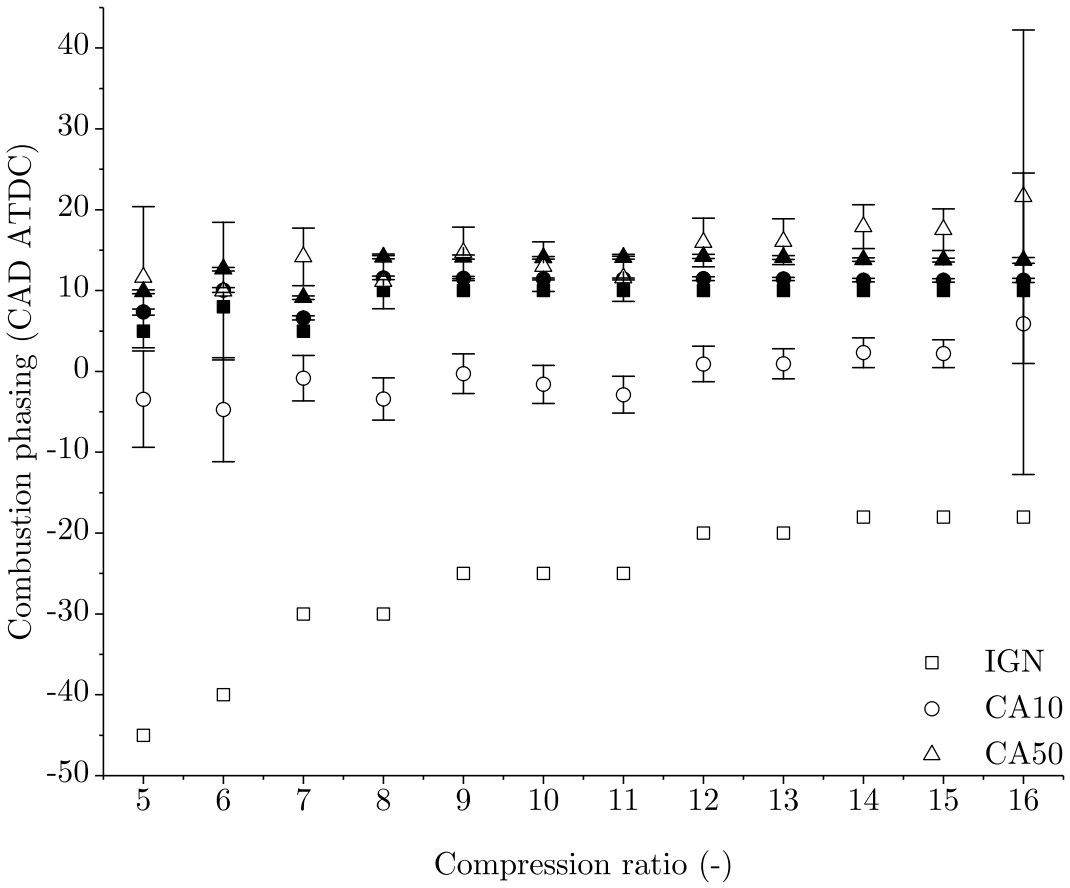

Figure 4.7: Ignition timing and combustion phasing for the air breathing engine fueled with methane and hydrogen at different compression rations. H_2: Solid •; CH_4:Open ○.

the experimental arrangement. When operating on hydrogen, the fuel was injected very early and directly into the cylinder preventing backfires. Injection of the fuel after IVC provides the engine with a larger amount of oxygen during the intake stroke, and consequently with a greater stoichiometric amount of fuel. This operating condition, combined with the larger energy density of hydrogen, resulted in higher engine loads but came at the cost of higher compression work, higher in cylinder peak pressures and temperatures, and ultimately higher blowby and heat losses. This can be seen in figure 4.9 where one can observe how a higher pressure increase develops during the compression stroke as the hydrogen begins to enter the cylinder (SOI). This can also be deduced by looking at the cumulative heat release profile. A substantial amount of piston work is consumed prior to TDC while the difference between fuel energy in the cylinder and the total energy remaining in exhaust gas is substantially larger for the hydrogen case, indicative of higher heat losses to the environment (given combustion efficiency is relatively high in both cases).

It is worth noting that hydrogen yielded more stable operating conditions than

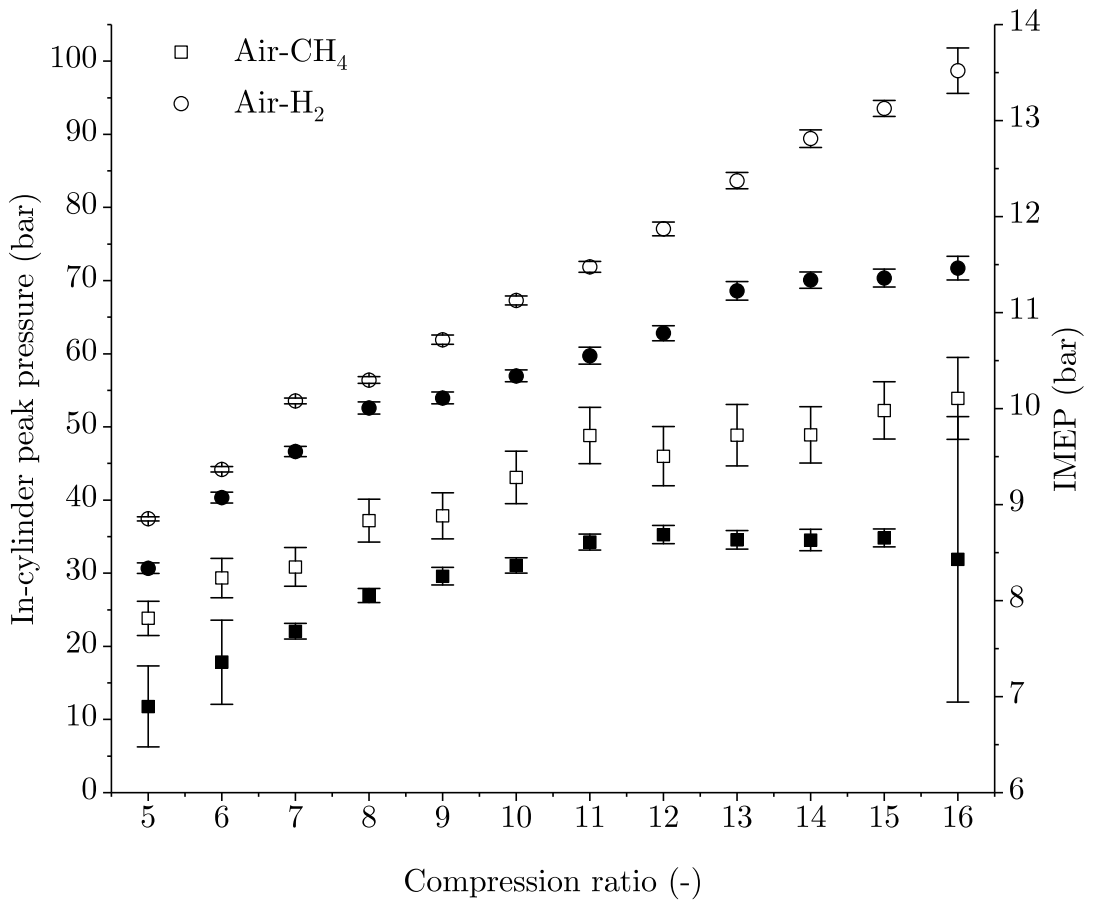

Figure 4.8: Indicated mean effective pressure and peak pressure for the air breathing engine fueled with CH_4 and H_2 at different compression ratios.IMEP: Solid •; Peak pressure:Open ∘.

methane at the lower and higher ends of the compression ratio range. Methane depicts clear instabilities at low compression ratios, where in-cylinder temperatures are substantially lower, hindering flame propagation.

A more general look at the engine performance allows to dissect its performance based on the four different efficiency terms described in chapter 2. The resulting trends are shown in figure 4.10. The first observation is the disparity in the combustion efficiency for both fuels. Whereas hydrogen operation showcases combustion efficiency of nearly 100% all across the compression ratio domain, methane shows a continuous decrease with increasing compression ratio. This can be attributed to the increased ratio of fuel-air charge trapped in the piston crevices. Because hydrogen is directly injected into the cylinder, the air in the crevices partially prevents the fuel plume from reaching these areas.

It is worth mentioning that the gas exchange efficiency term is in some cases slightly above 100%. This is the result of slight error in the exhaust pressure control system which provides a slightly higher vacuum than desired. Furthermore, the

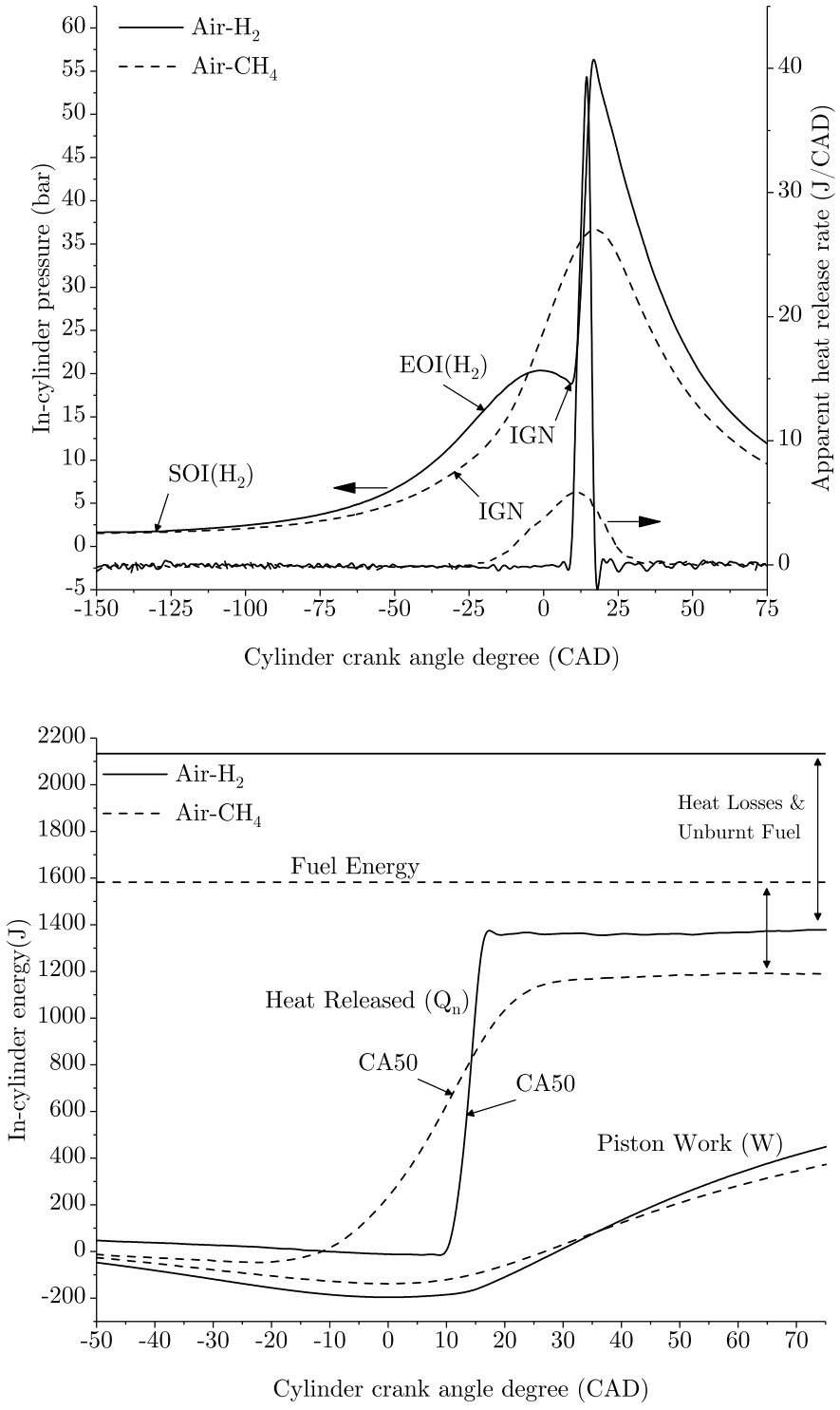

Figure 4.9: Methane and hydrogen comparison for air at a constant compression ratio of 8. Top: average in cylinder pressure and apparent heat release rate trace. Bottom: average cumulative apparent heat released and piston work profile.

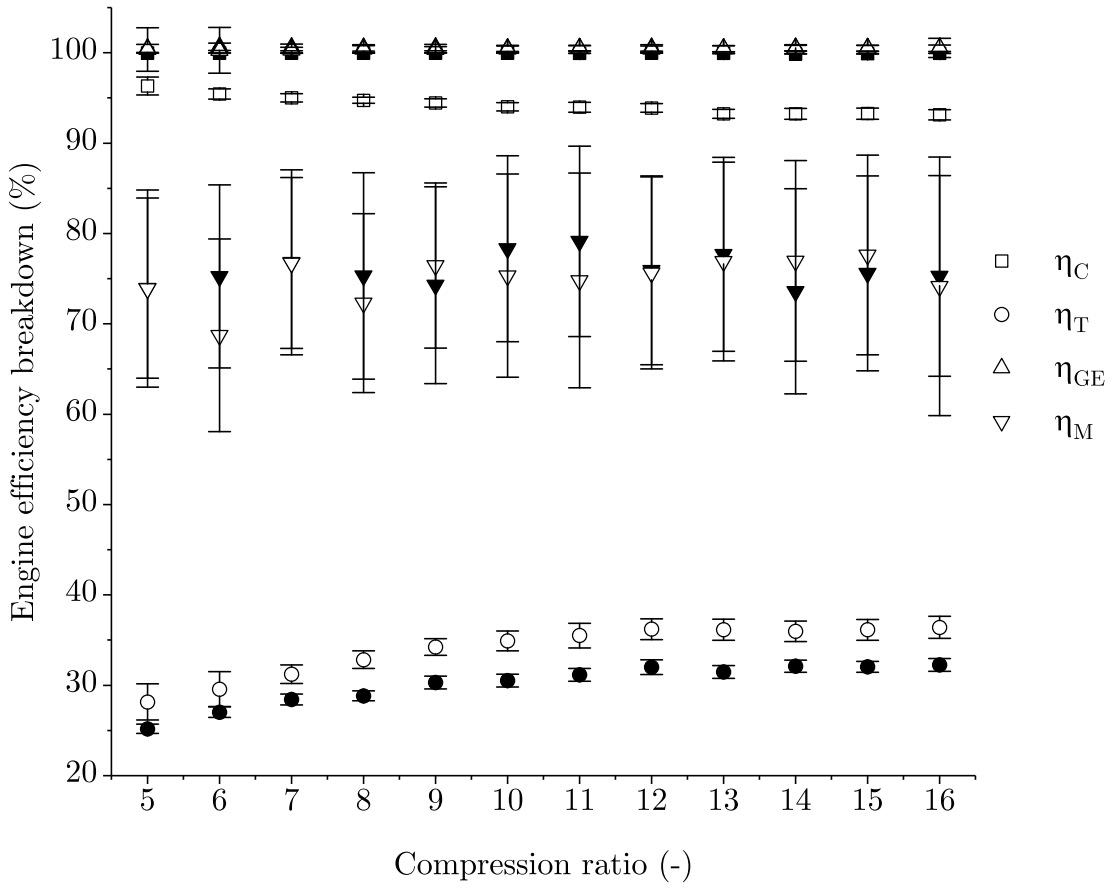

Figure 4.10: Engine efficiency breakdown for the air breathing engine fueled with methane and hydrogen at different compression ratios. H_2: Solid •; CH_4:Open ∘.

mechanical efficiency is nearly constant and similar for both fuels as it would be expected. The large fluctuation observed in the mechanical efficiency is mainly due to the combination of low engine speed conditions and the single cylinder nature of it. This combination of factors create a very challenging condition for the dynamometer that struggles to match the power output of the engine. Despite these conditions, one could expect the mechanical efficiency to decay as the compression ratio and the cylinder pressures increase, result of larger pressure between the piston rings and the cylinder walls. The results here seem to indicate a lack of proper cylinder seal and thus large blowby flow. Properly sealed engine showcase mechanical efficiencies above 80%.

In the case of emissions, results for the methane case showed an increasing amount of unburnt hydrocarbons with increasing compression ratio (Figure 4.11). This can be attributed to the increased ratio of charge trapped in the crevices as aforementioned. Early direct injection (near IVC) of methane yielded much lower and nearly constant traces of unburnt hydrocarbon, supporting the assumption of the fuel plume not reaching the crevices. Traces of NOx and CO remained fairly constant, indicating

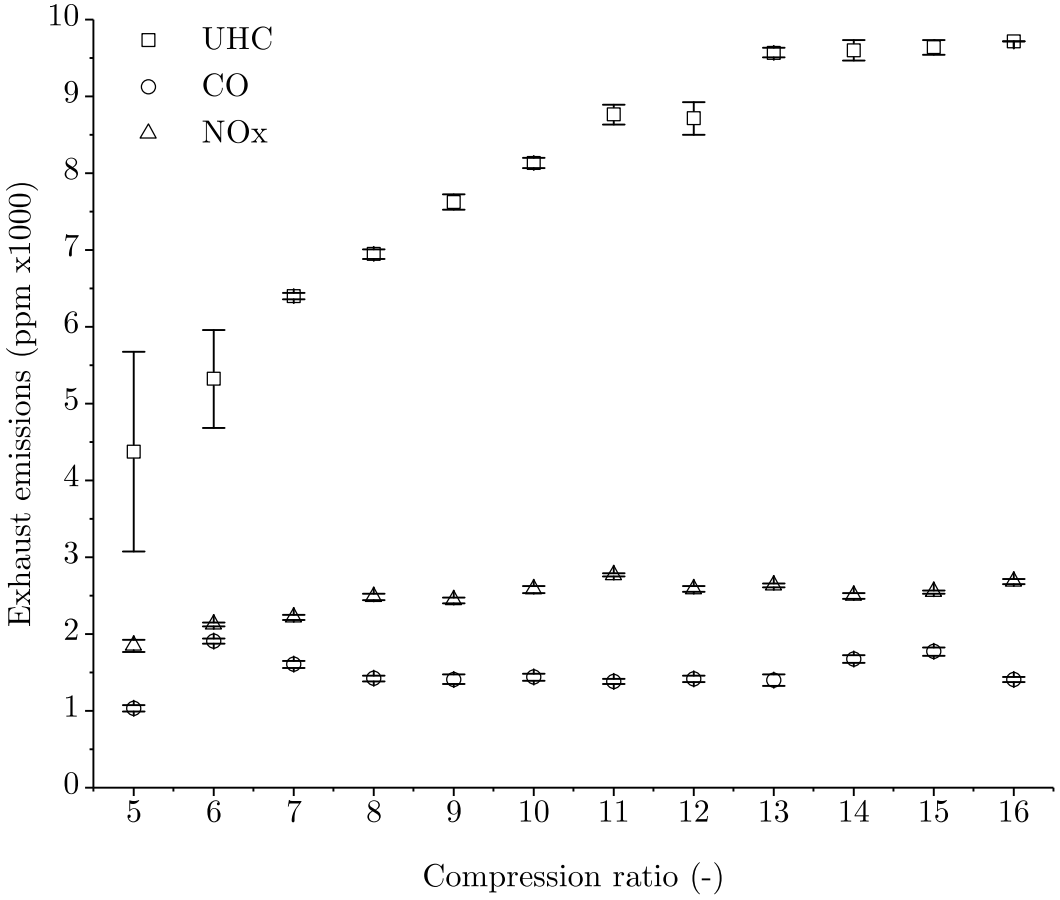

Figure 4.11: Main exhaust emission for the air breathing engine fueled with methane at different compression ratios.

little influence from the change in compression ratio. In the case of hydrogen, unburnt hydrogen was estimated based on fuel and air mass flow rates and exhaust oxygen trace. Estimates showed combustion was nearly completed (99%). Traces of NOx were above the measurable range and thus not presented here.

4.2.2 Argon breathing engine operation

For the argon case, the engine was operated under the same conditions as for the air case. The oxygen percentage was varied to evaluate the effect of dilution. First, the oxygen content in the artificial mixture was set to 21% in order to compare with the air case. Later, the oxygen concentration was decreased to 15% and 10% in order to evaluate the effect of increasing the working fluid ratio of heat capacities (γ).

Figure 4.12 shows the thermal efficiency resulting from the argon breathing engine. In the case of methane, we can observe a substantial gain in thermal efficiency for both oxygen dilutions. Compression ratios beyond 10 resulted in knock, identified by the pressure waves visible on the cylinder pressure trace and the characteristic sound

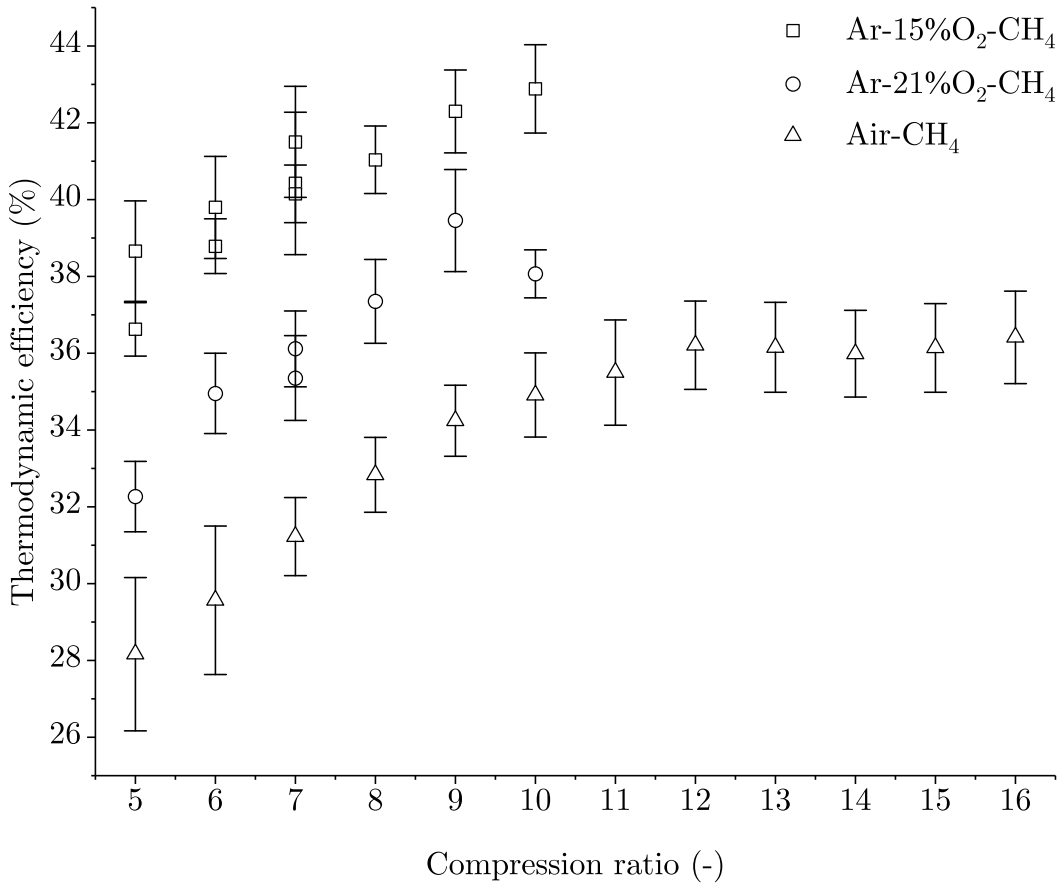

Figure 4.12: Thermodynamic efficiency comparison between the air breathing engine and argon fed engine fueled with methane at different compression ratios and oxygen dilutions.

emitted by the engine. At oxygen content of 15% the efficiency gains are highest across the entire range of operational compression ratios.

The engine IMEP was also highest for this case across the compression ratio range, yielding a maximum of 9.8 bar IMEP at compression ratio of 10, 1.4 bar higher than its air counterpart (Figure 4.13). However, peak pressures were not a clear indicative of load. Operating the engine with 79% argon yielded lower IMEP than the 80% argon, but resulted in similar and sometimes higher peak pressures.

Figure 4.14 shows the combustion phasing characteristics of both cases. Ignition timing approaches top dead center as we increase the compression ratio, more noticeable with higher argon content as the temperature in the cylinder increases to the power of the ratio of heat capacities. Nonetheless, the higher oxygen content in the 79% argon case results in higher oxidation reaction rates and noticeable shorter period between ignition and CA10 and CA10-CA50, mainly driven by a combination of higher oxygen concentration and working fluid temperatures. The air case, consequently, showcases the longest combustion duration, clearly seen by paying close

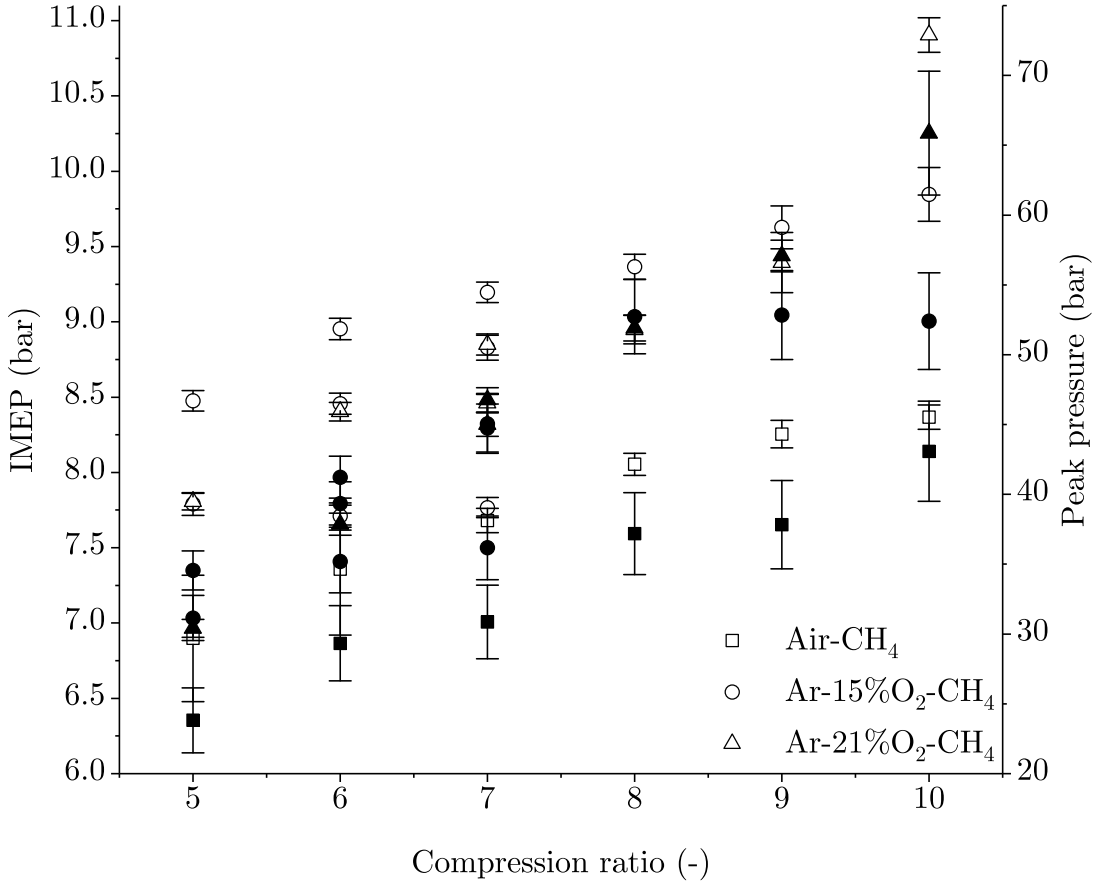

Figure 4.13: Indicated mean effective pressure and peak pressure comparison between the air breathing engine and argon fed engine fueled with CH_4 at different compression ratios and oxygen dilutions. IMEP: Open ○; Peak pressure: Solid ●.

attention to the time between ignition and CA10 as well as the period between CA10-CA50. In general, increasing the compression ratio does not seem to play a role on the burning rate between CA10-CA50.

Another interesting and yet foreseen result is the substantially lower exhaust gas temperatures resulting from the argon breathing engine. This is a clear consequence of higher thermodynamic efficiency, where a higher percentage of the thermal energy is converted into mechanical power. Nonetheless, the cooler exhaust yields what could be a great advantage for the argon breathing engine. As the gas in the cylinder cools down quicker, the temperature gradient between the gases and the coolant is reduced, supporting a reduction on heat losses to the system. This was contemplated during realization of the experiments, where the cooling system struggled to maintain the desired temperature of operation while running the argon breathing engine.

Operation of the engine at 10% oxygen was also investigated, although not as thoroughly as for the 15% oxygen case. At low compression ratios, the highly diluted oxygen mixture (10%) and the moderate in-cylinder temperature hinders flame

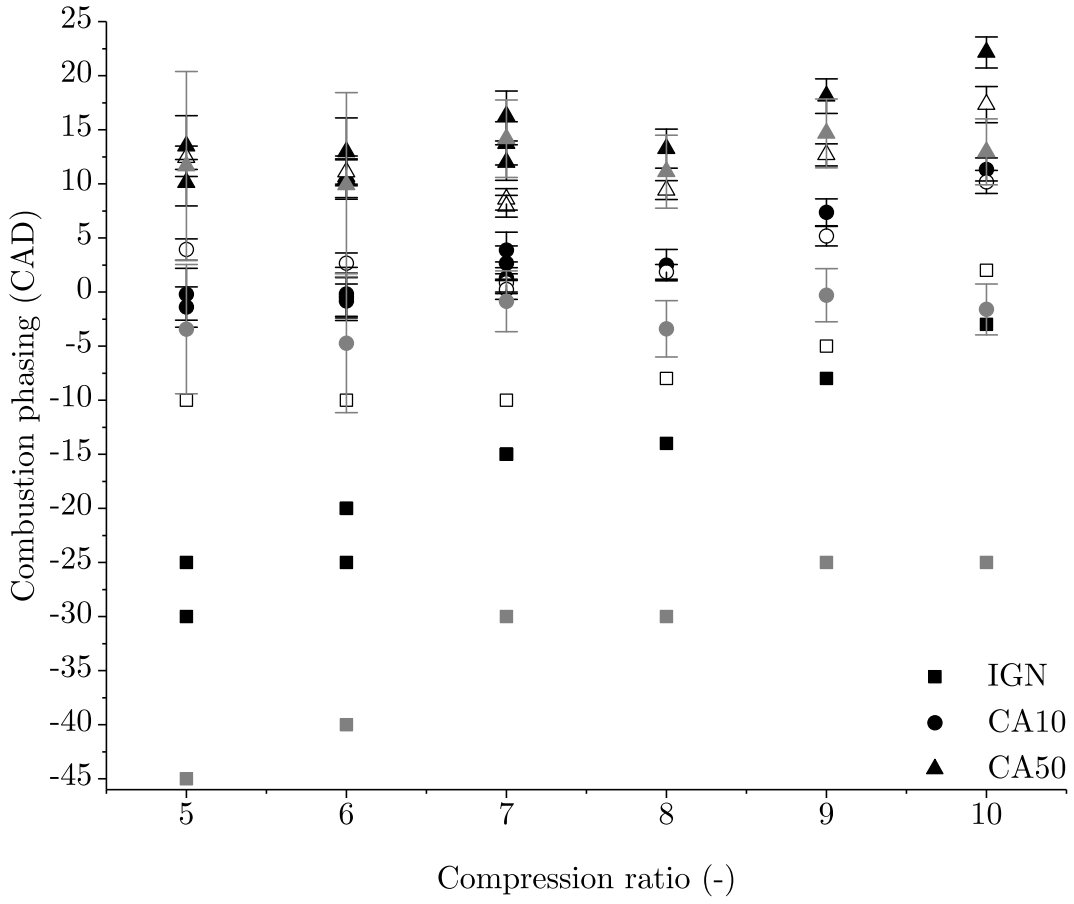

Figure 4.14: Combustion phasing comparison between the air and argon breathing engine fueled with methane at different compression ratios. White: Ar-21%O_2; Black: Ar-15%O_2; Grey: Air.

propagation, and consequently the stable operation of the engine. However, at higher compression ratios and corresponding higher temperatures, engine operation is feasible and thermal efficiencies as high as 45% were achieved at compression ratio of 10 (Figure 4.16). It can be observed how, as the oxygen is diluted further in argon, the burning duration is substantially increased, spreading the heat release from combustion more homogeneously over the cycle. In the case the system is properly optimized, the gain in efficiency due to increased dilution of oxygen comes at the cost of lower engine load. This can be seen as an efficient way to reduce engine load. Common air breathing engines today loose efficiency as the engine load is decreased. In the case where oxygen dilution could be used as a mean for load control, the engine would gain efficiency as load is reduced.

A similar but less noticeable effect can be achieved by mean of fuel dilution (λ). Maintaining the oxygen concentration constant at 15% and reducing the fuel to air ratio yields an increase in efficiency with a subsequent decrease on engine load. Because the oxygen concentration remains nearly constant, there is no major influence

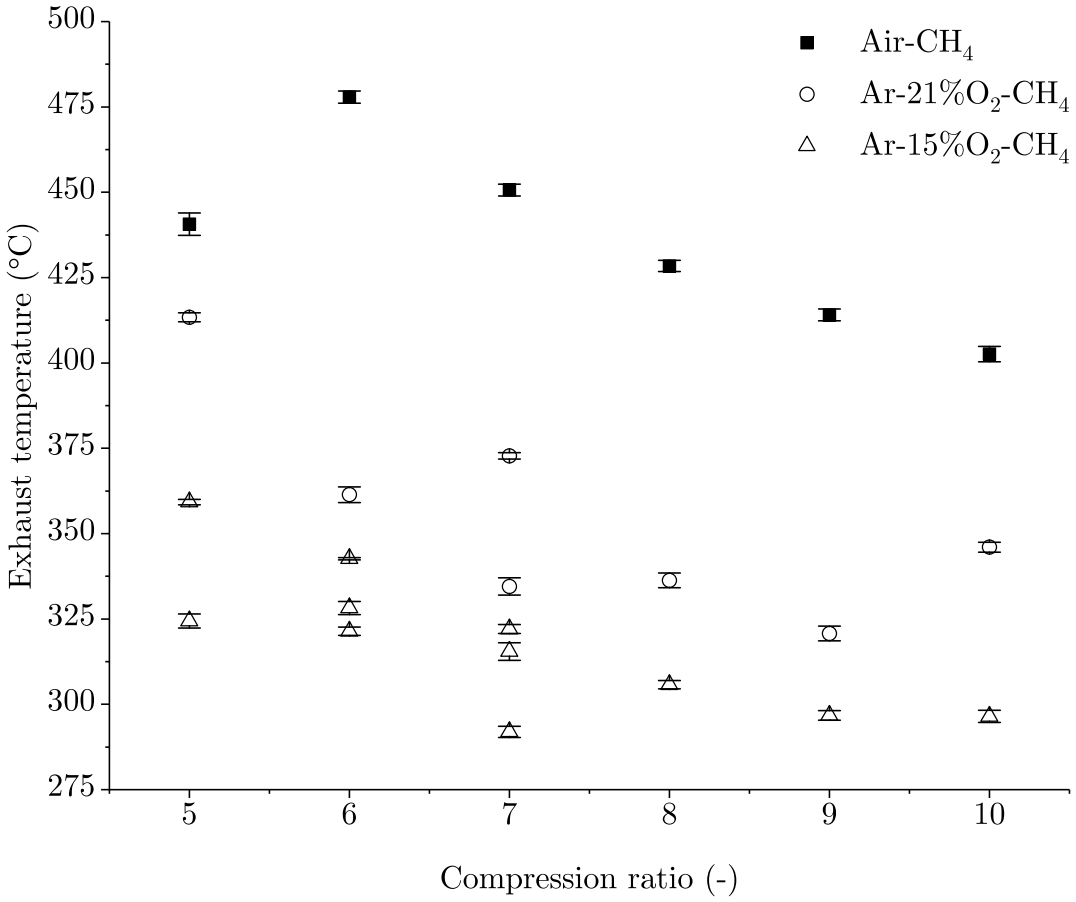

Figure 4.15: Exhaust temperature comparison between the air and argon breathing engine fueled with methane at different compression ratios.

on the burning duration beyond the fact that less fuel is there to be burnt. Regardless of the efficiency gain, in the case of the argon cycle, oxygen is as valuable as the fuel itself and fuel lean operation is a highly undesirable condition. The reason being that oxygen leaving with the exhaust stream will ultimately leak through the membrane unit and efforts to recover it would add to the energy penalty on the cycle.

In the case of hydrogen, we focus on the 15% oxygen case (Figure 4.17). Operation of the engine was quickly limited by knock which already occurred at compression ratios above 7. Thermodynamic efficiency increased as expected compared to the air case. Burning duration did not present a major difference and remained constant across the compression ratio range. This can be attributed to the fast flame propagation speed of hydrogen compared to the rotational speed at which the engine was operated. MBT Ignition timing on the other hand was delayed with increasing compression ratio. For the argon case particularly, the ignition timing was substantially delayed relative to the air case and this difference increases with increasing compression ratio.

Similarly, as for methane, exhaust gas temperatures were lower for the argon

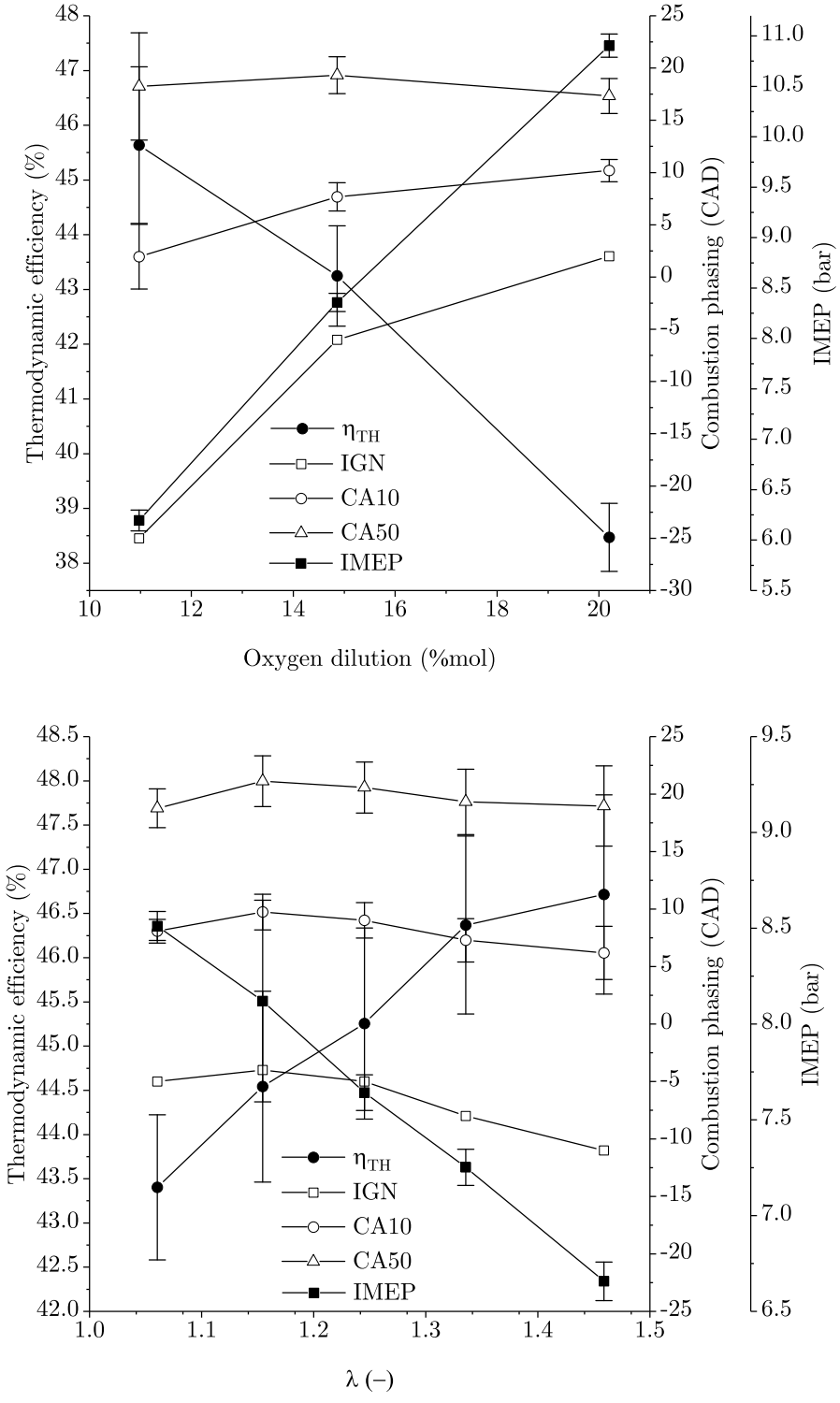

Figure 4.16: Influence of dilution (top) and lambda (bottom) on the thermodynamic efficiency and combustion phasing.

case. However, engine load and peak pressures were lower for the argon case at all compression ratios, proof that the efficiency gain was not enough to compensate for the lesser fuel amount in the cylinder. The reduction on peak pressures can be primarily attributed to the later ignition timing in the argon case relative to the air case.

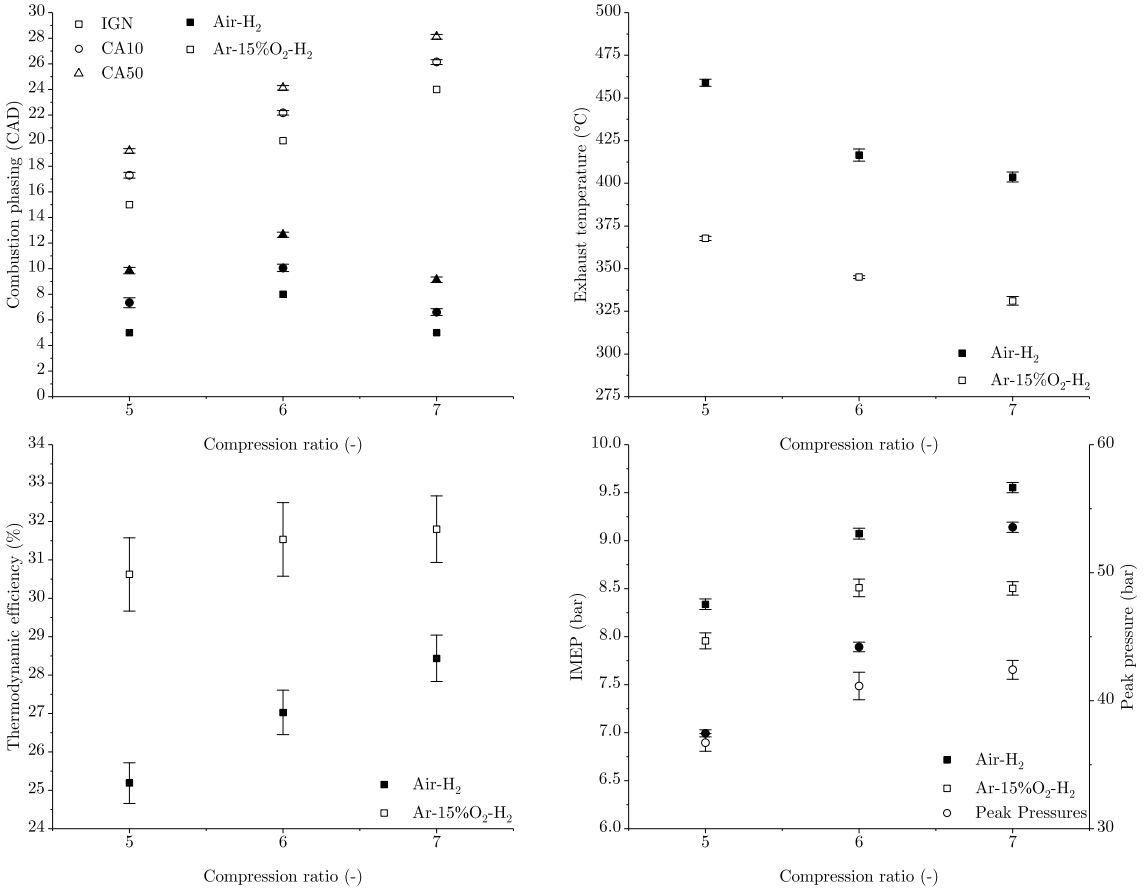

Figure 4.17: Several performance parameters comparison between the air and argon breathing engine fueled with hydrogen at different compression ratios.

Direct injection strategy

As seen previously, both methane and hydrogen engine operation is limited to compression ratios below 10 and 7 respectively due to knock. A reasonable workaround to this limitation is the use of direct fuel injection. Control over when the fuel enters in contact with the oxygen provides an extra control knob to better tune the phasing and efficiently realize the thermal to mechanical energy conversion. Direct injection however brings certain challenges that may not be overlooked. The first one of these challenges is the energetic cost of fuel compression. Because the fuel is injected later in the cycle, the working fluid is already compressed during the compression stroke

forcing the fuel to be at an even higher pressure. While this is not a challenge for liquid fuels, when considering the use of H_2 or CH_4 the energy required for compression amounts to as much as 10% of the fuel energy content. Figure 4.18 showcases the compression energy penalty for isentropic and isothermal compression processes for both H_2 and CH_4 as function of their LHV.

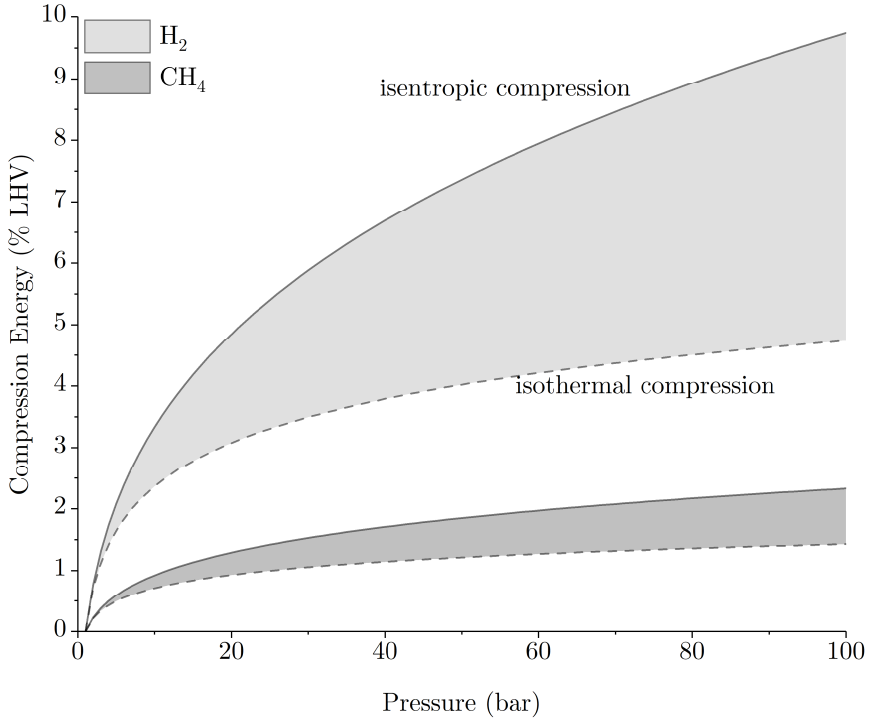

Figure 4.18: Isothermal and isentropic energy cost of compression as a percentage of fuel's LHV for methane and hydrogen, assuming ideal gas behavior.

Compressing hydrogen up to 100 bar already represents an efficiency penalty of 5% to 10%. Therefore, pursuing a direct injection strategy for H_2 requires that the effort results on an efficiency gain larger than 5% in the best case. A second challenge is the need for rapid fuel injection and mixing. The short duration of an engine cycle requires the fuel to enter the chamber and mix rapidly, allowing for the complete oxidation reaction to take place before the exhaust valve opens. Due to the low density of gaseous fuels, direct injection strategies require large fuel injection pressures and large injector nozzles in order to provide sufficient flow rate. Bigger nozzles however render large fuel plumes and consequently, poor fuel-oxygen mixing. Development of optimum injection systems requires accounting for both fuel and working fluid, but it is also influenced by the size and shape of the engine cylinder.

In this work the injector, kindly provided by Bosch, could not be modified and so it was not optimized for our engine characteristics. The injector in question was a modified gasoline direct injection, whose original tip has been removed and substituted by a single orifice. The characteristics listed in in table 4.4. We did not have

access to the characteristic curves of the injector and thus few tests were conducted to characterize and foresee the injector capabilities to serve in the engine platform.

Table 4.4: Solenoid direct injector specifications.

Property	Value	Units
Maximum feed Pressure	100	bar
Orifice number	1	-
Orifice diameter	650	μm

Two different constant volume chamber (CVC) tests were required to evaluate the injector behavior, the first using a smaller chamber designed to estimate the mass flow rate through the injector, and the second one using a larger chamber designed to evaluate the penetration depth and spread angle.

For the first test, a small cylindrical vessel was assembled and attached to the direct injector (figure 4.19). This vessel was equipped with a thermocouple and a piezoelectric pressure transducer for temperature and pressure measurement, respectively. Absolute pressure and temperature were also measured upstream of the injector.

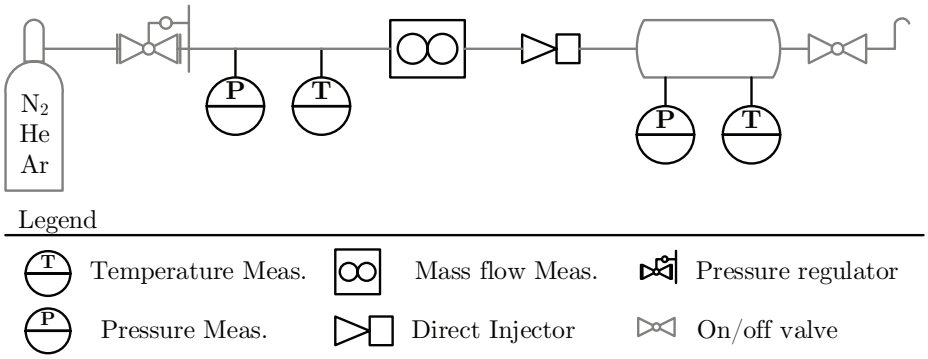

Figure 4.19: Injector flow rate measuring setup.

Holding injection pressure constant and allowing the constant volume chamber to discharge to atmosphere, the injector was operated at a specified frequency and pulse width to reduce the influence of the opening and closing events in the average mass flow rate calculation. In a second experiment the chamber is kept closed and the injector is operated, allowing the pressure upstream and downstream of the injector to equalize. By measuring the mass flow rate and the chamber pressure as a function of time, the mass of fuel injected across a continuous range of pressure differences between injection and chamber pressure could be determined. The tests were carried out with three different inert gases (Ar, N_2, and He) chosen to cover a wide range of molecular weights while preventing possible safety hazards. Using the isentropic nozzle flow equation for ideal gases

$$M_c = A_c \sqrt{\gamma P_0 \rho_0} \left(\frac{2}{\gamma + 1} \right)^{\frac{\gamma+1}{2(\gamma-1)}} \tag{4.9}$$

Table 4.5: Direct injector discharge coefficient calculated with Ar, He, N_2 at 100 bar and 23°C and discharging to atmospheric conditions. Estimated real flow rates for H_2 and CH_4 are also indicated.

Gas (-)	Theoretical flow (g/s)	Meas. flow (g/s)	C_d (-)
Ar	9.7090	1.142 ± 0.025	0.113
N_2	7.6734	0.866 ± 0.018	0.117
He	3.0723	0.342 ± 0.005	0.111
H_2	2.051	0.226	0.114
CH_4	5.675	0.624	0.114

an average discharge coefficient (C_d) for the injector was estimated based on the outcomes of injection mass flow experiments for N_2, Ar, and He. In this equation the properties are taken at temperature and pressure upstream of the injector. The resulting discharge coefficient was then calculated by

$$C_d = \frac{M_r}{M_c} \tag{4.10}$$

The results are shown in table 4.5. A discharge coefficient of $C_d = 0.114 \pm 0.002$ was assumed for the injector. Finally, the CH_4 and H_2 mass flow rates across the injector could be estimated from its theoretical values.

The transient pressure measurement results indicate that for CH_4 at 100 bar, the flow through the injector may be estimated as 624 mg/s. For H_2 at 100 bar, the flow through the injector was estimated at 225 mg/s. The CH_4 estimate corresponds to an injection duration of approximately 88 CAD for a stoichiometric amount of CH_4 in 20% O_2 mixtures at an engine speed of 600 rpm. Though the injection duration is feasible, it is not optimal given that the injection rate may, under some operation conditions, be the limiting factor for the fuel burning rate and thus the engine power output.

For measuring penetration depth and spread angle of CH_4 and H_2 in Ar and N_2, a high-speed schlieren imaging of a larger (1.45 L) optically accessible constant volume chamber was used. A Photron FASTCAM SA4 high speed camera was used. A diagram of the CVC geometry and the schlieren setup are shown in figure 4.20.

The purpose of this brief experiment was to qualitatively evaluate the potential for the injector to provide sufficient fuel penetration and spread within the engine chamber at relevant high pressure environments. With the upstream pressure limited to 100 bar, the density and consequently the momentum of the gaseous jet is limited. Knowledge before hand of the injection behavior was deemed necessary to safely operate the engine, more so when working with H_2 fuel. High speed schlieren images were recorded at f = 3600 Hz and f = 7200 Hz with a shutter speed of 25 μs. Non-reacting experiments were conducted injecting CH_4 at 15 ± 0.05 bar and 100 ± 0.05 bar, and H_2 at 15, 20, 30, 50, 80 and 100 bar into the chamber filled with Ar or N_2. The chamber pressure and the injection duration were kept constant at 10 ± 0.05 bar

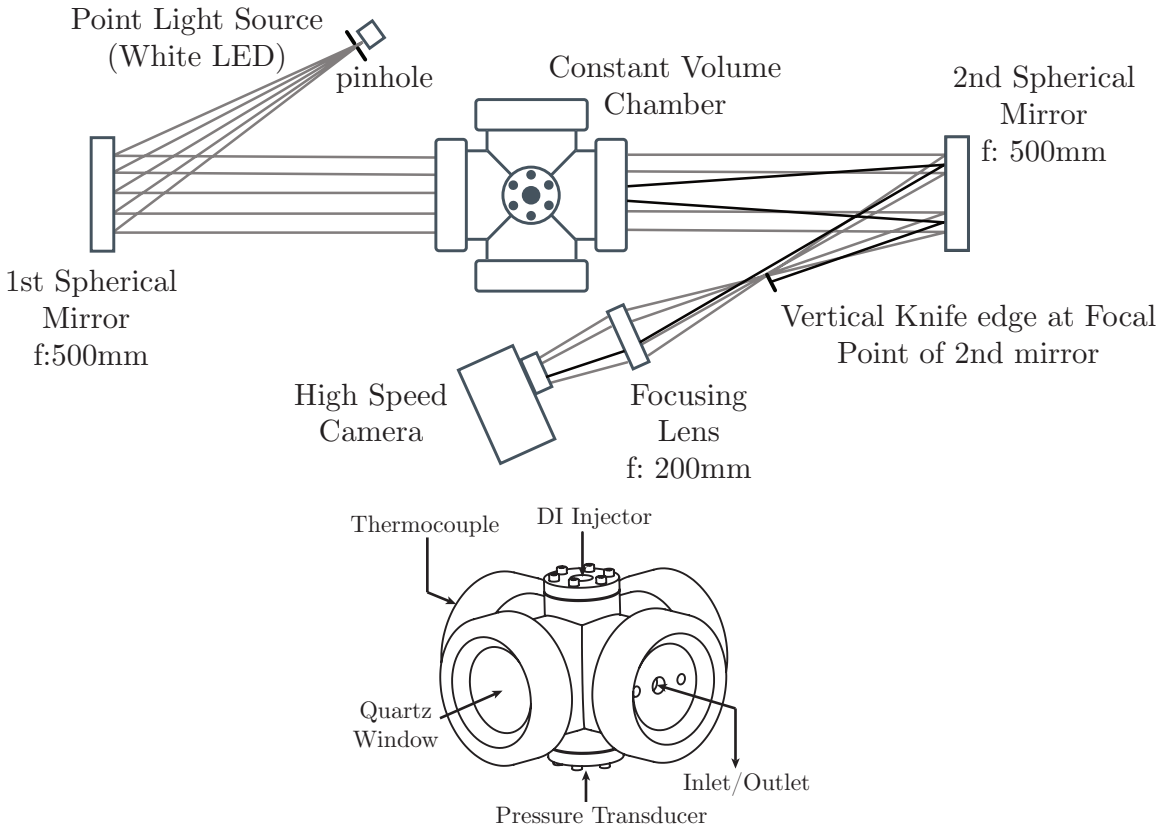

Figure 4.20: Top view of the schlieren setup (top) and instrument diagram of the constant volume chamber (bottom).

and 5 ms, respectively. The injection pressures were chosen to evaluate both sonic and subsonic flows. In addition, the chamber pressure was chosen to match the number density expected at engine conditions of approximately 40 bar at 1200 K. The spread angles and penetration depths were analyzed using an in-house image-processing code.

In the case of the high-speed schlieren experiments, the injection duration (5 ms) translated approximately into an estimated 3 mg of CH_4. The high-speed imaging results revealed that, relative to N_2 atmospheres, the penetration depth of CH_4 and H_2 jets are slightly shorter but not significantly reduced in an Ar atmosphere, as shown in figure 4.21. Reducing the injection pressure to non-choked pressure ratios across the injector yielded similar results. The lower penetration depth in Ar atmospheres seems to agree with theory that indicates that argon, being a heavier and bigger molecule, has a higher momentum dissipating effect than that of N_2.

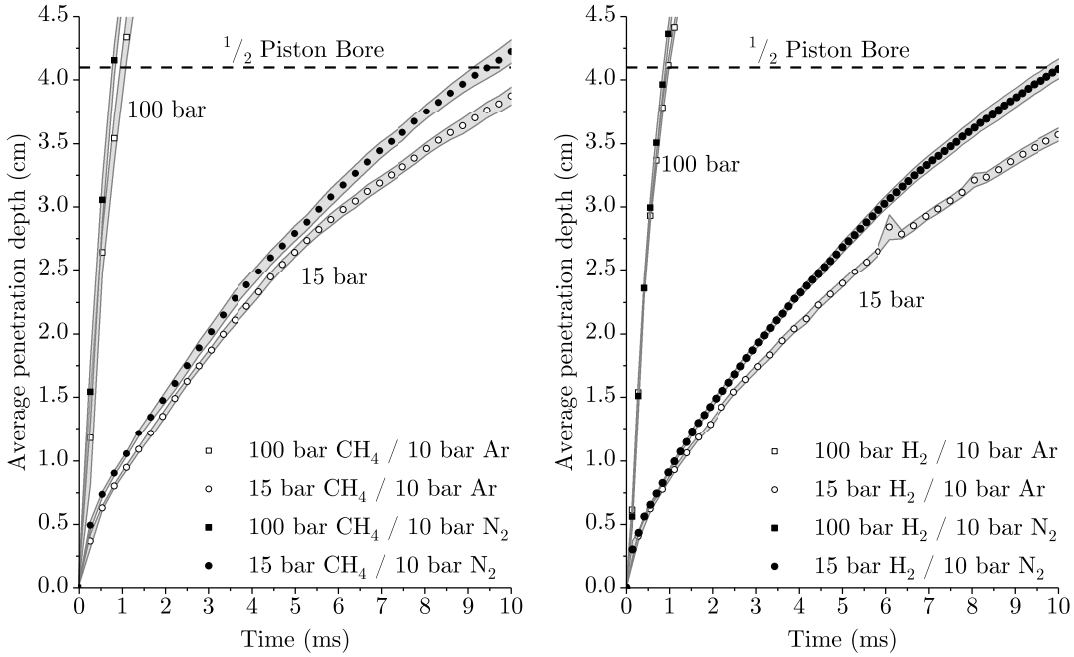

Figure 4.21: High-speed schlieren imaging results for CH_4 (left) and H_2 (right) injection at different pressures into a constant volume chamber filled with N_2 and Ar at 10 bar and 23°C.

The spread angles for CH_4, as can be seen in figure 4.22, similarly reflect little difference among the argon and nitrogen atmospheres. Nominally, a slightly wider spread angle is observed for Ar, but the uncertainties in the measured angles indicate that there is no substantial difference between the injection of CH_4 in Ar and N_2. In contrast, as seen in table 4.6, the same experiment carried out with hydrogen injection shows a more noticeable spread angle difference between Ar and N_2 atmospheres. In general, the results served as an indicator that no major difference would exist when changing the working fluid. Operating in Ar does not seem to present any added challenge which has not dealt with before with air.

Finally, the direct injector was installed on an access port located on the side of

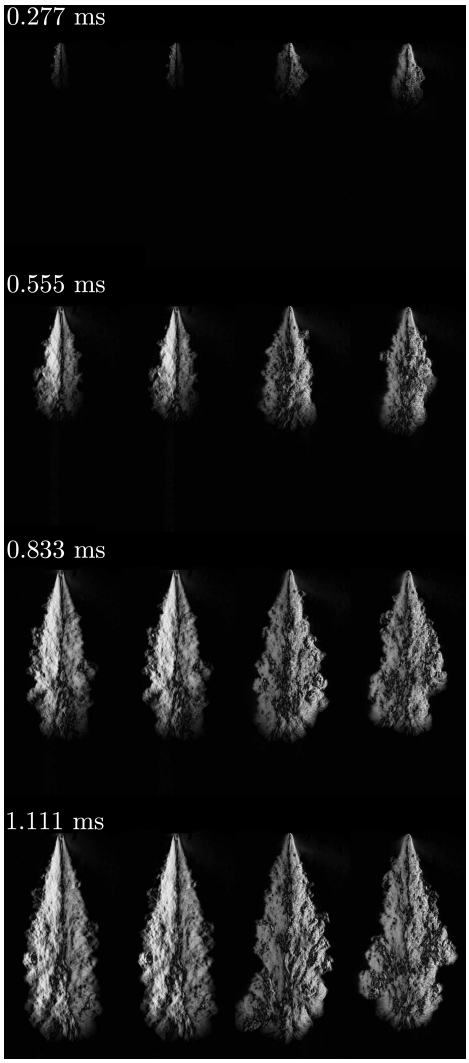

Figure 4.22: High-speed schliren imaging of CH_4 (col 1-2) and H_2 (col 3-4) jets at 100 bar into N_2(col 1-3) and Ar (col 2-4) atmospheres at 10 bar.

the engine cylinder. As can be seen in figure 4.23, the injectors seats opposite to the spark plug and horizontally oriented towards the cylinder wall, unlike more common engine designs where the injectors points toward the piston.

Results from direct injection of CH_4 in 15%O_2 at different compression ratios are plotted in figure 4.24. In this figure it can be observed how the use of direct injection provided a means to extend the operational range of compression ratios but at the cost of thermodynamic efficiency. Operation of the engine at a compression ratio of 10 was first evaluated in order to compare the potential that direct injection as oppose to port fuel injection could have on delivering better engine performance. A pressure trace and apparent heat release rate curve comparison is presented in figure 4.25. In all cases, the port fuel injection (PFI) case yielded higher thermodynamic efficiency, morover so if the energy of fuel compression would to be considered.

It can be seen how at low O_2 concentration (10%), optimum SOI is commanded

Table 4.6: Mean spread angle for CH_4 and H_2 in argon and nitrogen atmospheres. Values indicate mean and 90% confidence intervals.

Spread Angle	CH_4 (100 bar)	H_2 (100 bar)
Ar(10 bar)	26.06 ± 8.08	25 ± 3.6
N_2(10 bar)	24.58 ± 5.76	36.22 ± 2.62

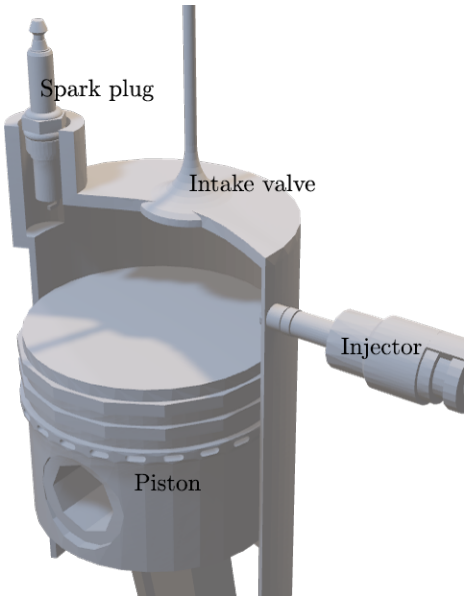

Figure 4.23: 3-Dimensional depiction of the engine cylinder with the spark plug, intake valve and direct injector in their corresponding locations.

much earlier, around 90 CAD before TDC whereas for higher O_2 content SOI is commanded later in the cycle. In all cases, spark assist was required to ignite the fuel oxygen mixture. At this specific compression ratio, the need for spark assist and early injection results in a similar behavior to PFI operation, although with worse mixing and the added cost of compression and piston work. Later injection could not be accomplished. As the fuel is injected closer to TDC, the isenthalpic expansion of CH_4 cools the gases in the chamber, preventing ignition of the charge. By the time the spark plug can be fired, more than 10 CAD after SOI, the mixture is too cold and the combustion is no longer stable. A closer look at figure 4.24 shows how for the case of 15% O_2, with later SOI, work against the piston was substantially higher. Furthermore, the heat release rate for this case was noticeable higher than for the pfi counterpart with a very pronounced gradient early after ignition and a lower but constant rate later that extend far into the expansion stroke. This behavior can be attributed to the ignition of a portion of fuel which have had time to mix during the period between SOI and IGN, and a later flame that propates as the remaining fuel continues to mix with the remaining oxygen in the chamber.

Increasing the compression ratio up to 13 still required the assistance of a spark to trigger ignition. Figure 4.26 depicts the resulting average pressure and apparent heat

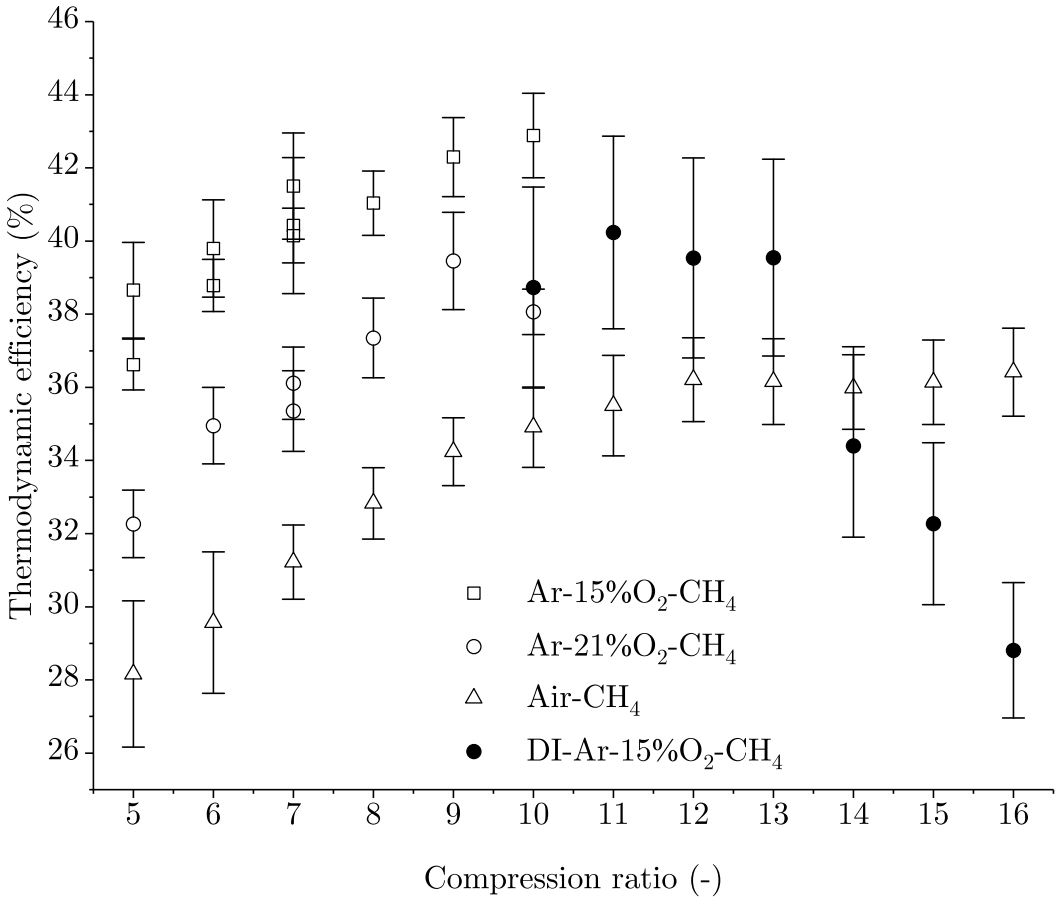

Figure 4.24: Thermodynamic efficiency comparison between the air breathing engine and argon breathing engine port and direct fuel injected with CH_4 at different compression ratios and oxygen dilutions.

release rate traces for the entire range of compression ratios. Beyond compression ratios of 13 ignition of the charge was achieved via compression ignition. While the combination of direct injection and spark assist provided a means to avoid knock, control over combustion timing and phasing was rather limited. The relatively low fuel flow rates and the need for fuel mixing forced early fuel injection. Injection during the compression stroke increases the work against the piston while simultaneously cooling the gases. If fuel is injected early enough, the cooling effect is compensated by the compression work provided to the gases. Later injection however does not provide travel for the piston to provide enough energy to the gas, ultimately preventing the fuel-oxygen mixture from igniting. A way around this issue is to make use of the spark plug inmediately after the fuel is injected, in which case the heat released from the combustion provides suficient energy to maintain the flame later on. Unfortunately, and due to the location of the spark plug relative to the injector, the spark could only be triggered once the fuel has reached the other end of the cylinder, more than 10 CAD from SOI. By then, the chamber is too cold for ignition to be maintained

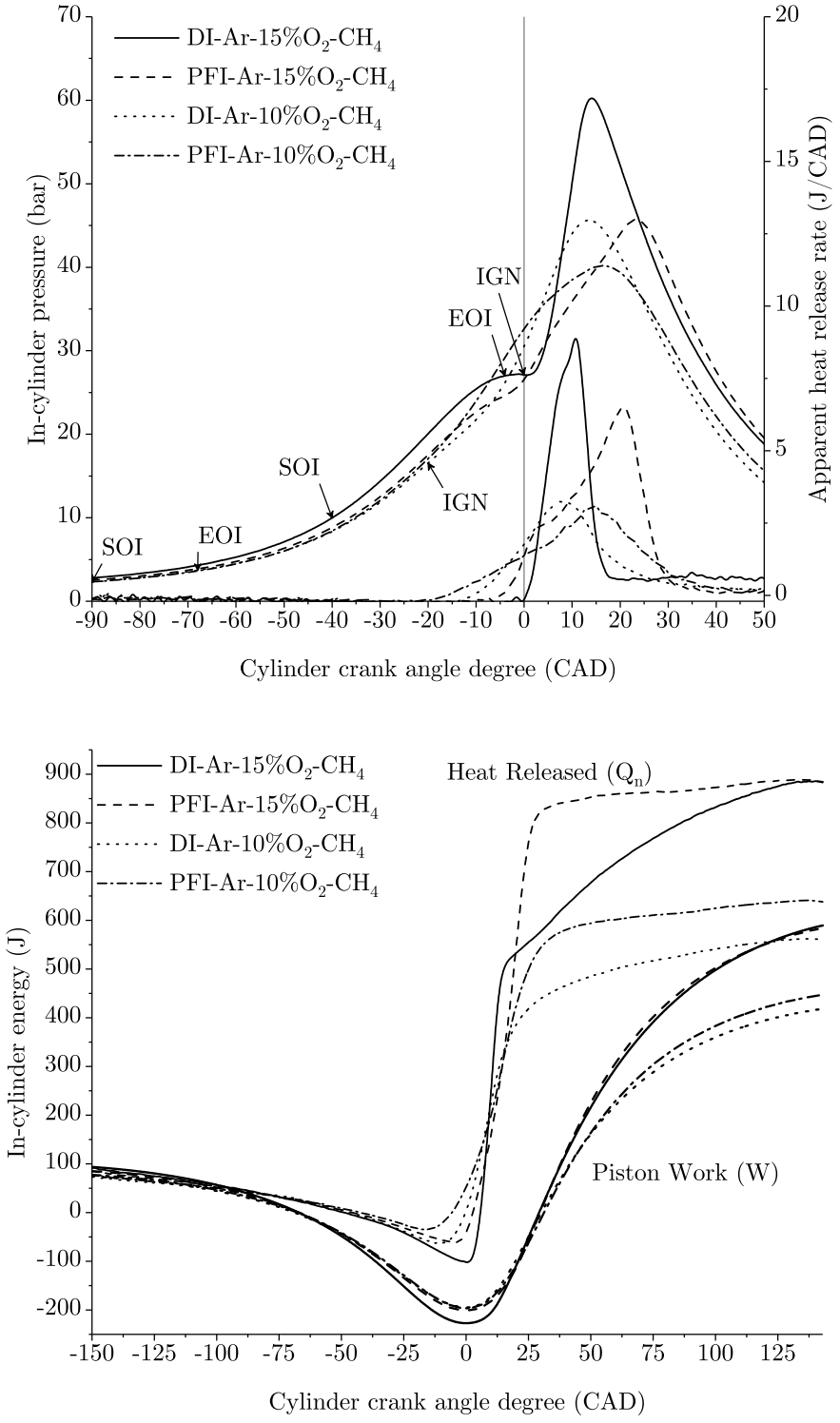

Figure 4.25: PFI and DI comparison for argon at a constant compression ratio of 10. Top: average in cylinder pressure and apparent heat release rate traces. Bottom: average cumulative apparent heat released and piston work profiles.

and only a small percentage od the fuel is consumed, with the remaining fuel leaving with the exhaust gases. Because of argon's high adiabatic index, the cooling effect is exacerbated if the injection occurs to far into the expansion stroke.

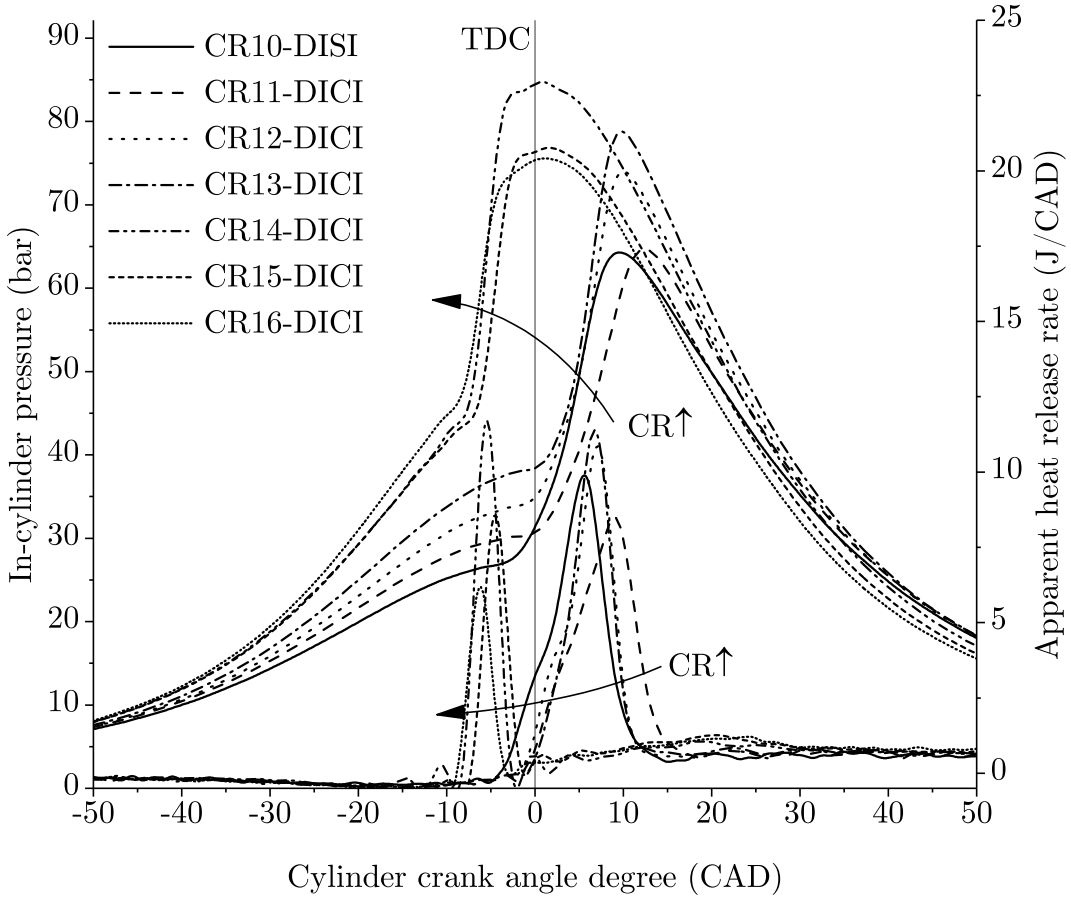

Figure 4.26: Average in cylinder pressure and apparent heat release rate traces for the argon breathing engine fed with 15% O_2 and direct injected methane at several compression ratios.

Because of the aforementioned, SOI had to be maintained relatively early preventing from realizing ideal combustion phasing. Figure 4.27 indicates the optimum SOI and IGN timing for the different compression ratios. At compression ratio of 14 and beyond the SOI was found to be a trade off between engine misfire, when SOI was pushed closer to TDC, and heavy knock if SOI was too early, in which case the engine behaved as in the port fuel injected case. No optimization at this condition could be carried out and the unfortunate geometry of the engine cylinder prevented from investigating other strategies such as spark assist.

In an effort to reduce the impact of the low fuel flow rate, the engine as operated at lamdas above 1 in order to reduce the injection duration. Figure 4.28 shows the resulting combustion phasing and thermodynamic efficiency for different lambdas at

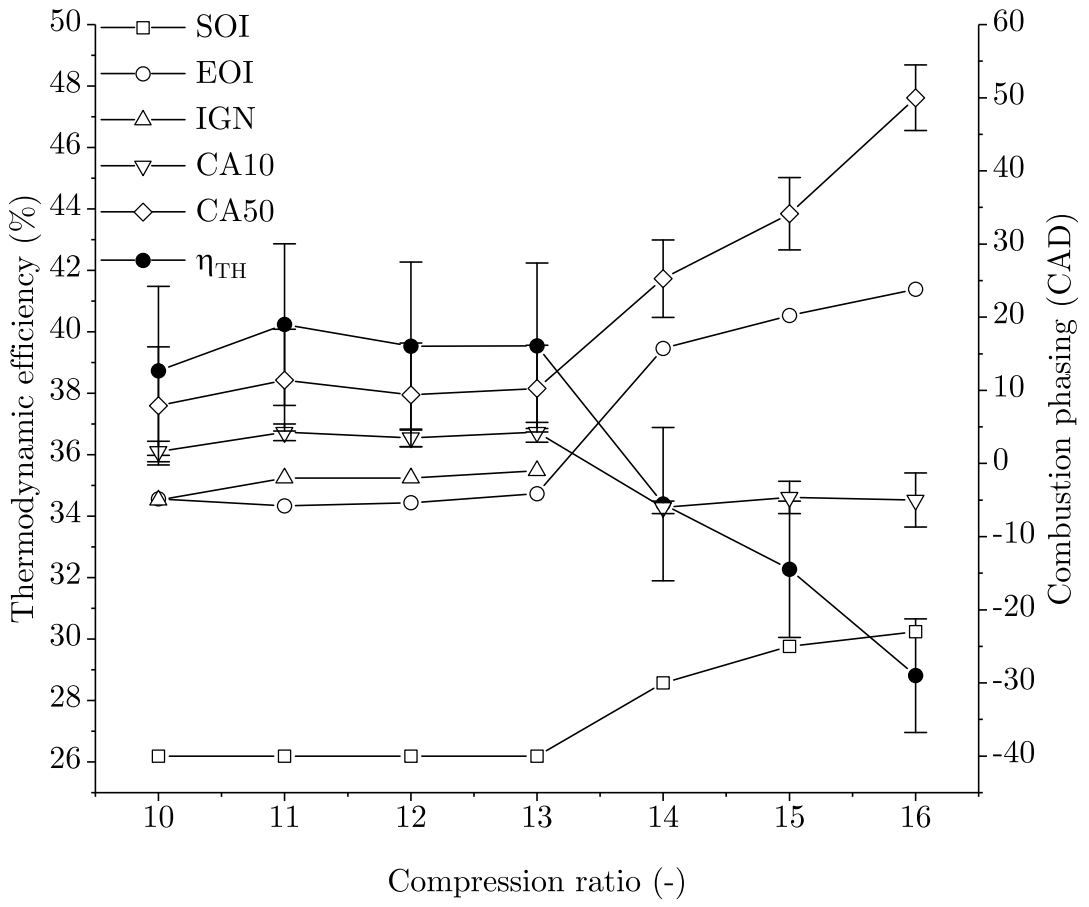

Figure 4.27: Thermodynamic efficiency and combustion phasing for the argon breathing engine fed with 15% O_2 and direct injected methane at several compression ratios.

a compression ratio of 14. SOI remained fairy constant given its optimum value was such that the cooling effect of the injection did not prevented ignition. Consequently, CA10 remained constant slightly ahead of TDC. CA50 on the other hand advanced closer to TDC although not at the same rate as EOI, indicating that the initial percentage of heat released originates from the early fuel which have had enough time to mix. Thermodynamic efficiency improves with increasing lambda, combination of lesser heat losses.

In general, direct fuel injection helped reduce the percentage of unburnt hydrocarbons (CH_4) by limiting the amount of fuel trapped in the cylinder-piston crevices (Figure 4.29). Traces of CO on the other hand sky rocketed (beyond measurable range) in comparison to PFI operation (1000-2000 ppm). This result from the combination of poor fuel mixing, and rapid cooling of the gas as it expands, which leads to localized partial fuel oxidation. Leaning the fuel mixture did not help reduce CO emissions but did noticeable reduce the traces of unburnt CH_4 in the exhaust beyond what was achieved during stoichiometric direct injection operation.

It is worth noticing how unburnt hydrocarbon remaining in the exhaust seem

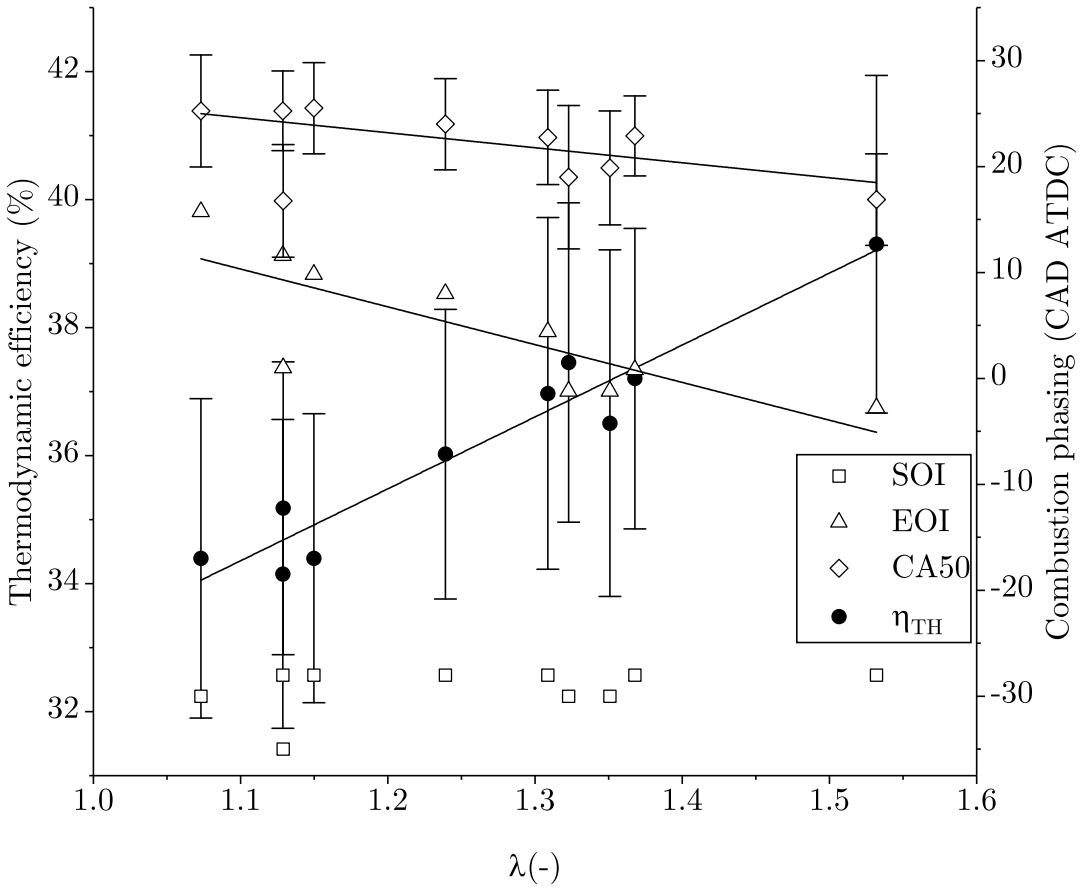

Figure 4.28: Thermodynamic efficiency and combustion phasing for the argon breathing engine fed with 15% O_2 and direct injected methane at a compression ratio of 14 and incresing fuel dilution.

to increase radically as the compression ratio increases beyond 14. The reason for this unusual increase is the location of the injector in combination with the engine configuration. Increasing the compression ratio of operation requires the engine head to be lowered, reducing the height of the combustion chamber. At the high end of compression ratio range the piston travels slightly over the injector access port, resulting in a fuel jet impinging onto the piston surface and substantially reducing the amount of oxygen entrained. Moreover, a substantial amount of fuel deposits in the piston cylinder crevice, preventing it from being consumed.

Direct injection of H_2 was also evaluated. In this case, direct injection allowed to extend the compression ratio of operation beyond 7. Operation of the engine at a compression ratio of 8 was possible. Unfortunately, the special spark plug hosting the pressure transducer broke after being subject to very high temperatures and pressure rise rates during H_2 operation at higher compression ratios. As a result, no more experiment could be carried out. Nonetheless, figure 4.30 shows the comparison between PFI and DI operation and shows the successful extension of compression

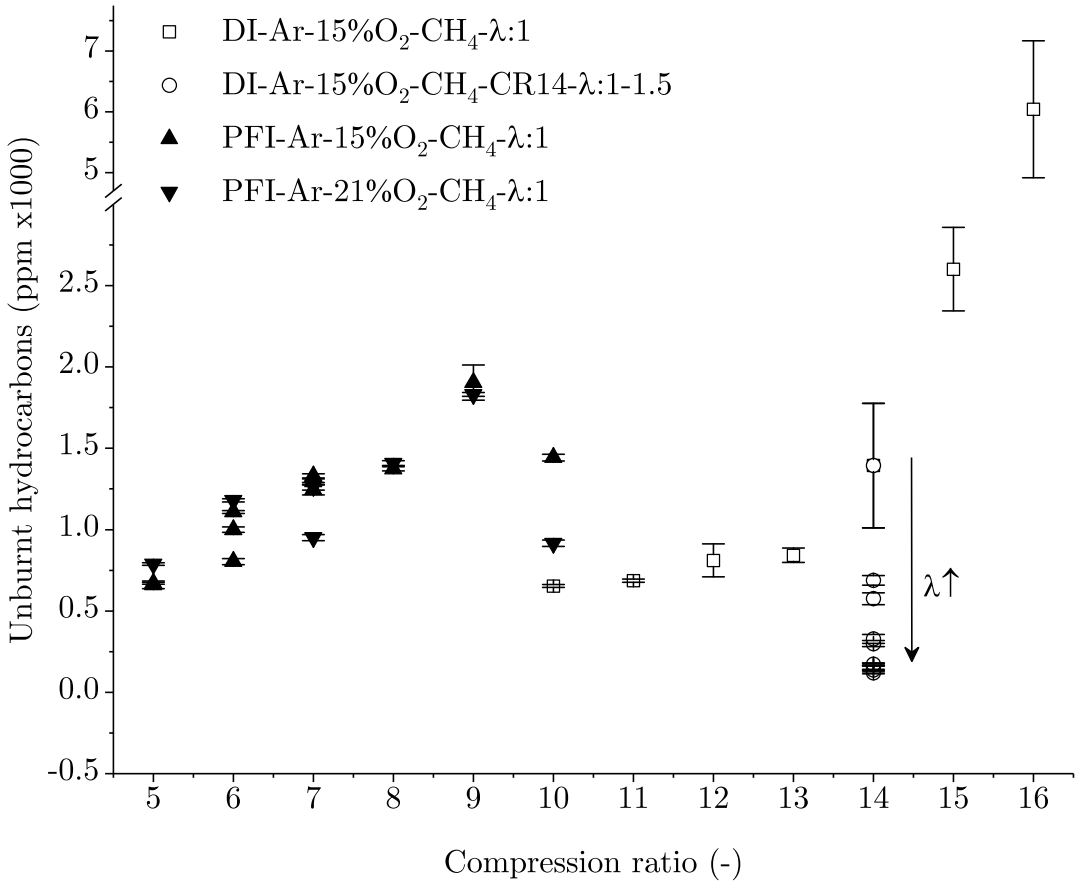

Figure 4.29: Unburnt hydrocarbon emissions for the argon breathing engine port fuel injected and direct fuel injected.

ratio with direct DI operation.

We can see how the heat release rate profile for all cases is very similar although offset by the corresponding ignition timing difference. This is indicative that compression ratio has little to no impact on the combustion duration of H_2. Although this is not truly the case, the relatively slow regime at which the engine is operated (600 rpm) allows the combustion of H_2 to take place at nearly constant volume, lending little importance to a slight increase in flame speed. It is worth mentioning that earlier ignition yielded very unstable combustion, resulting from the fact that in many cases the H_2 jet had yet not reached the spark plug or the mixture was very lean to sustain stable combustion. Unlike in the cases where the fuel was port injected, slight pressure oscillations occurred during direct injection operation. In contrast to the results obtained with CH_4, result were as expected, with a substantial increase in efficiency and consequent increase in IMEP in comparison to the previous cases at lower compression ratios. Results are shown in table 4.7.

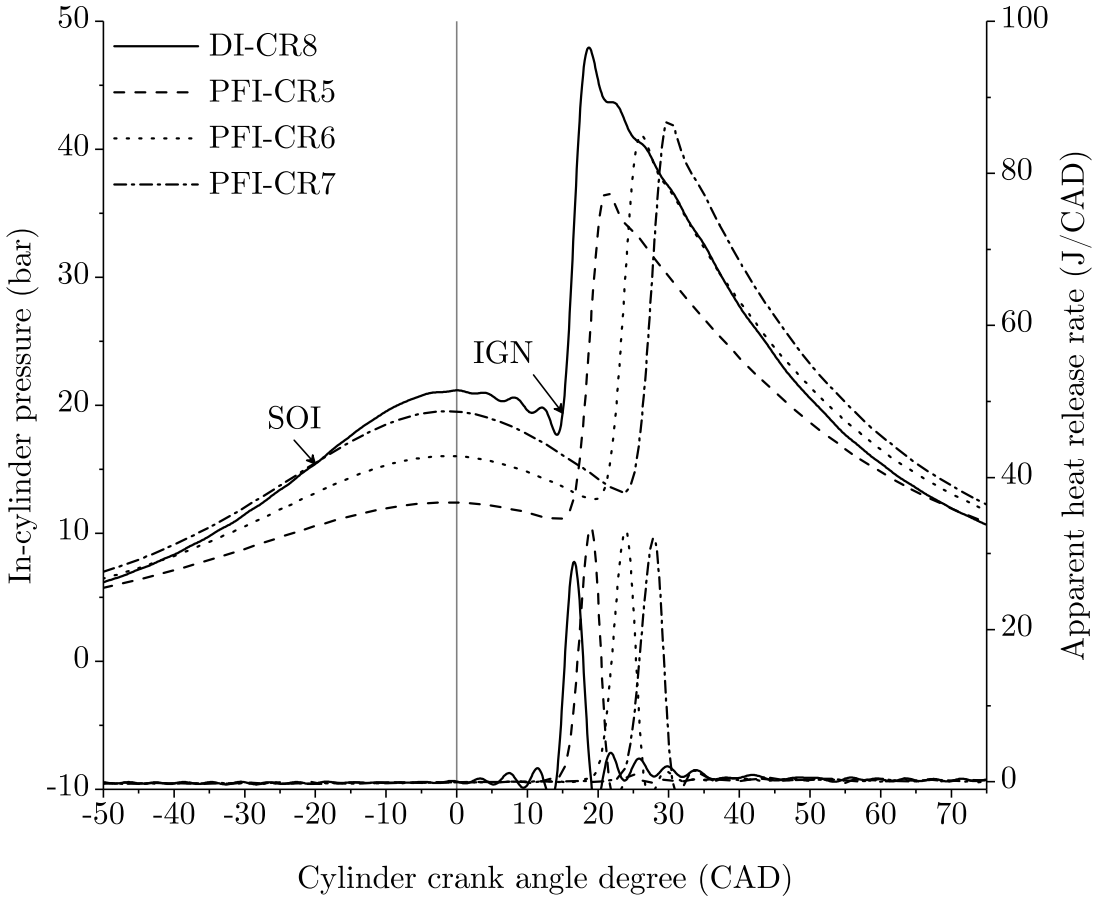

Figure 4.30: Average in cylinder pressure and apparent heat release rate traces for the argon breathing engine fed with 15% O_2 and H_2 at several compression ratios.

Table 4.7: General results from direct injection of H_2 at a compression ratio of 8 and 15% O_2

IGN	CA10	CA50	IMEP	η_{TH}	Exh. Temp
15	16±0.3	17.8±0.5	8.7±0.1	34.5±1.7	575±2

4.2.3 Carbon dioxide breathing engine operation

Carbon dioxide, as introduced in chapter 2, is another promising working fluid for zero emission power systems. Using CO_2 eliminates the need to perform exhaust gas separation, often the most energy intensive process of the entire plant, rendering cost effective zero emission power plants. Nevertheless, the use of such working fluid for RICE platforms do not theoretically yield very good results due to the low heat capacity ratio of CO_2. In addition, the overall cycle temperatures are expected to be lower than for working fluids such as N_2 or Ar, hindering the flame propagation speed and consequently constraining the optimization of combustion phasing. For this reason, a synthetic mixture of 50% CO and 50% H_2 (SYNGAS) was used, so that the high reaction rate of hydrogen would compensate for the lower in cylinder temperatures.

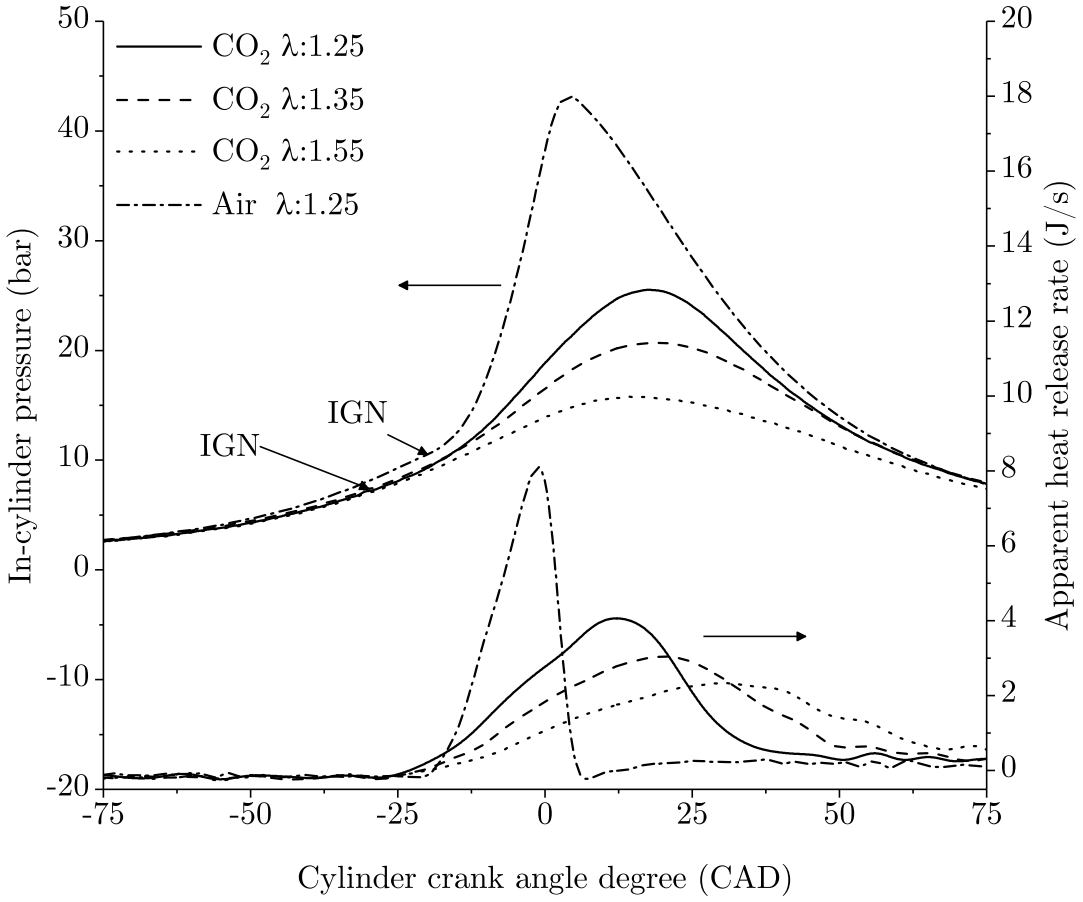

Figure 4.31: Average pressure and heat release rate traces for SYN-GAS in air and CO_2 working fluids.

Figure 4.31 shows the average pressure traces for air and CO_2. In this figure we can observe how the peak pressure reached while using CO_2 is substantially lower than when using air. Similarly, the heat release rates are much lower for the CO_2

case prolonging the combustion duration far into the expansion stroke.

These results substantiate the aforementioned expectation of lower flame propagation speeds. A closer look at the estimated average in-cylinder temperature (figure 4.32) shows how in-cylinder temperatures are higher for the air case although the exhaust gases after combustion remain hotter for the CO_2 case. This is the consequence of lower energy extracted by the piston and thus more energy remains in the exhaust gas. In the case of air, the relatively fast cool down of the exhaust gas is a combination of the energy being transferred to the piston and the heat loss to the cylinder walls.

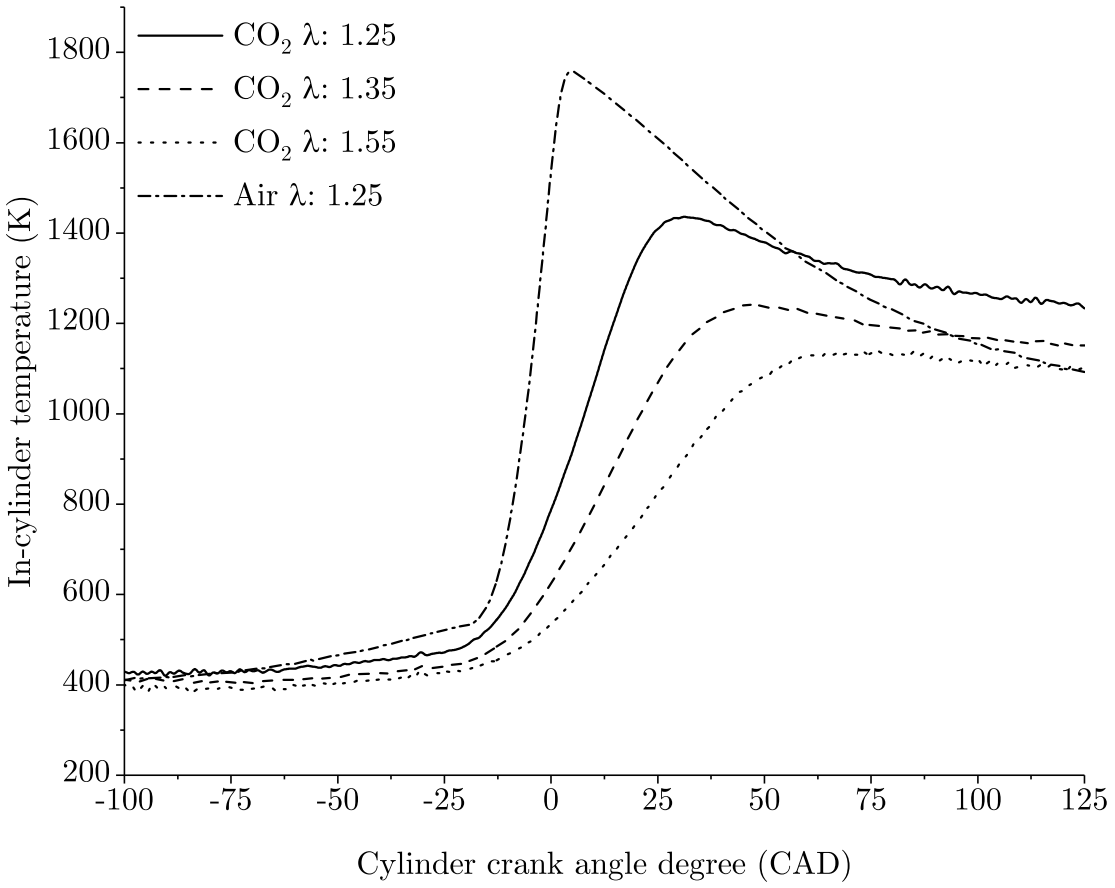

Figure 4.32: Estimated average in-cylinder temperature for SYN-GAS in air and CO_2 working fluids.

Figure 4.33 shows the resulting average fuel energy within the cylinder, the cumulative apparent heat released and the cumulative piston work as introduced previously in figure 4.5. We can see how, although the piston work is highest for the air case, the heat losses to the cylinder walls is highest. On the contrary, for the CO_2 the energy remaining on the exhaust gas is substantially higher, indicative of lower piston work but most importantly of substantially lower heat losses. This is due to the overall lower thermal conductivity of CO_2 and lower peak in cylinder temperatures.

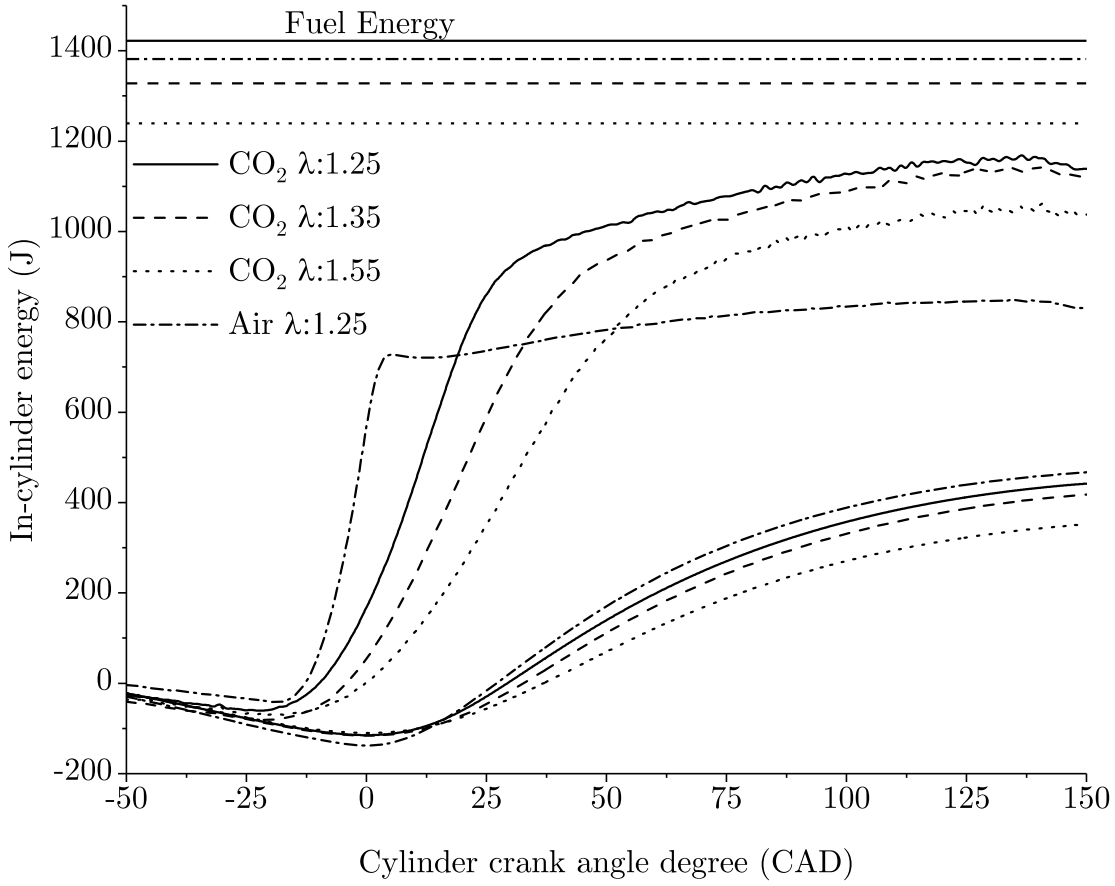

Figure 4.33: In-cylinder cumulative energy as a function of crank angle. The different forms of energy shown are fuel energy, gas internal energy and piston work.

In depth analysis of the cumulative heat released for different cases indicates noticeable longer combustion duration when operating on CO_2. We can observe in figure 4.34 how the period from ignition to CA10 and CA10 to CA50 is noticeable longer for CO_2 in comparison to the air cases. Furthermore, as the mixture is leaned further, the period between CA10 and CA50 seems to increase almost linearly and faster relative to the air case, where the period CA10-CA50 grows slightly. This is the compound result of lower fuel concentration but more importantly, of lower temperatures, causing the ignition delay to increase and the reaction rates to decrease. It is trivial to conclude that the higher susceptibility of the CO_2 cycle to fuel lean conditions is primarily due to the higher molar heat capacity at constant volume of CO_2. Consequently, one could expect the combustion phasing for the argon breathing engine to be less sensitive to the fuel leaning conditions, allowing for further dilution levels which could not be achieved otherwise with N_2 or CO_2.

Overall, results showed lower thermodynamic efficiency for the CO_2 driven mainly by extremely long heat release event, far from an isochoric heat addition. Figure 4.34 also shows the resulting thermodynamic efficiency for the air and CO_2 cases at

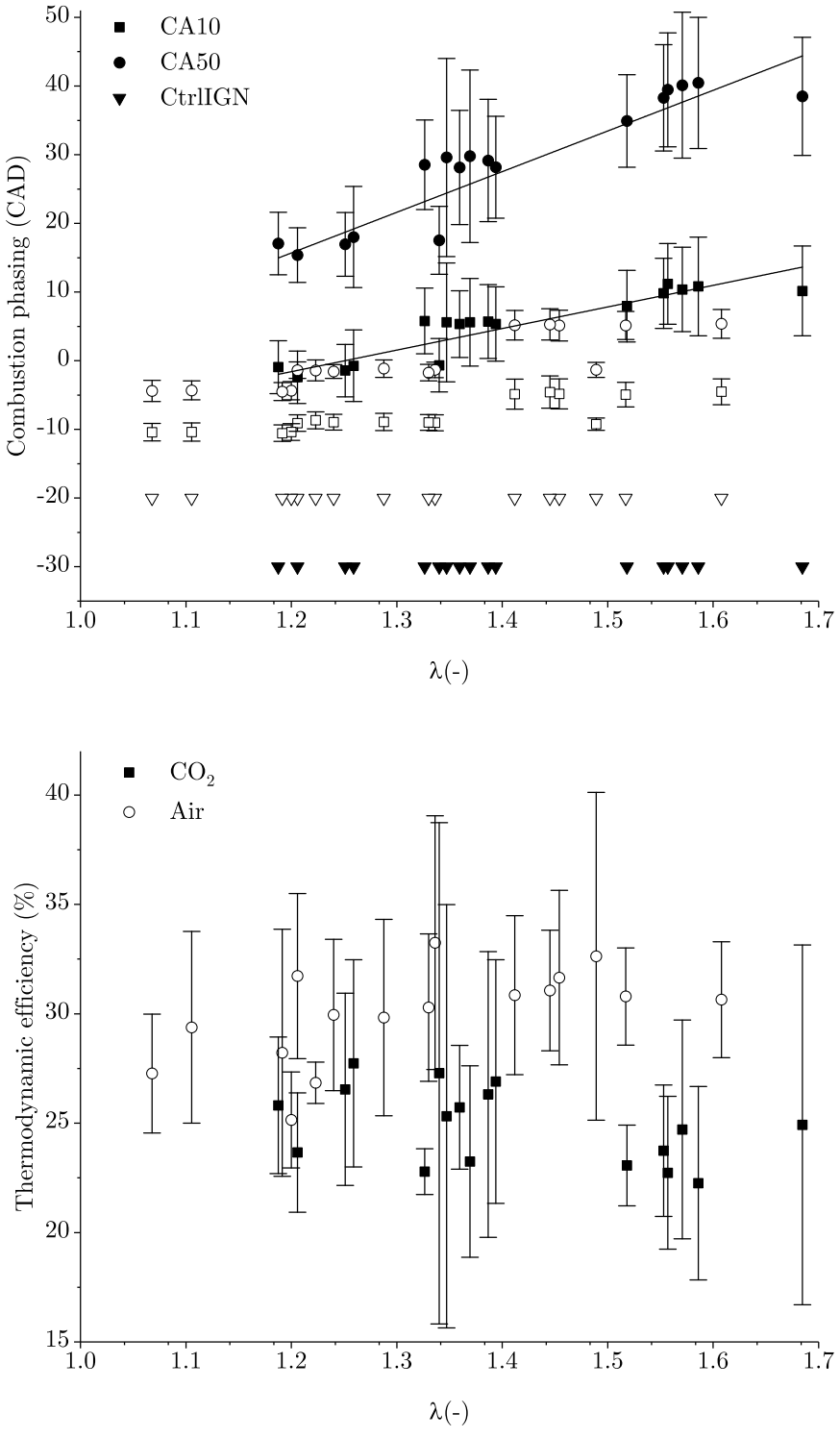

Figure 4.34: Influence of lambda on the combustion phasing (top) and thermodynamic efficiency (bottom) of the air and CO_2 breathing engines fueled with SYNGAS.

different λ. It is worth noticing how in the air case, the efficiency increases with increasingly lean mixtures, result of lower heat losses to the cylinder walls, while for the CO_2 case efficiency drops due to increasingly longer combustion duration and poor combustion phasing.

4.3 Summary

Along this chapter the different experimental results have been presented together with a brief discussion of the experimental setup and data processing methods. In general few conclusion can be drawn:

1. Operation of the engine with Ar yielded higher efficiency regarless of the fuel being used.

2. Increasing Ar content yield higher efficiency although limited by the level of dilution the flame can reasonable withstand. At low compression ratios, operation of 90% Ar was not possible due to the combination of low temperature and concentrations.

3. Using Ar as the working fluid reduces the combustion duration due to higher combustion temperatures and supports higher heat release rates.

4. Operation of Ar with as low as 10% O_2 was possible at sufficiently high compression ratios given that the increase in gas temperatures compensates for the highly diluted fuel-oxygen mixture.

5. Emissions of CO_2 in a kWh basis are reduced as a result of better efficiency, and emissions of NOx are eliminated. Emission of CO and unburnt fuel does not seem to be particularly affected by the use of either working fluids.

6. The use of direct injection strategies extends the compression ratio range of operation but optimum injection schemes are required to provide appropriate injection flow rates and mixing behavior. In lack of the later, emissions of CO increase radically as a result of partial mixing and rapid cooling of the Ar gas.

7. In the case of H_2, use of direct injection strategies did result in higher efficiency, but not a sufficient increse to compensate for the compression cost of H_2.

Chapter 5

Conclusions and recommendations

In this chapter, a brief summary of the conclusions drawn from this work is given. Moreover, some recommendations and suggestion for future research in this topic are also given.

5.1 Conclusions

The results of the numerical and experimental work hereby presented have proven there is potential for the APC to improve the efficiency and reduce emission of the RICE. Several conclusion has been drawn:

- Theory and experiments have shown that the use of argon as the working fluid substantially improves the thermodynamic efficiency of the reciprocating engine by as much as 30% over its air breathing counterpart.
- The combination of higher thermodynamic efficiency and the higher c_p of argon gas results in lower gas temperatures during the expansion stroke compared to the air case. As a consequence, the temperature gradient across the engine cylinder walls is reduced, which together with the lower thermal conductivity of argon results in lower heat losses. Being able to benefit from this occurrence seems conditioned to achieving optimum combustion phasing given the substantially higher combustion temperatures reached with argon.
- Stable and knock free operation with argon was achieved with port injected methane up to a compression ratio of 10, whereas with air the engine could operate at a compression ratio as high as 16. it is foreseen that when using common natural gas, which contains some percentage of ethane, knock will occur at lower compression ratios. In the case of hydrogen, the use of argon was limited to compression ratios below 7 resulting on really aggressive knock beyond that point.
- Combustion duration was reduced with argon, driven mainly by higher temperatures. The fastest combustion was achieved with argon and 21% O_2 due to a combination of higher temperature and O_2 concentration. The highest

efficiency however was reached with the lowest O_2 concentration (10%). Unlike combustion duration, the optimum combustion phasing (CA50) remained nearly constant around crank angles of 20±5 CAD irregardless of working fluid or compression ratio.

- The use of argon did not reduce the power density of the engine. In most cases, best exemplified by the 15% O_2, the engine load was higher than that of the air breathing engine. This was due to efficiency gains supporting a net increase in power output despite the reduction in fuel injected. Therefore, it can be concluded that the conversion of an air aspirated RICEs to the APC would yield equivalent or in some cases higher power densities at a higher efficiency.

- In terms of emissions, results from port fuel injection operation did not yield major changes between the air and argon cases beyond the obviously expected. CO_2 was reduced in a per kWh basis because of the higher efficiency achieved and NOx was eliminated due to the high purity of both the working fluid and fuel. Traces of UHC and CO did not show a noticeable difference between the two working fluids.

- In an effort to further expand the compression ratio range of engine operation, direct fuel injection was implemented allowing to expand on the operation range of H_2 and providing better combustion phasing. For the CH_4 however, the use of direct fuel injection yielded substantially lower thermodynamic efficiency, driven mainly by an increase in the combustion duration and a limited combustion phasing range constrained by the cooling and subsequent quenching of the charge due to the Joule-Thompson effect. Late injection, at or after TDC, resulted in really unstable combustion, misfires and very low indicated efficiency.

- Some of the challenges faced during direct fuel injection can be attributed to the location of the spark plug and the injector, showcasing the importance of optimum combustion chamber design. The injector's orifice was not optimum for the flow rates required, limiting the mixing rate and ultimately the heat release rate.

- Qualitative analysis of the gaseous jet in N_2 and Ar atmospheres indicated that no major difference exist on penetration depth or spread angle as theoretically assumed. This confirms that conventional gaseous injector development efforts are valid for argon based atmospheres. No effort was made to evaluate the surrounding gas entertainment into the fuel jet due to the lack of experimental resources.

- Use of direct injection for CH_4 yielded very high traces of CO, reinforcing the assumption of poor fuel and oxygen mixing.

- The use of CO_2 as a working fluid yielded lower thermodynamic efficiency as a result of CO_2 lower adiabatic index. Peak pressures and temperatures were

substantially lower than for the air case reducing the heat release rates and heat losses to the walls. These experiments indicate that controlled recirculation of CO_2 with argon may help reduce the heat release rate, specially useful when operating with hydrogen fuel.

- In terms of the APC feasibility, as much as an estimated 4% argon can be effectively brought in with the O_2 from a cryogenic air separation unit at an estimated energy cost of 200 kWh/tO_2, representing 6% absolute penalty over the efficiency of the plant. Numerical simulation of industrial polymeric membranes rendered a CO_2 separation system consuming as low as 2% of the LHV of the fuel if the system is operated at sufficient pressure and levels of CO_2 recirculation.

- The purity of the captured CO_2 fell above 95% for a wide range of CO_2 recirculation and pressure levels. This is the minimum purity allowed for pipeline standards. CO_2 purities as low as 92% are still feasible given a 4% make up argon stream coming together with the oxygen supply.

5.2 Recommendation

The work presented in this dissertation had the goal to discover the potential of the APC as a flexible, clean and efficient platform for power generation. Nevertheless, much of the pressing question regarding the feasibility of this cycle remain undressed. There is yet plenty of work needed to turn the APC from a concept to reality. A short list of such issues are presented below:

- Preliminary results of this work indicate that the balance of argon flowing through system is net positive. However, a deeper look at the systems indicates that argon leaking through the piston-cylinder interface may pose a feasibility challenge requiring the pressurization of the engine's crank case or the re-compression of the crankcase gases. Future studies need to prove or find ways in which the argon balance remain net positive.

- Direct injection strategies have proven effective in preventing knock at high compression ratios. However, optimization of such strategies is required to compensate for the cost of fuel compression. A combination of direct injection with pre-chamber have the potential to reduce the need for high fuel pressure while allowing knock free operation.

- Natural gas and hydrogen lend themselves beautifully to the application of the APC due to their low tendencies to generate soot. Operation of the APC with common fuels such as diesel may, unless great combustion optimization is achieved, not be feasible due to the quick clogging of the membrane unit and fouling of the condenser tubes. Experimental investigation of diesel combustion in APC like environments would discover the potential for the APC to be reliably retrofitted in transportation applications, where fuel density is crucial.

- While operating the APC at a higher nominal pressure than conventional cycles comes at no evident cost to the system, compression of the oxygen and fuel to cycle pressures adds to the list of parasitic losses that need to be compensated. Analysis and discovery of all parasitic losses the APC may be subject to is key to precisely carry out a feasibility analysis of this technology.

- RICEs are known for their flexibility, able to ramp their load up and down at the leisure of its operator. Maintaining this great feature when operating the APC requires the development of sophisticated controls that enable flexible operation of the membrane and condenser units while the flow, pressure and gas composition changes. Regardless of the level of sophistication of the control system, the change in operating conditions will results in different membrane and condenser performance, hurting more or less the efficiency of the system during transient operation. Future study of transient operation is recommended to bring this technology into the field.

- With the use of pipeline fuels and oxygen from air, it is certain that traces of foreign components such as N_2 will find their way into the cycle. Figuring out ways to prevent their accumulation is an issue to be addressed before a full size demonstration is to be built.

With all the above in mind the author of this work follows a path to entrepreneurship to continue the work started here and tackle the challenges that prevent the APC from reaching the power sector. The APC could be a power solution that awakens gigawatts of standby RICEs to provide the world with the flexible and clean capacity it so much demands, while transitioning towards a 100% renewable energy landscape.

Bibliography

[1] J.-B. J. Fourier, "Remarques Générales Sur Les Températures Du Globe Terrestre Et Des Espaces Planétaires.," *Annales de Chimie et de Physique*, vol. 27, pp. 136 – 167, 1824.

[2] E. Burgess, "General Remarks on the Temperature of the Terrestrial Globe and the Planetary Spaces; by Baron Fourier.," *American Journal of Science*, vol. 32, pp. 1–20, 1837.

[3] J. Tyndall, "The Bakerian Lecture: On the Absorption and Radiation of Heat by Gases and Vapours, and on the Physical Connexion of Radiation, Absorption, and Conduction," *Philosophical Transactions of the Royal Society of London*, vol. 151, pp. 1–36, 1861.

[4] S. Arrhenius, "On the Influence of Carbonic Acid in the Air upon the Temperature of the Ground," *Philosophical Magazine and Journal of Science*, vol. 41, no. 5, pp. 237–276, 1896.

[5] S. R. Weart, *The discovery of global warming*. Harvard University Press, 2 ed., 2008.

[6] UNTC, "7.d Paris Agreement," in *United Nations Treaty Collection*, ch. XXVII ENVI, Paris: United Nations, 2015.

[7] Intergovernmental Panel on Climate Change (IPCC), "Climate Change 2014 Synthesis report," tech. rep., IPCC, 2014.

[8] D. Lüthi, M. Le Floch, B. Bereiter, T. Blunier, J.-M. Barnola, U. Siegenthaler, D. Raynaud, J. Jouzel, H. Fischer, K. Kawamura, and T. F. Stocker, "High-resolution carbon dioxide concentration record 650,000800,000years before present," *Nature*, vol. 453, pp. 379–382, may 2008.

[9] D. Etheridge, L. Steele, R. Langenfelds, R. Francey, J.-M. Barnola, and V. Morgan., "Historical CO2 records from the Law Dome DE08, DE08-2, and DSS ice cores. In: Trends: A compendium of data on global change.," tech. rep., Carbon Dioxide Information Analysis Center, Oak Ridge National Laboratory, U.S. Department of Energy, Oak Ridge, Tenn., U.S.A., 1998.

[10] A. Neftel, H. Friedli, E. Moor, H. Lötscher, H. Oeschger, U. Siegenthaler, and B. Stauffer., "Historical CO2 record from the Siple Station ice core. In Trends: A Compendium of Data on Global Change.," tech. rep., Carbon Dioxide Information Analysis Center, Oak Ridge National Laboratory, U.S. Department of Energy, Oak Ridge, Tenn., U.S.A., 1994.

[11] P. Tans and R. Keeling, "Annual mean carbon dioxide concentrations for Mauna Loa, Hawaii.," tech. rep., National Oceanic and Atmospheric Administration and Scripps Institution of Oceanography, 2017.

[12] P. Tans and R. Keeling, "Monthly mean carbon dioxide concentrations for Barrow, Alaska; Cape Matatula, American Samoa; and the South Pole," tech. rep., National Oceanic and Atmospheric Administration and Scripps Institution of Oceanography, 2017.

[13] L. Steele, P. Krummel, and R. Langenfelds, "Atmospheric CO2 concentrations (ppmv) derived from flask air samples collected at Cape Grim, Australia, and Shetland Islands, Scotland.," tech. rep., Commonwealth Scientific and Industrial Research Organisation(CSIRO)., 2007.

[14] P. Chamard, L. Ciattaglia, A. di Sarra, and F. Monteleone, "Atmospheric carbon dioxide record from flask measurements at Lampedusa Island. In: Trends: A compendium of data on global change.," tech. rep., Carbon Dioxide Information Analysis Center, Oak Ridge National Laboratory, U.S. Department of Energy, Oak Ridge, Tenn., U.S.A., 2001.

[15] L. Loulergue, A. Schilt, R. Spahni, V. Masson-Delmotte, T. Blunier, B. Lemieux, J.-M. Barnola, D. Raynaud, T. F. Stocker, and J. Chappellaz, "Orbital and millennial-scale features of atmospheric CH4 over the past 800,000years," *Nature*, vol. 453, pp. 383–386, may 2008.

[16] D. Etheridge, L. Steele, R. Francey, and R. Langenfelds, "Historical CH4 Records Since About 1000 A.D. From Ice Core Data. In Trends: A Compendium of Data on Global Change.," tech. rep., Carbon Dioxide Information Analysis Center, Oak Ridge National Laboratory, U.S. Department of Energy, Oak Ridge, Tenn., U.S.A., 2002.

[17] P. Tans and R. Keeling, "Monthly mean CH4 concentrations for Cape Grim, Australia.," tech. rep., National Oceanic and Atmospheric Administration and Scripps Institution of Oceanography, 2017.

[18] P. Tans and R. Keeling, "Monthly mean CH4 concentrations for Mauna Loa, Hawaii.," tech. rep., National Oceanic and Atmospheric Administration and Scripps Institution of Oceanography, 2017.

[19] L. Steele, P. Krummel, and R. Langenfelds, "Atmospheric methane record from Shetland Islands, Scotland (October 2002 version). In: Trends: A compendium

of data on global change.," tech. rep., Carbon Dioxide Information Analysis Center, Oak Ridge National Laboratory, U.S. Department of Energy, Oak Ridge, Tenn., U.S.A., 2002.

[20] M. Battle, M. Bender, T. Sowers, P. P. Tans, J. H. Butler, J. W. Elkins, J. T. Ellis, T. Conway, N. Zhang, P. Lang, and A. D. Clarket, "Atmospheric gas concentrations over the past century measured in air from firn at the South Pole," *Nature*, vol. 383, pp. 231–235, sep 1996.

[21] A. Schilt, M. Baumgartner, T. Blunier, J. Schwander, R. Spahni, and T. F. Stocker, "Glacialinterglacial and millennial-scale variations in the atmospheric nitrous oxide concentration during the last 800,000 years," *Quaternary Science Reviews*, vol. 29, pp. 182–192, jan 2010.

[22] Commonwealth Scientific and Industrial Research Organisation (CSIRO), "Monthly mean N2O concentrations for Cape Grim, Australia.," tech. rep., Commonwealth Scientific and Industrial Research Organisation (CSIRO), 2017.

[23] International Energy Agency (IEA), "CO2 Emissions from Fuel Combustion 2016," tech. rep., International Energy Agency, oct 2016.

[24] World Resources Institute (WRI), "CAIT Climate Data Explorer.," 2015.

[25] British Petroleum (BP), "BP Energy Outlook 2017," tech. rep., British Petroleum, 2017.

[26] U.S. Energy Information Administration (EIA), "International Energy Outlook 2016: With Projections to 2040," tech. rep., U.S. Energy Information Administration, 2016.

[27] International Energy Agency (IEA), "World Energy Outlook 2016," tech. rep., International Energy Agency, nov 2016.

[28] ExxonMobil, "2017 Outlook for Energy: A View to 2040," tech. rep., ExxonMobil, 2017.

[29] Food and Agriculture Organization of the United Nations (FAO), "The future of food and agriculture : trends and challenges," tech. rep., FAO, 2017.

[30] The World Bank, "World Development Indicators," tech. rep., The World Bank, Washington DC, 2017.

[31] International Monetary Fund, "World Economic Outlook, April 2017: Gaining Momentum?," tech. rep., International Monetary Fund, 2017.

[32] A. Crimmins, J. Balbus, J. Gamble, C. Beard, J. Bell, D. Dodgen, R. Eisen, N. Fann, M. Hawkins, S. Herring, L. Jantarasami, D. Mills, S. Saha, M. Sarofim, J. Trtanj, and L. Ziska, "The Impacts of Climate Change on Human Health in the United States: A Scientific Assessment.," tech. rep., U.S. Global Change Research Program, Washington, DC, 2016.

[33] E. Massetti, M. A. Brown, M. Lapsa, I. Sharma, J. Bradbury, C. Cunliff, and Y. Li, "Environmental Quality and the U.S. Power Sector: Air Quality, Water Quality, Land Use and Environmental Justice," tech. rep., OAK RIDGE NATIONAL LABORATORY, Oak Ridge, 2017.

[34] T. B. Ryerson, M. Trainer, J. S. Holloway, D. D. Parrish, L. G. Huey, D. T. Sueper, G. J. Frost, S. G. Donnelly, S. Schauffler, E. L. Atlas, W. C. Kuster, P. D. Goldan, G. Hübler, J. F. Meagher, and F. C. Fehsenfeld, "Observations of Ozone Formation in Power Plant Plumes and Implications for Ozone Control Strategies," *Science*, vol. 292, no. 5517, 2001.

[35] OECD, "OECD Environmental Outlook to 2050: The Consequences of Inaction.," tech. rep., OECD, mar 2012.

[36] International Energy Agency (IEA), "World Energy Statistics 2017," tech. rep., International Energy Agency, aug 2017.

[37] U.S. Environmental Protection Agency, "Climate Change Indicators in the United States, 2016," tech. rep., EPA, 2016.

[38] J. Edmonds, T. Wilson, M. Wise, and J. Weyant, "Electrification of the economy and CO2 emissions mitigation," *Environmental Economics and Policy Studies*, vol. 7, pp. 175–203, sep 2006.

[39] J. H. Williams, A. DeBenedictis, R. Ghanadan, A. Mahone, J. Moore, W. R. Morrow, S. Price, and M. S. Torn, "The Technology Path to Deep Greenhouse Gas Emissions Cuts by 2050: The Pivotal Role of Electricity," *Science*, vol. 335, no. 6064, 2012.

[40] S. Strunz, E. Gawel, P. Lehmann, T. Ribera, A. Rüdinger, R. Boscheck, C. Egenhofer, and J. de Jong, "Energy policy: European, national, regional?," *Intereconomics*, vol. 49, pp. 244–267, sep 2014.

[41] U.S. Energy Information Administration (EIA), "International Energy Outlook 2017," tech. rep., U.S. Energy Information Administration, 2017.

[42] U.S. Energy Information Administration (EIA), "Annual Energy Outlook 2017 with projections to 2050," tech. rep., Energy Information Administration, U.S. Departmet of Energy, 2017.

[43] M. Milligan, E. Ela, J. Hein, T. Schneider, G. Brinkman, and P. Denholm, "Exploration of HighPenetration Renewable Electricity Futures. Vol. 4 of Renewable Electricity Futures Study," tech. rep., National Renewable Energy Laboratory, Golden, CO, 2012.

[44] California Independent System Operator (CAISO), "Production and Curtailments Data (May 1,2014 - September 30, 2017)," tech. rep., California Independent System Operator, Folsom, CA 95630, 2017.

[45] The California energy comission, "California Energy Commission Tracking Progress Renewable Energy Overview," tech. rep., California Energy Commission, Sacramento, 2017.

[46] Utility Dive, "2017 State of the Electric Utility Survey Report," tech. rep., Utility Dive, 2017.

[47] A. Ulbig, T. S. Borsche, and G. Andersson, "Impact of Low Rotational Inertia on Power System Stability and Operation," *IFAC Proceedings Volumes*, vol. 47, pp. 7290–7297, dec 2014.

[48] J. Mathias, C. Doughty, and L. Kelly, "Bulk Energy Storage in California," tech. rep., California Energy Commission, Sacramento, 2016.

[49] California Public Utilities Commission, "AB 2514 Energy Storage System Procurement Targets from Publicly Owned Utilities," 2013.

[50] M. S. Whittingham, "History, Evolution, and Future Status of Energy Storage," *Proceedings of the IEEE*, vol. 100, pp. 1518–1534, 2012.

[51] U.S. Department of Energy (DOE), "DOE Global Energy Storage Database," 2017.

[52] Center for Sustainable Systems - University of Michigan, "U.S. Grid Energy Storage Factsheet," tech. rep., Center for Sustainable Systems, University of Michigan, Michigan, 2017.

[53] U.S. Department of Energy (DOE), "Lithium-Ion Batteries for Stationary Energy Storage," tech. rep., Pacific Northwest National Laboratory, U.S. Department of Energy, Richland, Washington, 2012.

[54] LAZARD, "LAZARD's levelized cost of storage analysis - version 1.0," tech. rep., LAZARD, 2015.

[55] C. Curry, "Lithium-ion Battery Costs and Market," tech. rep., Bloomberg New Energy Finance, 2017.

[56] I. Gyuk, M. Johnson, J. Vetrano, K. Lynn, W. Parks, R. Handa, L. Kannberg, S. Hearne, K. Waldrip, and R. Braccio, "Grid Energy Storage," tech. rep., U.S. Department of Energy, 2013.

[57] D. Steward, G. Saur, M. Penev, and T. Ramsden, "Lifecycle Cost Analysis of Hydrogen Versus Other Technologies for Electrical Energy Storage," tech. rep., National Renewable Energy Laboratory, Golden, Colorado, 2009.

[58] T. Ramsden, B. Kroposki, and J. Levene, "OPPORTUNITIES FOR HYDROGEN-BASED ENERGY STORAGE FOR ELECTRIC UTILITIES," tech. rep., National Renewable Energy Laboratory, Golden, CO, 2008.

[59] G. Guandalini, S. Campanari, and M. C. Romano, "Power-to-gas plants and gas turbines for improved wind energy dispatchability: Energy and economic assessment," *Applied Energy*, vol. 147, pp. 117–130, jun 2015.

[60] G. Gahleitner, "Hydrogen from renewable electricity: An international review of power-to-gas pilot plants for stationary applications," *International Journal of Hydrogen Energy*, vol. 38, pp. 2039–2061, feb 2013.

[61] M. W. Melaina, O. Antonia, and M. Penev, "Blending Hydrogen into Natural Gas Pipeline Networks: A Review of Key Issues," tech. rep., National Renewable Energy Laboratory, U.S. Department of Energy, Golden, CO, 2013.

[62] Klaus Altfeld and Dave Pinchbeck, "Admissible hydrogen concentrations in natural gas systems," *Gas for Energy*, 2013.

[63] M. Hirscher, ed., *Handbook of Hydrogen Storage*. Weinheim, Germany: Wiley-VCH Verlag GmbH & Co. KGaA, mar 2010.

[64] D. Stolten, *Hydrogen energy*. Wiley-VCH, 2010.

[65] M. A. Pellow, C. J. M. Emmott, C. J. Barnhart, and S. M. Benson, "Hydrogen or batteries for grid storage? A net energy analysis," *Energy & Environmental Science*, vol. 8, pp. 1938–1952, jul 2015.

[66] U.S. Department of Energy, "Fuel Cell Technologies Office Multi-Year Research, Development, and Demonstration Plan," tech. rep., U.S. Department of Energy, 2017.

[67] B. Mcgrail, J. Cabe, C. Davidson, F. Knudsen, D. Bacon, M. Bearden, M. Chamness, J. Horner, S. Reidel, H. Schaef, F. Spane, and P. Thorne, "Techno-economic Performance Evaluation of Compressed Air Energy Storage in the Pacific Northwest," tech. rep., Pacific Northwest National Laboratory, U.S. Department of Energy, 2013.

[68] D. Rastler, "Electricity Energy Storage Technology Options. A White Paper Primer on Applications, Costs, and Benefits," tech. rep., Electric Power Research Institute (EPRI), Palo Alto, CA, 2010.

[69] W. Cole, T. Mai, J. Logan, D. Steinberg, J. Mccall, J. Richards, B. Sigrin, and G. Porro, "2016 Standard Scenarios Report: A U.S. Electricity Sector Outlook," tech. rep., National Renewable Energy Laboratory, 2016.

[70] M. Nyberg and E. G. Brown, "Thermal Efficiency of Gas-Fired Generation in California: 2015 Update," tech. rep., California Energy Commission, 2016.

[71] U.S. Energy Information Administration (EIA), "Drilling Productivity Report," tech. rep., U.S. Energy Information Administration (EIA), 2017.

[72] E. Crook, "Chevron transition will mark end of costly era," aug 2017.

[73] Oil and Gas 360, "Australia Set To Be Largest LNG Exporter By 2020," *Oilprice*, sep 2017.

[74] IEA, "GAS Medium-Term Market Report 2016," tech. rep., International Energy Agency, 2016.

[75] U.S. Energy Information Administration (EIA), "WHAT DRIVES CRUDE OIL PRICES?. An analysis of 7 factors that influence oil markets, with chart data updated monthly and quarterly," 2017.

[76] U.S. Energy Information Administration (EIA), "September 2017 - Monthly Energy Review," tech. rep., U.S. Energy Information Administration, 2017.

[77] International Energy Agency (IEA), "Energy Technology Perspectives 2017," tech. rep., International Energy Agency, 2017.

[78] Global CCS Institute, "The Global Status of CCS: 2017," tech. rep., Global CCS Institute, Docklands, 2017.

[79] IEA, "Five keys to unlock CCS investment," tech. rep., International Energy Agency, Paris, 2017.

[80] IEA, "20 Years of Carbon Capture and Storage - Accelerating Future Deployment," tech. rep., International Energy Agency, 2016.

[81] S. NILSEN, K. HOVLAND, C. DONS, and S. P. SLETTEN, "Effect of CO2 enrichment on photosynthesis, growth and yield of tomato," *Scientia Horticulturae*, vol. 20, pp. 1–14, may 1983.

[82] L.-M. Dion, M. Lefsrud, and V. Orsat, "Review of CO2 recovery methods from the exhaust gas of biomass heating systems for safe enrichment in greenhouses," *Biomass and Bioenergy*, vol. 35, pp. 3422–3432, aug 2011.

[83] T. K. Hartz, A. Baameur, and D. B. Holt, "Carbon Dioxide Enrichment of High-value Crops under Tunnel Culture," *Journal of the American Society for Horticultural Science*, vol. 116, no. 6, pp. 970–973, 1991.

[84] U.S. Department of Energy, *CARBON DIOXIDE CAPTURE HANDBOOK*. U.S. Department of Energy, 2015.

[85] IEA, "CO2 CAPTURE AT GAS FIRED POWER PLANTS," tech. rep., International Energy Agency, Paris, 2012.

[86] E. A. Laumann and R. K. Reynolds, "Hydrogen-fueled engine," 1978.

[87] P. de Boer and J.-F. Hulet, "Performance of a hydrogen-oxygen-noble gas engine," *International Journal of Hydrogen Energy*, vol. 5, pp. 439–452, jan 1980.

[88] M. Ikegami, K. Miwa, and M. Shioji, "A study of hydrogen fuelled compression ignition engines," *International Journal of Hydrogen Energy*, vol. 7, pp. 341–353, jan 1982.

[89] R. Kuroki, A. Kato, E. Kamiyama, and D. Sawada, "Study of High Efficiency Zero-Emission Argon Circulated Hydrogen Engine," *Society of Automotive Engineers (SAE)*, apr 2010.

[90] N. J. Killingsworth, V. H. Rapp, D. L. Flowers, S. M. Aceves, J.-Y. Chen, and R. Dibble, "Increased efficiency in SI engine with air replaced by oxygen in argon mixture," *Proceedings of the Combustion Institute*, vol. 33, no. 2, pp. 3141–3149, 2011.

[91] Siemens AG, "SILYZER 200 Spec Sheet," 2017.

[92] Hydrogenics Europe NV, "OnSite Hydrogen Generation HyLYZER® PEM Electrolysis Technology," 2017.

[93] McPhy Energy S.A., "Electrolyzers for continuous and automated hydrogen production, and/or of large quantity," 2017.

[94] J. Heywood, *Internal Combustion Engine Fundamentals*. McGraw-Hill Science/Engineering/Math, 1988.

[95] R. Stone, *Introduction to Internal Combustion Engines*. Society of Automotive Engineers Inc, 1999.

[96] G. P. Merker, C. Schwarz, and R. Teichmann, *Combustion Engines Development*. Berlin, Heidelberg: Springer Berlin Heidelberg, 2012.

[97] B. Johansson, "HCCI according to Lund," tech. rep., Lund University, Lund, 2011.

[98] C. A. Callaghan, *Kinetics and Catalysis of the Water-Gas-Shift Reaction: A Microkinetic and Graph Theoretic Approach*. PhD thesis, WORCESTER POLYTECHNIC INSTITUTE, 2006.

[99] K. Owen and T. Coley, *Automotive Fuels Reference Book*. Society of Automotive Engineers, Incorporated, 1995.

[100] V. P. Carey, *Statistical Thermodynamics and Microscale Thermophysics*. Cambridge University Press, 1999.

[101] MAN Diesel & Turbo, "Two-stroke Low Speed Diesel Engines for Independent Power Producers and Captive Power Plants," 2013.

[102] P. Häussinger, R. Glatthaar, W. Rhode, H. Kick, C. Benkmann, J. Weber, H.-J. Wunschel, V. Stenke, E. Leicht, H. Stenger, P. Häussinger, R. Glatthaar,

W. Rhode, H. Kick, C. Benkmann, J. Weber, H. Wunschel, V. Stenke, E. Leicht, and H. Stenger, "Noble Gases," in *Ullmann's Encyclopedia of Industrial Chemistry*, Weinheim, Germany: Wiley-VCH Verlag GmbH & Co. KGaA, mar 2001.

[103] P. Warneck, *Chemistry of the natural atmosphere*. Academic Press, 2000.

[104] G. B. Ellison, *Chemistry of Atmospheres: An Introduction to the Chemistry of the Atmospheres of Earth, the Planets, and their Satellites, 3rd Edition (Wayne, Richard P.)*, vol. 80. Division of Chemical Education, mar 2003.

[105] U.S. Department of Energy (DOE), *The Gas Turbine Handbook*. U.S. Department of Energy, 1 ed., 2006.

[106] G. Koszałka and M. Guzik, "Mathematical Model of Piston Ring Sealing in Combustion Engine," *Polish Maritime Research*, vol. 21, pp. 66–78, jan 2015.

[107] R. R. Malagi, "Estimation of Blowby in Multi-cylinder Diesel Engine Using Finite Element Approach," 2012.

[108] A. Arafat, Z. A. Ahmad, A. Syahrom, N. I. Mohd Ainon, M. N. Musa, A. Abdul-Latif, and W. A. Wan Mat, "Piston ring assembly for a new natural gas vehicle symmetrical multistage wobble-plate compressor," may 2006.

[109] H. W. Ebner and A. O. Jaschek, "The Importance of Blow-By Measurements, Measuring Equipment Required and Implementation," in *SAE Technical Paper*, SAE International, 1998.

[110] Gregory P. Smith, David M. Golden, Michael Frenklach, Nigel W. Moriarty, Boris Eiteneer, Mikhail Goldenberg, C. Thomas Bowman, Ronald K. Hanson, Soonho Song, William C. Gardiner Jr., Vitali V. Lissianski, and Zhiwei Qin, "GRI-Mech 3.0."

[111] D. G. Goodwin, H. K. Moffat, and R. L., "Cantera: An object- oriented software toolkit for chemical kinetics, thermodynamics, and transport processes.," 2017.

[112] B. J. Mcbride, S. Gordon, and M. A. Reno, "Coefficients for Calculating Thermodynamic and Transport Properties of Individual Species," tech. rep., National Aeronautics and Space Administration, Cleveland, OH, 1993.

[113] W. C. Gardiner and A. Burcat, *Combustion Chemistry*. London: Springer, 1984.

[114] G. Woschni, "A Universally Applicable Equation for the Instantaneous Heat Transfer Coefficient in the Internal Combustion Engine," feb 1967.

[115] A. Smith and J. Klosek, "A review of air separation technologies and their integration with energy conversion processes," *Fuel Processing Technology*, vol. 70, pp. 115–134, may 2001.

[116] Bert Metz, Ogunlade Davidson, Heleen de Coninck, Manuela Loos, and Leo Meyer, "IPCC Special Report on Carbon Dioxide Capture and Storage. Prepared by Working Group III of the Intergovernmental Panel on Climate Change," tech. rep., Intergovernmental Panel on Climate Change, Cambridge, United Kingdom, 2005.

[117] T. Banaszkiewicz, M. Chorowski, and W. Gizicki, "Comparative Analysis of Oxygen Production for Oxy-combustion Application," *Energy Procedia*, vol. 51, pp. 127–134, jan 2014.

[118] J. Yan, ed., *Handbook of clean energy systems*. 2015.

[119] D. D. Toporov, "Chapter 2 - coal combustion technologies," in *Combustion of Pulverised Coal in a Mixture of Oxygen and Recycled Flue Gas* (D. D. Toporov, ed.), pp. 5 – 22, Boston: Elsevier, 2014.

[120] H. Yang, Z. Xu, M. Fan, R. Gupta, R. B. Slimane, A. E. Bland, and I. Wright, "Progress in carbon dioxide separation and capture: A review," *Journal of Environmental Sciences*, vol. 20, no. 1, pp. 14–27, 2008.

[121] E. Favre, "Carbon dioxide recovery from post-combustion processes: Can gas permeation membranes compete with absorption?," *Journal of Membrane Science*, vol. 294, no. 1-2, pp. 50–59, 2007.

[122] S. P. Nunes and K. V. Peinemann, *Membrane Technology in the Chemical Industry*. 2016.

[123] S. Giglia, B. Bikson, J. E. Perrin, and A. A. Donatelli, "Mathematical and experimental analysis of gas separation by hollow fiber membranes," *Industrial & Engineering Chemistry Research*, vol. 30, no. 6, pp. 1239–1248, 1991.

[124] J. Marriott, *Detailed modelling and optimal design of membrane separation systems*. PhD thesis, University College London, 2001.

[125] R. W. Baker, *Membrane Technology and Applications*. Chichester, UK: John Wiley & Sons, Ltd, sep 2012.

[126] P. H. W. L. McCabe, J. C. Smith, "UNIT OPERATION HANDBOOK.pdf," 1993.

[127] R. B. Bird, W. E. Stewart, and E. N. Lightfoot, *Transport Phenomena*. John Wiley & Sons, Inc., 2006.

[128] C. Y. Pan, "Gas separation by permeators with high flux asymmetric membranes," *AIChE Journal*, vol. 29, no. 4, pp. 545–552, 1983.

[129] S. P. Kaldis, G. C. Kapantaidakis, T. I. Papadopoulos, and G. P. Sakellaropoulos, "Simulation of binary gas separation in hollow fiber asymmetric membranes by orthogonal collocation," *Journal of Membrane Science*, vol. 142, no. 1, pp. 43–59, 1998.

[130] S. P. Kaldis, G. C. Kapantaidakis, and G. P. Sakellaropoulos, "Simulation of multicomponent gas separation in a hollow fiber membrane by orthogonal collocation - Hydrogen recovery from refinery gases," *Journal of Membrane Science*, vol. 173, no. 1, pp. 61–71, 2000.

[131] Y. A. Cengel and M. A. Boles, *Thermodynamics: An Engineering Approach*. Mcgraw-Hill College, 2001.

[132] P. K. Kundu, I. M. Cohen, and D. R. D. P. A. C. I. of Technology, *Fluid Mechanics, Fifth Edition*. Academic Press, 2011.

[133] K. Lee, M. Kwon, M. Sunwoo, and M. Yoon, "An In-Cylinder Pressure Referencing Method Based on a Variable Polytropic Coefficient," 2007.

[134] R. S. Davis and G. J. Patterson, "Cylinder Pressure Data Quality Checks and Procedures to Maximize Data Accuracy," 2006.

[135] I. Fanelli, S. M. Camporeale, and B. Fortunato, "Efficient On-Board Pegging Calculation from Piezo-Electric Sensor Signal for Real Time In-Cylinder Pressure Offset Compensation," 2012.

Appendix A

US Patent: Recirculating Noble Gas Internal Combustion Power Cycle

(12) INTERNATIONAL APPLICATION PUBLISHED UNDER THE PATENT COOPERATION TREATY (PCT)

(19) World Intellectual Property Organization
International Bureau

(43) International Publication Date
4 February 2016 (04.02.2016)

WIPO | PCT

(10) International Publication Number
WO 2016/019357 A1

(51) International Patent Classification:
F02D 21/04 (2006.01) *F02D 13/02* (2006.01)
F02G 5/02 (2006.01)

(21) International Application Number:
PCT/US2015/043324

(22) International Filing Date:
31 July 2015 (31.07.2015)

(25) Filing Language: English

(26) Publication Language: English

(30) Priority Data:
62/032,067 1 August 2014 (01.08.2014) US

(71) Applicant: **THE REGENTS OF THE UNIVERSITY OF CALIFORNIA** [US/US]; 12th Floor, 1111 Franklin Street, Oakland, California 94607-5200 (US).

(72) Inventors: **DIBBLE, Robert Woodrow**; 6159 Etcheverry, Berkeley, California 94720 (US). **SIERRA AZNAR, Miguel**; Apt. D, 2737 Grant Street, Berkeley, California 94703 (US). **SENNOTT, Timothy Burke**; Apt. D, 2737 Grant Street, Berkeley, California 94703 (US). **CHEN, Jyh-Yuan**; 6163 Etcheverry, Berkeley, California 94720 (US).

(74) Agent: **BLIZZARD, Christopher**; PO Box 366, Haynes Beffel & Wolfeld LLP, 637 Main Street, Half Moon Bay, California 94019 (US).

(81) Designated States *(unless otherwise indicated, for every kind of national protection available)*: AE, AG, AL, AM, AO, AT, AU, AZ, BA, BB, BG, BH, BN, BR, BW, BY, BZ, CA, CH, CL, CN, CO, CR, CU, CZ, DE, DK, DM, DO, DZ, EC, EE, EG, ES, FI, GB, GD, GE, GH, GM, GT, HN, HR, HU, ID, IL, IN, IR, IS, JP, KE, KG, KN, KP, KR, KZ, LA, LC, LK, LR, LS, LU, LY, MA, MD, ME, MG, MK, MN, MW, MX, MY, MZ, NA, NG, NI, NO, NZ, OM, PA, PE, PG, PH, PL, PT, QA, RO, RS, RU, RW, SA, SC, SD, SE, SG, SK, SL, SM, ST, SV, SY, TH, TJ, TM, TN, TR, TT, TZ, UA, UG, US, UZ, VC, VN, ZA, ZM, ZW.

(84) Designated States *(unless otherwise indicated, for every kind of regional protection available)*: ARIPO (BW, GH, GM, KE, LR, LS, MW, MZ, NA, RW, SD, SL, ST, SZ, TZ, UG, ZM, ZW), Eurasian (AM, AZ, BY, KG, KZ, RU, TJ, TM), European (AL, AT, BE, BG, CH, CY, CZ, DE, DK, EE, ES, FI, FR, GB, GR, HR, HU, IE, IS, IT, LT, LU, LV, MC, MK, MT, NL, NO, PL, PT, RO, RS, SE, SI, SK, SM, TR), OAPI (BF, BJ, CF, CG, CI, CM, GA, GN, GQ, GW, KM, ML, MR, NE, SN, TD, TG).

Published:

— *with international search report (Art. 21(3))*

(54) **Title**: RECIRCULATING NOBLE GAS INTERNAL COMBUSTION POWER CYCLE

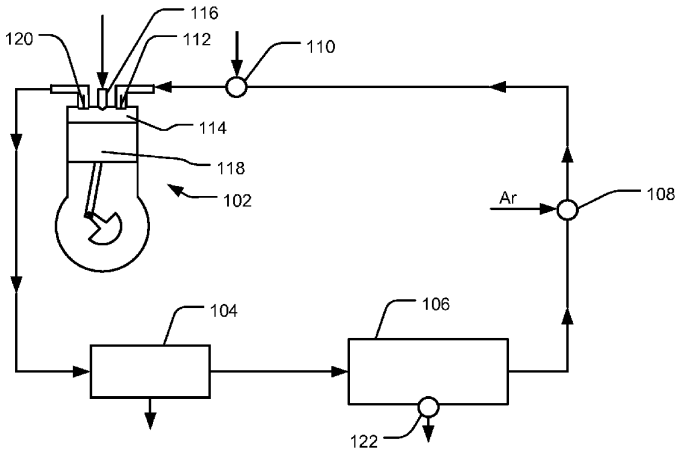

FIG. 1A

(57) **Abstract**: The present technology provides embodiments of recirculating noble gas combustion power cycles and systems including engines utilizing these power cycles. Embodiments of the cycles may include a combination of a high intake/exhaust pressure, very late or early intake valve closure, late exhaust valve opening, intake preheating using exhaust gases, sensible heat recovery, direct injection of fuel and/or oxidizer, and a condenser to remove combustion products and dissolved trace contaminant gases. An engine operating on these principles could provide motive force for electrical production, for example at power plants, or for transit, for example for ship engines. An engine operating with the cycles disclosed herein has high thermal efficiency and low cost. For example an argon power cycle using natural gas feedstock and cryogenic oxygen air separation could exceed 60% overall efficiency.

WO 2016/019357 A1

Recirculating Noble Gas Internal Combustion Power Cycle

TECHNICAL FIELD

This disclosure relates to combustion cycles for recirculating noble gas combustion power cycles and to systems including engines operating with the disclosed combustion cycles.

BACKGROUND

Power conversion cycles turning fuel into heat and heat into power are limited by basic thermodynamic considerations that have an effect on the efficiency of these conversion cycles. For example, gas turbines approach efficiencies of 35%, large bore internal combustion engines reach efficiencies of 50%, fuel cells reach efficiencies of 55%, and combined power plants, for example a combination of a Brayton cycle and a Rankine bottoming cycle that benefits from the waste heat of a gas turbine, approach efficiencies of 60%.

The efficiency of the gas power cycles used in for example turbines and engines is limited by the specific heat ratio of the working fluid. For economic and practical reasons, combustion cycles generally use ambient air to provide both the oxidizer and working fluid. Power cycles have been developed that uses a monoatomic gas in place of air as the working fluid. The power cycles can have a greater thermal efficiency than similar cycles using air because the specific heat ratio of air, 1.4, is less than the specific heat ratios of monoatomic gases, for example the specific heat ratio of Argon is 1.66. Based on the specific heat ratios, the use of a monoatomic gas may increase cycle efficiency by a factor of 1.3-1.4 compared to similar cycles using air. Further, engines running on cycles with a monoatomic gas working fluid may reuse exhausted working fluid by recirculating it back to the inlet of the engine.

Using hydrogen to generate power is being explored in applications including gas turbines, internal combustion engines, and fuel cells. Hydrogen combustion in gas turbines produces nitric oxide emissions, and is limited in efficiency and temperature by the material strength of the turbines to that of current power plants. Fuel cells have the disadvantage of being very expensive. Internal combustion engines running cycles including recirculating monoatomic gas working fluids have been made to utilize hydrogen, hydrocarbons, or oxigenates as a fuel and oxygen as an oxidizer. In the case of hydrogen as a fuel and oxygen as an oxidizer the resulting byproduct is water. This water may be removed easily from the recirculating working fluid. These recirculating monoatomic gas cycles have previously not been seriously considered because burning in air is inexpensive and convenient.

Methods of storing energy prior to using the energy is a growing field, particularly relating to efficiently utilizing the stored energy. Methods for electrical energy storage are various and include batteries, pumped hydro, flywheels, hydrogen energy storage, and compressed air energy storage. One area of energy storage that is being developed is 'load-leveling' energy storage that can shift power over hours or days. Technologies for load leveling energy storage include batteries, hydrogen energy storage, and compressed air energy storage. Batteries have high round-trip efficiencies but are cost-prohibitive for load-leveling energy storage. Compressed air energy storage has poor efficiency and poor energy density.

It is therefore desirable to provide technology for using stored energy that is inexpensive, has high energy density, is efficient, and is environmentally friendly. It is further desirable to provide methods to efficiently utilize carbonaceous fuels and produce pure carbon dioxide which may be utilized or sequestered. As such, it is desirable to provide technology for a high-efficiency combustion power cycle that is well adapted to carbon capture with low energy cost.

SUMMARY

The present technology provides embodiments of recirculating noble gas combustion power cycles and systems including engines utilizing these power cycles. Embodiments of the cycles may include a combination of a high intake/exhaust pressure,

very late or early intake valve closure, late exhaust valve opening, intake preheating using exhaust gases, sensible heat recovery, direct injection of fuel and/or oxidizer, a condenser to remove combustion products and dissolved trace contaminant gases, and a carbon dioxide separation unit if carbonaceous fuels are to be used. An engine operating on these principles could provide motive force for electrical production, for example at power plants, or for transit, for example for ship engines. An engine operating with the cycles disclosed herein has high thermal efficiency and low cost. For example an argon power cycle using natural gas fuel and cryogenic oxygen air separation could reach 60% overall efficiency.

The cycles disclosed herein can be incorporated into new engine designs. Further, existing engines may be reconfigured to operate with the technology disclosed herein. In embodiments, engines operating with the disclosed recirculating noble gas combustion power cycles include features which allow the engine to also run open-looped using ambient air and direct-injected fuel (e.g. natural gas) as an alternative to the closed loop monoatomic gas recirculating, pure hydrogen and pure oxygen burning operation mode.

Embodiments of the recirculating noble gas combustion power cycles disclosed may include high-quality exhaust heat that energy is extracted from. For example, high-quality exhaust heat is supplied to a steam reforming process, or to a Rankine-type or similar "bottoming" cycle. In embodiments, the quality of the exhaust heat can be increased by preheating of the intake fluid by heat exchange, through use of a heat exchanger, with exhaust fluid.

Embodiments of the technology may include various injection methods including direct injection of both fuel and oxygen, e.g. for energy storage application, or oxygen or fuel alone, e.g. for applications where fuel and/or oxygen are not stored at high pressure.

Embodiments of the technology may include various valve timing schemes. The valve timing schemes may reduce the effective volume ratio of compression stroke, and the peak pressure and temperature can be limited. Due to the high specific heat ratio of the argon working fluid, embodiments may include very late intake valve closure in the valve timing scheme. This large ratio of expansion stroke to compression stroke affords higher thermal efficiencies and limits peak pressure and temperature within the engine.

Late intake valve closure may result in power loss which in embodiment may be offset by increasing the cycle pressure, i.e. 'boosting', to increase the charge density and regain this power loss. The increased cycle pressure is above the ambient pressure. Boosting also assists in reducing recirculating water content. Boosting the cycle working pressure by large amounts, for example 3-4 bar, has the additional effect of reducing the absolute humidity of the condenser exit stream. This reduces or eliminates the need for additional exhaust drying to prevent substantial efficiency penalty from the recirculating water and its effect on working fluid specific heat ratio. Further, high cycle working pressure allows for membrane or adsorbent separation with low parasitic energy cost for power cycles using carbonaceous fuels and having carbon dioxide as a combustion byproduct.

Applications for embodiments of the technology include enhanced hydrogen energy storage systems for load-leveling applications in the electrical grid. Embodiments of the disclosed cycle technology are a lower cost and more efficient means of converting stored hydrogen and oxygen back into electricity. Hydrogen energy storage systems including the technology disclosed herein have a higher energy density than compressed air energy storage, and much lower per kWh capital costs than batteries. In addition, because recirculating noble gas combustion power cycles utilize internal combustion engines, the technology has good grid electrical characteristics, including good load-following and frequency regulation. Further, in embodiments, hydrogen energy storage systems including recirculating noble gas combustion power cycles could be configured to generate electricity conventionally with carbonaceous fuels, for example, methane burning in air, when grid conditions did not make storage economically viable.

Further applications for embodiments of the noble gas combustion power cycles include medium-scale utility power generation units using hydrogen as a fuel, or alternatively direct use of carbonaceous fuels. The hydrogen fuel may be generated from steam reforming methane or coal gasification in a pre-combustion carbon capture context. High-efficiency plants of this type have excellent load-response characteristics compared to existing combined cycle plant technology, making them integrate better with increasing portfolios of variable generation. Further applications for embodiments of the technology include electrical production collocated with, and using, hydrogen byproduct

from methane steam reforming employed to produce CO2 for enhanced oil recovery operations or carbon capture and sequestration schemes. Direct use of carbonaceous fuels in the power cycle, including both gaseous (e.g. natural gas) and liquid (e.g. methanol, dimethyl ether), coupled with appropriate carbon capture technology (e.g. membrane separation, pressure swing adsorption), allows for high-efficiency utilization of these fuels while producing pure CO2 for enhanced oil recovery or other carbon sequestration schemes.

Other aspects and advantages of the present technology can be seen on review of the drawings, the detailed description and the claims, which follow.

BRIEF DESCRIPTION OF THE DRAWINGS

FIG. 1A shows a simplified block of an embodiment of recirculating engine.

FIG. 1B shows a simplified block of an embodiment of recirculating engine including intake preheating and boosting.

FIG. 1C shows a simplified block of an embodiment of recirculating engine including intake preheating.

FIG. 1D shows a simplified block of an embodiment of recirculating engine including a CO_2 separation membrane.

FIG. 2A, FIG. 2B, FIG.2C, FIG. 2D, FIG. 2E, FIG. 2F, FIG. 2G, FIG. 2H, FIG. 2l, FIG. 2J, FIG. 2K, FIG. 2L, and FIG. 2M illustrate various aspects of a power cycle including very late intake valve closure with a high quality of exhaust heat.

FIG. 3A, FIG. 3B, FIG.3C, FIG. 3D, FIG. 3E, FIG. 3F, FIG. 3G, FIG. 3H, FIG. 3l, FIG. 3J, FIG. 3K, FIG. 3L, and FIG. 3M illustrate various aspects of a power cycle including very early intake valve closure with a high quality of exhaust heat.

Figure 4 shows a schematic of an argon power cycle in a hydrogen energy storage system.

DETAILED DESCRIPTION

The following description will typically be with reference to specific structural embodiments and methods. It is to be understood that there is no intention to be limited to the specifically disclosed embodiments and methods but that other features, elements, methods and embodiments may be used for implementations of this disclosure. Preferred

embodiments are described to illustrate the technology disclosed, not to limit its scope, which is defined by the claims. Those of ordinary skill in the art will recognize a variety of equivalent variations on the description that follows. Unless otherwise stated, in this application specified relationships, such as parallel to, aligned with, or in the same plane as, mean that the specified relationships are within limitations of manufacturing processes and within manufacturing variations. When components are described as being coupled, connected, being in contact or contacting one another, they need not be physically directly touching one another unless specifically described as such. Like elements in various embodiments are commonly referred to with like reference numerals. A detailed description of embodiments of the present technology is provided with reference to the Figures.

FIG. 1A is an illustration of a system including a recirculating power cycle. The system includes a piston engine **102** in a substantially closed loop. Also within the closed loop are a sensible heat recovery element **104,** and a condenser **106.** Flowing around the closed loop is a working fluid. In the example recirculating power cycle systems shown, the working fluid comprises Argon. However, in embodiments the working fluid comprises one or more monoatomic gas including Helium, Neon, Krypton, and Xenon. Monoatomic gases only store energy on a translation mode of motion, and therefore thermodynamically they are identical. However, monoatomic gases do have different heat transfer characteristics, and therefore in embodiments the monoatomic gases for the working fluid may be selected based on a desired heat transfer characteristic of the working fluid. From a cost and practicality standpoint, Argon is preferable for many applications as it is abundant in the atmosphere, and may be isolated during a process of separating oxygen, to use in combustion in the engine, from ambient air.

Small portions of the monoatomic gas of the working fluid may leave the closed-loop system through various processes or leaks in the system. Therefore the system includes a low volume working fluid input port **108.** The input port **108** may be positioned anywhere in the closed loop. In embodiments, the working fluid may continually be introduced through the input port into the closed loop at a rate corresponding to the rate of working fluid lost from the closed loop. In embodiments, the working fluid may be intermediately introduced through the input port into the closed

loop at predetermined time increments or based on sensed concentration of working fluid in the closed loop.

In embodiments, the piston engine **102** is configured to run on hydrogen as a fuel and oxygen as an oxidizer. In the embodiment shown in FIG. 1, oxygen is introduced to the closed loop at an oxygen premixing port **110** located near the intake valve **112** of the piston engine **102.** Further, in the embodiment shown in FIG. 1, hydrogen is directly injected into the cylinder **114** of the piston engine **102** through a direct injection nozzle **116.** The Oxygen and Hydrogen are stored separately in high or low pressure storage units (not shown). As will be discussed below, the hydrogen may be injected during the end of the compression stroke of the piston **118** within the cylinder **114** and the pressure and temperature of the working fluid will reach an ideal injection temperature which will cause spontaneous auto-ignition of the hydrogen and oxygen to occur as the hydrogen is injected.

In embodiments, the piston engine **102** includes a crank case purge (not shown). In these embodiments, the crankcase is sealed and ventilated with the Argon working fluid. The crank case purge is configured to allow any argon and combustion gases that escape through the piston ring pack to be re-introduced into the intake, which reduce losses.

In embodiments, as an alternative to premixing of oxygen, the oxygen may be directly injected, into the cylinder **114** of the piston engine **102** through one or more direct injection nozzles **116.** Advantages of direct Oxygen injection include a smaller volumetric flow rate needed for a stoichiometric reaction, and therefore less compression work. Further oxygen has a higher density and therefore direct injection provides greater jet momentum.

In embodiments, to ensure combustion of the desired amount of fuel and oxidizer an excess of one may be provided. In embodiments, excess oxygen may be introduced into the closed loop which will ensure complete combustion of the hydrogen and the oxygen will recirculate to be burned during subsequent cycles. However, it is advantageous not to provide too much excess of either fuel or oxidizer as this will dilute the concentration of working fluid which will lower the specific heat of the fluid within the system which has adverse effects on the thermal efficiency of the system.

After combustion, the exhaust gases leave the piston engine **102** through the exhaust valve **120** and passes through the sensible heat recovery element **104.** Heat is extract from the exhaust gas in the sensible heat recovery element **104** which may be used as a heat supply for a steam reforming process of converting natural gas into hydrogen, or for other purposes such as a bottoming cycle. For example, the sensible heat recovery element **104** may include an air to liquid heat exchange that can be used to preheat a natural gas stream or to generate the steam necessary for the reforming process. The hydrogen created during the reforming process may be stored and later used as the fuel injected into the piston engine. The exhaust stream will run at temperatures that strongly depend on the valve timing and level of dilution of the working fluid, as will be discussed later in this application.

In the embodiment illustrated in FIG. 1, the exhaust is cooled down to saturation temperatures at the given pressure as it exits the sensible heat recovery element **104** and enters the condenser **106.** The condenser **106** is configured to remove byproducts of combustion and dissolved trace contaminant gases, for example CO_2 and NOx, from the exhaust of the piston engine **102.** In the embodiments including a monoatomic gas working fluid, hydrogen fuel, and oxygen oxidizer, the byproducts of combustion include water which condensates within the condenser **106.** Water and other contaminants, including trace contaminant gases and heavy particles precipitated in the water, leave the closed loop through an exit port **122** of the condenser **106.** The fluid leaving the condenser toward the intake valve **112** of the piston engine **102** is mainly composed of the working fluid, in the example Argon, though small amounts of water and minor traces of gases may also remain.

FIG. 1B is an illustration of a system including a recirculating power cycle similar to the system of FIG. 1A and including additional features. Similar to FIG. IA, the system illustrated in FIG. 1B includes a substantially closed loop including a piston engine **102** with an intake valve **112,** an exhaust valve **120,** a cylinder **114,** and a direct injection nozzle **116.** In the embodiment shown in FIG. 1B, both hydrogen and oxygen may be directly injected into the cylinder **114** through one or more direct injections nozzles **116.** The loop also includes a condenser **106** and a low volume working fluid input port **108,** as discussed above.

The closed loop further includes a trace gas removal element **124,** located after the condenser **106** in the closed loop. Trace gases may build up during operation, and may be attributed to impurities in reactant streams and combustion of lubricating oils. However, in embodiments, non-combustible lubricating oils, for example, silicone oils, are used to prevent buildup of CO2 in hydrogen based cycles. The trace gas removal element **124** is configured to remove trace gases in the fluid leaving the condenser **106.** The trace gas removal element **124** may include processes including catalysts, urea treatment, adsorbents, and absorbents.

To remove contaminants not removed by the condenser **106** or trace gas removal element **124,** the closed loop further includes a low value purge valve **126.** The low value purge valve **126** may be configured to continuously allow removal of fluid from within the closed-loop. For example, the low value purge valve **126** may be configured to allow gases to leave the system at a rate of up 1% of the total volume of gas in the closed loop per cycle of the piston engine **102.** As discussed above, the working fluid that leaves the closed loop system, such as through the low value purge valve **126,** may be replaced through the low volume working fluid input port **108.**

In the systems described herein, the term "closed-loop", also referred to as "substantially closed-loop", is used to describe a system in which exhaust gases expelled from an engine are not exhausted into the ambient. In a "closed-loop" system the exhaust gases are processed to separate working fluid of the system from combustion byproducts and contaminants. The working fluid is then recirculated into the engine intake. As previously disclosed, in a closed loop system a portion of the working fluid may be lost from the system due to leaks and as part of the combustion byproduct and contaminant removal processes. Despite these losses a system is still considered to be "substantially closed-loop" because the exhaust gases are no expelled into the ambient and a substantially portion, >90%, of exhausted working fluid is returned to the intake of the engine in subsequent cycles.

In the systems illustrated in FIGs. 1A and 1B, the piston engine may maintain, or increase, pressure within the closed loop. Increasing pressure within the closed loop is referred to as "boosting". The embodiment illustrated in FIG. 1B includes a compressor **128** in the closed loop, between the low value purge valve **126** and the low volume

working fluid input port **108,** which is configured to boost the pressure in the closed loop. The boost created by the compressor, or the piston engine, may make up for pressure losses caused by recirculation through the closed-loop of ducts. Further, the boost of a compressor may make up for pressure losses in embodiments wherein the piston engine is a two-stroke cycle engine as opposed to a four-stroke cycle engine.

After the intake gas passes through the compressor **128** the intake gas passes through a heat exchanger **130** to be warmed by the exhaust gas from the piston engine **102.** The heat exchanger **130** includes a first chamber fluidly coupling the exhaust valve **120** of the piston engine **102** to the condenser **106,** and a second chamber fluidly coupling the intake gas from the condenser **106** and compressor **128** to the intake valve **112** of the piston engine **102.** The heat exchanger is configured to preheat working fluid entering the piston engine with heat extracted from working fluid exiting the piston engine. In embodiments, the heat exchanger may be of the flat plate, shell or tube type. Additionally, the heat exchanger may comprise an adiabatic wheel, or include direct contact in the case of heat recovery to a liquid. Rapid auto ignition of the injected reactants is important to limit premixing and reduce rapid pressure rise from premixed combustion, and thus the ideal injection temperature is likely to be higher than that afforded by the ideal compression volume ratio. Preheating the intake gases using the exhaust gases affords decoupling these cycle parameters, and also accomplishes some of the exhaust cooling required before the condenser step. Though auto ignition is desired, it is important to have control over when the auto ignition occurs and how the auto ignition influences the combustion event. The level of premixing before auto ignition temperatures are reached is an important parameter to adjust combustion phasing. A large amount of premixed mixture before ignition may shift backwards the combustion phasing which will lower the thermodynamic efficiency and potentially cause the breakdown of the piston engine due to extreme pressure rise rates. By adjusting the intake temperature, another control parameter is added for auto ignition to be advanced/delayed. Varying the intake temperature influences the amount of premixed mixture that the auto ignition event will include and consequently the pressure rise rate. In addition, intake preheating increases the exhaust temperature, 'quality', which is advantageous if the

exhaust is to be utilized, for example combined with steam reforming facilities or used in a bottoming cycle.

FIG. 1C is an illustration of a system including a recirculating power cycle similar to the system of FIG. 1B. Similar to FIG.1B, the system illustrated in FIG. 1C includes a substantially closed loop including a piston engine **102** with an intake valve **112,** an exhaust valve **120,** a cylinder **114,** and a direct injection nozzle **116.** In the embodiment shown in FIG. 1C, oxygen may be premixed through oxygen premixing port **110.** The closed-loop also includes a condenser **106,** a sensible heat recovery element **104,** a low volume working fluid input port **108,** a trace gas removal element **124,** a low volume purge valve **126,** and a heat exchanger **130,** as discussed above.

FIG. 1D is an illustration of a system including a recirculating power cycle, similar to discussed above, using direct use of carbonaceous fuels and post-combustion separation technology. Similar to FIG.1A, the system illustrated in FIG. 1D includes a substantially closed loop including a piston engine **102** with an intake valve **112,** an exhaust valve **120,** a cylinder **114,** and a direct injection nozzle **116.** In the embodiment shown in FIG. 1D, oxygen may be premixed by through oxygen premixing port **110.** The closed-loop also includes a condenser **106, and** a low volume working fluid input port **108,** as discussed above.

In system in FIG. 1D, a carbonaceous fuel is directly injected into the cylinder **114** through the direct injection nozzle **116.** Combustion of the carbonaceous fuel, along with oxygen premixed with the working fluid at oxygen premixing port **110,** occurs in the piston engine **102** and the resulting combustion byproducts include water and carbon dioxide, CO_2**.** The water is removed from the exhaust gases in the condenser **106,** as is discussed above in other embodiments.

The system in FIG. 1D further includes a CO_2 separation membrane unit **132** configured to remove the CO_2 resulting from the combustion of the carbonaceous fuel. Fluids leaving the condenser **106** enter the CO_2 separation membrane unit **132** and the CO_2 is separated from the fluid and enters a compressor **128.** The working fluid continues from the CO_2 separation membrane unit **132** back toward the intake valve **112** of the piston engine **102,** similar to the systems shown in FIG. 1A. In embodiments, CO_2 separation technologies may be utilized, including a combination of one or more of

membrane separation, cryogenic separation, amine absorption, and pressure swing adsorption.

The CO_2 leaves the compressor and enters a cryogenic separation device **134.** The Argon produced in the cryogenic separation device enters the closed-loop system as is shown. The CO_2 leaves the cryogenic separation device and may be used in applications such as enhanced oil recovery.

The power cycles disclosed above may include various ratios of fuel, oxidizer, and workings fluid. Example 1: (0.5-2 part) 0 2 to 1 part H2 to (2-20 parts) Ar. Example 2: (2-8 parts) 0 2 to 1 part CH4 to (8-80parts) Ar. Example 3: (3-12 parts) 0 2 to 1 part CH3OCH3 to (12-120 parts) Ar. Example 4: (1.5-6 parts) 0 2 to 1 part CH3OH to (8-80 parts) Ar. Further, systems as disclosed may include features allowing for dual use as a closed-loop recirculating power cycle system and an open-loop ambient air breathing power cycle system. This system is advantageous when hydrogen, oxygen or a monoatomic gas working fluid are not readily available.

FIGs. 1A, 1B, 1C and 1D, illustrate example combinations of features in recirculating power cycles, however other combinations of the components illustrated and discussed herein are envisioned within the scope of the technology disclosed herein. Further, while a piston engine with a single cylinder and single piston has been shown, the technology may be used with multiple cylinder and piston engines. Further, each piston may include one or more intake and exhaust valves.

The recirculating power cycles of the piston engines disclosed herein include valve timing schemes which are designed for the closed loop recirculating nature of the systems and high overall efficiency in mind. A key aspect of the valve time scheme is the intake valve closure. The intake valve closure determines the pressure ratio and thus the highest temperature of the working fluid. Intake valve closure time can be used to reduce the compression ratio of the compression stroke, while the expansion stroke ratio remains fixed, which helps control the load and the ignition timing.

In embodiments of the recirculating power cycles the intake valve closure is configured to reduce a compression ratio between 4: 1 and 25: 1; and reduce the amount of charge in the cylinder. To reduce the charge in the cylinder the intake valve is closed very early or very late relative to the intake valve closing times in an Otto cycle.

FIGs. 2A-M illustrate various aspects of a power cycle including very late intake valve closure with a high quality of exhaust heat. FIG. 2A illustrates the beginning of an intake stroke of a power cycle including very late intake valve closure. In figure 2A the piston **118** is at top dead center and both the intake and exhaust valves **112 and 120** are closed. FIG. 2B illustrates an intermediate position in the intake stroke where the piston **118** is located between end positions and the piston **118** is traveling toward bottom dead center and the intake valve **112** is open. FIG. 2C illustrates the end of the intake stroke with the piston **118** at bottom dead center and the intake valve **112** is open and the exhaust valve **120** is closed. FIG. 2D illustrates an intermediate position in the compression stroke where the piston **118** is located between bottom dead center and top dead center and the intake valve **112** remains open. The intake valve **112** remaining open during the beginning of the compression strokes cause gases inside of the cylinder **114** to be expelled through the open intake valve. FIG. 2E illustrates another stage in the compression stroke, after the stage illustrated in FIG. 2D, wherein the piston **118** is located between bottom dead center and top dead center. The piston **118** is travelling toward top dead center and the intake valve **112** is now closed. The closure of the intake valve **112** during the compression stroke occurs for example between 0 and 120 degrees past bottom dead center. This late closure of the intake valve and is referred to as very late intake valve closure. The very late intake valve closure results in reduced effective volume ratio of the compression stroke and a large ratio of expansion stroke to compression stroke. The very late intake valve closure occurs prior to a fuel injection angle where fuel is injected into the cylinder and auto ignition occurs. Reason being, if auto ignition occurs while the intake valve is open damage to the valve train may occur.

FIG. 2F illustrates the end of the compression stroke with the piston **118** located at top dead center. In the embodiment illustrated, at this point the fuel **202** is directly injected into the cylinder **117** and combustion occurs initiating the power stroke, as illustrated in FIG. 2F. In embodiments, fuel is injected during the compression stroke, for example up to 20-40 degrees before top dead center. The timing of the fuel injection helps control combustion phasing and control power level. The expanding gases caused by combustion push the piston toward bottom dead center as shown in FIG. 2H. At the end of the power stroke the piston is located at bottom dead center as shown in FIG. 2I.

Once at bottom dead center the exhaust valve **120** may be opened as shown in FIG. 2I. With the exhaust valve **120** open the piston travels toward top dead center during the exhaust stroke forcing gases to exit the cylinder **114** through the open exhaust valve **120** as shown in FIG. 2J. The exhaust stroke ends with the piston 118 located at top dead center and the exhaust valve **120** closed as shown in FIG. 2J. After the exhaust stroke is complete the intake stroke begins and the cycle as shown in FIGs. 2A-2K repeats.

In embodiments the exhaust valve opening and closing timing may be different than shown in FIGs. 2A-2K. For example, power cycles may include late exhaust valve opening wherein the exhaust valve does not open until the initiation of the exhaust stroke which is much later than in an Otto cycle wherein the exhaust valve opens during the power stroke. In embodiments the exhaust valve opens for example between -10 degrees and 20 degrees after bottom dead center of the beginning of the exhaust stroke.

FIG. 2L illustrates an embodiment valve timings and relative opening distance of the intake and exhaust valve in a power cycle including later intake valve closure. FIG. 2M illustrates an embodiment the pressure and volume of the in a piston engine with a power cycle including late intake valve closure.

FIGs. 3A-M illustrate various aspects of a power cycle including very early intake valve closure with a high quality of exhaust heat. FIG. 3A illustrates the beginning of an intake stroke of a power cycle including very late intake valve closure. In FIG. 3A the piston **118** is at top dead center and both the intake and exhaust valves **112 and 120** are closed. FIG. 3B illustrate an intermediate position in the intake stroke where the piston **118** is located between end positions and the piston **118** is traveling toward bottom dead center and the intake valve **112** is open. FIG. 3C illustrates a second intermediate position in the intake stroke, after the position illustrated in FIG. 3B. In FIG, 3C the piston is still traveling toward bottom dead center and the intake valve **112** is now closed. FIG. 3D illustrates a position at the end of the intake stroke and beginning of the compression stroke wherein the piston **118** is at bottom dead center and the intake valve **112** and the exhaust valve **120** are closed. The intake valve **112** closing before the end of the intake stroke cause less than the full volume of the stroke to pulled in through the intake valve during the intake stroke. The closure of the intake valve **112** during the intake stroke occurs between 120 and Odegrees before bottom dead center. This early

closure of the intake valve and is referred to as very early intake valve closure. The very early intake valve closure results in reduced effective volume ratio of the compression stroke and a large ratio of expansion stroke to compression stroke.

FIG. 3E illustrates a stage in the compression stroke, wherein the piston **118** is located between bottom dead center and top dead center, and the piston **118** is travelling toward top dead center.

FIG. 3F illustrates the end of the compression stroke with the piston **118** located at top dead center. At this point the fuel **202** is directly injected into the cylinder **117** and combustion occurs initiating the power stroke, as illustrated in FIG. 3F. The expanding gases caused by combustion push the piston toward bottom dead center as shown in FIG. 3H. At the end of the power stroke the piston is located at bottom dead center as shown in FIG. 3l. Once at bottom dead center the exhaust valve **120** may be opened as shown in FIG. 3l. With the exhaust valve **120** open the piston travels toward top dead center during the exhaust stroke forcing gases to exit the cylinder **114** through the open exhaust valve **120** as shown in FIG. 3J. The exhaust stroke ends with the piston 118 located at top dead center and the exhaust valve **120** closed as shown in FIG. 3J. In embodiments the exhaust valve opening and closing timing may be different than shown in FIGs. 3A-3K. For example, power cycles may include late exhaust valve opening as discussed above, such that exhaust valve closure may overlap with inlet valve opening. After the exhaust stroke is complete the intake stroke begins and the cycle as shown in FIGs. 3A-3K repeats.

FIG. 3L illustrates an embodiment valve times and relative opening distance of the intake and exhaust valve in a power cycle including early intake valve closure. FIG. 3M illustrates an embodiment the pressure and volume of the in a piston engine with a power cycle including early intake valve closure.

FIG. 4 shows a schematic of an argon power cycle in a hydrogen energy storage system. As shown, various energy sources including wind farms, solar farms, and gas/oil/coal power plants provide energy to the AC electric grid. The consumer demand is addressed with the energy in the grid and excess energy may go to an electrolyzer to create hydrogen and oxygen which may be stored. When consumer demand on the grid exceeds the output of the primary energy sources the stored hydrogen and oxygen may be

used in the Argon Powers cycle, which utilizes the technology disclosed herein, to efficiently convert the stored hydrogen and oxygen into energy usable by the consumers.

While the present technology is disclosed by reference to the preferred embodiments and examples detailed above, it is to be understood that these examples are intended in an illustrative rather than in a limiting sense. It is contemplated that modifications and combinations will readily occur to those skilled in the art, which modifications and combinations will be within the spirit of the technology and the scope of the following claims. What is claimed is:

CLAIMS

1. A recirculating energy system comprising:

a piston engine comprising;

a cylinder;

an intake valve at a first end of the cylinder,

an exhaust valve at the first end of the cylinder, and

a piston located within the cylinder configured to be able to reciprocate between a top dead center position proximate to the first end of the cylinder and a bottom dead center position towards a second end of the cylinder;

wherein the piston engine is configured to include a valve timing scheme to reduce a compression ratio; and

wherein the recirculating energy system is configured so that a substantially closed loop path, through which a working fluid is flowable, is formed from:

the engine exhaust valve,

to a sensible heat recovery device configured to allow heat to be extracted from exhaust fluids;

to a condenser configured to remove combustion byproducts introduced into the substantially closed loop path,

to the engine intake valve,

to the cylinder, and

back to the engine exhaust valve.

2. The recirculating energy system of claim 1, further comprising a heat exchanger comprising a first chamber fluidly coupling the exhaust valve and an intake of the condenser, and a second chamber fluidly coupling an exhaust of the condenser and the intake valve; and configured to preheat working fluid entering the piston engine with heat extracted from working fluid exiting the piston engine.

3. The recirculating energy system of claim 1, further comprising a carbon dioxide separation element fluidly coupled within the closed loop path and configured to separate carbon dioxide, from combustion of carbonaceous fuels, from the working fluid.

4. The recirculating energy system of claim 1:

wherein the piston engine is configured to be able to operate as a four stroke cycle internal combustion engine including an intake stroke, a compression stroke, a power stroke and an exhaust stroke; and

wherein the intake valve opens during the intake stroke between 200 degrees and 170 degrees before bottom dead center; and wherein the intake valve closes during the compression stroke between 0 degrees and 120 degrees past bottom dead center.

5. The recirculating energy system of claim 1:

wherein the piston engine is configured to be able to operate as a four stroke cycle internal combustion engine including an intake stroke, a compression stroke, a power stroke and an exhaust stroke; and

wherein the intake valve opens during the intake stroke between 200 degrees and 170 degrees before bottom dead center; and wherein the intake valve closes during the intake stroke between 120 degrees and 0 degrees before bottom dead center.

6. The recirculating energy system of claim 1:

wherein the piston engine is configured to be able to operate as a four stroke cycle internal combustion engine including an intake stroke, a compression stroke, a power stroke and an exhaust stroke; and

wherein the exhaust valve opens during the exhaust stroke between 10 degrees before bottom dead center and 20 degrees after bottom dead center; and wherein the exhaust valve closes during the intake stroke between 10 degrees before top dead center and 20 degrees after top dead center.

7. The recirculating energy system of claim 1, wherein the piston engine is configured to include a valve timing scheme to reduce the compression ratio between 4: 1 and 25:1.

8. The recirculating energy system of claim 1 further comprising:

one or more valves configurable to open the substantially closed loop path to ambient air; and

wherein the piston engine is configured to be able to use oxygen in the ambient air as an oxidizer and be able to exhaust into the ambient air.

9. The recirculating energy system of claim 1 wherein the piston engine is configured to run with argon as the working fluid, pure hydrogen as a fuel, and pure oxygen as an oxidizer.

10. The recirculating energy system of claim 1 wherein the piston engine is configured to run with argon as the working fluid, a hydrocarbon or oxigenate as a fuel, and pure oxygen as an oxidizer.

11. A method of operating a recirculating energy system comprising:

in a piston engine comprising;

a cylinder;

an intake valve at a first end of the cylinder,

an exhaust valve at the first end of the cylinder, and

a piston located within the cylinder configured to be able to reciprocate between a top dead center position proximate to the first end of the cylinder and a bottom dead center position towards a second end of the cylinder;

operating the piston engine to include a valve timing scheme to reduce a compression ratio; and

operating the recirculating energy system as a substantially closed loop path, through which a working fluid is flowable, the closed loop path being formed from:

the engine exhaust valve,

to a sensible heat recovery device configured to allow heat to be extracted from exhaust fluids;

to a condenser configured to remove combustion byproducts introduced into the closed loop path,

to the engine intake valve,

to the cylinder, and

back to the engine exhaust valve.

12. The method of claim 11, wherein the recirculating energy system further comprises a heat exchanger comprising a first chamber fluidly coupling the exhaust valve and an intake of the condenser, and a second chamber fluidly coupling an exhaust of the condenser and the intake valve; and

wherein operating the recirculating energy system further comprises preheating working fluid entering the piston engine with heat extracted from working fluid exiting the piston engine.

13. The method of claim 11, wherein the recirculating energy system further comprises a carbon dioxide separation element fluidly coupled within the closed loop path; and

wherein operating the recirculating energy system further comprises separating carbon dioxide, from combustion of carbonaceous fuels, from the working fluid.

14. The method of claim 11, further comprising:

operating the piston engine as a four stroke cycle internal combustion engine including an intake stroke, a compression stroke, a power stroke and an exhaust stroke;

opening the intake valve during the intake stroke between 200 degrees and 170 degrees before bottom dead center; and

closing the intake valve during the compression stroke between 0 degrees and 120 degrees past bottom dead center.

15. The method of claim 11, further comprising:

operating the piston engine as a four stroke cycle internal combustion engine including an intake stroke, a compression stroke, a power stroke and an exhaust stroke;

opening intake valve during the intake stroke between 200 degrees and 170 degrees before bottom dead center; and

closing the intake valve during the intake stroke between 120 degrees and 0 degrees before bottom dead center.

16. The method of claim 11, further comprising:

operating the piston engine as a four stroke cycle internal combustion engine including an intake stroke, a compression stroke, a power stroke and an exhaust stroke;

opening the exhaust valve during the exhaust stroke between 10 degrees before bottom dead center and 20 degrees after bottom dead center; and

closing the exhaust valve during the intake stroke between 10 degrees before top dead center and 20 degrees after top dead center.

17. The method of claim 11, further comprising operating the piston engine to include a valve timing scheme to reduce the compression ratio between 4:1 and 25:1.

18. The method of claim 11, wherein the recirculating energy system further comprises one or more valves, and

wherein operating the recirculating energy system further comprises opening the substantially closed loop path to ambient air; and

operating the piston engine to use oxygen in the ambient air as an oxidizer and to exhaust into the ambient air.

19. The method of claim 11, further comprising operating the piston engine to run with argon as the working fluid, pure hydrogen as a fuel, and pure oxygen as an oxidizer.

20. The method of claim 11, further comprising operating the piston engine to run with argon as the working fluid, a hydrocarbon or oxigenate as a fuel, and pure oxygen as an oxidizer.

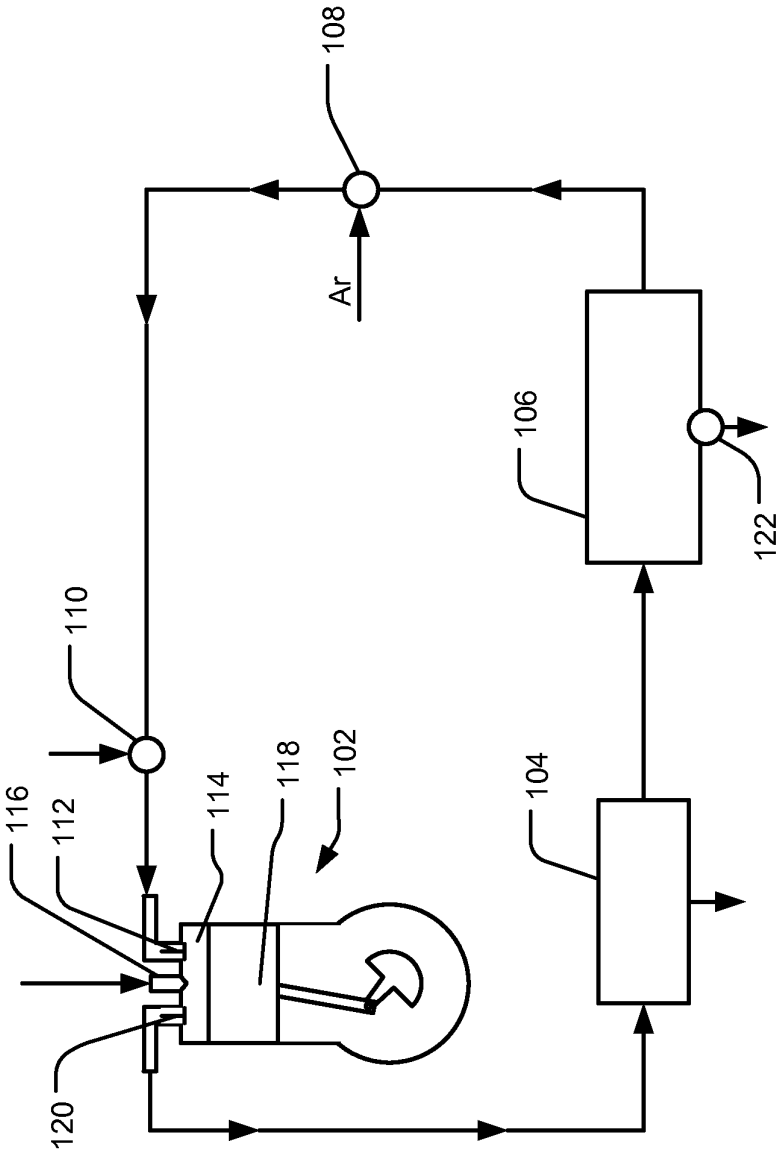

FIG. 1A

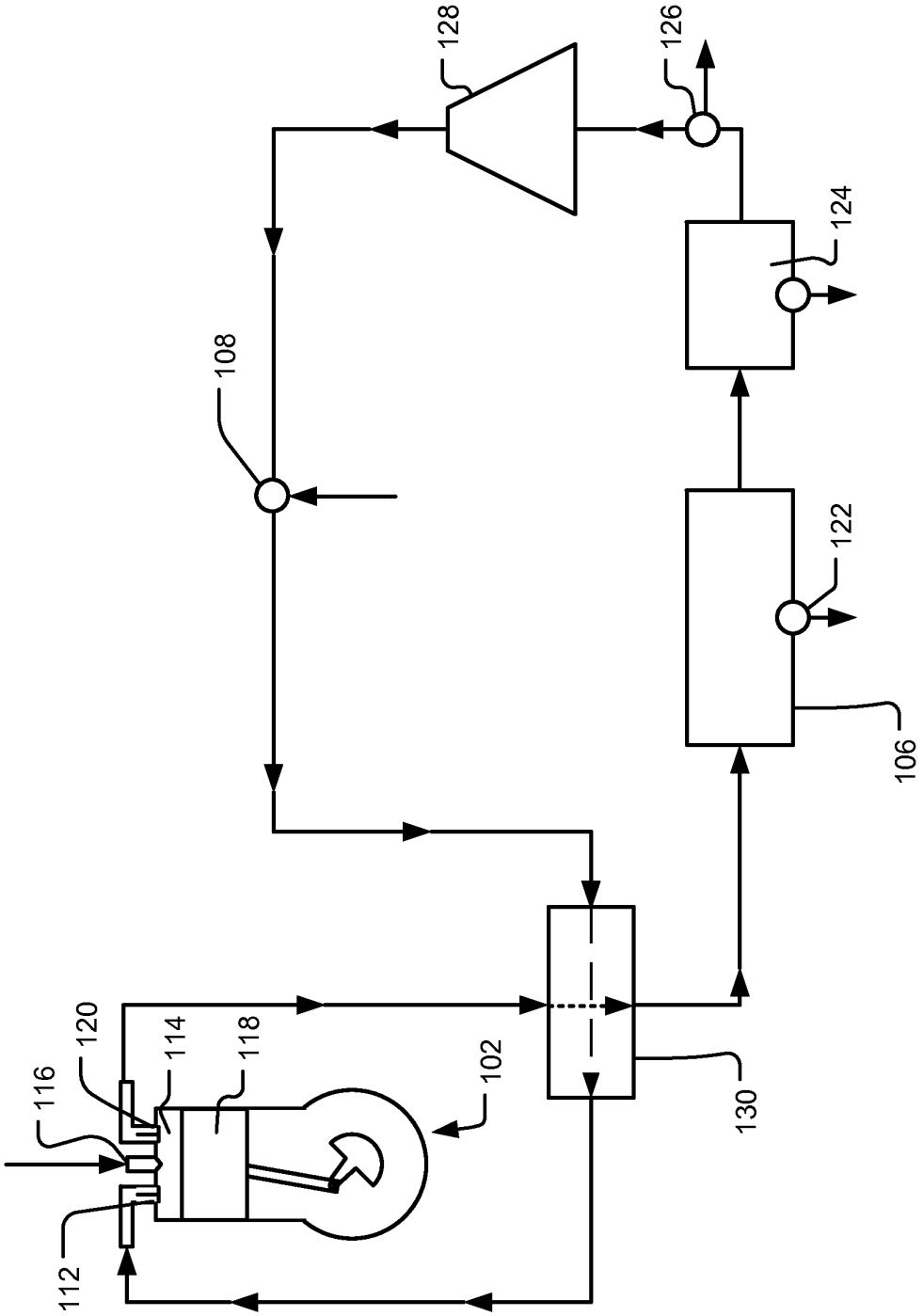

FIG. 1B

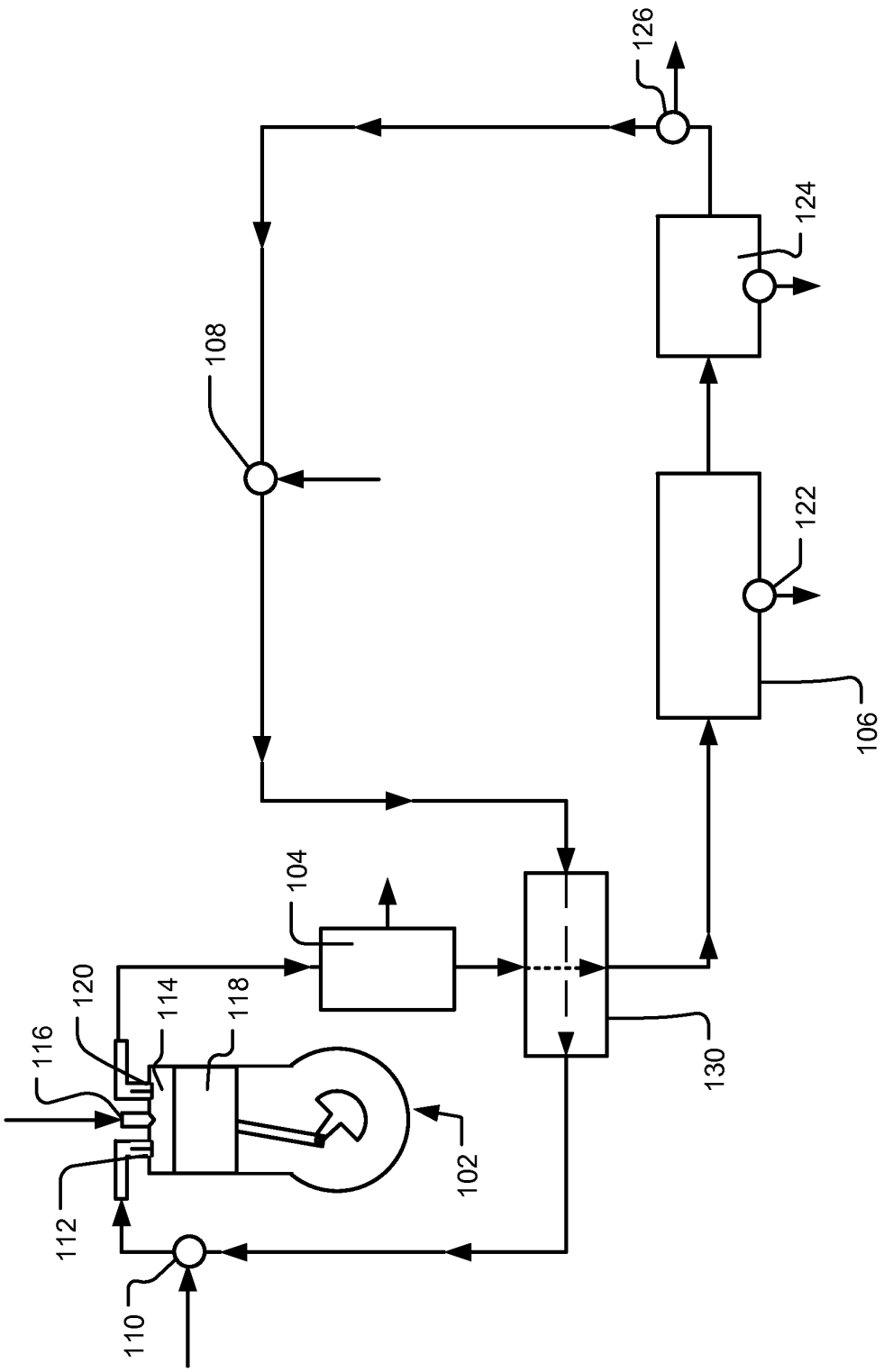

FIG. 1C

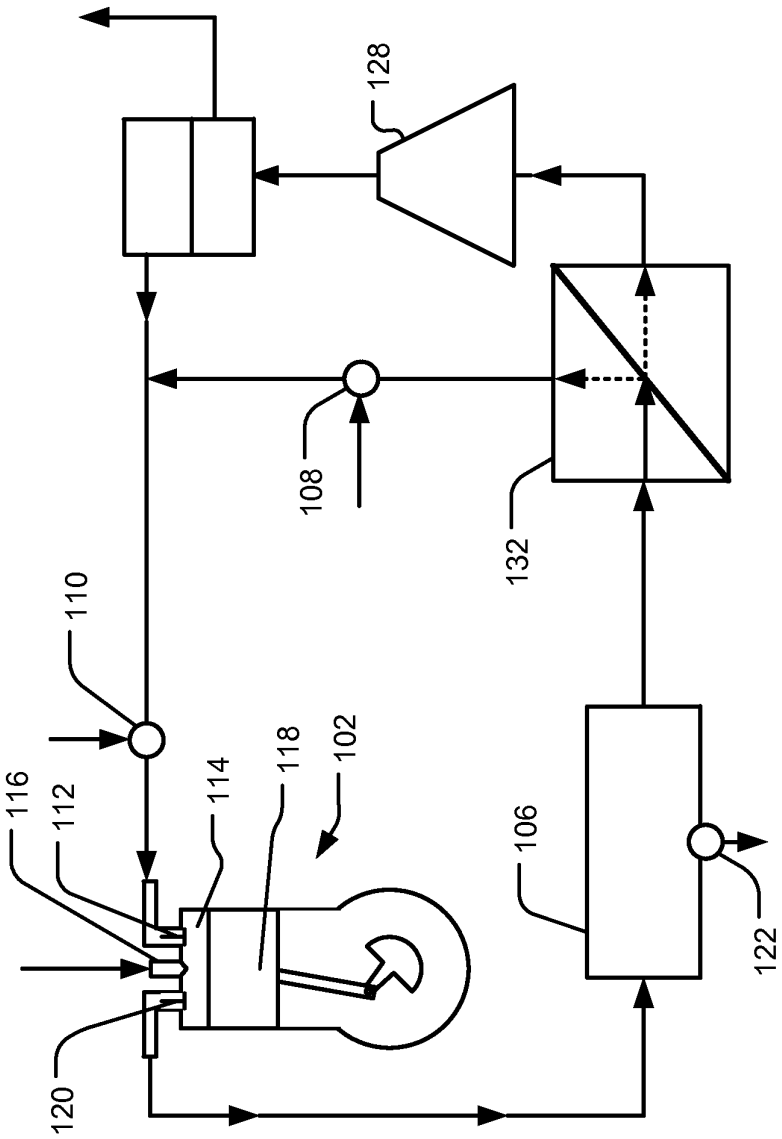

FIG. 1D

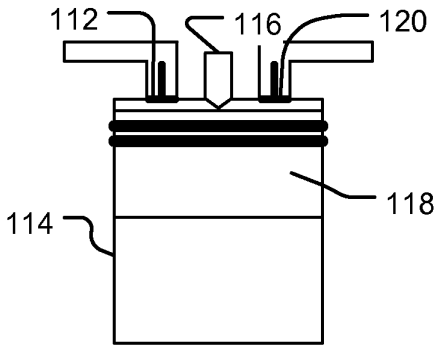

FIG. 2A

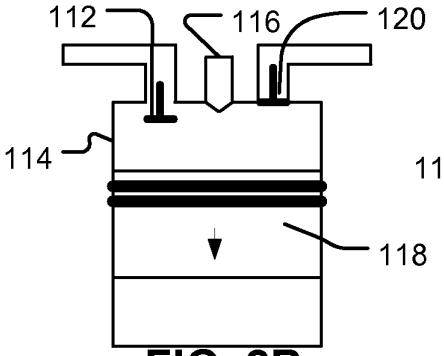

FIG. 2B

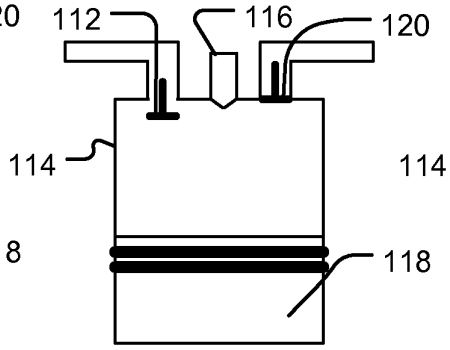

FIG. 2C

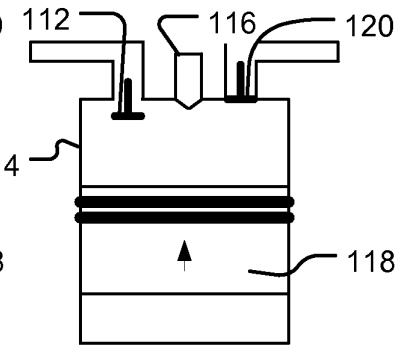

FIG. 2D

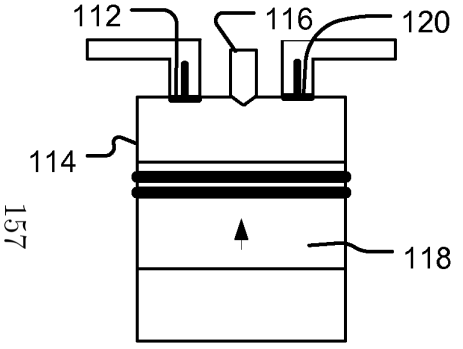

FIG. 2E

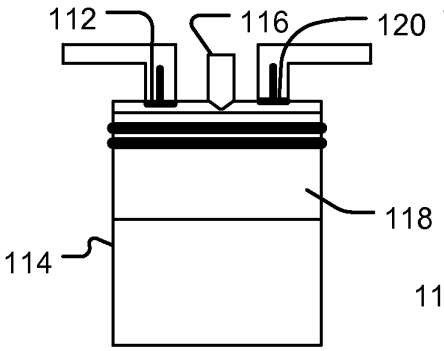

FIG. 2F

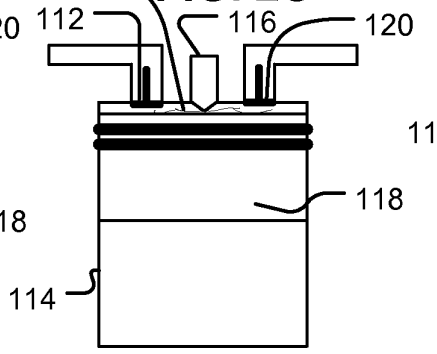

FIG. 2G

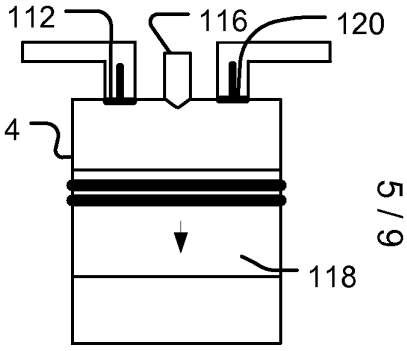

FIG. 2H

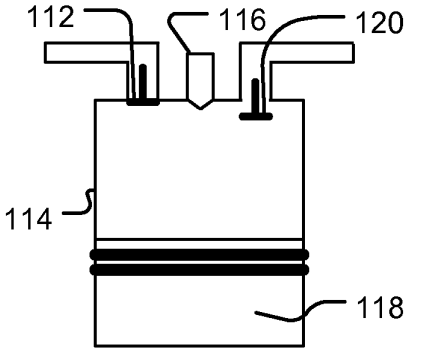

FIG. 2I

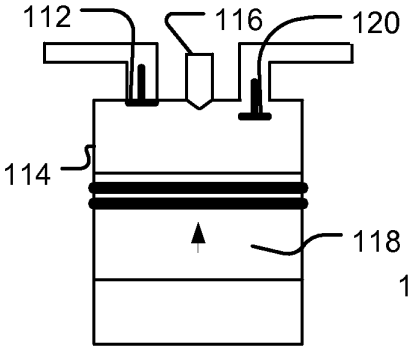

FIG. 2J

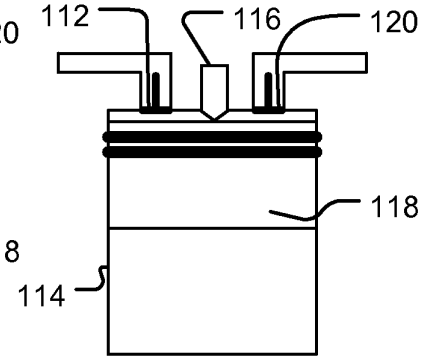

FIG. 2K

FIG. 2L

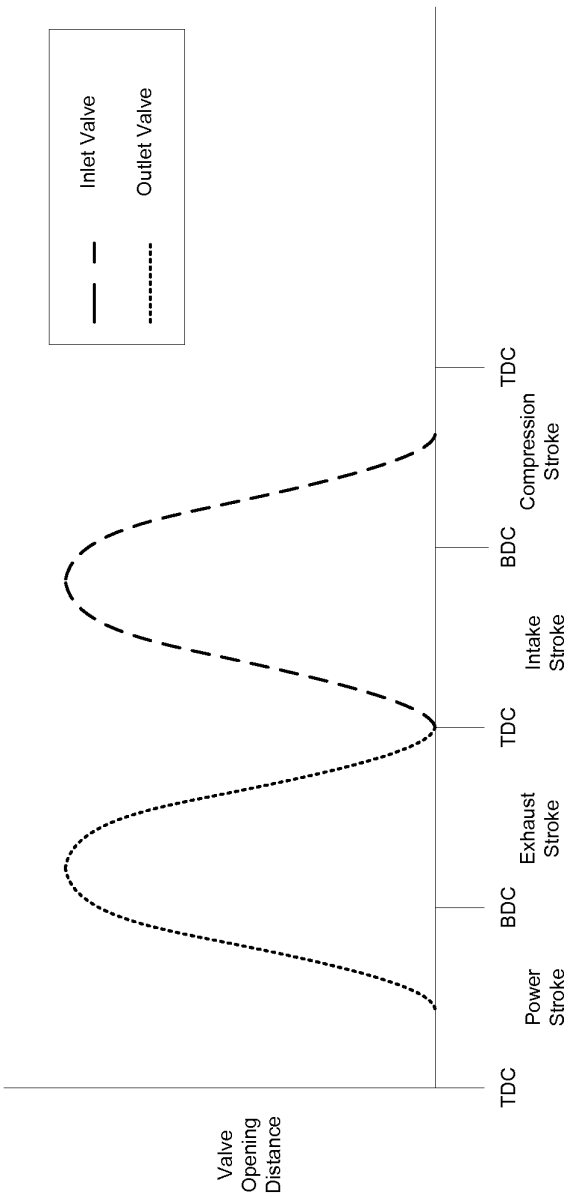
Inlet Valve
Outlet Valve
Valve Opening Distance
TDC
Power Stroke
BDC
Exhaust Stroke
TDC
Intake Stroke
BDC
Compression Stroke
TDC

FIG. 2M

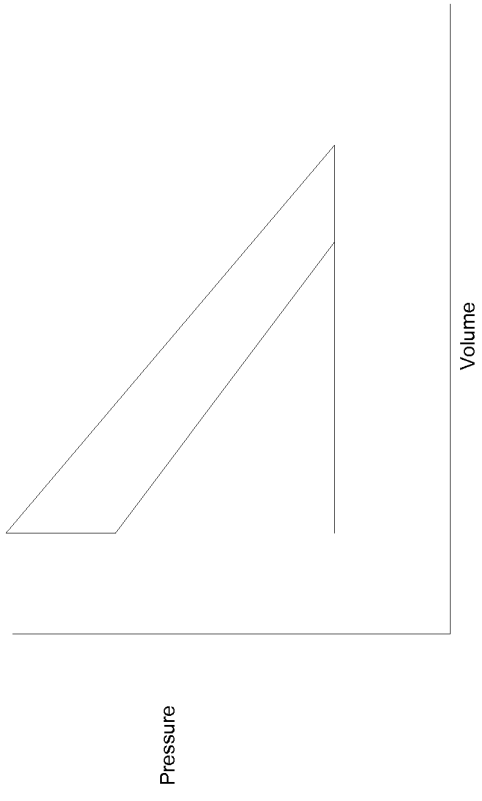
Pressure
Volume

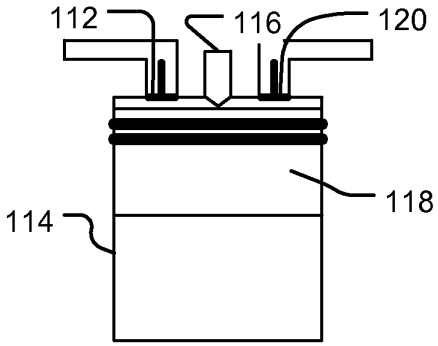

FIG. 3A

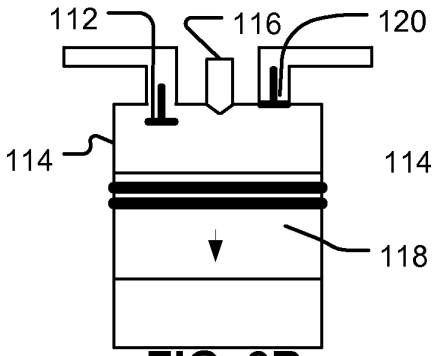

FIG. 3B

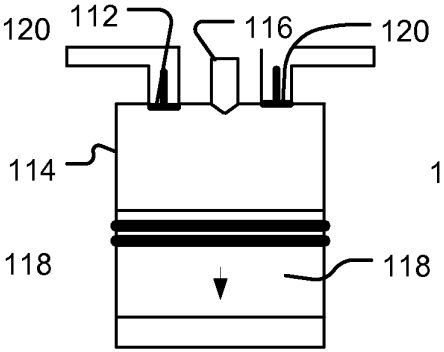

FIG. 3C

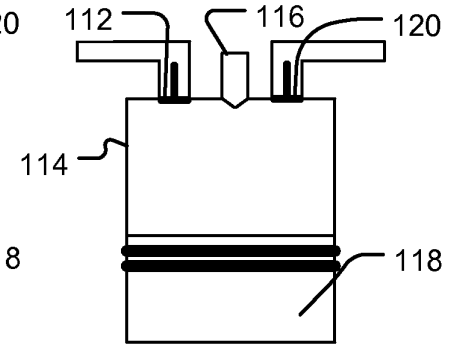

FIG. 3D

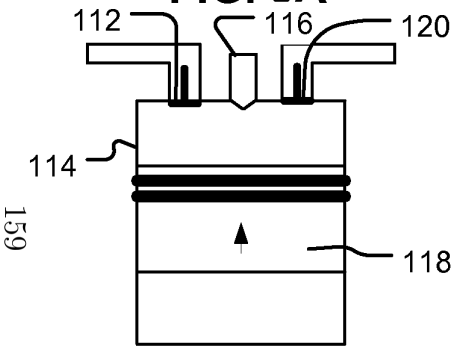

FIG. 3E

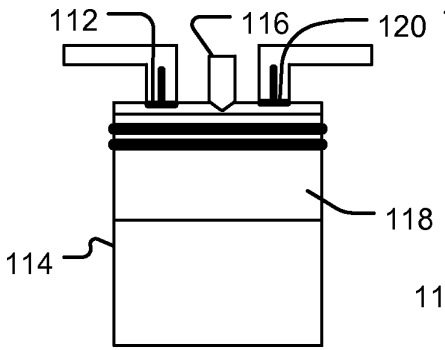

FIG. 3F

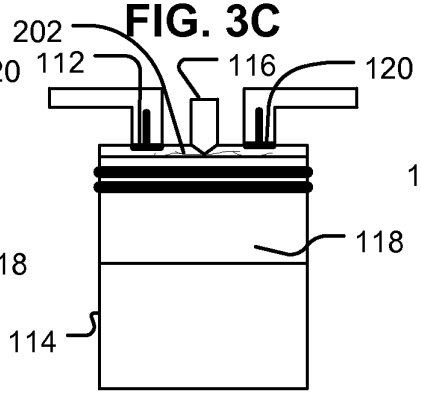

FIG. 3G

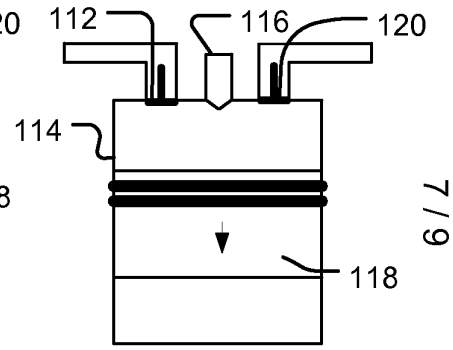

FIG. 3H

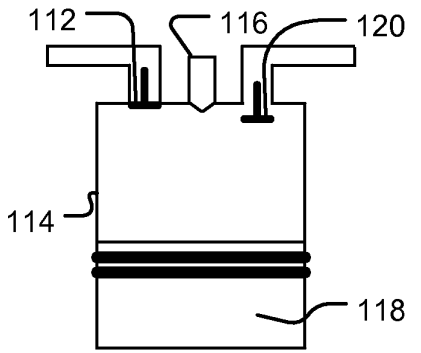

FIG. 3I

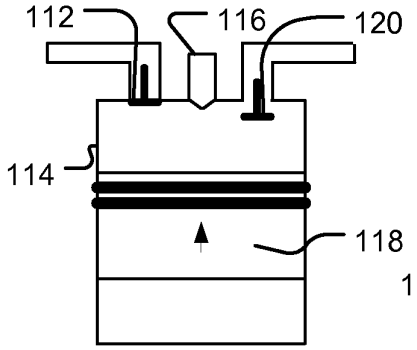

FIG. 3J

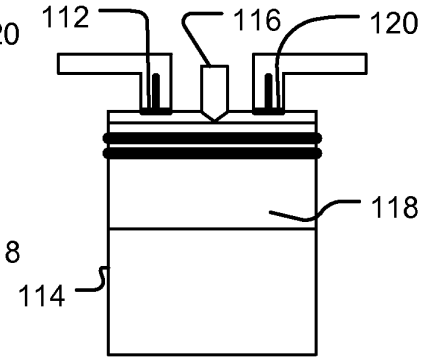

FIG. 3K

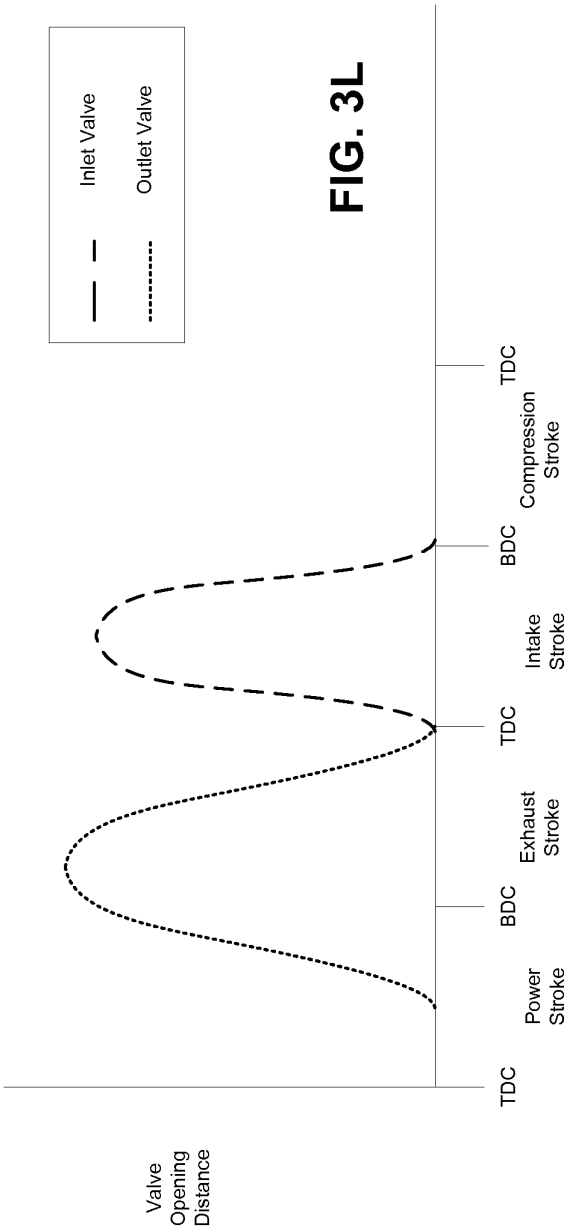
Inlet Valve
Outlet Valve
Valve Opening Distance
TDC
Power Stroke
BDC
Exhaust Stroke
TDC
Intake Stroke
BDC
Compression Stroke
TDC

FIG. 3L

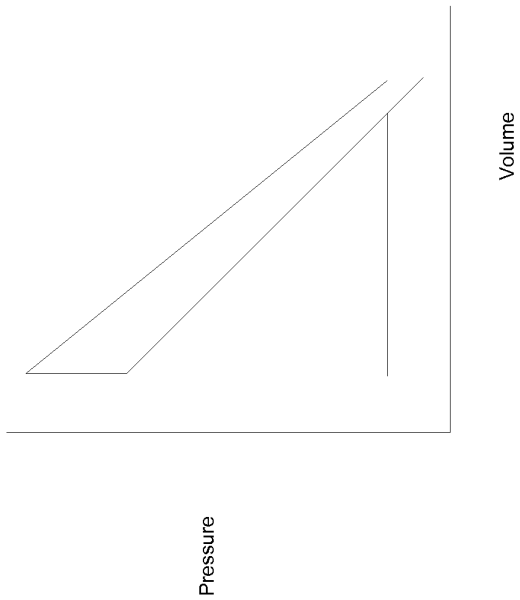
Pressure
Volume

FIG. 3M

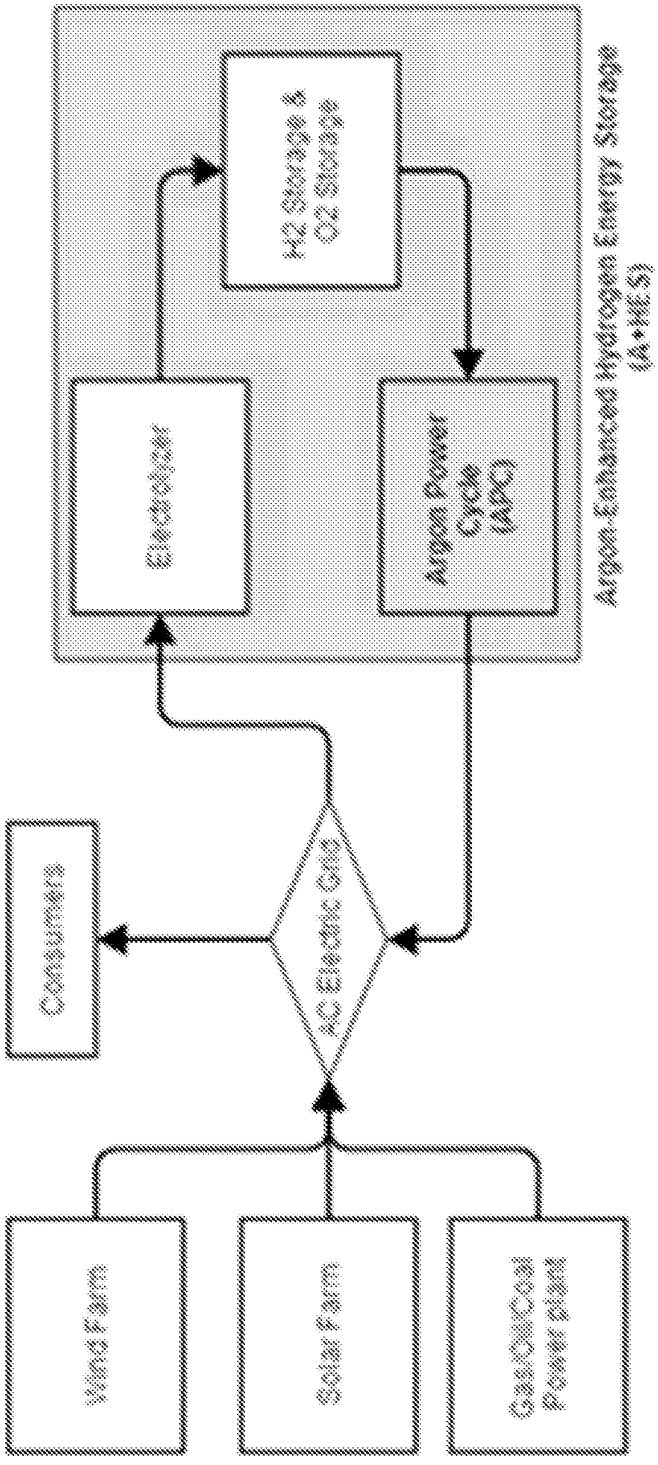
Argon-Enhanced Hydrogen Energy Storage
(A-HES)
H2 Storage &
O2 Storage
Electrolyser
Argon Power
Cycle
(APC)
Consumers
AC Electric Grid
Wind Farm
Solar Farm
Gas/Oil/Coal
Power plant

Fig. 4

Appendix B

Air separation process results

Table B.1: Air separation unit process state properties.

	Temperature °C	Pressure bar	X_{N_2} -	X_{O_2} -	X_{Ar} -
1	10	1.013	0.78	0.21	0.01
2	8	4.2	0.78	0.21	0.01
3	8	4.2	0.78	0.21	0.01
4	8	4.2	0.78	0.21	0.01
5	12	35	0.78	0.21	0.01
6	12	35	0.78	0.21	0.01
7	12	35	0.78	0.21	0.01
8	-40	34.9	0.78	0.21	0.01
9	-170	34.9	0.78	0.21	0.01
10	-191.58	1.3	0.78	0.21	0.01
11	-148.93	1.3	0.78	0.21	0.01
12	-170	4.1	0.78	0.21	0.01
13	-177.103	4.1	0.55504	0.42907	0.01588
14	-189.572	1.3	0.55504	0.42907	0.01588
15	-181.744	4	0.9945	0.0011	0.00439
16	-189.199	3.85	0.9945	0.0011	0.00439
18	-194.169	1.2	9.98E-01	3.27E-04	1.84E-03
19	-185.342	1.2	9.98E-01	3.27E-04	1.84E-03
20	-180.849	1.3	1.17E-11	0.96042	0.03958
21	9.327	1.1	9.98E-01	3.27E-04	1.84E-03
22	9.327	1.2	1.17E-11	0.96042	0.03958
23	-180.849	1.3	3.20E-12	0.97251	0.02749

Table B.2: Air separation unit process state properties continued.

	Molar flow kmol/h	Mass flow t/h	Specific Enthalpy kJ/kg	Specific Entropy kJ/kg K
1	9665.257	280	-15.369	110.191
2	9665.257	280	-18.37	-307.873
3	8988.689	260.4	-18.37	-307.873
4	676.568	19.6	-18.37	-307.873
5	676.568	19.6	-23.206	-927.729
6	20.297	0.588	-23.206	-927.729
7	656.271	19.012	-23.206	-927.729
8	20.297	0.588	-80.209	-1147.798
9	656.271	19.012	-374.73	-3207.986
10	656.271	19.012	-374.73	-3105.108
11	20.297	0.588	-175.84	-793.714
12	8988.689	260.4	-201.96	-1341.43
13	4387.446	131.242	-389.15	-3227.901
14	4387.446	131.242	-389.15	-3205.105
15	4601.243	129.158	-401.5	-3637.663
16	4601.243	129.158	-417.12	-3815.686
18	7.56E+03	2.12E+02	-2.30E+03	-1.44E+03
19	7.56E+03	2.12E+02	-2.21E+02	-1.33E+03
20	2045.218	66.088	-185.69	-1079.952
21	7.56E+03	2.12E+02	-1.66E+01	-7.65E+01
22	2045.218	66.088	-14.437	-50.08
23	64.746	2.086	-394.09	-3341.629

Appendix C

Engine data postprocessing code

Contents

- Individual CFR postprocessing data file
- Request file, extracts all relevant data and ask for extra information.
- Postprocessing Engine system data (DYNO)
- Write to file
- Postprocessing Combustion Analysis Data (CAS)
- Write CAS to file
- Write mean Cylinder Data to matlab file structure.
- Functions list
- Outputs

Individual CFR postprocessing data file

```
% Revision 7 made on 12/11/2016

% This code postprocess engine cylinder pressure, and system data for a
% given operating condition. It processes the pressure data to evaluate the
% combustion process together with the system data to output the engines
% performance in terms of power, efficiency and emissions.
%%%%%%%%%%%%%%%%%% Notes %%%%%%%%%%%%%%%%%%%%%%%%%%%%%%%%%%%%%%%%%%%%%%%
% 1. Exhaust Pressure transducer has NOW BEEN CONVERTED from V to Pa!
% 2. LP Fuel Temp and LP Fuel Press has not been converted because...
% a resisitor is required 2.49kOhm and 4.7kOhm. See manual under:
% "C:\Users\Combustion\Google Drive\_TEAM ARGON_\03. Experimental Setup...
% \04. Fuel supply system\CONFIDENTIAL INFORMATION FROM WESTPORT - DO NOT
% COPY OR PUBLISH"
% 2/18/2018
% Change line 615 nIMEP for gIMEP on etaTh!
% 2/26/2018
% Added condition when computing CylY for SYNGAS.
% Changed in cylinder mass calculation
% Changed Woschni. The cylinder are is only the cylinder wall without
```

```
% accounting for area of the piston Ap and the area of the chamber Ach.
%%%%%%%%%%%%%%%%%%%%%%%%%%%%%%%%%%%%%%%%%%%%%%%%%%%%%%%%%%%%%%%%%%%%%%%%%%%
```

Request file, extracts all relevant data and ask for extra information.

```
clear variables
clc
[CR, ind, CAD, CylV, Cyls, CylA, CylY, Cylsp, gas, CylP, CylPf, IntP,...
    Temperature, Pressure, Flow, Emissions, Dyno, Control,DYNO] =
        extractTDMS;
```

Postprocessing Engine system data (DYNO)

```
DYNO = BrakeAnalysis(DYNO); %
[DYNO_Summary] = dynosum(DYNO);
```

Write to file

```
dynofile(DYNO, DYNO_Summary);
```

Postprocessing Combustion Analysis Data (CAS)

```
%[CAS] = CombAnalysis(
%[CAS_Summary] = datasum(CAS)
%[nHRR, gHRR, nHR, gHR, CylT, CylM] = PressAnalysis(ind,CAD,CylV,CylA,CylP,
    IntP,CylY,DYNO);
%%%%% Constant Cylinder mass CylM = mIVC -> NetHRR
[CYL, CAS, ind] = PressAnalysis(ind,CAD,CylV,CylPf,CylY,CylA,DYNO);
[CAS_Summary] = cassum(CAS);
```

Write CAS to file

```
casfile(CAS, CAS_Summary);
```

Write mean Cylinder Data to matlab file structure.

```
M = table(CAD, CylV, CylA, Cyls, Cylsp, mean(CylPf,2),mean(IntP,2),...
    mean(CYL.pmot,2), mean(CYL.CylTc,2),mean(CYL.Cylm,2),...
    mean(CYL.dnQ,2), mean(CYL.nQ,2),...
    mean(CYL.hc,2), mean(CYL.dQw,2), mean(CYL.Qw,2));
```

```
M.Properties.VariableNames = {'CAD' 'Vol' 'Area' 's' 'sp' 'P' 'IntP'...
    'Pmot' 'T' 'm' 'dnQ' 'nQ' 'hc' 'dQw' 'Qw'};
M.Properties.VariableUnits = {'CAD' 'm3' 'm2' 'm' 'm/s' 'Pa' 'Pa'...
    'Pa' 'K' 'kg' 'J/CAD' 'J' 'W/m2K' 'J/CAD' 'J'};

global Datafile
filename = strrep(Datafile,'data.tdms','Cyl_Mean.csv');
writetable(M,filename);


%%%%%%%%%%%%%%%%%%%%%%%%%%%% ---- END --- %%%%%%%%%%%%%%%%%%%%%%%%%%%%
```

Functions list

```
function [CR, ind, CAD, CylV, Cyls, CylA, CylY, Cylsp, gas, CylP, CylPf,
    IntP,...
    Temperature, Pressure, Flow, Emissions, Dyno, Control, DYNO] =
        extractTDMS
% Extracts data from data.TDMS and press.TDMS files. It finds both files
% and converts them into two Matlab extructures.

% Global variables
global Y_H2O MW_Fuel MW_WF mO2 mWF nO2 nWF dil sOFR LHV Datafile Res...
    B S l R Ap Vd Vc Ach Sp

% Request user for "*data.tdms" full filepath.
[Datafile,filepath]=uigetfile({'*data.tdms','All Files (*data.tdms)'},'
    Choose a TDMS File');

% Finds correxponding "*press.tdms" file in the same directory.
Pressfilename = strrep(Datafile,'data','press');
Pressfile=fullfile(filepath,Pressfilename);

% Extracts data from both files using "convertTDMS.m"
Data = convertTDMS(false,Datafile);
Press = convertTDMS(false,Pressfile);

%%%%%%%%%%%%%%%%%%%% Reads information from file name %%%%%%%%%%%%%%%%%%%%
try
    remain = Datafile;
catch
    remain = Pressfile;
end

% Reads each term between '_' delimiters
info = textscan(remain,' %s %s %s %s %s %s %s %s %s %s %s %s',...
```

```
    'Delimiter','_'); % Parse file info from name

INJmode = info{2}; % DI vs PFI
IGNmode = info{3}; % SI vs CI
Fuel = info{4}; % H2 vs CH4
WF = info{5}; % Air vs Ar vs CO2
CR = strrep(info{7},'CR',''); % Compression ratio

%%%%%%%%%%%%%%%%%%% Request Confirmation from User %%%%%%%%%%%%%%%%%%%%%
prompt = {'Injection mode (DI vs PFI):',...
    'Ignition mode (SI vs CI):'...
    'Fuel (H2vsCH4):',...
    'Working Fluid (Ar,N2,CO2):',...
    'Compression ratio:'};
dlg_title = 'Confirm information.'; % Dialogue title
num_lines = [1 50; 1 50; 1 50; 1 50; 1 50]; % Size of input forms
defaultans = {char(INJmode) char(IGNmode) char(Fuel) char(WF) char(CR)};
answer = inputdlg(prompt,dlg_title,num_lines,defaultans);

INJmode = answer{1}; % DI vs PFI
IGNmode = answer{2}; % SI vs CI
Fueltype = answer{3}; % H2 vs CH4
WFluid = answer{4}; % Air vs Ar vs CO2
CR = str2double(answer{5}); % Compression ratio

%%%%%%%%%%%%%%%%%%% Request Extra Information from User %%%%%%%%%%%%%%%%%
prompt = {'Encoder Resolution (CAD/tick)',...
    'Ignition offset (CAD)',...
    'Injection offset (CAD)'...
    'Cyl. Pressure Gain (bar/V)',...
    'Int. Pressure Gain (bar/V)'};

dlg_title = 'Input System Parameters '; % Dialogue title
num_lines = [1 50; 1 50; 1 50; 1 50; 1 50]; % Size of input forms
defaultans = {'0.125' '10' '0' '15' '0.2'};
answer = inputdlg(prompt,dlg_title,num_lines,defaultans);
Res = str2double(answer{1}); % [CAD/tick]
IgnOff = str2double(answer{2}); % [CAD ATDC]
InjOff = str2double(answer{3}); % [CAD ATDC]
CylP_Gain = str2double(answer{4}); % [bar/V]
IntP_Gain = str2double(answer{5}); % [bar/V]

%%%%%%%%%%%%%%%%%%%% CFR Engine Kinematics %%%%%%%%%%%%%%%%%%%%%%%%%%%%%
B = 82.5/1000; % [m]
S = 114.3/1000; %[m]
l = 254/1000; %[m]
R = 2*l/S; % [-]
```

```
IVO = -343; % [CAD ATDC]
IVC = -153; % [CAD ATDC]
EVO = 148; % [CAD ATDC]
EVC = -353; % [CAD ATDC]
ind.IVO = angle2index(IVO,Res); % [vector index]
ind.IVC = angle2index(IVC,Res); % [vector index]
ind.EVO = angle2index(EVO,Res); % [vector index]
ind.EVC = angle2index(EVC,Res); % [vector index]

% Compute the ramining kinematic parameters:
Ap = (1/4) * pi() * (B^2); % [m2] Piston Area
Vd = Ap * S; % [m3] Displacement Volume
Vc = Vd/(CR-1); % [m3] Combustion chamber Volume
Ach = (Vc/Ap) * pi()* B+ Ap; % [m2] Combustion Chamber Area (Flat head)

% Kinematics vectors
CAD(:,1) = (-360:Res:360-Res); % -360 to (360 - 1* Encoder resolution)
CylV(:,1) = Vc *(1 + 0.5 * (CR - 1) * (R + 1 - cosd(CAD) - sqrt(R^2 - sind(
    CAD).^2))); % [m3]
Cyls(:,1) = S/2*cosd(CAD)+sqrt(l^2-(S/2)^2*sind(CAD).^2); % [m]
CylA(:,1) = pi()*B*(l+S/2-Cyls); % + Ach + Ap [m2]

%%%%%%%%%%%%%%%%%% Thermodynamic Parameters %%%%%%%%%%%%%%%%%%%%%%%%%%%%%%

gas = GRI30; % Initiates a gas phase for the cylinder charge
nsp = nSpecies(gas); % Number of species on the library
% Search for the indexes of the species of interest
ind.CH4 = speciesIndex(gas,'CH4');
ind.H2 = speciesIndex(gas,'H2');
ind.O2 = speciesIndex(gas,'O2');
ind.N2 = speciesIndex(gas,'N2');
ind.Ar = speciesIndex(gas,'Ar');
ind.CO2 = speciesIndex(gas,'CO2');
ind.H2O = speciesIndex(gas,'H2O');
ind.CO = speciesIndex(gas,'CO');
ind.NO2 = speciesIndex(gas,'NO2');

%%%%%%%%%%%%%%%%%%%% Extract Pressure Data %%%%%%%%%%%%%%%%%%%%%%%%%%%%%%%%
% Split the pressure data [V] in cycles based on encoder position data [
    ticks].
% Interpolates possible pressure missing values based on available data for
     each
% cycle using interp1 function and 'pchip' method. Also, it scales the
% signals to pressure values. FInally, it returns the mean cylinder and
% cylinder pressure traces.

EC = Press.Data.MeasuredData(3).Data * Res; % Enc ticks * Enc Resolution
```

```
Pp = Press.Data.MeasuredData(4).Data * CylP_Gain * 1e5; % Pegged Cyl.Press
    [Pa]
IP = Press.Data.MeasuredData(6).Data * IntP_Gain * 1e5; % Int.Press [bar]

% Allocates memory
Nc = sum(diff(EC)<-710)+1; % number of cycle in the vector
CylP = zeros(numel(CAD),Nc); % In Cylinder Pressure Vector
IntP = zeros(numel(CAD),Nc); % Intake Pressure Vector

% Split pressure trace into cycles by checking when the vector EC changes
% signs. it outputs 2 [CAD x #cycles] matrix containing all pressure traces

j = 1; % Cycle #
jjlast = 0; % First index
for jj = 2:1:length(EC)
    if (EC(jj-1)-EC(jj)>710)
        cad = EC((jjlast+1):(jj-1));
        ECc = zeros(numel(cad),1);
        ECc(1)= cad(1);
        for i=2:1:numel(cad)
            if cad(i)-ECc(i-1)~= Res
                ECc(i)= ECc(i-1)+Res;
            else
                ECc(i)= cad(i);
            end
        end
        [angle, index] = unique(ECc);
        %[angle, index] = unique(EC((jjlast+1):(jj-1)));
        Cylpeg = Pp((jjlast+1):(jj-1));
        Intpeg= IP((jjlast+1):(jj-1));
        CylP(:,j) = interp1(angle,Cylpeg(index),CAD,'pchip'); % [Pa]
        IntP(:,j) = interp1(angle,Intpeg(index),CAD,'pchip'); % [Pa]
        jjlast = jj-1;
        j = j + 1;


    elseif jj == length(EC) % Last cycle
        cad = EC((jjlast+1):(jj));
        ECc = zeros(size(cad));
        ECc(1)= cad(1);
        for i=2:1:numel(cad)
            if cad(i)-ECc(i-1)~= Res
                ECc(i)= ECc(i-1)+Res;
            else
                ECc(i)= cad(i);
            end
        end
```

```
        [angle, index] = unique(ECc);
        %[angle, index] = unique(EC((jjlast+1):(jj)));
        Cylpeg = Pp((jjlast+1):(jj));
        Intpeg = IP((jjlast+1):(jj));
        CylP(:,j) = interp1(angle,Cylpeg(index),CAD,'pchip'); %[Pa]
        IntP(:,j) = interp1(angle,Intpeg(index),CAD,'pchip'); %[Pa]
    end

end

%CylP_mean = mean(CylP,2);
%IntP_mean = mean(IntP,2);

% Find misfires and clean pressure trace for SYNGAS runs.
if strcmp(Fueltype,'SYNGAS') == 1
pp = max(CylP);
meanpp = mean(pp(1));
xx=1;

while pp(xx)> (meanpp(xx)-8e5) && xx < length(pp)
    xx = xx + 1;
    meanpp(xx) = mean(pp(1:xx));
end
Nc = xx-1;
else
end

%---------------------Fourier Transform and Filter-------------------------
% Fourier Transform filter: Only frequencies below 0.5 Hz
CylPf = zeros(numel(CAD),Nc); % Filtered In Cylinder Pressure Vector
for jj = 1:1:Nc
[CylPf(:,jj)] = fftf(CAD,CylP(:,jj),0.5,250)*max(CylP(:,jj));
end
% ------------------------------------------------------------------

%%%%%%%%%%%%%%%%%%%%%%Extract System Data %%%%%%%%%%%%%%%%%%%%%%%%%%%%%%%%
% Extract all the data to a table call DYNO.
% Temp, Press, Flow, Ctrl, Emiss, Eng are the data categories.

% Temperature values
 TempCoolantHot = Data.Data.MeasuredData(20).Data + 273; % [K]
 TempCoolantCold = Data.Data.MeasuredData(21).Data+ 273; % [K]
 TempCoolantEng = Data.Data.MeasuredData(25).Data + 273; % [K]
 TempIntake = Data.Data.MeasuredData(22).Data + 273; % [K]
 TempWaterIn = Data.Data.MeasuredData(23).Data + 273; % [K]
 TempWaterOut = Data.Data.MeasuredData(24).Data + 273; % [K]
 TempExhaust = Data.Data.MeasuredData(26).Data + 273; % [K]
```

```
 %LPFuel = Data.Data.MeasuredData(14).Data; % [V] Not valid. A 10kOhm
     resistor needs to be put in place.
    Temperature = table(TempCoolantHot,TempCoolantCold,TempCoolantEng,
       TempIntake,...
     TempWaterIn, TempWaterOut,TempExhaust); % LPFuel (add when fixed)
    Temperature.Properties.VariableUnits = {'K' 'K' 'K' 'K' 'K' 'K' 'K'}; %
        'K' add when LPFuel sensor fixed

% Slow Pressure values
 PressHPFuel = ((Data.Data.MeasuredData(12).Data.*1000 - 500)./15.38)*1e5;
     % [Pa]
 PressExhaust = Data.Data.MeasuredData(15).Data * 30/(5.025 - (-0.018)) *
     6894.76; % [Pa] -> 1 psia = 6894.76 Pa; Sensor calibration: Min scale
     -0.018 V @ 0 psia Max scale 5.025V @ 30psia
 % LPFuel = ((Data.Data.MeasuredData(13).Data./5 - 6.52)./0.0696)*1000; %
     Vout/Vcc = K1*P+K2 -> P = [kPa]; % [V]
    Pressure = table(PressHPFuel,PressExhaust);
    Pressure.Properties.VariableUnits = {'Pa' 'Pa'}; % 'Pa' add when LP
       Fuel sensor fixed

% Dyno values
 EngAmp = Data.Data.MeasuredData(16).Data * (30 / 5); % [A] 30 A dyno
     nominal current. 5V maximum signal range.; % [V]
 EngRPM = Data.Data.MeasuredData(17).Data * (1750 / 5); % [rpm] 1750 rpm
     dyno mnominal speed. 5V maximum signal range.; % [V]
 EngT = Data.Data.MeasuredData(18).Data * (101.02 / 6.6) * 1.05 * 1.35582 *
      (-1); % [Nm] 1.05 ft arm length, 1lbft=1.35582Nm, 6.6V = 101.02 lb; %
     [V]
 EngSpeed = EngRPM * 2 * pi() / 60; % [rad/s]
 EngSp = 2 * S * EngSpeed; % [m/s] Mean piston speed
 EngPWR = EngT .* EngSpeed; % [W]
 DynoPWR = EngAmp * 440; % [W] 440 V is the Dyno nominal voltage.
 DynoT = DynoPWR ./ EngSpeed; % [Nm]
    Dyno = table(EngRPM, EngSp, EngT, EngPWR, EngAmp, DynoPWR, DynoT);
    Dyno.Properties.VariableUnits = {'rpm' 'm/s' 'Nm' 'W' 'A' 'W' 'Nm'};

% Mass flow values
 FlowWF = Data.Data.MeasuredData(32).Data/1000; % [kg/s] Working Fluid (WF)
 FlowFuel = Data.Data.MeasuredData(33).Data/1000; % [kg/s]
 Flowfuel = FlowFuel ./ (EngRPM / 2 / 60); % [kg/cycle]
 FlowO2 = Data.Data.MeasuredData(34).Data/1000; % [kg/s]
 FlowAir = Data.Data.MeasuredData(48).Data/1000; % [kg/s]
 FlowCycle = (FlowWF + FlowFuel + FlowO2 + FlowAir) ./ (EngRPM / 2 / 60); %
      [kg/cycle]
    Flow = table(FlowFuel, Flowfuel, FlowAir, FlowO2, FlowWF, FlowCycle);
    Flow.Properties.VariableUnits = {'kg/s' 'kg/cycle' 'kg/s' 'kg/s' 'kg/s'
        'kg/cycle'};
```

```
% Emission values
 EmissTHC = Data.Data.MeasuredData(40).Data; % [ppm]
 EmissCO = Data.Data.MeasuredData(41).Data; % [ppm]
 EmissNOx = Data.Data.MeasuredData(42).Data; % [ppm]
 EmissO2 = Data.Data.MeasuredData(44).Data; % [%]
 EmissCO2 = Data.Data.MeasuredData(46).Data; % [%]
    Emissions = table(EmissTHC, EmissO2, EmissCO, EmissCO2, EmissNOx);
    Emissions.Properties.VariableUnits = {'ppm' '%' 'ppm' '%' 'ppm'};

% Control values
 CtrlSOI = Data.Data.MeasuredData(37).Data + InjOff; % [CAD]
 ind.SOI = angle2index(CtrlSOI(1),Res); % [vector index]
 CtrlINJPW = (Data.Data.MeasuredData(38).Data) * mean(EngRPM) * 360 / 60 /
     1000; % [CADs]
 ind.EOI = ind.SOI + round(CtrlINJPW(1)/Res);
 CtrlIGN = Data.Data.MeasuredData(35).Data + IgnOff; % [CAD]
 ind.IGN = angle2index(CtrlIGN(1),Res); % [vector index]
 CtrlIGNPW = Data.Data.MeasuredData(36).Data * mean(EngRPM) * 360 / 60 /
     1000; % [CADs]
    Control= table(CtrlSOI,CtrlINJPW, CtrlIGN, CtrlIGNPW);
    Control.Properties.VariableUnits = {'CAD ATDC' 'CAD' 'CAD ATDC' 'CADs
        '};

% Creates the DYNO data table!
DYNO = table(TempCoolantHot,TempCoolantCold,TempCoolantEng,...
    TempIntake, TempWaterIn, TempWaterOut,TempExhaust,...
    PressHPFuel,PressExhaust,...
    EngRPM, EngSp, EngT, EngPWR, EngAmp, DynoPWR, DynoT,...
    FlowFuel, Flowfuel, FlowAir, FlowO2, FlowWF, FlowCycle,...
    EmissTHC, EmissO2, EmissCO, EmissCO2, EmissNOx, ...
    CtrlSOI,CtrlINJPW, CtrlIGN, CtrlIGNPW);
DYNO.Properties.VariableUnits = {'K' 'K' 'K' 'K' 'K' 'K' 'K'...
    'Pa' 'Pa'...
    'rpm' 'm/s' 'Nm' 'W' 'A' 'W' 'Nm'...
    'kg/s' 'kg/cycle' 'kg/s' 'kg/s' 'kg/s' 'kg/cycle'...
    'ppm' '%' 'ppm' '%' 'ppm'...
    'CAD ATDC' 'CAD' 'CAD ATDC' 'CADs'};
DYNO.Properties.VariableDescriptions = {...
    'Temperature (RTD) Coolant pre HX'...
    'Temperature (RTD) Coolant post HX'...
    'Temperature (TC) at pre HX'...
    'Temperature (RTD) Intake port'...
    'Temperature (TC) City water In'...
    'Temperature (TC) City water Out'...
    'Temperature (TC) Exhaust port'...
    'Pressure HP Fuel line'...
```

```
    'Pressure Exhaust manifold'...
    'Engine rpm (dyno)'...
    'Engine mean piston speed (Sp)'... % recently added
    'Engine brake torque (BT)'...
    'Engine brake power (BP)'...
    'Dynamometer current (@ 440V)'...
    'Dynamometer power (eP)'...
    'Dynamometer torque (eT)'...
    'Fuel mass flow rate'...
    'Fuel flow per cycle'... should not be included here!
    'Air mass flow rate'...
    'O2 mass flow rate'...
    'Working fluid mass flow rate'...
    'Mass flow per cycle'... should not be included here!
    'Emissions THC'...
    'Emissions O2'...
    'Emissions CO'...
    'Emissions CO2'...
    'Emissions NO2'...
    'Start of injection (INJ)'...
    'Injection Pulse Width (PW)'...
    'Ignition timing (IGN)'...
    'Spark dwell'};

% Cut DYNO table
DYNO([Nc+1:end],:)=[];

%%%%%%%%%%%%%%%% Computes piston spedd with the given rpm %%%%%%%%%%%%%%%%
Sp = mean(DYNO.EngSp);
Cylsp(:,1) = Sp * pi / 2 * sind(CAD) .* (1 + cosd(CAD)./sqrt(R^2 - sind(CAD
    ).^2));
%%%%%%%%%%%%%%%% Gas composition and Thermodynamic statevariables %%%%%%%%%
% Select fuel and working fluid based on previus user input
    switch Fueltype
        case 'H2'
            ind.Fuel = ind.H2;
            Y_H2O = 9; % 9 grams of water for every 1 gr of H2
            MW_Fuel = 0; % Hydrogen is not measured at exhaust so "0"
            LHV = 119.96e6; % [J/kg]
            sOFR = 8; % 8gr O2 per 1 gr H2
        case 'CH4'
            ind.Fuel = ind.CH4;
            Y_H2O = 2.25; % 2.25 grams of water for every 1 gr of CH4
            MW_Fuel = 16; % Methane molecular weight [kg/kmol]
            LHV = 50e6; % [J/kg]
            sOFR = 4; % 4 gr O2 per 1 gr CH4
        case 'SYNGAS'
```

```
            ind.Fuel = ind.H2;
            ind.Fuel2 = ind.CO;
            Y_H2O = 0.6; % 0.6 grams of water for every 1 gr of (H2+CO)
            MW_Fuel = 15; % SYNGAS 50%H2 50%CO molecular weight [kg/kmol]
            LHV = 17.4e6; % [J/kg]
            sOFR = 1.06667; % 32 gr O2 per 30 gr (H2 + CO)


    end
    mF = DYNO.FlowFuel;
    % Select Working Fluid
    switch WFluid
        case 'Ar'
            ind.WF = ind.Ar;
            mO2 = DYNO.FlowO2;
            nO2 = mO2/32;
            mWF = DYNO.FlowWF;
            MW_WF = 40;
            nWF = mWF./MW_WF;
            dil = nO2./(nO2+nWF);
        case 'CO2'
            ind.WF = ind.CO2;
            mO2 = DYNO.FlowO2;
            nO2 = mO2/32;
            mWF = DYNO.FlowWF;
            MW_WF = 44;
            nWF = mWF./MW_WF;
            dil = nO2./(nO2+nWF);
        case {'CAir','Air'}
            ind.WF = ind.N2;
            mO2 = 1/4.29 * DYNO.FlowAir; % 21% O2 79% N2 (%mol) -> 23.3% O2
                (%mass)
            nO2 = mO2/32;
            mWF = DYNO.FlowAir - mO2;
            MW_WF = 28;
            nWF = mWF./MW_WF;
            dil = nO2./(nO2+nWF);
    end
%%%%%%%%%%%%%% Mass fractions "CylY" base on flow rates %%%%%%%%%%%%%%%%%
% The mass fraction are computed as a direct relation to the mass flow
% ratios. If differenciates between DI and PFI operation to estimate the
% initial mass fraction at IVC.
% A more accureta way, woudl assume a mixture of fresh charge and cylinder
% trap burn gases (assuming stoichiometric burn). This would be amixture of
% O2, WF, Fuel, CO2 and H2O.

% Declare vector:
```

```
CylY = zeros(nsp,Nc); % Mass fraction vector
    switch INJmode
        case 'DI'
            CylY(ind.O2,:) = mO2 ./ (mO2 + mWF); % [%mass]
            CylY(ind.WF,:) = 1 - CylY(ind.O2,:); % [%mass]
        otherwise
            if strcmp(Fueltype,'SYNGAS') == 1
            CylY(ind.Fuel,:) = (mF ./ (mO2 + mWF + mF))*(2/30); % [%mass]
                fraction of H2
            CylY(ind.Fuel2,:) = (mF ./ (mO2 + mWF + mF))*(28/30); % [%mass]
                fraction of CO
            CylY(ind.O2,:) = mO2 ./ (mO2 + mWF + mF); % [%mass]
            CylY(ind.WF,:) = 1 - CylY(ind.O2,:)- CylY(ind.Fuel,:)- CylY(ind.
                Fuel2,:); % [%mass]
            else
            CylY(ind.Fuel,:) = mF ./ (mO2 + mWF + mF); % [%mass]
            CylY(ind.O2,:) = mO2 ./ (mO2 + mWF + mF); % [%mass]
            CylY(ind.WF,:) = 1 - CylY(ind.O2,:)- CylY(ind.Fuel,:); % [%mass]
            end
    end
end

function [DYNO] = BrakeAnalysis(DYNO) % [phi, AFR, sAFR, BSTHC, BSO2, BSCO,
     BSCO2, BSNOx, FuelMEP, CLMEP, QMEP, BSFC, BFCE, BMEP, ]Dyno,Flow)
global Y_H2O MW_Fuel MW_WF mO2 mWF sOFR dil Vd LHV

% Gas Analyzer and Mass flow Air Fuel ratio (Heywood1988).
K = 3.5; % Equilibrium constant water gas shift reaction
y = 4; % Hydrogen to Carbon ratio of Methane
Mm = (mO2 + mWF) ./ (mO2/32 + mWF/MW_WF); % Molecular weight of the working
     fluid
vWF = 1 ./ dil .* (1 - dil) + 1; % Accounts for different working fluids

% Dry mole fractions of Gas Analyzer species in %
xTHC = DYNO.EmissTHC / 1e4; % [%]
xO2 = DYNO.EmissTHC; % [%]
xCO = DYNO.EmissTHC / 1e4; % [%]
xCO2 = DYNO.EmissTHC; % [%]
xNOx = DYNO.EmissTHC / 1e4; % [%]
xH2O = 0.5 .* y .* (xCO2 + xCO) ./ (xCO ./ (K .* xCO2) + 1); % [%]

% Air Fuel ratio based on dry basis molar concentration
AFR = vWF .* ( Mm ./ MW_Fuel).*(xCO2 + 0.5 * xCO + 0.5 * xH2O + xNOx + xO2)
    ./(xTHC + xCO + xCO2); % Based on Emissions
OFR = mO2 ./ DYNO.FlowFuel;
phi = OFR ./sOFR; % Based on FLow Rates
sAFR = phi .* AFR; % Stoichiometric AFR for a different mixture
```

```
%%%%%%% Combustion efficiency (Fuel Eneegy In - Emissions Energy Out)%%%%%

Qf = DYNO.FlowFuel .* LHV; % [W]

% The concentration of H2 has been computed assuming that per each mol CO2
% there are 2 mol H2O. and using the equation K = xCO*xH2O / xCO2*xH2 ->
% xH2 = 2*xCO / K; This also assumes that THC is all CH4.
m_dry = (mO2 + mWF + DYNO.FlowFuel)-Y_H2O * DYNO.FlowFuel; % Y_H2O is the
    mass ratio of stoich fuel to water
MWexh = (DYNO.EmissTHC / 1e6 * MW_Fuel + DYNO.EmissO2 /100 * 32 + DYNO.
    EmissCO / 1e6 * 28 ...
+ DYNO.EmissCO2 / 100 * 44 + DYNO.EmissNOx / 1e6 * (0.1 * 46+0.9 * 30) +...
(1-(DYNO.EmissTHC / 1e6 + DYNO.EmissO2 /100 + DYNO.EmissCO / 1e6 ...
+ DYNO.EmissCO2 / 100 + DYNO.EmissNOx / 1e6 ))*MW_WF);

Qem = m_dry ./ MWexh .* ((DYNO.EmissTHC * 1e-6 * MW_Fuel) * LHV...
    + (DYNO.EmissCO * 1e-6 * 28) * 10.112e6...
    + (DYNO.EmissCO * 1e-6 * 2 / K)* 2 * 119.19e6); % [W]

%%%%%%%%%%%%%%%%%%%% Brake Emissions %%%%%%%%%%%%%%%%%%%%%%%%%%%%%%%%%%%
BSTHC = (m_dry .* (DYNO.EmissTHC* 1e-6 * MW_Fuel) ./ MWexh )*1e6 ./ DYNO.
    EngPWR * 3600; % [g/kWh] (% 1e4 ppm = 1% = 0.01)
BSO2 = (m_dry .* (DYNO.EmissO2 /100 * 32) ./ MWexh)*1e6 ./ DYNO.EngPWR *
    3600; % [g/kWh]
BSCO = (m_dry .* (DYNO.EmissCO * 1e-6 * 28) ./ MWexh)*1e6 ./ DYNO.EngPWR *
    3600; % [g/kWh] 1e4 ppm = 1%
BSCO2 = (m_dry .* (DYNO.EmissCO2 /100 * 44) ./ MWexh)*1e6 ./ DYNO.EngPWR *
    3600; % [g/kWh]
BSNOx = (m_dry .* (DYNO.EmissNOx * 1e-6 * (0.1 * 46+0.9 * 30))./ MWexh)*1e6
     ./ DYNO.EngPWR * 3600; % [g/kWh] 1e4 ppm = 1%

%%%%%%%%%%%%%%%%%%%% Brake Performance %%%%%%%%%%%%%%%%%%%%%%%%%%%%%%%%%%%
FuelMEP = Qf *2 ./ (DYNO.EngRPM / 60 * Vd)*1e-5; % [bar] Fuel Energy
CLMEP = Qem *2 ./ (DYNO.EngRPM / 60 * Vd)*1e-5; % [bar] Combustion Losses
QMEP = FuelMEP - CLMEP; % [bar] Effective energy provided to the cylinder
BSFC = DYNO.FlowFuel./DYNO.EngPWR * 1000 * 1000 * 3600; % [g/kWh] kg/s / W
    * 1000W/kW * 1000 g/kg * 3600 s/hr
BFCE = DYNO.EngPWR ./ (DYNO.FlowFuel * LHV); % [%]
BMEP = DYNO.EngPWR * 2 ./ (DYNO.EngRPM / 60 * Vd)*1e-5; % [bar]

% Store in DYNO table

BRAKE = table(phi, AFR, sAFR,...
    BSTHC, BSO2, BSCO, BSCO2, BSNOx,...
    FuelMEP, CLMEP, QMEP, BSFC, BFCE, BMEP);
BRAKE.Properties.VariableUnits = {'-' '-' '-'...
```

```
    'g/kWh' 'g/kWh' 'g/kWh' 'g/kWh' 'g/kWh'...
    'bar' 'bar' 'bar' 'g/kWh' '%' 'bar'};
BRAKE.Properties.VariableDescriptions = {...
    'Equivalence ratio (based on mass flow rates)'...
    'Air to Fuel Ratio based on Emissions (only valid for CH4)'...
    'Stoichiometric AFR based on oxygen emissions (only valid for CH4)'...
    'Brake specific THC emissions (BSTHC)'...
    'Brake specific O2 emissions (BSO2'...
    'Brake specific CO emissions'...
    'Brake specific CO2 emissions'...
    'Brake specific NOx emissions'...
    'Fuel energy mean effective pressure (FuelMEP)'...
    'Combustion losses mean effective pressure (CLMEP)'...
    'Energy available mean effective pressure (QMEP)'...
    'Brake specific fuel consumption (BSFC)'...
    'Brake fuel conversion efficiency (BFCE)'...
    'Brake mean effective pressure (BEMP)'};

DYNO = [DYNO, BRAKE];


end

function [DYNO_Summary] = dynosum(DYNO)
% Generates the statistics for each measurement over all cycles.
% This includes: Mean, STD, Median, Min, Max, CV and LNV.
Units = {DYNO.Properties.VariableUnits{1:1:end}}.'; % variable units
Mean = mean(DYNO{:,:},1).'; % mean value
STD = std(DYNO{:,:},0,1).'; % standard deviation
Median = median (DYNO{:,:},1).'; % median
Max = max(DYNO{:,:},[],1).'; % maximum value obserbed
Min = min(DYNO{:,:},[],1).'; % minimum value observed
CV = STD ./ Mean; % Coefficient of variation
LNV = Min ./Mean; % Lowest normalized value
Description = (DYNO.Properties.VariableNames).';
DYNO_Summary = table( Units, Mean, STD, Median, Min, Max, CV, LNV,'RowNames
    ',Description);
end

function dynofile(DYNO, DYNO_Summary)
global Datafile
filename = strrep(Datafile,'data.tdms','DYNO.csv');
fid = fopen(filename, 'w');
fprintf(fid, '%s, %s, %s, %s, %s, %s, %s, %s, %s, %s, %s,%s, %s, %s, %s, %s
    , %s, %s, %s, %s, %s,%s, %s, %s, %s, %s, %s, %s, %s, %s, %s,%s, %s, %s,
     %s, %s, %s, %s, %s, %s, %s,%s, %s, %s, %s\n', DYNO.Properties.
    VariableDescriptions{1,1:end}); %DYNO.Properties.VariableNames
```

```
fprintf(fid, '%s, %s, %s, %s, %s, %s, %s, %s, %s, %s, %s,%s, %s, %s, %s, %s
    , %s, %s, %s, %s, %s,%s, %s, %s, %s, %s, %s, %s, %s, %s, %s,%s, %s, %s,
     %s, %s, %s, %s, %s, %s, %s,%s, %s, %s, %s\n', DYNO.Properties.
    VariableUnits{1,1:end});
fclose(fid);
DYNOarray = table2array(DYNO);
dlmwrite(filename, DYNOarray, '-append');

% Write Dyno summary to file
filename = strrep(Datafile,'data.tdms','DYNO_Summary.csv');
writetable(DYNO_Summary,filename,'WriteRowNames',true);
end

function [CYL, CAS, ind] = PressAnalysis(ind,CAD,CylV,CylP,CylY,CylA,DYNO)

% Declare global variables
global Res Vd Sp B Vc

% Specify heat loss model
Heatmodel = 'Woschni'; % 'Hohenberg' or 'Woschni'

%%%%%%%%%%%%%%%%%%%% Allocation of memory %%%%%%%%%%%%%%%%%%%%%%%%

CylTc=zeros(length(CAD),size(CylP,2)); % Corrected In Cylinder Temperature
CylU=zeros(length(CAD),size(CylP,2)); % Internal energy CAD+1
CyldU=zeros(length(CAD),size(CylP,2)); % Internal energy CAD+1
Cylm = zeros(length(CAD),size(CylP,2)); % Instantaneous Work
PolyC = zeros(size(CylP,2),1); % Polytropic coefficiency compression
PolyE = zeros(size(CylP,2),1); % Polytropic coefficiency expansion

dgQ = zeros(length(CAD),size(CylP,2)); % Instant Heat loss to wall [J/CAD]
gQ = zeros(length(CAD),size(CylP,2)); % Cumulative Heat loss to wall [J]
hc = zeros(length(CAD),size(CylP,2)); % Cylinder Heat transfer coefficient

gas = GRI30;

%%%%%%%%%%%%%%%%% Specifies some useful parameters %%%%%%%%%%%%%%%%%%%
BDC1 = angle2index(-180,Res); %BDC indices for Gross calculations
BDC2 = angle2index(180,Res); %TDC indices for Gross calculations

%%%%%%%%%%%%%%%%% Main Pressure Cylinder parameters %%%%%%%%%%%%%%%%%%

% Peak pressures and locations
[PeakP, PeakPang] = max(CylP); % [bar] [tick]
PeakP = PeakP.'; % Transpose to a column
PeakPang= PeakPang.'; % Transpose to a column

% Compression and Expansion Polytropic coeff
```

```
Y = log(CylP);
X = log(CylV);
for i = 1:1:size(CylP,2)
pcomp = polyfit(X(ind.IGN-400:ind.IGN-200),Y(ind.IGN-400:ind.IGN-200,i),1);
pexp = polyfit(X(ind.EVO-1000:ind.EVO-10),Y(ind.EVO-1000:ind.EVO-10,i),1);
PolyC(i,1) = abs(pcomp(1));
PolyE(i,1) = abs(pexp(1));
end

% Cylinder Cumulative and Instantaneous work
CylW = cumtrapz(CylV,CylP); % [J] Cumulative Work
[~, CylpdV] = gradient(CylW); % [J/tick] Intantaneous Work

nW = trapz(CylV,CylP).'; % [J] Net Indicated Work
nIMEP = nW/ Vd * 1e-5; %[bar] Net Indicated Mean Effective Pressure
nP = nW .* DYNO.EngRPM / 2 / 60; %[W] Gross Indicated Power

gW = trapz(CylV(BDC1:BDC2),CylP(BDC1:BDC2,:)).'; % [J] Gross Indicates Work
gIMEP = gW/ Vd * 1e-5; %[bar] Gross Indicated Mean Effective Pressure
gP = gW .* DYNO.EngRPM / 2 / 60; % [W] Gross Indicated Power

IFE = DYNO.FuelMEP * Vd * 1e5; %[J] Indicated Fuel Energy
ISFC = DYNO.Flowfuel * 1000 ./ ( nW / 3600); % [g/kWh] Indiccated specific
    fuel consumption
IFCE = nW ./ IFE; % [%] Indicated Fuel conversion efficiency

% Engine Efficiencies and MEPs
PMEP = gIMEP - nIMEP; % [bar] Pumping Indicated mean effective pressure
PMEPp = ((CylP(end,:)-CylP(1,:))*(CylV(BDC1)-CylV(1))/ Vd * 1e-5).'; % [bar
    ]
PMEPv = PMEP - PMEPp;% [bar]
FMEP = nIMEP - DYNO.BMEP; % [bar]

etaC = DYNO.QMEP./DYNO.FuelMEP; % [%]
etaGE = nIMEP./gIMEP; % [%]
etaTh = gIMEP./DYNO.QMEP; % [%]
etaM = DYNO.BMEP./nIMEP; % [%]

%%%%%%%%%%%%%%%%%% Cylinder mass and Internal Energy %%%%%%%%%%%%%%%%%%

for j = 1:1:size(CylP,2) % Loops over each cycle

    %%%%%% Cylinder Mass (Corrected by Blow By)%%%%%%%%%%%%%%%%%%%%%%%
    set(gas, 'T', DYNO.TempExhaust(j), 'P', CylP(ind.EVC,j), 'Y', CylY(:,j)
        )
    CylM = density(gas) * CylV(ind.EVC); % [kg] Cylinder mass at EVC.
    CylM = CylM + DYNO.FlowCycle(j);
```

```
    Cylrho = CylM/CylV(ind.IVC);
    set(gas, 'Rho', Cylrho , 'P', CylP(ind.IVC,j), 'Y', CylY(:,j))
    CylTc(ind.IVC,j) = temperature(gas); % [K] Initial Temperature
       assumption.
    CylU(ind.IVC,j) = CylM * intEnergy_mass(gas); % [J/kg] Initial Internal
        Energy.


    % Sets IVC conditions at specified conditions by the user (T = Avg
    % Temp coolant and Temp intake.
    %set(gas, 'T', (DYNO.TempCoolantHot(j)+DYNO.TempExhaust(j))/2, 'P',
       CylP(ind.IVC,j), 'Y', CylY(:,j))
    %CylM = density(gas) * CylV(ind.IVC); % [kg] Cylinder mass at IVC.
    %CylTc(ind.IVC,j) = temperature(gas); % [K] Initial Temperature
       assumption.
    %CylU(ind.IVC,j) = CylM * intEnergy_mass(gas); % [J/kg] Initial
       Internal Energy.

    % Corrected Mass after % blowby
    Bb = 0.01; % Percentage of Blowby
    Mbb = Bb * CylM; % Total mass leaked by Blowby
    Cbb = Mbb / trapz(CAD(ind.IVC:ind.EVO),CylP(ind.IVC:ind.EVO,j).^2); %
       Blowby constant
    dMbb = zeros(length(CAD),1);
    dMbb(ind.IVC:ind.EVO) = Cbb * CylP(ind.IVC:ind.EVO).^2; % Blowby mass
       flow rate
    Cylm(:,j)= CylM * ones(length(CAD),1) - cumtrapz(CAD,dMbb); % Cylinder
       mass at given angle.

    %%%%%%% In-Cylinder Temperature (Tc) & Int. Energy (U) %%%%%%%%%%%

    for i = ind.IVC+1:1:ind.EVO % Loops over crank angle IVC to EVO
            v = CylV(i)/Cylm(i,j); % Specific volume
            set(gas, 'V', v, 'P', CylP(i,j)) % Assumes constant mixture
               composition
            CylU(i,j) = Cylm(i,j) * intEnergy_mass(gas); % [J]
            CylTc(i,j) = temperature(gas);
    end

end

% Peak pressures and locations
[PeakT, PeakTang] = max(CylTc); % [K] [tick]
PeakT = PeakT.'; % Transpose to a column
PeakTang= PeakTang.'; % Transpose to a column

%%%%%%%%%%%%%%%% Apparent Heat Release Rate (aHRR) %%%%%%%%%%%%%%%%%%%%
```

```
CylU(ind.EVO+1,:) = CylU(ind.EVO,:); % For differentiation purposes only
CylU(ind.IVC-1,:) = CylU(ind.IVC,:); % For differentiation purposes only

[~, CyldU(ind.IVC:ind.EVO,:)] = gradient(CylU(ind.IVC:ind.EVO,:));
dnQ = CyldU + CylpdV; % apparent Heat Release Rate (J/CAD)
nQ = cumtrapz(dnQ); % apparent cumulative heat released

%%%%%%%%%%Combustion timing CASOC CA10 CA50 CA90 CAEOC %%%%%%%%%%%%%%%%%%%

nQN = nQ./(max(nQ)-min(nQ));
CAXX = [0.03, 0.1, 0.5, 0.9, 0.97]; % Combustion percentages
idx = zeros(5,size(CylP,2));
for i=1:1:numel(CAXX)
[~, idx(i,:)] = min(abs(nQN(ind.IGN:ind.EVO,:) - CAXX(i))); % Find the
    closest index to a given percentage
end
ind.CASOC = idx(1,:).' + ind.IGN;% ind.IVC+idx(1);
ind.CA10 = idx(2,:).' + ind.IGN;%ind.IVC+idx(2);
ind.CA50 = idx(3,:).' + ind.IGN;%ind.IVC+idx(3);
ind.CA90 = idx(4,:).' + ind.IGN;%ind.IVC+idx(4);
ind.CAEOC = idx(5,:).' + ind.IGN;%ind.IVC+idx(5);

CASOC = CAD(ind.CASOC); % [CAD] 3%
CA10 = CAD(ind.CA10); % [CAD] 10%
CA50 = CAD(ind.CA50); % [CAD] 50%
CA90 = CAD(ind.CA90); % [CAD] 90%
CAEOC = CAD(ind.CAEOC); % [CAD] 97%

Burn1090 = CA90 - CA10; % [dCAD] Combustion duration

%%%%%%%%%%%%%% Gross Heat Release Rate (gHRR) %%%%%%%%%%%%%%%%%%%%%
switch Heatmodel
    case 'Hohenberg'
        [dgQ, hc] = Hohenberg(CylV, CylP, CylTc, CylA, Sp, (DYNO.
            TempCoolantHot+DYNO.TempExhaust)/2, DYNO.EngRPM, ind);

    case 'Woschni'
        % Computes emulated motoring trace based on polytropic coefficient.
        pmot = CylP;
        for j = 1:1:size(CylP,2)
            for i=ind.IGN+1:1:numel(CylV)
                pmot(i,j) = pmot(i-1,j) * (CylV(i-1)/CylV(i))^PolyC(j);
            end
        end
        [dQw, hc] = Woschni (B, CylV, CylP, CylTc, CylA, Sp, Vd, Vc, ind,
            pmot, nIMEP,CylTc(ind.IVC,j), DYNO.EngRPM); %(DYNO.
```

```
            TempCoolantHot+DYNO.TempExhaust)/2
        Qw = cumtrapz(CAD, dQw);
        gQ = nQ + Qw;

    otherwise

end
```

Outputs

```
CYL.CylTc = CylTc;
CYL.Cylm = Cylm;
CYL.pmot = pmot;
CYL.nQ = nQ;
CYL.dnQ = dnQ;
CYL.hc = hc;
CYL.Qw = Qw;
CYL.dQw = dQw;
CYL.gQ = gQ;

% Creates the CAS data table!
CAS = table(PolyC, PolyE, PeakP, PeakPang, PeakT, PeakTang,...
    gW, nW, IFE, gP, nP, gIMEP, nIMEP, PMEP, PMEPp, PMEPv, FMEP,...
    ISFC, IFCE,...
    CASOC, CA10, CA50, CA90, CAEOC, Burn1090,...
    etaC, etaTh, etaGE, etaM);
CAS.Properties.VariableUnits = {'-' '-' 'bar' 'CAD' 'K' 'CAD'...
    'J' 'J' 'J' 'W' 'W' 'bar' 'bar' 'bar' 'bar' 'bar' 'bar'...
    'g/kWh' '%'...
    'CAD' 'CAD' 'CAD' 'CAD' 'CAD' 'CAD'...
    '%' '%' '%' '%'};
CAS.Properties.VariableDescriptions = {...
    'Polytropic Compression coefficient (kc)'...
    'Polytropic Expansion coefficient (kc)'...
    'Peak Pressure (Pmax)'...
    'Peak Pressure location (CADpmax)'...
    'Peak Pressure (Tmax)'...
    'Peak Temperature location (CADTmax)'...
    'Gross Indicated Work (gW)'...
    'Net Indicated Work (nW)'...
    'Indicated Fuel Energy (IFE)'...
    'Gross Indicated power (gP)'...
    'Net Indicated power (nP)'...
    'Gross Indicated mean effective pressure (gIMEP)'...
    'Net Indicated mean effective pressure (nIMEP)'...
    'Pumping mean effective pressure (PMEP)'...
    'Pumping throttle mean effective pressure (PMEPp)'...
```

```
    'Pumping valves mean effective pressure (PMEPv)'... % recently added
    'Friction mean effective pressure (FMEP)'...
    'Net indicated specific fuel consumption (ISFC)'...
    'Net indicated fuel coonversion efficiency (IFCE)'...
    'Start of Combustion (CASOC)'...
    'Start of Combustion (CA10)'... %should not be included here!
    'Start of Combustion (CA50)'...
    'Start of Combustion (CA90)'...
    'Start of Combustion (CAEOC)'...
    'Combustion duration (Burn1090)'... %should not be included here!
    'Combustion efficiency (etaC)'...
    'Combustion efficiency (etaTh)'...
    'Combustion efficiency (etaGE)'...
    'Combustion efficiency (etaM)'};

end

function [CAS_Summary] = cassum(CAS)
% Generates the statistics for each measurement over all cycles.
% This includes: Mean, STD, Median, Min, Max, CV and LNV.
Units = {CAS.Properties.VariableUnits{1:1:end}}.'; % variable units
Mean = mean(CAS{:,:},1).'; % mean value
STD = std(CAS{:,:},0,1).'; % standard deviation
Median = median (CAS{:,:},1).'; % median
Max = max(CAS{:,:},[],1).'; % maximum value obserbed
Min = min(CAS{:,:},[],1).'; % minimum value observed
CV = STD ./ Mean; % Coefficient of variation
LNV = Min ./Mean; % Lowest normalized value
Description = (CAS.Properties.VariableNames).';
CAS_Summary = table( Units, Mean, STD, Median, Min, Max, CV, LNV,'RowNames
    ',Description);
end

function casfile(CAS, CAS_Summary)
global Datafile
filename = strrep(Datafile,'data.tdms','CAS.csv');
fid = fopen(filename, 'w');
fprintf(fid, '%s, %s, %s, %s, %s, %s, %s, %s, %s, %s, %s, %s, %s, %s, %s, %
    s, %s, %s, %s, %s,%s, %s, %s, %s, %s, %s, %s, %s, %s\n', CAS.Properties
    .VariableDescriptions{1,1:end}); %DYNO.Properties.VariableNames
fprintf(fid, '%s, %s, %s, %s, %s, %s, %s, %s, %s, %s, %s, %s, %s, %s, %s, %
    s, %s, %s, %s, %s,%s, %s, %s, %s, %s, %s, %s, %s, %s\n', CAS.Properties
    .VariableUnits{1,1:end});
fclose(fid);
CASarray = table2array(CAS);
dlmwrite(filename, CASarray, '-append');

% Write Dyno summary to file
```

```
filename = strrep(Datafile,'data.tdms','CAS_Summary.csv');
writetable(CAS_Summary,filename,'WriteRowNames',true);
end

function [index] = angle2index(angle,Res)
    % This function requires TDC to be represented by 0 CAD
    % 0-720, -360 to 360, -180 to 540.
    index = (360+Res)/Res + round(angle/Res);
end


function [dQw, hc] = Hohenberg(CylV, CylP, CylTc, CylA, Sp, Tc, EngRPM, ind
    )
% Hohenberg 1979
dQw = zeros(numel(CylV),1);

hc = 130 .* (CylV.^-0.06) .* ((CylP .*(1e-5)).^0.8) .* (CylTc) - 0.4 * (Sp
    + 1.4)^0.8;% [W/m2 K]
d = 0.0079248; % [m] From CFR specs 0.312 in
kw = 54 ; % [W/mK] Heywood1988 pg 706
Ut = 1./ (1./hc + d/kw); % Overall heat transfer coeffcient (Assumes temp
    of outer wall equal to temp of coolant)
dQw(ind.IVC:ind.EVO) = CylA(ind.IVC:ind.EVO) .* Ut(ind.IVC:ind.EVO) .* (
    CylTc(ind.IVC:ind.EVO) - Tc); % [J/s]
dQw = dQw / (EngRPM/60) / 360; % [J/CAD]
end

function [dQw, hc] = Woschni (B, CylV, CylP, CylTc, CylA, Sp, Vd, Vc, ind,
    pmot, nIMEP, Tc, EngRPM)
% Merker 2012 page 235-239
% Specify paramters
sw = 0; % Engine Swirl 0 < Sw < 3
dQw = zeros(numel(CylV),size(CylP,2));

% Writes parametric constants
C1(1:ind.IVC-1,1) = 6.18 + 0.417 * sw; % [-]
C1(ind.IVC:ind.EVO,1) = 2.28 + 0.308 * sw; % [-]
C1(ind.EVO+1:numel(CylV),1) = 6.18 + 0.417 * sw; % [-]
C2(:) = 3.24e-3; % [m/s K] % Direct injection engine
% C2 = 6.22e-3; % [m/s K] % Prechamber engine

% Builds w which is equal to a corrected mean piston speed SP
% Note that values of pressure are converted from [Pa] to [bar] by 1e5
w1 = C1 .* Sp + (C2 * (Vd * CylTc(ind.IVC)) ./ ((CylP(ind.IVC)* (1e-5)) .*
    CylV(ind.IVC))) .* ((CylP - pmot) * 1e-5); % [W/m2 K]
% if nIMEP<1
%     nimep = 1;
```

```
% else
%     nimep = nIMEP;
% end
% w2 = C1 .* Sp .* ( 1 + 2 * (Vc ./ CylV).^2 .* nimep^(-0.2)); %[W/m2 K]
% w = max(w1,w2);
w = w1;
% Computes convective heat transfer coeffcient (hc)
hc = 127.93 * (B^(-0.2)) .* ((CylP*(1e-5)).^0.8) .* (w.^0.8) .* (CylTc
    .^(-0.53)); % [W/m2 K]

% Computes instant heat transfer losses(dQw)
d = 0.0079248; % [m] From CFR specs 0.312 in
kw = 20 ; % [W/mK] Heywood1988 pg 706
Ut = hc; %1./ (1./hc + d/kw); % Overall heat transfer coeffcient (Assumes
    temp of outer wall equal to temp of coolant)
dQw(ind.IVC:ind.EVO,:) = CylA(ind.IVC:ind.EVO) .* Ut(ind.IVC:ind.EVO,:) .*
    (CylTc(ind.IVC:ind.EVO,:) - Tc.'); % [J/s]
dQw = dQw ./ (EngRPM.'/60) / 360; % [J/CAD]
end
```